A New Era of Nuclear Structure Physics

editors Yasuyuki SUZUKI Masayuki MATSUO
Susumu OHYA Takashi OHTSUBO

A New Era of

Nuclear Structure Physics

Proceedings of the International Symposium

This page intentionally left blank

A New Era of
Nuclear Structure Physics

Proceedings of the International Symposium

Kurokawa Village, Niigata, Japan
19 – 22 November 2003

editors

Yasuyuki SUZUKI
Susumu OHYA
Masayuki MATSUO
Takashi OHTSUBO
Niigata University, JAPAN

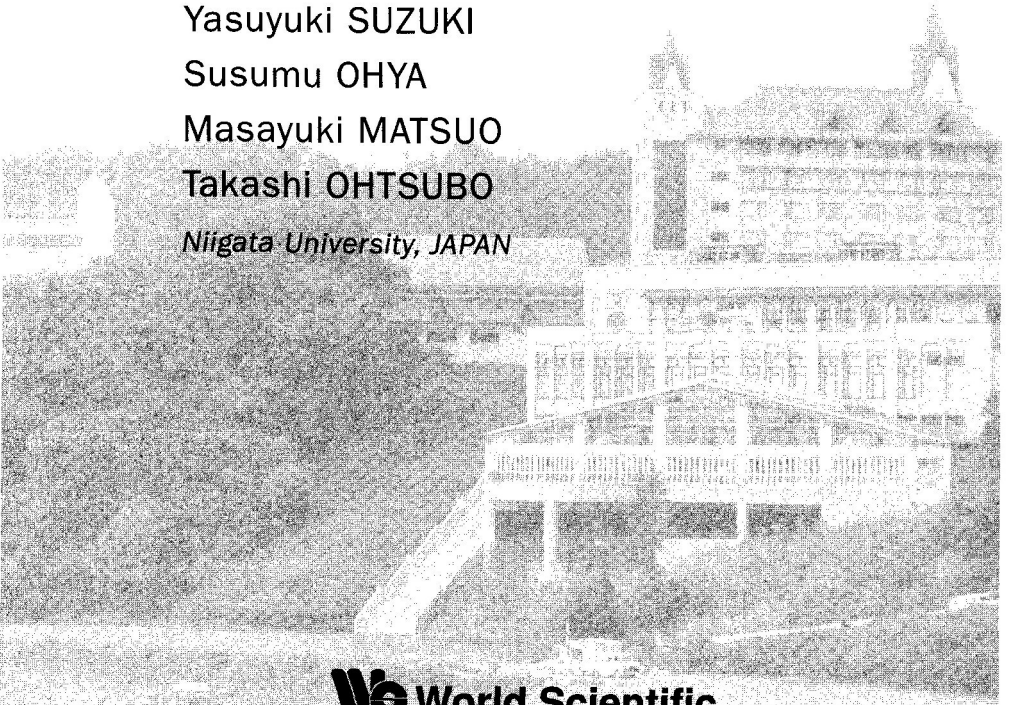

World Scientific

NEW JERSEY • LONDON • SINGAPORE • BEIJING • SHANGHAI • HONG KONG • TAIPEI • CHENNAI

Published by

World Scientific Publishing Co. Pte. Ltd.

5 Toh Tuck Link, Singapore 596224

USA office: 27 Warren Street, Suite 401-402, Hackensack, NJ 07601

UK office: 57 Shelton Street, Covent Garden, London WC2H 9HE

British Library Cataloguing-in-Publication Data

A catalogue record for this book is available from the British Library.

A NEW ERA OF NUCLEAR STRUCTURE PHYSICS

Proceedings of the International Symposium

ISBN 981-256-054-8

Printed by FuIsland Offset Printing (S) Pte Ltd, Singapore

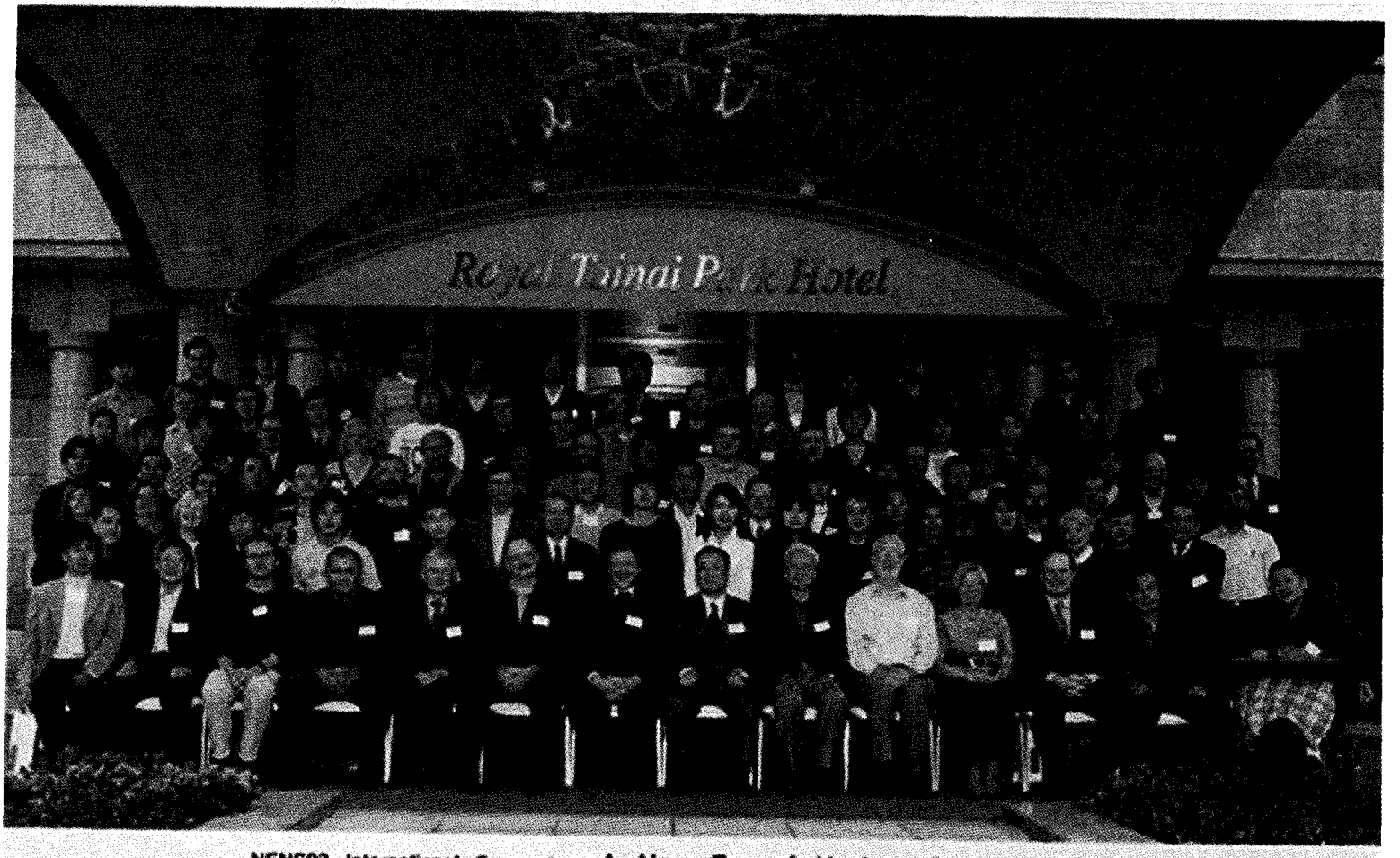

NENS03 International Symposium **A New Era of Nuclear Structure Physics**
NOVEMBER 19-22 2003

ADVISORY COMMITTEE

Y. Akaishi (KEK), A. Arima (House of Councilors), K. Ikeda (RIKEN), M. Ishihara (RIKEN), H. Sakai (Tokyo)

ORGANIZE COMMITTEE

K. Asahi (RIKEN/TIT), Y. Fujiwara (Kyoto), Y. Gono (Kyushu), K. Kato (Hokkaido), T. Kishimoto (Osaka), T. Kobayashi (Tohoku), Y. Koike (Hosei), M. Matsuo (Niigata, Scientific Secretary), K. Matsuyanagi (Kyoto), T. Ohtsubo (Niigata, Scientific Secretary), S. Ohya (Niigata, Co-Chairman), T. Otsuka (Tokyo/RIKEN), T. Suzuki (Saitama), Y. Suzuki (Niigata, Chairman),

HOST INSTITUTE

Niigata University

SPONSORS

Toshiyuki Tanaka Foundation for International Activities, Niigata University
Kurokawa Village
Inoue Foundation for Science
Uchida Energy Science Promotion Foundation
Research Foundation for the Electrotechnology of Chubu
Intelligent Cosmos Academic Foundation
Niigata Visitors and Convention Bureau
Mr. Masakatsu Hatta

SUPPORTERS

The Physical Society of Japan
The Institute of Physical and Chemical Research (RIKEN)
High Energy Accelerator Research Organization (KEK),
Institute of Particle and Nuclear Studies
Niigata Prefecture

Preface

The International Symposium "A New Era of Nuclear Structure Physics" took place in Kurokawa Village, Niigata, Japan, from November 19 to 22, 2003. The symposium was hosted by Niigata University.

The symposium was attended by about 100 physicists from 19 countries. The participants were accommodated at Tainai hotels with good service and welcomed by the village as well as the beauty of rural surroundings.

The purpose of the symposium was to discuss the recent developments in experimental and theoretical studies on nuclear structure physics, which are more or less motivated by the desire of extending the knowledge acquired in studies on stable nuclei to such more general level that is valid under some extreme conditions. Naturally the largest part of the articles was devoted to the physics of exotic nuclei with the connections to nuclear forces, mean-field description, and excitation to continuum states.

This volume contains 46 papers out of the 48 lectures delivered at the symposium as well as 28 papers out of the posters displayed at the poster session of the symposium. The 46 papers are arranged according to the sessions of the symposium: nuclear force and few-body systems, hypernuclei and computational methods, nuclear structure from realistic forces and shell model, nuclear shapes and rotation, light exotic nuclei, light exotic nuclei and clustering, heavy exotic nuclei, mean-field methods and effective interactions, shell structure in exotic nuclei, deformation and shell structure, excitation of exotic nuclei, density and gamma-transitions of unstable nuclei, and spectroscopy of unstable nuclei.

The editors are very grateful to the speakers for their nice presentations and their manuscripts. The publication of the proceedings would not be possible without the support from the sponsors for the symposium. The editors thank all of them for their financial aid.

Niigata, April 2004

Editors Y. Suzuki
S. Ohya
M. Matsuo
T. Ohtsubo

This page intentionally left blank

Contents

[a]not received

[b]not received

This page intentionally left blank

Opening address

This page intentionally left blank

Welcome address

Ladies and gentlemen,

I am Akira Hasegawa, the President of Niigata University. Welcome to the International Symposium: A New Era on Nuclear Structure Physics. It is a great honor for me to give a word of welcome to this symposium. I am very pleased to welcome about 100 leading scholars and researchers from 20 countries, here in Kurokawa village. Kurokawa area was first referred to in Nihonshoki, Chronicle of Japan, about 1300 years ago as the district of producing "burning water", crude petroleum. This is the reason why this area was named Kurokawa, Kuro stands for black and Kawa stands for river, namely, "black river".

I would like to introduce a little about Niigata University. We have 9 undergraduate faculties, 7 graduate schools, including humanities and social sciences, education, natural sciences, medical and dental sciences, and Brain Research Institute. As you know, all of the national universities in Japan are now on a big turning point. In next April, they will be independent agencies with legal personality for promoting further intense education, research and service. By this reformation, we will do encourage unique and characteristic researches in Niigata University.

We are proud of our nuclear physics group in both theory and experiment with a rich tradition, which is one of the most active research groups in Niigata University. I would like to mention the names of three retired professors who had made great contribution to this field in Niigata University. Late Professor T. Hikosaka proposed a pioneering idea of a shell-like model for an atomic nucleus in 1934 and a nuclear energy generation in 1944. Professor N. Mutsuro established a unique low-temperature nuclear-orientation experiment in Niigata. Professor K. Ikeda, through his well-known works on cluster models and unstable nuclei in particular, contributed to making Niigata University one of the active nuclear-physics-study centers in Japan.

I strongly hope that during this symposium a large number of epoch-making results will be presented, new ideas and deep insights will be stimulated and exchanged, and further developments and collaborations in nuclear physics will come out. Finally, I express again sincere gratitude to all of you who have come together here today, especially from abroad, and wish that this symposium may be fruitful.

Thank you for your attention.

Akira Hasegawa
the President of Niigata University

Opening address

Dear Ladies, Gentlemen, Colleagues and Friends,

It is my great honor and pleasure to give an opening address on behalf of the organizing committee. First of all, we would like to express our hearty thanks to all of you, especially to those who have come from abroad, for the participation in this symposium. This symposium is hosted by Niigata University, located in the city of Niigata which is, about 50 km west from here, situated on the coast of Sea of Japan.

About one hundred years have passed since Antoine Henri Becquerel discovered radioactivity in 1896 and Ernest Rutherford established the existence of an atomic nucleus in 1911. Since then nuclear physics has been actively studied in the last century. The discovery of nuclear fission by Hahn and Strassmann was probably the most prominent among others in having given profound influence of nuclear sciences on human life. At the same time we also recall many useful applications of nuclear sciences to medical care and examination such as a charged particle therapy and a magnetic resonance imaging. We could certainly call the 20th century as an era of nuclear sciences from the viewpoint of physics and politics as well.

As many of you may know, K. S. Krane gave a list of some of the major events in nuclear physics in his textbook 'Introductory Nuclear Physics' (1987). In the last fifteen years of the 20th century just after the list ends in 1983, we saw many important discoveries and major progress in the study of unstable nuclei. In the wake of this progress a new trend is taking shape in nuclear structure physics. A systematic exploration of nuclear properties is in progress, in which the investigations performed for stable nuclei are extended to those providing extreme conditions, such as large neutron/proton ratio and very weak binding. Moreover, these exotic conditions bear on few-body structure and cluster structure, shell structure, deformation and pairing correlations. The problems of hypernuclei are somewhat similar since they are also weakly bound systems of strongly interacting particles as strangeness increases. The study of such systems calls for more reliable description of fundamental interactions of constituents, new precise computational techniques and new versions of the nuclear models exploiting the knowledge of such interactions.

Several new accelerator facilities are being designed and built world-

wide for promoting nuclear sciences. For example, in Japan, the Radioactive Beam Factory Project of RIKEN producing elements up to Uranium is scheduled to be in operation in 2006 to achieve comprehensive understanding of nuclei, may it be stable or unstable, and Japan Proton Accelerator Research Complex (J-PARC) of a joint project of KEK and JAERI, using intense proton beam, will produce secondary particles (neutron, pion, K-meson, anti-proton) in 2007 to study nuclear and particle physics, material sciences, and promotion of nuclear transmutation technique. I am looking forward to interesting results and projects from GSI, GANIL, MSU, CERN and others. I hope that these stimulate the developments of nuclear structure theory in the 21st century.

A list of our sponsors for this symposium includes: Toshiyuki Tanaka Foundation for International Activities, Niigata University; Kurokawa Village; Inoue Foundation for Science; Uchida Energy Science Promotion Foundation; Research Foundation for the Electrotechnology of Chūbu; Intelligent Cosmos Academic Foundation; Niigata Visitors and Convention Bureau; and Mr. Masakatsu Hatta. We thank them for their financial support.

We hope that in this symposium new results are presented, interesting ideas and discussions are exchanged and the participants are stimulated to further future progress. The hotels where we house are located in beautiful natural surroundings and welcome all of you with different kinds of hot spas. I wish you a successful symposium and a good time here in Tainai, Kurokawa.

Thank you for your attention.

Yasuyuki Suzuki
Chairperson of the Organizing Committee
Niigata University

This page intentionally left blank

Nuclear force and few-body systems

This page intentionally left blank

NUCLEAR FORCES AND FEW-NUCLEON STUDIES BASED ON CHIRAL PERTURBATION THEORY

W.GLÖCKLE[1], E.EPELBAUM[2], U.G.MEIßNER[3],A.NOGGA[4],H.KAMADA[5], H.WITAŁA[6]

[1] *Inst. Theor. Phys., Ruhr-Universität Bochum, D-44780 Bochum, Germany*

[2] *Jefferson Laboratory, Newport News, VA 23606, USA*

[3] *Universität Bonn, Helmholtz-Institut für Strahlen- und Kernphysik (Theory) D-53115 Bonn and FZ Jülich, IKP (Theorie), D-52425 Jülich, Germany*

[4] *Inst. for Nuclear Theory, University of Washington, Seattle, WA 98195, USA*

[5] *Department of Physics, Faculty of Engineering, Kyushu Institute of Technology, 1-1 Sensuicho, Tobata, Kitakyushu 804-8550, Japan*

[6] *Jagellonian University, Institute of Physics, Reymonta 4, 30-059 Cracow, Poland*

After a brief review on the status of few–nucleon studies based on conventional nuclear forces, we sketch the concepts of the effective field theory approach constrained by chiral symmetry and its application to nuclear forces. Then first results for few–nucleon observables are discussed.

1. Introduction

The basic questions posed in few–nucleon physics have a long tradition. Already E.Wigner [1] and J.Schwinger [2] asked, whether one can understand the binding energies of the helium nuclei on the basis of two–nucleon (NN) forces and the Schrödinger equation. Over the years, robust mathematical formulations, which are strictly equivalent to the Schrödinger equation, have been developed. These are the Faddeev-Yakubovsky equations [3,4], the Greens Function Monte Carlo [5], the stochastic variational [6], the Gaussian basis [7] and the hyperspherical harmonics [8] methods, which together with modern NN forces like AV18 [9], Nijm I,II [10] and CD-Bonn [11] allow for an unambiguous answer: the available NN forces alone underbind light

Table 1. Binding energies in MeV based one NN forces only

NNF	^{3}H	^{4}He	^{6}He	^{6}Li
Nijm	7.74	24.98		
CDB	8.01	26.26		
AV18	7.60	24.10	23.90	26.90
Exp	8.48	28.30	29.30	32.00

Table 2. NNF +3NF predictions for ^{4}He

NNF + 3NF	^{3}H	^{4}He
CDB + TM	8.48	28.40
AV18 + TM	8.45	28.36
AV18 + URB	8.48	28.50
Exp	8.48	28.30

nuclei. Some examples for theoretical binding energies in comparison to experimental ones are displayed in Table 1. Also in 3N scattering quite a few discrepancies appear using NN forces only [12,13]. A missing dynamical ingredient, naturally suggested in meson theory, is the three–nucleon (3N) force. First trial models built around the old Fujita-Miyazawa force [14], a 2π–exchanges force with an intermediate Δ, are the Tucson-Melbourne (TM) [15] and the Urbana IX (URB) [16] forces, which contribute additional binding and can be adjusted to the ^{3}H binding energy in conjunction with the available NN forces. Then one can predict binding energies beyond A=3 and 3N scattering observables. As an example, we display in Table 2 the α–particle binding energies for various force combinations, which come rather close to the experimental value [17] . For the partially promising results in 3N scattering we refer the reader to [18,19] and [13]. For nuclei beyond A=4 see [20] and [21], where extensions to the Urbana IX model were applied. A systematic approach and consistency between NN and 3N forces are still missing. In the following we sketch the concepts of a consistent approach based on effective field theory (EFT) constrained by chiral symmetry, show resulting nuclear forces and first applications in the few–nucleon sector. We end with a brief outlook.

2. The Concepts

We start with a brief reminder. The QCD Lagrangian for massless up and down quarks is invariant under global flavor $SU(2)_L \times SU(2)_R$ transformations or, equivalently, under vector and axial vector transformations. This is called chiral symmetry. Among other facts, the absence of parity doublets of low mass hadrons suggests that the axial symmetry is spontaneously broken. The pions are natural candidates for the required Goldstone bosons. They acquire a nonvanishing mass due to the explicit symmetry breaking caused by the small up and down quark masses. We are interested in low

energy nuclear physics, where the degrees of freedom are the composite hadrons. Their interaction has to be described by an effective Lagrangian, which could not yet be derived from QCD. Nevertheless, at least one important requirement is known: the effective Lagrangian has to be constrained by chiral symmetry and should include explicitly symmetry breaking parts proportional to powers of the quark masses. The application we have in mind is for generic nucleon momenta comparable to the π–mass and somewhat higher, but still smaller than the ρ–mass. In that case a standard one–boson exchange picture turns into NN contact forces for the heavy meson exchanges and only the one-pion exchange is kept explicitly. The construction of the most general effective Lagrangian out of pion and nucleon fields constrained by chiral symmetry is nontrivial due to the fact that no nontrivial linear realization (representation) of $SU(2) \times SU(2)$ with pion fields can be formed. The formalism has been worked out in seminal papers by [22,23]. The chirally invariant expressions are build up out of the nucleon fields and covariant derivatives (nonlinear in the pion fields) and of the pion and nucleon fields. There is an infinite number of possible terms, which can be ordered according to the parameter

$$\Delta = d + \frac{1}{2}n - 2 \tag{1}$$

characterizing the vertices. Here d is the number of derivatives and n the number of nucleon field operators. Spontaneously broken chiral symmetry enforces $\Delta \geq 0$.

The first few terms for the interacting effective Lagrangian after a p/m expansion (for heavy baryon formalism see [24]) look like

$$\begin{aligned}
\mathcal{L}_{eff} \;=\; & \left.\begin{array}{l} -N^\dagger \left[\frac{g_A}{2F}\boldsymbol{\tau}\boldsymbol{\sigma}\cdot\boldsymbol{\nabla}\boldsymbol{\pi} + \frac{1}{4F^2}\boldsymbol{\tau}\cdot(\boldsymbol{\pi}\times\dot{\boldsymbol{\pi}}) + \cdots\right] N \\ -\frac{1}{2}C_S\left(N^\dagger N\right)\left(N^\dagger N\right) - \frac{1}{2}C_T\left(N^\dagger\boldsymbol{\sigma}N\right)\left(N^\dagger\boldsymbol{\sigma}N\right) \end{array}\right\} \Delta = 0 \\
& \left.\begin{array}{l} +\frac{1}{F^2}N^\dagger\left[-2c_1 m_\pi^2\pi^2 + c_3\partial_\mu\boldsymbol{\pi}\partial^\mu\boldsymbol{\pi}\right. \\ \left. -\frac{1}{2}c_4\varepsilon_{ijk}\varepsilon_{abc}\sigma_i\tau_a(\nabla_j\pi_b)(\nabla_k\pi_c) + \cdots\right] N \\ +\frac{D_1}{F}(N^\dagger N)(N^\dagger\boldsymbol{\sigma}\cdot\boldsymbol{\tau}N)\cdot\boldsymbol{\nabla}\boldsymbol{\pi} \\ +E_1(N^\dagger N)(N^\dagger\boldsymbol{\sigma}N)^2 \end{array}\right\} \Delta = 1 \\
& \left.\begin{array}{l} -\frac{1}{2}C_1\left[(N^\dagger\boldsymbol{\nabla}N)^2 + (\boldsymbol{\nabla}N^\dagger N)^2\right] \\ +\cdots \\ +C_7(\partial_i N^\dagger\sigma_l\partial_i N)(N^\dagger\sigma_l N) \end{array}\right\} \Delta = 2 \\
& +\cdots
\end{aligned} \tag{2}$$

The terms are grouped according to $\Delta = 0, 1$ and 2. The parameters of $\mathcal{L}_{eff}$, the so called low–energy constants (LEC's), can be partitioned in sev-

eral groups: some can be determined in the π-N system (g_A, F, c_1, c_3, c_4) and others from nucleonic systems only ($C_S, C_T, E_1, C_1, ...C_7$). The constant D_1 also affects the NNπ system. All these constants are of course not determined by chiral symmetry, but have to be adjusted to experimental data.

3. Nuclear Forces

To arrive at nuclear forces the pion degrees of freedom have to be eliminated. We use an unitary transformation of the field theoretical Hamiltonian [25,26] going back to Okubo [27]. That transformation decouples the purely nucleonic Fock space from the one, which includes at least one pion. That elimination process is controlled by the low–momentum expansion [25]. A resulting NN force V receives contributions of the order

$$V \sim (Q/\Lambda)^\nu \tag{3}$$

where Q is a generic external momentum and Λ is the mass scale, which enters the (renormalized) values of the LEC's. The power ν is given by

$$\nu = -4 + 2N + 2L + \sum_i V_i \Delta_i, \tag{4}$$

here L is the number of loops and V_i the number of vertices of type i. Therefore, if one sticks to momenta Q such that $Q \ll \Lambda$ and Q/Λ is a small quantity, the effects of nuclear forces decrease with increasing ν. Clearly, since $\Delta \geq 0$, one has $\nu \geq 0$. Thus, if one wants to derive nuclear forces in the low–Q regime with a given accuracy, one needs only a finite number of terms in $\mathcal{L}_{eff}$ with the smallest Δ's and the finite number of pions.

The first few orders for nuclear forces can easily be listed using the terms in Eq. (2). The leading order (LO) for $\nu = 0$ and $N = 2$ requires $L = 0$ and $\Delta_i = 0$. This leads to two types of vertices with $d = 1$, $n = 2$ and $d = 0$, $n = 4$, which occur in the one-pion exchange and two contact forces, respectively. ν =1 does not exist and the next-to-leading order (NLO) with $\nu = 2$ and $N = 2$ requires either $L = 1$, $\Delta_i = 0$ or $L = 0$, $\Delta_i = 2$. In the first case one can form various types of 2π–exchange processes with $d = 1$, $n = 2$ vertices; in the second case one encounters additional NN contact forces with 7 different types of vertices with $d = 2$, $n = 4$. At NNLO ($\nu = 3$) additional 2π–exchange NN forces with higher order vertices occur. Also the first nonvanishing 3N forces of three different topologies show up. They are without loops ($L = 0$) and with $\Delta \leq 1$ vertices. A 2π–exchange process, a 1π–exchange between a NN contact force and the third nucleon

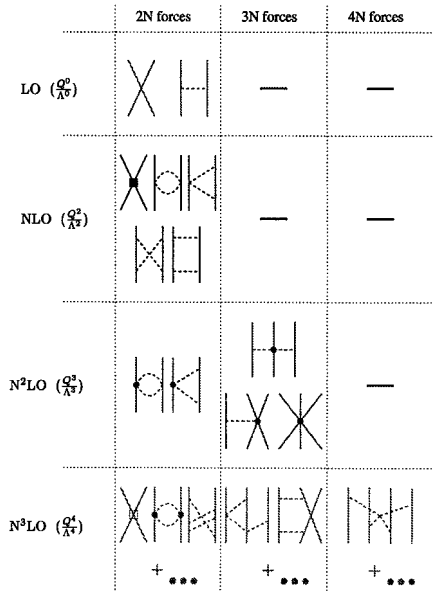

Figure 1. Hierarchy of nuclear forces.

and a pure 3N contact force are of this form. Each of the latter two depends on one unknown LEC, whereas the 2π–exchange is parameter–free in the sense that the LEC's are determined in the πN–system. That hierarchy of nuclear forces is illustrated in Fig. 1. Thus, chiral EFT provides a natural explanation why 3N forces are less important than 2N forces, 4N forces are less important than 3N forces, etc. We would also like to emphasize that all forces are analytically given and we refer the reader to [28].

The derived nuclear forces are valid only at low Q and have unphysical behavior at large Q (they grow with increasing momenta). The Schrödinger equation needs therefore to be regularized. This is achieved by introducing V_{reg} according to

$$V_{reg}(\mathbf{p}', \mathbf{p}) = e^{-(p'^2/\Lambda^2)^2} V(\mathbf{p}', \mathbf{p}) e^{-(p^2/\Lambda^2)^2} . \tag{5}$$

Λ should be not too small in order not to cut off the physics of the π-exchanges and not too large in order to exclude uncontrolled high–energy physics. It turned out that

$$500 \text{ MeV/c} \leq \Lambda \leq 600 \text{ MeV/c} \tag{6}$$

is a good choice. The Λ-dependence is expected to get weaker with increas-

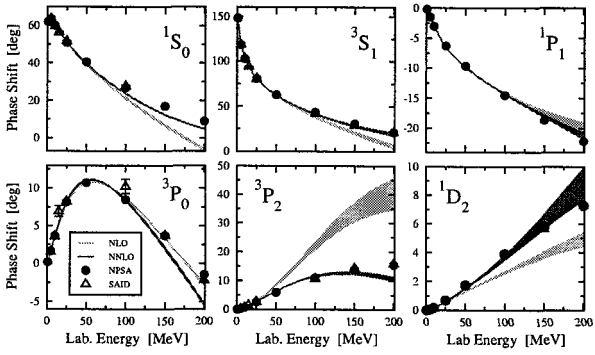

Figure 2. NN phase shifts for NLO versus NNLO.

ing order in the expansion [29,30]. Notice that the original idea and the first applications of chiral perturbation theory to nuclear systems go back to [31,32,33]. The higher orders have been worked out by N. Kaiser [34] and also applied in [35].

4. Application in the Few-Nucleon Sector

The first step is the adjustment of the LEC's. There are 2 (9) such constants at LO (NLO), which are adjusted to the NN S– and P–wave phase shifts. The only additional LEC's appearing at NNLO are $c_{1,3,4}$, which can in principle be taken from the pion–nucleon system (see [28] for more details). Our results for selected partial waves are illustrated in Fig. 2. In the 3N system we adjust the two LEC's entering the 3N force to the ^{3}H binding energy and the doublet nd scattering length a_{nd} [36]. Then, up to and including NNLO, all constants are fixed. We now display some results and refer the reader to [36] for more details. The α-particle binding energy for Λ = 500 (600) MeV/c turns out to be 29.51 (29.98) MeV which comes close to the "experimental" value 29.8 MeV (This is a corrected value for np forces only). Also the results for 3N scattering look mostly promising and we display a few examples in Figs. 3 and 4. Finally we show in Fig. 5 an application to ^{6}Li which has been elaborated in the no–core shell model framework [37].

5. Summary and Outlook

EFT and chiral symmetry is a systematic path towards nuclear forces. The nuclear forces are built out of multi-pion exchanges, which áre parameter

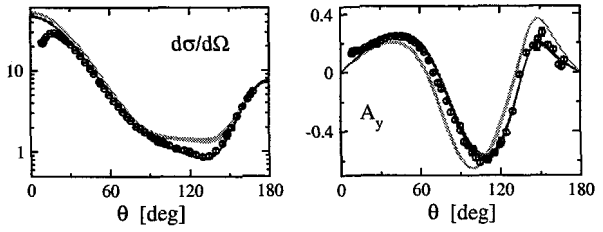

Figure 3. pd elastic observables at 65 MeV. Curves as in Fig.2. For data see [36]

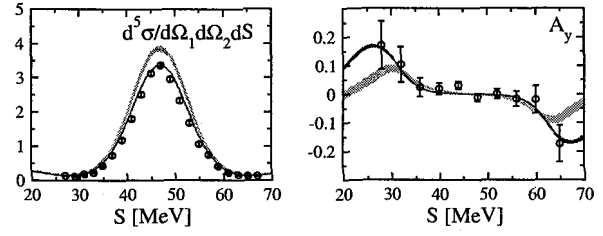

Figure 4. pd break up data versus theory. Curves as in Fig. 2. For data see [36]

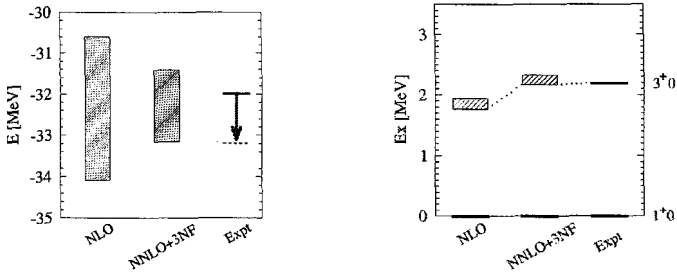

Figure 5. Predictions for the ^{6}Li ground and excited state.

free and a string of contact forces, which parameterize the not yet understood short range physics. 3N forces are consistent to 2N forces. The dominance of 2N forces over 3N forces is naturally explained in this theoretical framework. The regularization of the pion loops, which removes uncontrolled high energy (short range) physics, has recently been formulated using the spectral function representation [38,39] and the application to NN forces at NNNLO(ν=4) is in progress [40]. At this order quite a few new 3N forces appear. They are parameter free and, therefore, their effects on few–nucleon observables will be of special interest. Relativistic corrections can be taken into account and are expected to converge rapidly since the

nucleon momenta stay well below the nucleon mass.

References

1. E. Wigner, Phys. Rev. 43 (1933) 252.
2. E. Gerjuoy, J. Schwinger, Phys. Rev. 61 (1942) 138.
3. L. D. Faddeev, Sov. Phys. JETP 12 (1961) 1014.
4. O. A. Yakubovsky, Sov. J. Nucl. Phys. 5 (1967) 937.
5. J. Carlson, Phys. Rev. C 36 (1987) 2026.
6. Y. Suzuki, K. Varga, Phys. Rev. C 52 (1995) 2885.
7. M. Kamimura, Phys. Rev. A 38 (1988) 621.
8. M. Fabre de la Ripelle, Ann. Phys. (N.Y.) 147 (1983) 281.
9. R. B. Wiringa, V. G. J. Stoks, R. Schiavilla, Phys. Rev. C 51 (1995) 38.
10. V. G. J. Stoks *et. al.*, Phys. Rev. C 49 (1994) 2950.
11. R. Machleidt, F. Sammarruca, Y. Song, Phys. Rev. C 53 (1996) R1483.
12. W. Glöckle *et. al.*, Phys. Rep. 274 (1996) 107.
13. K. Sekiguchi, contribution to this conference.
14. J. Fujita and H. Miyazawa, Progress of Theor. Phys. 17 (1957) 360.
15. S. A. Coon, H. K. Han, Few Body Systems 30 (2001) 131.
16. B. S. Pudliner *et. al.*, Phys. Rev. C 56 (1997) 1720.
17. A. Nogga *et. al.*, Phys. Rev. C 65 (2002) 054003.
18. H. Witała *et. al.*, Phys. Rev. C 63 (2001) 024007.
19. J. Kuroś-Żołnierczuk *et. al.*, Phys. Rev. C 66 (2002) 024004.
20. J. Carlson, R. Schiavilla, Rev. of Mod. Phys. 70 (3) (1998) 743.
21. S. C. Pieper *et. al.*, Phys. Rev. C 64 (2001) 014001.
22. S. Weinberg, Phys. Rev. 166 (1968) 1568.
23. S. Coleman, J. Wess, B. Zumino, Phys. Rev. 177 (1969) 2239.
24. E. Jenkins, A. V. Manohar, Phys. Lett. B 255 (1991) 558.
25. E. Epelbaum, Ph.D. thesis, Ruhr-Universität, Bochum (2000).
26. E. Epelbaoum, W. Glöckle, U.-G. Meißner, Nucl. Phys. A637 (1998) 107.
27. S. Okubo, Progr. Theor. Phys. 12 (1954) 603.
28. E. Epelbaum *et. al.*, Eur. Phys. J. A 15 (2002) 543.
29. G. P. Lepage, nucl-th/9706029.
30. J. Gegelia, G. Japaridze, Phys. Lett. B 517 (2001) 476.
31. S. Weinberg, Nucl. Phys. B363 (1991) 3.
32. C. Ordóñez, L. Ray, U. van Kolck, Phys. Rev. C 53 (1996) 2086.
33. N. Kaiser, R. Brockmann, W. Weise, Nucl. Phys. A625 (1997) 758.
34. N. Kaiser, Phys. Rev. C 61 (1999) 014003; Phys. Rev. C 62 (2000) 024001; Phys. Rev. C 64 (2001) 057001.
35. D. R. Entem, R. Machleidt, Phys. Rev. C 68 (2003) 041001(R).
36. E. Epelbaum *et. al.*, Phys. Rev. C 66 (2002) 064001.
37. A. Nogga *et. al.*, to appear in the proceedings of the 17th International Conference on Few-Body Problems in Physics, Durham, NC, 2003.
38. E. Epelbaum, W. Glöckle, U.-G. Meißner, nucl-th/0304037.
39. E. Epelbaum, W. Glöckle, U.-G. Meißner, nucl-th/0308010.
40. E. Epelbaum *et. al.*, in preparation.

MEASUREMENT OF NUCLEON-DEUTERON SCATTERING AS A GOOD PROBE TO STUDY THREE NUCLEON FORCES

K. SEKIGUCHI [A], H. SAKAI [B], H. OKAMURA [C], A. TAMII [D], T. UESAKA [B], K. SUDA [E], N. SAKAMOTO [A], T. WAKASA [F], Y. SATOU [G], T. OHNISHI [A], K. YAKO [B], S. SAKODA [B], H. KATO [B], Y. MAEDA [B], M. HATANO [B], J. NISHIKAWA [E], T. SAITO[B], N. UCHIGASHIMA [B], N. KALANTAR-NAYESTANAKI [H] AND K. ERMISCH [H]

[A] *RIKEN, Saitama 351-0198, Japan*
[B] *Department of Physics, University of Tokyo, 113-0033, Japan*
[C] *Cyclotron and Radioisotope Center, Tohoku University, 980-8578,Japan*
[D] *Research Center for Nuclear Physics, Osaka University, Osaka 567-0047, Japan*
[E] *Department of Physics, Saitama University, Saitama 338-8570,Japan*
[F] *Department of Physics, Kyushu University, 812-8581, Japan*
[G] *Department of Physics, Tokyo Institute of Technology, 152-8551, Japan*
[H] *Kernfysisch Versneller Instituut (KVI), NL-9747 AAGroningen, The Netherlands*

Precise data on the cross section and analyzing powers were measured for the d–p elastic scattering at 70, 100 and 135 MeV/u. Also deuteron to proton polarization transfer coefficients $K_y^{y'}$, $K_{xz}^{y'}$, $K_{yy}^{y'}$, $K_{xx}^{y'}$ were measured at 135 MeV/u. The measurement yielded proton induced polarization $P^{y'}$. The data were compared with Faddeev calculations with high precision nucleon–nucleon forces combined with different three-nucleon forces(3NFs), the 2π-exchange Tucson-Melbourne model, a modification thereof closer to chiral symmetry TM′, and the Urbana IX 3NF.

1. Introduction

Recent advance in computational resources has made it possible to obtain rigorous numerical Faddeev–type calculations for the three–nucleon scattering processes by using two–nucleon(2N) and three–nucleon forces (3NF). It has also allowed us to search for 3NF effects by direct comparison between such theoretical predictions and precisely measured data. To study the dynamical aspects of the 3NF effects, we have made precise measurements of cross sections and all deuteron analyzing powers and deuteron to proton polarization transfer coefficients at intermediate energies. Part of the data

are published in Refs.[1-3]

2. Experiment

The experiment was performed at the RIKEN Accelerator Research Facility (RARF) using vector and tensor polarized deuteron beams at 70, 100 and 135 MeV/u. The direction of the polarization axis was controlled by a Wien Filter system prior to acceleration [4]. At RARF the single turn extraction was available so that the polarization amplitudes were maintained. In this respect, RARF was a unique facility which provided the highly polarized deuteron beams whose spin axis was freely controlled at the target position. The beam polarization was monitored by using d–p elastic scattering[1] and it was 60 – 80% of the theoretical maximum values during the experiments. A liquid hydrogen or CH_2 (93.4 mg/cm^2) was bombarded and either scattered deuteron or recoil proton was momentum analyzed by the magnetic spectrometer SMART [5] (see Fig. 1) depending on the scattering angle and detected at the focal plane. The polarization of the scattered protons were measured with the focal-plane polarimeter DPOL [6]. The measured observables were cross section, deuteron analyzing powers (A_y^d,A_{yy},A_{xx}, and A_{xz}) in the angular range of $\theta_{\rm c.m.} = 10^\circ - 180^\circ$. Deuteron to proton polarization transfer coefficients ($K_y^{y'}$, $K_{xx}^{y'}$,$K_{yy}^{y'}$, and $K_{xz}^{y'}$) were measured at the angles $\theta_{\rm c.m.} = 90^\circ - 180^\circ$. The measurement also yielded an induced polarization ($P^{y'}$) of the outgoing protons.

3. Results and Discussion

Figure 2 shows a part of the experimental data for d–p elastic scattering with open circles. The statistical errors are only shown.

In Fig. 2, four theoretical predictions in terms of Faddeev theory are shown together with the experimental results. The dark (light) shaded bands in the figure are the Faddeev calculations with (w/o) Tucson-Melbourne (TM) 3NF [7] based on the modern nucleon–nucleon(NN) potentials, namely CDBonn [8], AV18 [9], Nijimegen I, II and 93 [10]. The dashed lines are the calculation with including Urbana IX 3NF [11] based on AV18 potential. The dotted lines are the predictions in which TM′ 3NF is taken into account and CDBonn potential is considered as the NN potential. The TM′ 3NF is a modified version of the TM 3NF closer to chiral symmetry [12,13].

Comparing the theoretical predictions with the observed values, the clear discrepancies exist between the data and the 2N force predictions

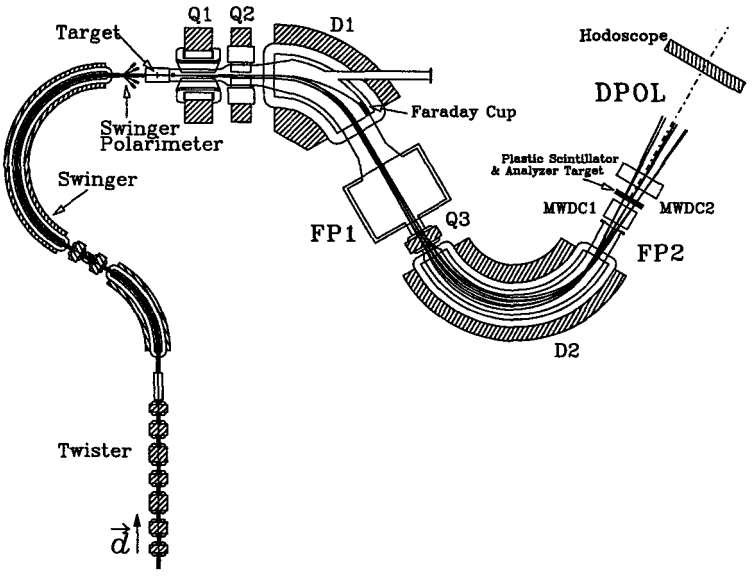

Figure 1. RIKEN magnetic spectrograph SMART

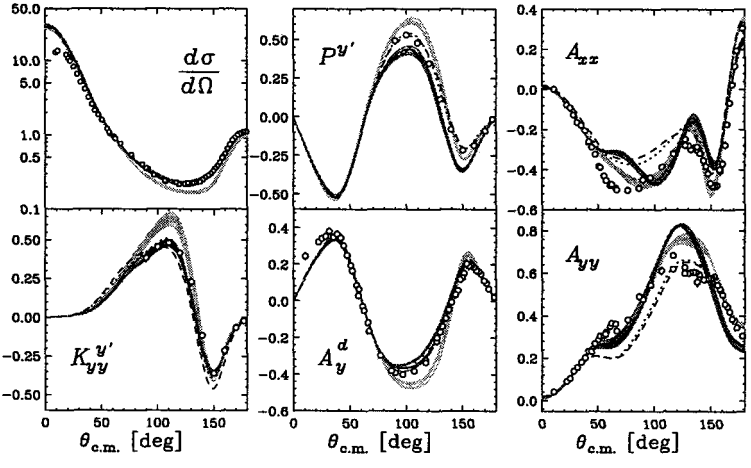

Figure 2. Differential cross section and polarization observables for d–p elastic scattering at 135 MeV/u.

and these deviations are explained well by inclusion of 3NFs for the cross section, deuteron vector analyzing power A_y^d, and polarization transfer co-

efficients $K_{xx}^{y'}$,$K_{yy}^{y'}$. All 3NF potentials considered here (TM, TM′, Urbana IX) provide almost the same 3NF effects (magnitude and direction). However for the other polarization transfer coefficients $K_{y}^{y'}$ and $K_{xz}^{y'}$ which are not shown here, large differences between the data and the 2N force predictions are not reproduced by including the 3NF models. For the induced polarization $P^{y'}$, the TM′ and Urbana-IX 3NFs well reproduce the data, however the Tucson-Melbourne 3NF fails to describe the data.

The results of the comparison for the polarization transfer coefficients reveal that the present 3NF models have deficiencies in its spin parts and that these observables are useful to clarify the spin dependence of 3NF effects.

4. Summary

In order to study of the properties of the three nucleon forces, we have measured cross sections, all deuteron analyzing powers, deuteron to proton polarization transfer coefficients and proton induced polarization for d–p elastic scattering at intermediate energies. Highly accurate data have been obtained. These results are compared with the Faddeev calculations with and without the Tucson-Melbourne 3NF, or a modification thereof closer to chiral symmetry TM′, or the Urbana IX 3NF. The large difference are obtained between the data and the 2N force predictions. Cross section and part of the spin observables show the significance of 3NFs. However not all spin observables are reproduced by incorporating the present three nucleon force models and the results show the deficiency of these models in spin parts.

5. Acknowledgement

We would like to thank W. Glöckle, and H. Witała, and H. Kamada for their strong theoretical support. We would also like to express our appreciation to the continuous help of the staff of RIKEN Accelerator Research Facility.

References

1. N. Sakamoto *et al.*, Phys. Lett. B **367**, 60 (1996).
2. H. Sakai *et al.* Phys. Rev. Lett. **84**, 5288 (2000).
3. K. Sekiguchi *et al.* Phys. Rev. C **65**, 034003 (2002).
4. H. Okamura *et al.*, AIP Conf. Proc. **293**, 84 (1994).
5. T. Ichihara *et al.*, Nucl. Phys. **A569**, 287c (1994).
6. S. Ishida *et al.*, AIP Conf. Proc. **343**, 182 (1995).

7. S. A. Coon, and M. T. Peña, Phys. Rev. C **48**, 2559 (1993).
8. R. Machleidt, Phys. Rev. C **63**, 024001 (2001).
9. R. B. Wiringa *et al.*, Phys. Rev. C **51**, 38 (1995).
10. V. G. J. Stoks *et al.*, Phys. Rev. C **49**, 2950 (1994).
11. B. S. Pudliner *et al.* Phys. Rev. C **56**, 1720 (1997).
12. J. L. Friar, D. Hüber, and U. van Kolck, Phys. Rev. C **59**, 53 (1999).
13. D. Hüber, J. L. Friar, A. Nogga, H. Witała, and U. van Kolck, Few-Body Syst. **30**, 95 (2001).

FOUR-BODY FADDEEV-YAKUBOVSKY CALCULATION USING COMPLEX ENERGY METHOD

EIZO UZU

Department of Physics, Faculty of Science and Technology,
Tokyo University of Science,
2641 Yamazaki, Noda, Chiba 278-8510, Japan
e-mail: j-uzu@ed.noda.tus.ac.jp

HIROYUKI KAMADA

Department of Physics, Faculty of Engineering, Kyushu Institute of Technology,
1-1 Sensuicho, Tobata, Kitakyushu 804-8550, Japan

YASURO KOIKE

Science Research Center, Hosei University,
2-17-1 Fujimi, Chiyoda-ku, Tokyo 102-8160, Japan,
Center for Nuclear Study, University of Tokyo,
2-1 Hirosawa, Wako, Saitama, 351-0198, Japan

The Complex Energy Method [Prog. Theor. Phys. **109**, 869L (2003)] is applied to the four body Faddeev-Yakubovsky equations in the four nucleon system. We obtain well converged solutions in all energy regions below and above the four-nucleon breakup threshold.

1. Introduction

Three-nucleons force (3NF) is studied actively on three-nucleon systems in these several years. We can expect its larger influence in four-nucleon systems due to a naive idea that there is only one combination to choose three particles in a three-body system, while there are four in a four-body system. This is an advantage to study 3NF on four-nucleon systems. On the other hand, recent investigations show that influence of 3NF appears larger in higher energy region. Therefore, it is beneficial to study reaction problems of four-nucleon systems at higher incident energies. However, nobody have succeeded to solve the four-body Faddeev-Yakubovsky (FY) equations above the four-body breakup threshold due to complexity of boundary con-

ditions in configuration space, or difficulty to handle singularities on Green's functions in momentum space.

Recently the Complex Energy Method[1] (CEM) has been revived to handle these singularities. We applied it to the four-nucleon system for a feasibility study[2]. This is a report of the result that we obtained well converged value.

2. Complex Energy Method

Fig. 1 shows threshold energies for a four-nucleon system without Coulomb force. Three-body, [2+2], and two-body propagators and four-body Green's function have singularities above 3N+N, 2N+2N, 2N+N+N (three-body), and N+N+N+N (four-body) thresholds, respectively. The singularities on the first two propagators have a similar nature to those on two-body Green's function. Two-body propagator has so-called moving singularities similar to that on three-body Green's function in a born term of Alt-Grassberger-Sandhas[3] or Amado-Mitra-Faddeev-Lovelace (e.g. [4]) equations. We can handle these singularities using the principal value prescription and (half) the residue theorem (PVR) (e.g. [5]) or the contour deformation technique (e.g. [6]). However, nobody have succeeded to extend these techniques into the energy region above the four-body threshold due to difficulty to trace the motion of singularities on four-body Green's function.

Green's functions are expressed as $G_0 = 1/(E + i\varepsilon - H_0)$ where E and H_0 are the total and kinetic energies, respectively. In above techniques, first we take the limit $\varepsilon \to 0$ and next we solve the equation avoiding the integration path on the complex plane. On the other hand, the first step

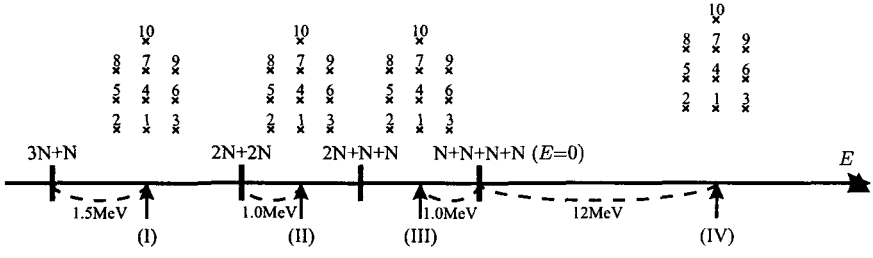

Figure 1. Illustration of threshold energies for the four-nucleon system. We choose E=0 at the four-body threshold. The various energies for the calculations are measured relative to the thresholds. The crosses indicate the complex energies where we solve the FY equations in the CEM. They are numbered by n for each choice of the energy region (I-IV).

of CEM is to solve the equation with some finite ε's. These calculations are easily carried out since there are no singularities on the real momentum axis. After obtaining solutions with various ε's, the limiting value $\varepsilon \to 0$ is taken numerically with an analytic continuation method. This technique is applicable not only for the four-body FY equations, but also two-, three-, and five- or more-body equations, for instance, it is applied to two- and three-body system[1].

3. Results

Our aim is to generate solutions applying this method to the FY equations in all energy regions including energies above the four body break-up threshold. We performed calculations in the $J^\pi = 0^+$ and $T = 0$ state for the four nucleon system. For this feasibility study the $J^\pi = 1/2^+$ state is included in the three body subsystem and the $^1S_0$ and $^3S_1$-$^3D_1$ states in the two body subsystem. All allowed spins and angular momenta within this restriction are included. The Yamaguchi potential [7, 8] is employed as the nucleon-nucleon interaction and the Coulomb force is neglected.

The FY equations are solved at four energies: (I) 1.5MeV above the 3N+N threshold, (II) 1MeV above the 2N+2N threshold, (III) 1MeV below the four body break-up threshold, and (IV) 12MeV above it (see Fig. 1). We define the $i\varepsilon$ term of the four body Green's function as $i\varepsilon + \zeta$, where ε and ζ are real. Thus G_0 turns into $G_0 = 1/(E + i\varepsilon + \zeta - H_0)$. Solutions of the FY equation satisfy uniqueness even at the limit for $\varepsilon \to 0$, which is not the case for simple four-body LS equation [9]. Therefore the results by the analytic continuation do not depend on the choice of ε's within the radius of convergence. Thus we empirically choose 0.5MeV as the minimum ε value for the cases (I)-(III) and 0.75MeV for the case (IV) (see crosses in Fig. 1), with attention only to a better numerics. They are increased in steps of 0.125MeV. ζ is chosen as 0 and $\pm$0.125MeV.

We employ the point method [10] as an analytic continuation technique in CEM. It's convergence behavior is shown in Table 1 where the phase shift δ and the inelasticity parameter η is defined by $S = \eta \exp(2i\delta)$. Here S is the S-matrix of elastic 3N+N scattering

In case (I) η must be 1 due to unitarity and our result satisfies it within six digits. Also in cases (II) and (III) we reach a very high accuracy. In case (IV), we still obtain converged solutions within 4 digits. In the cases (I and II) our results agree very well with the solutions based on PVR.

Table 1. Phase shifts (in deg) and inelasticity parameters for 3N+N → 3N+N elastic scattering. $n_{\max}$ denotes the number of sample energies which are included in the point method. For instance, $n_{\max} = 5$ means that the solutions from n=1 to 5 (see Fig. 1) are included. The row PVR shows results from a direct solution of the FY equations using PVR. The agreement is perfect.

	(I)		(II)		(III)		(IV)	
$n_{\max}$	δ	η	δ	η	δ	η	δ	η
1	53.31351	1.018810	14.62234	0.675088	-8.0617	0.692391	-62.093	0.83875
2	46.21307	0.973139	10.47942	0.853658	-5.9428	0.815698	-61.965	0.75946
3	44.27898	0.989232	12.38204	0.948787	-5.5022	0.899150	-61.620	0.74499
4	44.27129	1.000623	12.38254	0.948044	-5.5101	0.898666	-61.676	0.74570
5	44.34441	0.999787	12.38211	0.948046	-5.5095	0.898656	-61.682	0.74589
6	44.34157	0.999994	12.38284	0.948053	-5.5094	0.898655	-61.669	0.74580
7	44.34022	1.000005	12.38198	0.948070	-5.5096	0.898654	-61.666	0.74570
8	44.34012	0.999997	12.38198	0.948069	-5.5095	0.898657	-61.669	0.74581
9	44.34013	0.999999	12.38198	0.948069	-5.5096	0.898656	-61.670	0.74580
10	44.34016	1.000000	12.38198	0.948069	-5.5095	0.898657	-61.669	0.74582
PVR	44.34016	1.000000	12.38198	0.948069	——	——	——	——

4. Summary

We showed that well converged solutions of the FY equations are obtained in all energy regions. In relation to the application of EDPE we confirmed that converged solutions are obtained in the cases (I-III). In the case (IV), however, there is a report that EDPE is not applicable [11]. We also found that EDPE did not converge. Therefore, in this study we just kept the rank fixed by 4. We are now investigating this problem in a forthcoming study.

Further we shall include higher partial waves and employ realistic NN forces to discuss physics, for instance, study of 3NF as mentioned at the first section.

Alpha particle is the smallest nucleus on magic number with many levels which is totally different from two- and three-nucleon systems. And then, to reproduce many energy levels of ^{4}H, ^{4}He, and ^{4}Li nuclei is our another research interest. This will be the first step to study nuclear structure by Faddeev calculations, and we expect that CEM has an advantage for this purpose.

Acknowledgments

The calculations are performed on SX-5/128M8 (Research Center for Nuclear Physics), SX-5/6B (National Institute for Fusion Science), a workstation (Frontier Research Center for Computational Science, Tokyo University of Science) in Japan, and partly on Hitachi SR8000 (Leibnitz-Rechenzentrum für die Münchener Hochschule) in Germany.

References

1. H. Kamada, Y. Koike and W. Glöckle, *Prog. Theor. Phys.* **109**, 869L (2003).
2. E. Uzu, H. Kamada, and Y. Koike, *Phys. Rev.* **C68**, 061001 (2003).
3. E. O. Alt, P. Grassberger, and W. Sandhas, Nucl. Phys. **B2** 167 (1967); Phys. Rev. C **1**, 85 (1970).
4. W. C. Parke, Y. Koike, D. R. Lehman, and L. C. Maxmon, Few-Body Systems **11**, 89 (1991).
5. E. Uzu, S. Oryu, M. Tanifuji, Few-Body Systems Suppl. **12**, 491 (2000).
6. A. C. Fonseca, Phys. Rev. Lett. **83**, 4021 (1999); Nucl. Phys. **A631**, 675c (1998).
7. Y. Yamaguchi, Phys. Rev. **95**, 1628 (1954); Y. Yamaguchi and Y. Yamaguchi, Phys. Rev. **95**, 1635 (1954).
8. A. C. Phillips, Nucl. Phys **A107**, 209 (1968).
9. W. Glöckle, *The Quantum Mechanical Few-Body Problem* (Springer-Verlag, Berlin Heidelberg, 1983).
10. L. Schlessinger, Phys. Rev. **167**, 1411 (1968).
11. A. C. Fonseca, H. Haberzettl, and E. Cravo, Phys. Rev. C **27**, 939 (1983).

A REALISTIC BARYON-BARYON INTERACTION IN THE SU_6 QUARK MODEL AND ITS APPLICATIONS TO FEW-BODY SYSTEMS

Y. FUJIWARA[1], K. MIYAGAWA[2], M. KOHNO[3], Y. SUZUKI[4], D. BAYE[5] AND J.-M. SPARENBERG[6]

[1] *Department of Physics, Kyoto University, Kyoto 606-8502, Japan*
[2] *Department of Applied Physics, Okayama Science University, Okayama 700-0005, Japan*
[3] *Physics Division, Kyushu Dental College, Kitakyushu 803-8580, Japan*
[4] *Department of Physics, Niigata University, Niigata 950-2181, Japan*
[5] *Physique Nucléaire Théorique et Physique Mathématique, CP 229, Université Libre de Bruxelles, B-1050 Brussels, Belgium*
[6] *TRIUMF, 4004 Wesbrook Mall, Vancouver, British Columbia, Canada V6T 2A3*

The recent quark-model baryon-baryon interaction by the Kyoto-Niigata group is applied to the triton, hypertriton, $2\alpha\Lambda$ and $2\Lambda\alpha$ systems, in which a new three-cluster Faddeev formalism, using the 2-cluster resonating-group method (RGM) kernel, is developed for the exact treatment of the Pauli forbidden states between clusters.

1. THREE-CLUSTER FADDEEV FORMALISM USING THE TWO-CLUSTER RGM KERNEL

The QCD-inspired spin-flavor SU_6 quark model for the baryon-baryon interaction, proposed by the Kyoto-Niigata group, is a unified model for the complete baryon octet ($B_8 = N$, Λ, Σ and Ξ), which has achieved very accurate descriptions of the NN and YN interactions.[1,2,3] In particular, the nucleon-nucleon (NN) interaction of the most recent model fss2 [2] is accurate enough to compare with the modern realistic meson-exchange models. These quark-model interactions can be used for realistic calculations of few-baryon and few-cluster systems, once an appropriate three-body equation is developed for the pairwise interactions described by the RGM kernel. The desired 3-cluster equation should be able to deal with non-locality and energy-dependence intrinsically involved in the quark-exchange RGM kernel. Furthermore, quark-model descriptions of the hyperon nucleon (YN) and hyperon hyperon (YY) interactions in the full coupled-channel formal-

ism sometimes involve a Pauli forbidden state, which excludes the most compact spatial configuration, resulting in strongly repulsive nature of the interactions in some particular channels. We have recently formulated a new 3-cluster equation which uses two-cluster RGM kernels explicitly.[4] This equation exactly eliminates 3-cluster redundant components by the orthogonality of the total wave function to the pairwise two-cluster Pauli-forbidden states. The explicit energy dependence inherent in the exchange RGM kernel is self-consistently determined. This equation is entirely equivalent to the Faddeev equation which uses a modified singularity-free T-matrix (which we call the RGM T-matrix) constructed from the two-cluster RGM kernel. We first applied this formalism to a 3-dineutron system and the 3α system, and obtained complete agreement between the Faddeev calculations and variational calculations which use the translationally invariant harmonic-oscillator (h.o.) basis.[4,5] For the 3α system, the input is the 3-range Minnesota force (MN force) with the exchange mixture $u = 0.946869$, together with the h.o. width parameter, $\nu = 0.257$ fm^{-2}, for the $(0s)^4$ α-clusters. The 2α phase shifts are nicely reproduced in the 2α RGM. We find that the 3α ground-state energies obtained by solving the present 3α Faddeev equations are only about $1.0 \sim 1.7$ MeV higher than those of the full microscopic 3α RGM calculations.[5]

2. TRITON AND HYPERTRITON FADDEEV CALCULATIONS

The present 3-cluster RGM formalism was applied to the Faddeev calculations of the $3N$ bound state [6] and the (ΛNN)-(ΣNN) system for the hypertriton, employing the off-shell T-matrices which are derived from the non-local and energy-dependent RGM kernel for our quark-model NN and YN interactions of fss2 and FSS. The model fss2 yields the triton energy $E(^3\mathrm{H}) = -8.519$ MeV in the 50 channel calculation, when the np interaction is employed for any NN pairs in the isospin basis.[7] The charge rms radii for ^{3}H and ^{3}He are also correctly reproduced. This triton binding energy is the closest to the experimental value, $B_t^{\mathrm{exp}} = 8.48$ MeV, among many Faddeev calculations employing modern realistic NN interactions. A characteristic description of the short range correlations in the quark model is essential to reproduce the large binding energy and the correct size of the three-nucleon bound state without reducing the D-state probability of the deuteron. For the hypertriton calculation, exact treatment of the ΛN-ΣN coupling and the resulting Pauli forbidden state with the SU_3 $(11)_s$ sym-

metry is very important to obtain precise results. In the final calculation with 150 ΛNN and ΣNN channels included, we find $B_\Lambda(^3_\Lambda\mathrm{H}) = 289$ keV and the ΣNN component $P_{\Sigma NN} = 0.805\,\%$ for the fss2 prediction. For our previous model FSS, we obtain $B_\Lambda(^3_\Lambda\mathrm{H}) = 878$ keV and $P_{\Sigma NN} = 1.36\,\%$. Since $B_\Lambda{}^{\mathrm{exp}} = 130 \pm 50$ keV, the fss2 result is slightly overbound, which implies that the $^1S_0$ attraction of the ΛN interaction is slightly too attractive in comparison to the $^3S_1$ attraction. From these results, we can extrapolate the desired difference of the $^1S_0$ and $^3S_1$ phase shifts at the maximum values. It turns out to be $3° \sim 7°$ more attractive in the $^1S_0$ state, which is consistent with the result in ref. [8] which uses simulated interactions of the Nijmegen models.

3. $2\alpha\Lambda$ FADDEEV CALCULATION FOR $^9_\Lambda$Be

The formalism is now applied to the $2\alpha\Lambda$ Faddeev calculation for $^9_\Lambda$Be, by using the 2α RGM kernel and $\Lambda\alpha$ folding potentials for various ΛN effective forces. The effective ΛN force, denoted by SB (Sparenberg-Baye potential) in Table 1, is constructed from the $^1S_0$ and $^3S_1$ phase shifts predicted by the YN sector of the model fss2 [3], by using an inversion method based on supersymmetric quantum mechanics.[9] These are simple 2-range Gaussian potentials which reproduce the low-energy behaviour of the ΛN phase shifts obtained by the full coupled-channel calculations. Since any central and single-channel effective ΛN forces lead to the well-known overbinding problem of $^5_\Lambda$He [10] by about 2 MeV (in the present case, it

Table 1. The ground-state energy $E_{\mathrm{gr}}(0^+)$ and the 2^+ excitation energy $E_{\mathrm{x}}(2^+)$ in MeV, calculated by solving the Faddeev equation for the $2\alpha\Lambda$ system. In the last column, ΔE is a simple estimate of the ℓs splitting for the $5/2^+$ and $3/2^+$ excited states, using the $\boldsymbol{P}$=0 Wigner transform of the fss2 and FSS ΛN LS interactions. The model fss2 involves an extra σ-meson contribution, which is indicated by "$+\sigma$".

$V_{\Lambda N}$	$E_{\mathrm{gr}}(0^+)$ (MeV)			$E_{\mathrm{x}}(2^+)$ (MeV)	ΔE (keV)	
	ours	Hiyama [11]	diff.		fss2	FSS
SB	−6.837	–	–	2.915	$103+\sigma$	164
NS	−6.742	−6.81	0.07	2.916	$97+\sigma$	154
ND	−7.483	−7.57	0.09	2.935	$106+\sigma$	169
NF	−6.906	−7.00	0.09	2.930	$86+\sigma$	138
JA	−6.677	−6.76	0.08	2.919	$86+\sigma$	138
JB	−6.474	−6.55	0.08	2.911	$85+\sigma$	136
Exp't	-6.62 ± 0.04			3.029(3)/3.060(3)	43 ± 5	

is 1.63 MeV), the attractive part of the ${}^3S_1$ ΛN potential is adjusted to reproduce the correct binding energy $E^{\rm exp}({}^5_\Lambda{\rm He}) = -3.12 \pm 0.02$ MeV. The odd-state ΛN force is assumed to be zero. The partial waves up to $\lambda_{\rm Max} = \ell_{1{\rm Max}} = 6$ are included both in the 2α and $\Lambda\alpha$ channels. The direct and exchange Coulomb kernel between two α-clusters is introduced at the nucleon level with a cut-off radius, $R_C = 14$ fm (central case) or 10 fm (ℓs included). Table1 shows the ground-state (0^+) and the excited-state (2^+) energies of ${}^9_\Lambda$Be, predicted by the SB and other various ΛN potentials used by Hiyama *et al.*[11] In the present calculations using only central forces, the SB potential with the pure Serber character can reproduce the ground-state and excited-state energies within the accuracy of 100 - 200 keV. Table 1 also shows a simple estimate of the ℓs splitting for the $5/2^+$ and $3/2^+$ excited states, due to the spin-orbit interaction predicted by fss2 and FSS.

4. $2\Lambda\alpha$ FADDEEV CALCULATION FOR ${}^6_{\Lambda\Lambda}$He

Next, we use the $\Lambda\alpha$ T-matrix in the $2\alpha\Lambda$ Faddeev calculation, to calculate the ground-state energy of ${}^6_{\Lambda\Lambda}$He. The full coupled-channel T-matrices of fss2 and FSS with the strangeness $S = -2$ and the isospin $I = 0$ [3] are employed for the $\Lambda\Lambda$ RGM T-matrix. We find that the Hiyama's 3-range Gaussian $\Lambda\Lambda$ potential and our old model FSS yield very similar results with the large $\Delta B_{\Lambda\Lambda}$ values, $\Delta B_{\Lambda\Lambda} = B_{\Lambda\Lambda}({}^6_{\Lambda\Lambda}{\rm He}) - 2B_\Lambda({}^5_\Lambda{\rm He}) \sim 3.6 - 3.7$MeV, since the $\Lambda\Lambda$ phases shifts predicted by both interactions increase up to about 40°. The improved quark model fss2 yields $\Delta B_{\Lambda\Lambda} = 1.41$ MeV. (For the $\Lambda\Lambda$ single-channel T-matrix, this value is reduced to 1.14 MeV.) If we use a simple 2-range Gaussian potential, $V_{\Lambda\Lambda}$(SB), derived from the fss2 ${}^1S_0$ $\Lambda\Lambda$ phase shift by the supersymmetric inversion method, we obtain $\Delta B_{\Lambda\Lambda} = 1.90$ MeV. We think that the 0.5 MeV difference between the fss2 and $V_{\Lambda\Lambda}$(SB) results is probably because we neglected the coupled-channel effects of the $\Lambda\Lambda\alpha$ channel to the $\Xi N\alpha$ and $\Sigma\Sigma\alpha$ channels. We should also keep in mind that in all of these 3-cluster calculations the Brueckner rearrangement effect [10] of the α-cluster with the magnitude of about -1 MeV (repulsive) is very important. It is further reported in ref. [12] that the quark Pauli effect among the α cluster and the Λ hyperons gives a non-negligible repulsive contribution of 0.1 - 0.2 MeV for the Λ separation energy of ${}^6_{\Lambda\Lambda}$He, even when a rather compact ($3q$) size of $b = 0.6$ fm is assumed. Taking all of these effects into consideration, we can conclude that the present results by fss2 are in good agreement with the recent experimental value, $\Delta B^{\rm exp}_{\Lambda\Lambda} = 1.01 \pm 0.20$ MeV, [13] deduced from the Nagara event.

5. SUMMARY

The 3-cluster Faddeev formalism using the 2-cluster RGM kernel opens a way to solve few-baryon systems interacting by the quark-model baryon-baryon interactions without spoiling the essential features of the RGM kernel; i.e., non-locality, energy dependence and the existence of the pairwise Pauli-forbidden state. They can also be used for the 3-cluster systems involving α-clusters, like the ${}^{9}_{\Lambda}$Be system. A nice point of this formalism is that the underlying NN and YN interactions are more direcly related to the structure of the hypernuclei than the models assuming simple 2-cluster potentials. In particular, we have found that the most recent quark-model interaction, the model fss2, yields a realistic description of many systems including the triton, hypertriton, ${}^{9}_{\Lambda}$Be and ${}^{6}_{\Lambda\Lambda}$He.

Acknowledgments

This work was supported by Grants-in-Aid for Scientific Research (C) (Nos. 15540270, 15540284 and 15540292) from the Japan Society for the Promotion of Science (JSPS).

References

1. Y. Fujiwara, C. Nakamoto and Y. Suzuki, *Phys. Rev.* **C54**, 2180 (1996).
2. Y. Fujiwara, T. Fujita, M. Kohno, C. Nakamoto and Y. Suzuki, *Phys. Rev. C* **65**, 014002 (2002).
3. Y. Fujiwara, M. Kohno, C. Nakamoto and Y. Suzuki, *Phys. Rev. C* **64**, 054001 (2001).
4. Y. Fujiwara, H. Nemura, Y. Suzuki, K. Miyagawa and M. Kohno, *Prog. Theor. Phys.* **107**, 745 (2002).
5. Y. Fujiwara, Y. Suzuki, K. Miyagawa, M. Kohno and H. Nemura, *Prog. Theor. Phys.* **107**, 993 (2002).
6. Y. Fujiwara, K. Miyagawa, M. Kohno, Y. Suzuki and H. Nemura, *Phys. Rev. C* **66**, 021001(R) (2002).
7. Y. Fujiwara, K. Miyagawa, Y. Suzuki, M. Kohno and H. Nemura, *Nucl. Phys.* **A721**, 983c (2003).
8. H. Nemura, Y. Akaishi and Y. Suzuki, *Phys. Rev. Lett.* **89**, 142504 (2002).
9. J.-M. Sparenberg and D. Baye, *Phys. Rev.* **C55**, 2175 (1997).
10. M. Kohno, Y. Fujiwara and Y. Akaishi, *Phys. Rev. C* **68**, 034302 (2003).
11. E. Hiyama, M. Kamimura, T. Motoba, T. Yamada and Y. Yamamoto, *Prog. Theor. Phys.* **97**, 881 (1997).
12. Y. Suzuki and H. Nemura, *Prog. Theor. Phys.* **102**, 203 (1999).
13. H. Takahashi et al., *Phys. Rev. Lett.* **87**, 212502 (2001).

This page intentionally left blank

Hypernuclei and computational methods

This page intentionally left blank

SPECTROSCOPY AND STRUCTURE OF Λ HYPERNUCLEI

OSAMU HASHIMOTO
Department of Physics, Tohoku University
Sendai 980-8578, JAPAN
hashimot@lambda.phys.tohoku.ac.jp

Reaction spectroscopy and γ-ray spectroscopy of Λ hypernuclei has made significant progresses and has provided indispensable information on Λ hypernuclear structure and ΛN interaction in the recent years. In addition, the (e,e'K^+) spectroscopy was, for the first time, successfully carried very recently. Based on these development, the future prospect of hypernuclear physics is discussed.

Introduction

Hypernuclear investigation provides valuable information in shedding lights on many-body system with a new degree of freedom "strangeness". Baryon structure in nuclear medium can be better studied by bringing a "strangeness" degree of freedom into deep inside a nucleus, since a Λ hyperon is free from Pauli exclusion principle.

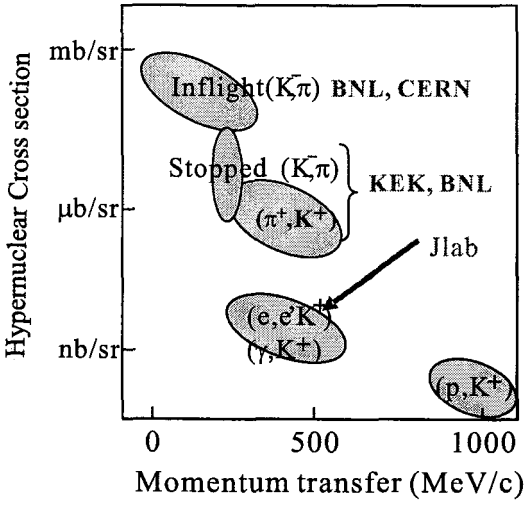

Figure 1. Momentum transfer vs. hypernuclear production cross section for typical reactions.

Widths of excited Λ hypernuclear states are expected to be relatively narrow compared with normal nuclei at comparable excitation energies, because the ΛN interaction is weak. Even for the states above the nucleon emission threshold, spreading widths of Λ hypernuclei are calculated to be less than a few 100 keV. Therefore, with a Λ hyperon as a probe, interior of nuclear medium and also new structure of nuclei can be spectroscopically investigated. In addition, hyperon-nucleon interaction, which is not easy to be investigated by hyperon-nucleon scattering experiments, can be qualitatively studied by the spectroscopy of Λ hypernuclei.

In Fig. 1, momentum transfer vs. typical cross section is pictorially shown for some of the reactions which can be employed for Λ hypernuclear spectroscopy, as they characterize the reactions for the spectroscopy. Among them, the (K^-, π^-) and (π^+, K^+) reactions have been most widely used for hypernuclear production until recently. The (π^+, K^+) reaction is suitable to populate high-spin stretched states because the momentum transfer is large and of the order of the Fermi momentum, while the (K^-, π^-) reaction prefereably excites substitutional hypernuclear states with its small momentum transfer. With these reactions, two types of hypernuclear spectroscopy, one reaction spectroscopy and the other γ-ray spectroscopy, made considerable progress in the past years. The reaction spectroscopy reveals hypernuclear states even above the nucleon emission threshold and all the way up to the Λ unbound region. The γ-ray spectroscopy achieves almost 3 orders of magnitude better energy resolution and powerful for investigating spin-dependent ΛN interaction.

In this paper, status and some topics of the spectroscopy of Λ hypernuclei are presented.

The reaction spectroscopy and the (π^+, K^+) ***reaction***

The reaction spectroscopy by the (π^+, K^+) reaction was first applied to a carbon target at BNL AGS, and later it was extended to heavier systems both at BNL and KEK.[1,2] The reaction has an advantage over the (K^-, π^-) reaction, which was widely used for hypernuclear study in early days, that it can populate deeply bound hypernuclear states. The (π^+, K^+) reaction converts a neutron in a high-l orbital of the target nucleus to a Λ hyperon in a low-l orbital.

A series of experiments for the investigation of hypernuclei by the (π^+, K^+) reaction were carried out using the SKS spectrometer[3] at KEK 12 GeV PS in the past years. The SKS spectrometer has the good resolution of 1.5-2MeV FWHM and simultaneously covers a large solid angle

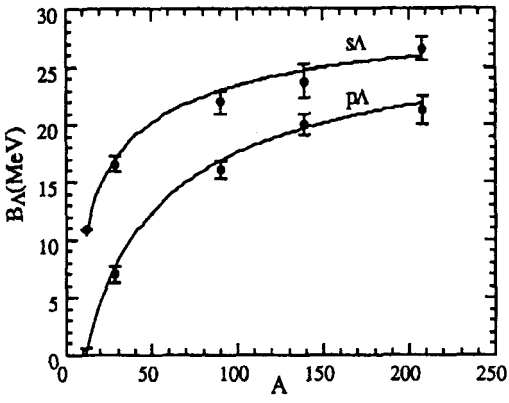

Figure 2. Hypernuclear mass dependence of the Λ hyperon binding energies in s and p orbits.

of 100 msr, accepting, for example, 60 % of ${}^{12}_{\Lambda}$C ground-state yield in the (π^+, K^+) reaction.[2] The large acceptance allows us to perform not only high-quality spectroscopy but also efficient coincidence experiments such as study of hypernuclear weak decay and γ-ray spectroscopy. The E140a experiment of KEK-PS was the first of the series of experiments and investigated the nature of a Λ hyperon deeply bound to heavy nuclei. The binding energies of a Λ hyperon in a wide variety of Λ hypernuclei for ${}^{89}_{\Lambda}$Y, ${}^{139}_{\Lambda}$La and even ${}^{208}_{\Lambda}$Pb were derived from the excitation spectra as shown in Fig. 2. It revealed that the single-particle orbitals of a Λ hyperon persists to the first order even in nuclei as heavy as A=208.[2] Much improved statistics and resolution were obtained for ${}^{89}_{\Lambda}$Y in the most recent E369 experiment, and demonstrated new structure of medium-heavy Λ hypernuclei.[4]

The (π^+, K^+) reaction spectroscopy was also applied to the investigation of p-shell region Λ hypernuclei. An example of the spectra is shown in Fig. 3 for ${}^{9}_{\Lambda}$Be. The ${}^{9}_{\Lambda}$Be hypernucleus can be described as the ^{8}Be core plus a Λ hyperon and it was first pointed out by Dalitz and Gal that unique Λ hypernuclear states should manifest itself as "supersymmetric states"[5]. Later, Bando *et. al.* studied ${}^{9}_{\Lambda}$Be in the framework of a cluster model and predicted "genuine hypernuclear states", which cannot be formed in ordinary nuclei of ^{9}Be because of the Pauli exclusion principle[6]. As seen in Fig. 3, peaks can be attributed to the genuine hypernuclear states with configurations that an s_Λ couples to the core of ^{8}Be 1^- and 3^- excited by the (π^+, K^+) reaction. The ${}^{9}_{\Lambda}$Be spectrum will serve as a testing ground of cluster nature of Λ hypernuclei which has unique features due to the strangeness degree of freedom.

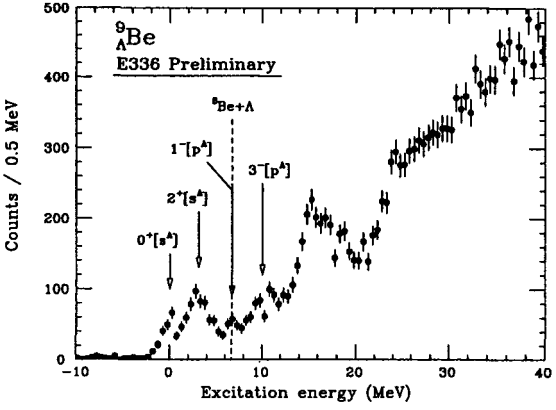

Figure 3. Preliminary excitation spectrum of $^{9}_{\Lambda}$Be measured by the (π^+, K^+) reaction with the SKS spectrometer system. Orbital angular momentum and parity for the core ^{8}Be are labeled for each peak.

It can be said now that the (π^+, K^+) reaction spectroscopy is established as a powerful tool for the investigation of Λ hypernuclear structure. However, it is also clear that the resolution of these spectra are not sufficient to extract precise information on nuclear structure and/or ΛN interaction. Further efforts are required to intensively explore high quality hypernuclear spectroscopy.

Hypernuclear γ-ray spectroscopy

The γ-ray spectroscopy offers best energy resolution for those hypernuclear states below the nucleon emission threshold. However, it has been difficult to perform hypernuclear γ-ray spectroscopy, since the rates of hypernuclear photon yields are very much limited due to small cross section and low γ detection rates, and high background associated with the secondary beam. The KEK E419 experiment was the first that succeeded in observing hypernuclear γ rays with Ge detectors.[8,9] It was carried out by installing the "HYPERBALL" system in the target region of the SKS spectrometer system. It consists of 14 Ge detectors surrounded by BGO counters and also equipped with a fast transistor-reset preamplifiers that allow the operation in high-count rate environment, The overall photopeak detection efficiency of $\epsilon\Omega = 2.5$ % for 1 MeV γ rays was achieved. Two γ rays were identified as associated with the $^{7}_{\Lambda}$Li, which are shown in Fig. 4.

One of the peaks, whose energy was 689 $\pm$ 4 keV, was assigned to be the M1 transition between $3/2^+ \rightarrow 1/2^+$. The γ-ray energy was directly

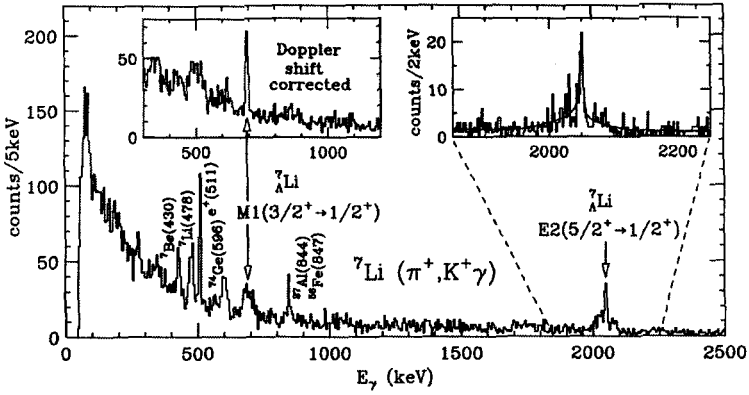

Figure 4. Energy spectrum of γ rays emitted from the decay of $^{7}_{\Lambda}$Li(KEK E419).

compared with the recent calculation based on a cluster model and the magnitude of spin-spin interaction was derives. It was consistent with the widely adopted value of Δ=0.5 MeV.[8] The 2050 keV peak, which was assigned to the $5/2^{+} \rightarrow 1/2^{+}$ transition, had broad peak shape due to the Doppler effect. After line shape fitting in which the hypernuclear recoil momenta were taken into accounted, the lifetime of the $5/2^{+}$ state was obtained to be $\tau = 5.2 \pm 0.8 \pm 0.6$ ps. It was concluded by the comparison of the B(E2) value with that of the corresponding core ^{6}Li transition that the spatial distance between α and (p+n) shrinks due to the presence of a Λ hyperon. The phenomenon was theoretically predicted as a glue like role of a Λ hyperon.[6] It is an example of the power of hypernuclear γ spectroscopy in the investigation of hypernuclear structure. Effort to further increase the detection efficiency with clover-type Ge detectors are under way, aiming to double the photo-peak efficiency.

The (e,e'K^{+}) hypernuclear spectroscopy

So far, only the (K^{-}, π^{-}) and (π^{+}, K^{+}) reactions, which convert a neutron in the target to a Λ hyperon, have been intensively used for the spectroscopic investigation of Λ hypernuclei. However, it has been recognized that the (e,e'K^{+}) reaction has a unique and advantageous characteristics for the Λ hypernuclear spectroscopy. It preferentially populates high-spin hypernuclear states as (π^{+}, K^{+}) reaction does, since the magnitude of the momentum transfer is almost the same magnitude. In addition, the (e,e'K^{+}) reaction has an advantage that it can populate spin-flip hypernuclear states as well as non-spin-flip states in contrast to the reactions

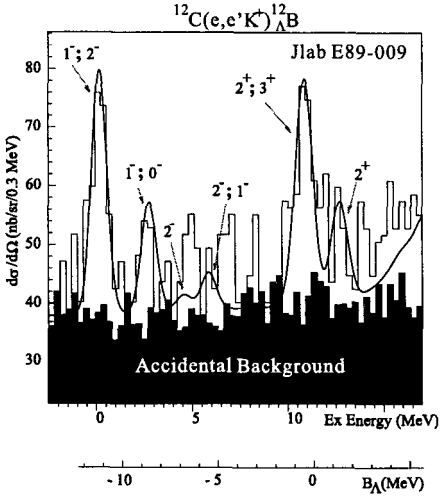

Figure 5. Hypernuclear missing mass spectrum in the reaction of ^{12}C(e,e'K$^+$)$^{12}_\Lambda$B

with meson beams. The (e,e'K$^+$) reaction excites proton-hole-Λ-particle states which have the configuration $[(l_j)_N^{-1}(l_k)^\Lambda]_J$, by converting a proton to a Λ hyperon. This is in contrast to the (K^-,π^-) and (π^+,K^+) reaction, in which a neutron is converted to a Λ hyperon and spin-nonflip states are favorably populated at 0 degrees. The characteristics are important for spectroscopy as it allows us to directly study the spin-dependent structure of Λ hypernuclei. Experimentally, however, the most important characteristics of the (e,e'K$^+$) reaction might be the possibility that significantly better energy resolution is achieved because a primary electron beam of extremely good beam quality, small beam emittance and narrow momentum spread. Although the (e,e'K$^+$) reaction has such advantages for hypernuclear spectroscopy, the experiments require more effort, since hypernuclear production cross sections are much smaller than those by reactions using hadronic beams, and both scattered electrons and kaons have to be analyzed with high precision in coincidence under high background condition. Very recently, we have succeeded in the first hypernuclear spectroscopy experiment(E89-009) by the (e,e'K$^+$) reaction at Hall C of Jefferson National Laboratory(Jlab) with a 1.8 GeV CW electron beam.[10] The measured mass spectrum of the ^{12}C(e,e'K$^+$)$^{12}_\Lambda$B reaction is shown in Fig. 5. The ground state peak, though it should be a doublet but very small splitting(¡a few 10 keV), demonstrates that the experimental resolution of sub-MeV is achieved(0.9 MeV(FWHM)). However, the statistics are low and accidental background level is high even though it took about a month to take the data. In spite of the success of the first (e,e'K$^+$) spectroscopy, it

is obvious that considerable improvement is necessary in order to intensively employ the (e,e'K^+) reaction for hypernuclear structure study.

Aiming to significantly upgrade the (e,e'K^+) hypernuclear spectroscopy, a new experiment is under preparation at Jlab(E01-011)[11] in which Λ hypernuclei will be investigated in the p-shell region and beyond the p-shell region as well. In the E01-011 experiment, we introduce the "Tilt method" in order to avoid electron background due to the bremsstrahlung process and Moeller scattering, and overcome the limitation of luminosity in the previous E89-009 experiment, which adopted the "0 degree tagging method".[11] Moreover, a new high-resolution large-acceptance kaon spectrometer(HKS) with momentum resolution of $\Delta p/p = 2 \times 10^{-4}$ at 1.2 GeV/c is to be introduced. In the experimental configuration, which is schematically shown in Fig. 6, scattered electrons and kaons are firstly bent to the opposite directions to each other by a splitter magnet.

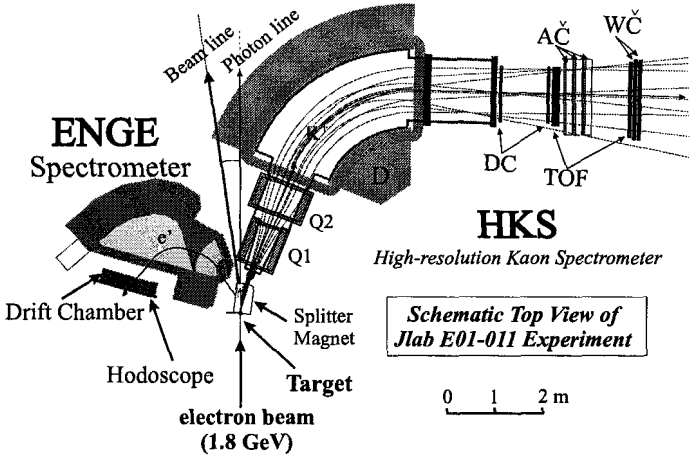

Figure 6. Schematic drawing of the high-resolution kaon spectrometer dedicated to the (e,e'K^+) hypernuclear spectroscopy.

In E01-011, it is expected that we can run with a 100 mg/cm^2 ^{12}C target and a beam intensity of 30 μA, resulting in more than 50 times greater hypernuclear yield rate and an order of magnitude better signal-to-noise ratio compared with the previous experiment. The mass resolution will be also improved to 3-400 keV(FWHM) because of the higher momentum resolution of the HKS spectrometer. Spectrometer magnets and most of the detector system have been already completed and it is scheduled that

the installation start in the winter of 2004 at Jlab Hall C.

Summary

The recent progress has demonstrated the power of hypernuclear reaction spectroscopy and γ-ray spectroscopy. The (π^+, K^+) reaction spectroscopy with the SKS spectrometer obtained excitation spectra for a wide mass region of Λ hypernuclei, providing basic information on the structure of light and heavy Λ hypernuclei. The γ-ray spectroscopy has been developed and provided invaluable information on the magnitude of spin-dependent ΛN interaction with its unprecedented energy resolution. Now, the (e,e'K^+) reaction spectroscopy has just started. We expect the reaction spectroscopy by the (e,e'K^+) reaction at Jlab and the γ-ray spectroscopic studies with meson beams at J-PARC will be fully developed in the near future.

The experiments with the SKS spectrometer were carried out under the KEK-PS SKS collaboration and those by the (e,e'K^+) reaction under Jlab E89-009 and E01-011 collaboration. The author deeply thanks to the collaborators for their effort and useful discussions. The program is partly supported by Specially promoted program of Grant-in-Aid by MEXT, Japan.

References

1. C. Milner *et. al.*, Phys. Rev. Lett. **54**, 1237 (1985). P. H. Pile *et al.*, Phys. Rev. Lett. **66**, 2585 (1991).
2. T. Hasegawa, *et. al.*, Phys. Rev. Lett. **74**, 224 (1995). T. Hasegawa, *et. al.*, Phys. Rev. **C53** (1996) 1210.
3. T. Fukuda, *et. al.*, Nucl. Instr. Meth. **A361**, 485 (1995) .
4. H. Hotchi *et. al.*, Phys. Rev. **C64** 044302 (2001).
5. R.H. Dalitz and A. Gal, Phys. Rev. Lett. **36** (1976) 362.
6. T. Motoba, H. Bando and K. Ikeda, Prog. Theor. Phys. **70**, 189 (1983).
7. T. Yamada, K. Ikeda, T. Motoba and H. Bando, Phys. Rev. **C38** (1988) 854.
8. H. Tamura *et al.*, Phys. Rev. Lett. **84**, 5963 (2000).
9. K. Tanida *et al.*, Phys. Rev. Lett. **86**, 1982 (2001).
10. T. Miyoshi *et al.*, Phys. Rev. Lett. **90**, 232502 (2003)
11. Jlab proposal E01-011(2001), Spokespersons O. Hashimoto, L. Tang, J. Reinhold and S.N. Nakamura.

BRUECKNER REARRANGEMENT ENERGIES IN S-SHELL HYPERNUCLEI

M. KOHNO

Physics Division, Kyushu Dental College, Kitakyushu 803-8580, Japan
E-mail: kohno@kyu-dent.ac.jp

Y. FUJIWARA

Department of Physics, Kyoto University, Kyoto 606-8502, Japan
E-mail: fujiwara@ruby.scphys.kyoto-u.ac.jp

Y. AKAISHI

Institute of Particle and Nuclear Studies, KEK, Tsukuba 305-0801, Japan
E-mail: yoshinori.akaishi@kek.jp

We consider rearrangement effects in light hypernuclei in the framework of the lowest order Brueckner theory. The energy change of the ^{4}He core of ${}^{5}_{\Lambda}$He when the Λ hyperon is added to ^{4}He is first estimated without much numerical computations. Next, rearrangement contributions in $\Delta B_{\Lambda\Lambda}({}^{6}_{\Lambda\Lambda}\mathrm{He})$ are estimated, which are important to deduce the strength of the $\Lambda\Lambda$ interaction from the experimental $\Delta B_{\Lambda\Lambda}({}^{6}_{\Lambda\Lambda}\mathrm{He})$.

1. INTRODUCTION

Hypernuclear physics is one of the most developing fields in nuclear structure physics, both in experiments and theories. Masses of hypernuclei and double hypernuclei are an invaluable source of information on hyperon-nucleon and hyperon-hyperon interactions and thus the starting point toward the understanding of the octet baryon world. On the other hand, a fresh motivation for improving the standard framework of nuclear many-body theories is provided in studying hyperons in nuclear medium.

Recently, a new discovery of the double lambda hypernucleus ${}^{6}_{\Lambda\Lambda}$He was reported[1], which revised our understanding of the strength of the $\Lambda\Lambda$ interaction. On the theoretical side, exact few-body calculations have been attempted for light hypernuclei in Faddeev formulation and in variational methods. Two groups[2,3] reported their results of variational calculations

on ${}^{5}_{\Lambda}$He . One of the intriguing results in these calculations is the change of properties of the α core, when the Λ hyperon is added. It was shown that the energy of the α core is reduced by a few MeV, while the density distribution changes little.

In this study[4], we discuss Brueckner rearrangement effects[5] in these s-shell hypernuclei in a nuclear single-particle (s.p.) model description. We first estimate the rearrangement energy of the α core of ${}^{5}_{\Lambda}$He . Next, we consider rearrangement contributions in $\Delta B_{\Lambda\Lambda}({}^{6}_{\Lambda\Lambda}\mathrm{He}) = B_{\Lambda\Lambda}({}^{6}_{\Lambda\Lambda}\mathrm{He}) - 2B_{\Lambda}({}^{5}_{\Lambda}\mathrm{He})$. This quantity is meant to give the matrix element of the $\Lambda\Lambda$ interaction, $-\langle\Lambda\Lambda|v_{\Lambda\Lambda}|\Lambda\Lambda\rangle$, in a naive s.p. picture. The old data suggested that $\Delta B_{\Lambda\Lambda}({}^{6}_{\Lambda\Lambda}\mathrm{He})$ was larger than 4 MeV and thus the $\Lambda\Lambda$ interaction was fairly strong. The recent experimental discovery[1] of ${}^{6}_{\Lambda\Lambda}$He mentioned above gave more reliable data of $\Delta B_{\Lambda\Lambda}({}^{6}_{\Lambda\Lambda}\mathrm{He}) \sim 1$ MeV, which indicated that the $\Lambda\Lambda$ interaction is rather weak. This quantity, $\Delta B_{\Lambda\Lambda}({}^{6}_{\Lambda\Lambda}\mathrm{He})$, contains many-body effects. In order to deduce the magnitude of the $\Lambda\Lambda$ interaction, however, we have to subtract rearrangement energies.

2. REARRANGEMENT ENERGIES

We consider the potential energy change ΔE_r of the α core in ${}^{5}_{\Lambda}$He from ^{4}He in the lowest order Brueckner theory. Assuming that the $0s$ wave function is given by the same h.o. function both for the ^{4}He and the ${}^{5}_{\Lambda}$He , ΔE_r is expressed as

$$\Delta E_r = \frac{1}{2}\sum_{hh'} < hh'|G_{NN}(5,\omega = e_h(5) + e_{h'}(5)) - G_{NN}(4,\omega = e_h(4) + e_{h'}(4))|hh' >_{as}, \quad (1)$$

where G_{NN} is defined by the G-matrix equation

$$G_{NN}(n,\omega) = v_{NN} + v_{NN}\frac{Q}{\omega - QTQ}G_{NN}(n,\omega), \quad (2)$$

with Q being a Pauli exclusion operator. The Brueckner s.p. energy $e_h(n)$ is defined as

$$e_h(4) = \langle h|t_N|h\rangle + \sum_{h'}\langle hh'|G_{NN}(4,\omega = e_h(4) + e_{h'}(4))|hh'\rangle_{as}, \quad (3)$$

$$e_h(5) = \langle h|t_N|h\rangle + \sum_{h'}\langle hh'|G_{NN}(5,\omega = e_h(5) + e_{h'}(5))|hh'\rangle_{as} + \langle h\Lambda|G_{N\Lambda}(5,\omega = e_h(5) + e_{\Lambda}(5))|h\Lambda\rangle. \quad (4)$$

The self-consistency of e_h and G means that the hole-line potential insertion, a part of three-body correlations, is taken into account. Rewriting the difference $G_{NN}(5) - G_{NN}(4)$ in eq. (1) by using the relation

$$G_{NN}\frac{Q}{\omega - QTQ}\frac{Q}{\omega - QTQ}G_{NN} = -\frac{\partial G_{NN}}{\partial \omega}, \tag{5}$$

and introducing the wound integral $\kappa_N \boxminus -\sum_{h'} < hh'|\frac{\partial G_{NN}}{\partial \omega}|hh' >_{as}$, the potential energy change ΔE_r becomes

$$\Delta E_r \simeq \frac{1}{2}\sum_{hh'} \Delta e_h \langle hh'|\frac{\partial G_{NN}}{\partial \omega}|hh'\rangle_{as} = -\frac{1}{2}\sum_{h} \Delta e_h \kappa_N, \tag{6}$$

where Δe_h is

$$\Delta e_h \equiv e_h(5) + e_{h'}(5) - e_h(4) - e_{h'}(4) = 2(e_h(5) - e_h(4)). \tag{7}$$

Noticing that the Λ separation energy $\epsilon_\Lambda(5)$, which is experimentally -3.12 MeV, also contains ΔE_r as

$$\begin{aligned}\epsilon_\Lambda(5) &= E(^5_\Lambda\mathrm{He}\ ) - E(^4\mathrm{He}\ ) \\ &= <\Lambda|t_\Lambda|\Lambda> + \sum_h <\Lambda h|G_{\Lambda N}|\Lambda h> + \Delta E_r + \Delta T_{cm},\end{aligned} \tag{8}$$

where ΔT_{cm} is the difference of the c.m. kinetic energy. it is straightforward to obtain the expression:

$$\Delta E_r \simeq -\frac{\kappa_N}{1+\kappa_N}(\epsilon_\Lambda(5) - <\Lambda|t_\Lambda|\Lambda> - \Delta T_{cm}). \tag{9}$$

This energy difference ΔE_r appears through the energy-dependence of NN G-matrices by the change of the nucleon s.p. energy from ^{4}He to $^5_\Lambda$He . Using $\kappa_N \sim 0.2$ from the ω-dependence of the G-matrices and a Λ oscillator constant of $\nu_\Lambda = 0.5$ fm^{-2}, we obtain $\Delta E_r = 2.9$ MeV. The corresponding values calculated by Nemura, Akaishi and Suzuki[2] and by Usmani and Murtaza[3] by their variational calculations are 4.7 MeV and 3.2 MeV, respectively. The difference may be due to the actual change of wave functions and higher order effects. It is noted that our estimation is obtained by avoiding specific numerical calculations as much as possible.

Similar effects have to be estimated to establish the strength of $\Lambda\Lambda$ interaction from the observed mass of $^{\ 6}_{\Lambda\Lambda}$He by evaluating $\Delta B_{\Lambda\Lambda} \equiv 2E(^5_\Lambda\mathrm{He}\ ) - E(^{\ 6}_{\Lambda\Lambda}\mathrm{He}\ ) - E(^4\mathrm{He}\ )$. This quantity is decomposed into each matrix ele-

ment:

$$\Delta B_{\Lambda\Lambda} = \frac{1}{2}\sum_{hh'}\langle hh'|2G_{NN}(5) - G_{NN}(4) - G_{NN}(6)|hh'\rangle_{as}$$
$$+2\sum_{h}\langle h\Lambda|G_{N\Lambda}(5) - G_{N\Lambda}(6)|h\Lambda\rangle$$
$$-\langle\Lambda\Lambda|G_{\Lambda\Lambda}(6)|\Lambda\Lambda\rangle_{as} + \Delta T_{\Lambda\Lambda}, \qquad (10)$$

where the s.p. wave functions are assumed to be common in ^{4}He , $^5_\Lambda$He and $^6_{\Lambda\Lambda}$He , and $\Delta T_{\Lambda\Lambda}$ is the contribution of kinetic energy terms. Rearrangement contributions appear in the first and the second terms of the above expression.

The expression of $\Delta B_{\Lambda\Lambda}(^6_{\Lambda\Lambda}\mathrm{He})$ can be transformed in a similar manipulation to derive that of ΔE_r. The final expression for $\Delta B_{\Lambda\Lambda}(^6_{\Lambda\Lambda}\mathrm{He})$ becomes $\Delta B_{\Lambda\Lambda} = -\langle\Lambda\Lambda|G_{\Lambda\Lambda}(6)|\Lambda\Lambda\rangle - R$. The rearrangement contribution R is given by

$$R = \frac{2}{1+\kappa_\Lambda\frac{3+4\kappa_N}{2(1+2\kappa_N)}}\left(\frac{-\kappa_\Lambda\langle h\Lambda|G_{N\Lambda}(5)|h\Lambda\rangle}{1+2\kappa_N} - \kappa_\Lambda\langle\Lambda\Lambda|G_{\Lambda\Lambda}(6)|\Lambda\Lambda\rangle + P\right)$$
$$-\Delta T_{\Lambda\Lambda}, \qquad (11)$$

where P stands for the contribution through the Pauli effect. Since the simple qualitative consideration[4] proves that R is negative, the $\Delta B_{\Lambda\Lambda}(^6_{\Lambda\Lambda}\mathrm{He})$ becomes smaller than $-\langle\Lambda\Lambda|G_{\Lambda\Lambda}(6)|\Lambda\Lambda\rangle$. The reaction matrix calculation using the SU_6 quark model baryon-baryon interaction fss2[6] developed by Kyoto-Niigata group[7,8] yields $\langle\Lambda\Lambda|G_{\Lambda\Lambda}(6)|\Lambda\Lambda\rangle \sim -2.17$ MeV for $\nu_\Lambda = 0.4$ fm^{-2}. The estimation of R turns out to be $R = -0.93$ MeV. Thus, the quark model potential fss2 accounts well for the experimental $\Delta B_{\Lambda\Lambda}(^6_{\Lambda\Lambda}\mathrm{He})$ of ~ 1 MeV.

3. SUMMARY

We have estimated rearrangement contributions in the energy expectation values of the $^5_\Lambda$He and $^6_{\Lambda\Lambda}$He systems. In the standard framework of the lowest order Brueckner theory, the principal contribution to rearrangement energies is due to the starting energy dependence of the effective interaction as well as the change of Pauli blocking effect. The energy of the α core part of $^5_\Lambda$He is reduced by about 2.9 MeV when the s.p. energy becomes deeper by the addition of Λ to ^{4}He . Bando and Shimodaya[9] discussed this problem in 1980 to resolve the so-called overbinding problem of the s-shell hypernulcei. Instead of calculating the matrix element $\langle\Lambda h|G_{\Lambda N}|\Lambda h\rangle$

directly, we relate it to the Λ separation energy, which is by itself influenced by the rearrangement energy. It is gratifying to see that the magnitude of the estimated rearrangement energy has a good correspondence with those of variational calculations[2,3].

The experimental determination of the $\Delta B_{\Lambda\Lambda}({}^{6}_{\Lambda\Lambda}\mathrm{He})$ does not directly give the strength of the $\Lambda\Lambda$ interaction, since it contains rearrangement energies. The present estimation of the rearrangement contribution in $\Delta B_{\Lambda\Lambda}({}^{6}_{\Lambda\Lambda}\mathrm{He})$ is about 1 MeV. Thus, the s-wave matrix element of the $\Lambda\Lambda$ interaction in ${}^{6}_{\Lambda\Lambda}\mathrm{He}$ should be around -2 MeV. It is noted that the SU_6 quark model potential[6] in the $\Lambda\Lambda$-$\Sigma\Sigma$-ΞN sector predicts a proper magnitude of the $\Lambda\Lambda$ interaction.

Finally we note that the consideration of the structure dependence, such as the density- and energy-dependences, of the effective interaction is important in studying unstable nuclei, which is also an expanding field in nuclear structure physics. The subject was discussed in ref. 10 in the early stage of studying neutron rich He-isotopes.

References

1. H. Takahashi *et al.*, *Phys. Rev. Lett.* **87**, 212502 (2001).
2. H. Nemura, Y. Akaishi and Y. Suzuki, *Phys. Rev. Lett.* **89**, 142504 (2002).
3. A.A. Usmani and S. Murtaza, *Phys. Rev.* **C68**, 024001 (2003).
4. M. Kohno, Y. Fujiwara and Y. Akaishi, *Phys. Rev.* **C68**, 034302 (2003).
5. K.A. Brueckner and D.T. Goldman, *Phys. Rev.* **117**, 207 (1960).
6. Y. Fujiwara, M. Kohno, C. Nakamoto and Y. Suzuki, *Phys. Rev.* **C64**, 054001 (2001).
7. Y. Fujiwara, C. Nakamoto and Y. Suzuki, *Phys. Rev.* **C54**, 2180 (1996).
8. Y. Fujiwara, T. Fujita, M. Kohno, C. Nakamoto and Y. Suzuki, *Phys. Rev.* **C65**, 014002 (2002).
9. H. Bando and I. Shimodaya, *Prog. Theor. Phys.* **63**, 1812 (1980).
10. M. Kohno, S. Nagata and R. Tamagaki, *Prog. Theor. Phys.* **59**, 230 (1978).

THE 2003 UPDATE OF ANTIPROTON MASS BY PRECISION THREE-BODY CALCULATION OF ANTIPROTONIC HELIUM ATOM

Y. KINO AND H. KUDO

Department of Physics, Kyushu University, Fukuoka 812-8581, Japan

M. KAMIMURA

Department of Physics, Kyushu University, Fukuoka 812-8581, Japan

The Particle Listings 2000 edition gave the recommended value of antiproton mass, for the first time, to be within 5×10^{-7} in the relative deviation from the proton mass; this can be a test of the CPT invariance. The value was derived by our precision 3-body calculation, using the Gaussian Expansion Method, to analyze the laser spectroscopy data of metastable states in antiprotonic helium atoms taken at CERN. The 2002 edition and the 2003 updated version reported an one-order smaller value, 6×10^{-8}, based on further development of both the experiment and our calculation.

In the Particle Listings 1998 edition by the Particle data Group gave no recommended value of the mass of antiproton. Instead, they only cited several scattered values so far obtained. The reason why it is difficult to determine antiproton mass is as follows: The charge-to-mass ratio is determined very precisely, within error of 10^{-11}, by the periodic motion of antiproton in a magnetic field. But, one more relation is necessary between charge and mass. It is given by observing the energy of the X-ray decay in $\bar{p}$ atoms, but, the error of this observation is as large as 10^{-5} to 10^{-4}.

The antiproton mass is believed to be the same as the proton mass, but there had been no precise experimental information about itself before Particle Listings 2000 [1] in which a recommended information of antiproton mass is given for the first time; deviation of antiproton mass from proton mass is relatively within 5×10^{-7}. This can be a test of CPT invariance. This number was derived by the present authors [2,3,4] by analyzing the high-resolution laser experiment on the antiprotonic helium atoms done at

CERN [5].

Antiprotons injected into matter annihilate within pico second. But, it was surprising that much delayed annihilation phenomena was observed at KEK in 1991: About 3 % of antiprotons injected into the helium target survived as long as a few microseconds. This phenomena was soon understood as production of metastable states of antiprotonic helium atoms ($\bar{p}\mathrm{He}^+ \equiv \mathrm{He}^{2+} + e^- + \bar{p}$). This exotic atom can be obtained by replacing one of the electrons by an antiproton. Therefore the principal quantum number n of antiproton is estimated to be $n \approx 38$, so highly excited states. About 3 % of the injected antiprotons are caught and located in nearly the circular orbitals ($l = n - 1$) with $n \approx 38$.

In the vicinity of circular states, the Auger transition in $\bar{p}\mathrm{He}^+$ is strongly suppressed because the Auger electron needs here a large gap in angular momentum ($\Delta l_e \geq 4$). Thus, $\bar{p}\mathrm{He}^+$ in metastable states are deexcited only by a slow radiative decay. More than a dozen of transition-frequencies between metastable states of $\bar{p}\mathrm{He}^+$ were measured with fine laser spectroscopy in CERN (see Refs. [5,8], and further references therein). Such long-lived antiprotonic atoms have stimulated spectroscopic studies from a viewpoint of antimatter science: CPT invariance and weak equivalence principle, interaction between matter and antimatter, etc.

The antiprotonic helium atom has two different faces of three-body systems at the same time. (i) From a viewpoint of interaction, the helium nucleus attracts the electron and the antiproton. This shows an atomic picture like a helium atom. (ii) From a viewpoint of dynamics, on the other hand, the electron moves around the two massive particles like a molecule. Calculational methods should describe these two pictures flexibly. Moreover, difficulty in calculation is that accuracy of 8 significant figures in transition frequency is necessary to analyse the high-resolution laser data and that the metastable states concerned are so-called Feshbach states and therefore suitable resonance condition is to be taken into account in calculation.

To precisely solve this three-body system, we employ the Gaussian Expansion Method (GEM) [6,7] which is suited for describing the different types of pictures simultaneously and treating the electron-antiproton correlation. The three-body total wave function Ψ_{JM} is described as a sum of amplitudes of three rearrangement channels $c = 1 - 3$ (Fig. 1).

$$\Psi_{JM} = \Phi_{JM}^{(c=1)}(\mathbf{r}_1, \mathbf{R}) + \Phi_{JM}^{(c=2)}(\mathbf{r}_2, \mathbf{R}) + \Phi_{JM}^{(c=3)}(\mathbf{r}_3, \mathbf{R}) \ . \qquad (1)$$

Each amplitude is expanded in terms of the Gaussian basis functions of the

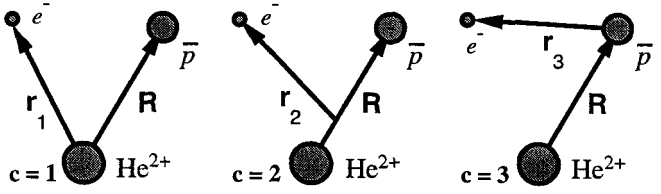

Figure 1. Three rearrangement channels ($c = 1 - 3$) of $\bar{p}\mathrm{He}^+$.

coordinates $\mathbf{r}_c$ and $\mathbf{R}$:

$$\Phi^{(c)}_{JM}(\mathbf{r}_c, \mathbf{R}) = \sum_{nl,NL} A_{c,nl,NL} \left[\phi^{\mathrm{G}}_{nl}(\mathbf{r}_c)\, \psi^{\mathrm{G}}_{NL}(\mathbf{R})\right]_{JM} \quad (c = 1 - 3)\,, \quad (2)$$

$$\phi^{\mathrm{G}}_{nlm}(\mathbf{r}) = r^l\, e^{-\nu_n r^2}\, Y_{lm}(\hat{\mathbf{r}}) \qquad (n = 1 - n_{\max})\,, \quad (3)$$

$$\psi^{\mathrm{G}}_{NLM}(\mathbf{R}) = R^L\, e^{-\lambda_N R^2}\, Y_{LM}(\hat{\mathbf{R}}) \qquad (N = 1 - N_{\max}). \quad (4)$$

The Gaussian ranges are chosen to lie in a geometrical progression [6,7]. This type of choice of Gaussian ranges is very suited for describing both the short-range correlations and long-range tail behaviour.

Channel $c = 1$ is suited for describing the atomic picture mentioned above. Channel $c = 2$ is for describing the molecular picture. Channel $c = 3$ is for describing the electron-antiproton correlation which plays an essential role in long lifetime of the atoms by reducing the Auger transition.

Energies are calculated with the complex coordinate rotation method to take a resonant boundary condition of metastable states into account. Using the first order perturbation theory, the relativistic and QED corrections are considered [3]. We carefully evaluate the accuracy of our calculations and conclude that we have achieved an eight-digits accuracy in the transition frequency.

First, we assume $m_{\bar{p}} = m_p$, $e_{\bar{p}} = -e_p$ and calculate the transition frequencies for $(J_i, v_i) - (J_f, v_f)$ and compare the results with the latest experimental values [8] in Table 1. The calculated values are in good agreement with the experimental values. The best agreement is the transition (33,1)-(32,1). The worst agreement is the transition (34,1)-(33,3); the discrepancy is due to a unique character of the daughter state which we do not discuss here.

Second, we examine uncertainty of the antiproton mass by slightly changing the antiproton mass when the calculated values are in good agreement with the experimental values. We scale the antiproton mass by a small fraction x as well as the charge: $m_{\bar{p}} = (1+x)m_p$, $e_{\bar{p}} = (1+x)e_p$ which keeps

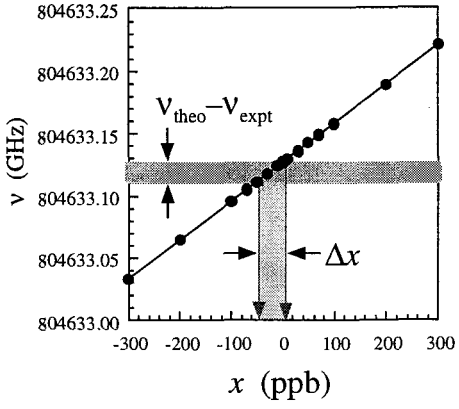

Figure 2. The calculated frequencies of the transition (33,1)-(32,1) as a function of the $\bar{p}$ mass shift parameter x. Closed circles show calculated values and solid line is a guide for eyes. $\Delta m_{\bar{p}}/m_p(\Delta e_{\bar{p}}/e_p) = \Delta x = (\nu_{\rm th} - \nu_{\rm exp})/\frac{d\nu_{\rm th}}{dx}$

the measured charge-to-mass ratio of antiproton. We recalculate transition frequencies as a function of the scaling parameter x. An example for the transition (33,1)-(32,1) is shown in Fig. 2. The uncertainty of antiproton mass (or equivalently charge) is given by $\Delta m_{\bar{p}}/m_p(\Delta e_{\bar{p}}/e_p) = \Delta x = (\nu_{\rm th} - \nu_{\rm exp})/\frac{d\nu_{\rm th}}{dx}$ where $\frac{d\nu_{\rm th}}{dx}$ is obtained from the slope of Fig. 2.

Table 1. Transition frequencies between metastable states of $\bar{p}{\rm He}^+$; theoretical values ($\nu_{\rm th}$), experimental values ($\nu_{\rm exp}$) [8], discrepancies between $\nu_{\rm th}$ and $\nu_{\rm exp}$, transition frequency shifts due to the scaling of antiproton mass and charge ($\nu_{\rm th}/\frac{d\nu_{\rm th}}{dx}$) and uncertainty of antiproton mass ($\frac{\Delta m_{\bar{p}}}{m_p} = (\nu_{\rm th} - \nu_{\rm exp})/\frac{d\nu_{\rm th}}{dx}$) .

$(J_i, v_i) - (J_f, v_f)$	$\nu_{\rm th}$ (GHz)	$\nu_{\rm exp}$ (GHz)	$\frac{\nu_{\rm th}-\nu_{\rm exp}}{\nu_{\rm th}}$ (ppm)	$\nu_{\rm th}/\frac{d\nu_{\rm th}}{dx}$	$\frac{\Delta m_{\bar{p}}}{m_p}$ (ppm)
(33,1)-(32,1)	804 633.127(5)	804 633.11(11)	0.021	2.56	0.054
(32,0)-(31,0)	1 012 445.559	1 012 445.52(17)	0.039	2.45	0.094
(35,3)-(34,3)	501 948.828(8)	501 949.01(13)	-0.36	4.44	-1.6
(35,1)-(34,3)	412 885.131(8)	412 885.18(12)	-0.12	6.05	-0.72
(34,2)-(33,4)	420121.53(1)	420121.9(10)	-0.88	2.73	-2.4
(34,1)-(33,3)	486 104.43(7)	486 102.6(7)	3.8	3.40	13

In conclusion, we obtained the best limit of the antiproton mass with 5.4×10^{-8} uncertainty. In the experimental paper [8], based on this value but taking some more statistics, $\Delta m_{\bar{p}}/m_p < 6 \times 10^{-8}$ was reported and this value was cited in Particle Listings 2002 [9] and 2003 [10]. The uncertainty is ten times smaller than the previously estimated value, in Particle Listings 2000 [1], based on our calculation [2,3,4] and the experimental data [5].

References

1. Particle Data Group, D. E. Groom et al., Eur. Phys. J. **C15**, 1 (2000).
2. Y. Kino, M. Kamimura, H. Kudo, Nucl. Phys. **A31**, 649 (1998).
3. Y. Kino, M. Kamimura, H. Kudo, Hyperfine Interact., **119**, 201 (1999).
4. Y. Kino, M. Kamimura, H. Kudo, Few-Body Syst. Suppl. **12**, 40 (2000).
5. H. A. Torii et al., Phys. Rev. **A59**, 223 (1999).
6. M. Kamimura, Phys. Rev. **A38**, 621 (1988).
7. E. Hiyama, Y. Kino and M. Kamimura, Prog. Part. Nucl. Phys. **51**, 223 (2003).
8. M. Hori et al., Phys. Rev. Lett., 093401 **87** (2001).
9. Particle Data Group, K. Hagiwara et al., Phys. Rev. **D 66**, 010001 (2002).
10. Particle Data Group, http://pdg.lbl.gov/2003/contents_listings.html.

RESONANCES OF POSITRONIUM COMPLEXES WITH STOCHASTIC VARIATIONAL METHOD

JUNKO USUKURA

Department of Physics, Tokyo University of Science, Kagurazaka 1-3, Shinjuku-ku, Tokyo 162-8601, JAPAN
E-mail: usukura@neppliza.ph.kagu.tus.ac.jp

YASUYUKI SUZUKI

Department of Physics, Niigata University, Ikarashi Nihocho 8050, Niigata 950-2181, JAPAN
E-mail: suzuki@nt.sc.niigata-u.ac.jp

We calculated resonances of positronium complexes, Ps^- and Ps_2, with the stochastic variational method combined with the complex scaling method (SVM+CSM). The method was successfully applied to predict resonances with nonzero angular momentum with high accuracy.

1. Introduction

Among Ps complexes, consisting of electrons and positrons, Ps^- has only one bound state at $E = -0.262$a.u. and it was observed two decades ago[1]. On the other hand, the four-body system, Ps_2, has not been found experimentally in spite of theoretical predictions[2,3,4]. This is because a pair annihilation is not a good signal to distinguish whether it comes from Ps atom or Ps_2. For more-than-four-body systems, any bound state has not been predicted theoretically.

The aim of this work is to investigate energy levels and structures of Ps^- and Ps_2. Though the spectrum of bound states is rather well studied, there are only few calculations for resonance, and no resonance of Ps complexes has been observed experimentally. In this talk, we will present our resonance calculations obtained by a combined method of stochastic variation and complex scaling. The interest of the study is to develop *ab initio* calculations for resonating motion in highly non-adiabatic systems such as Ps complexes.

2. Method

A resonance wave function asymptotically goes to zero at infinity if it is rotated, $U(\theta) : r \to re^{i\theta}$. This is a basis of the complex scaling method (CSM)[5], which makes it possible to find a resonance as a bound state-like solution. To represent the resonance wave function with square integrable bases as $U(\theta)\Psi = \sum_i C_i^\theta \psi_i$, we expand it in terms of explicitly correlated Gaussians[6],

$$\psi_i(\mathbf{x}) = |\mathbf{v}_i|^L Y_{LM}(\hat{\mathbf{v}}_i) \exp\left\{ \frac{1}{2} \sum_{j,k=1}^{N-1} A_{jk}^{(i)} \mathbf{x}_j \cdot \mathbf{x}_k \right\}, \tag{1}$$

where L is a total orbital angular momentum, N is the number of particles and $\mathbf{v}_i = \sum_j^{N-1} u_j^{(i)} \mathbf{x}_j$. Here $A_{jk}^{(i)}$ and $u_j^{(i)}$ are variational parameters.

Energies are determined by diagonalizing the rotated Hamiltonian

$$\sum_{j=1}^{K} \langle P\psi_i\chi | U(\theta) H U^{-1}(\theta) | P\psi_j\chi \rangle C_j(\theta) = E^\theta \sum_{j=1}^{K} \langle P\psi_i\chi | P\psi_j\chi \rangle C_j(\theta). \tag{2}$$

According to the ABC theorem[5], the resonance energy $E = E_r - \frac{i}{2}\Gamma$ is given independently of θ provided that $\theta > \frac{1}{2}\tan^{-1}\left(\frac{\Gamma}{2E_r}\right)$. In practice, the energy obtained by the diagonalization slightly depends on θ.

In atomic or molecular systems, a decay width becomes very small, so calculations of high accuracy are needed. One has to increase the basis dimension to attain accurate results, but for more-than-three-body systems or for states with angular momentum the basis size needed usually becomes huge. To express the wave function with rather small dimension, we selected important bases for the resonance with the stochastic variational method[7], where the basis dimension is increased one by one and the one that gives the lowest energy is selected among many candidates created randomly.

Keeping $\theta = 0$ we first examine the energy eigenvalues by increasing the basis dimension with SVM. We observe some energy eigenvalues stabilized against the basis increase. The stabilized state is a candidate for a resonance (real stabilization method)[8]. Next we study the energy trajectory of the eigenstate with respect to the change of angle θ. The trajectory is obtained by diagonalizing the rotated Hamiltonian in the basis found by the stabilization method. A stationary energy giving a minimum of $|\frac{\delta E}{\delta \theta}|$ may be identified a resonance. To check accuracy, we have to confirm that the stationary point converges to a virtually same point with increasing dimension. Then the converged point is identified to give the resonance parameter.

3. Resonances of Ps^-

Figure 1 shows S-, P-, D- and F resonances of Ps^- below the $Ps(n = 3) + e^-$ threshold. Table 1 compares our results with other calculations. Though the resonance energy agrees with each other, the decay width does not always agree. The widths of the $^3S^e$ and $^3D^e$ states are found to be very small. For the $^3S^e$ state our result agrees with Faddeev-Merkuriev calculation. Our result for the $^3D^e$ state does not agree with the previous calculation. As the width is so small, we studied the state very carefully. We think that our result appears more reliable.

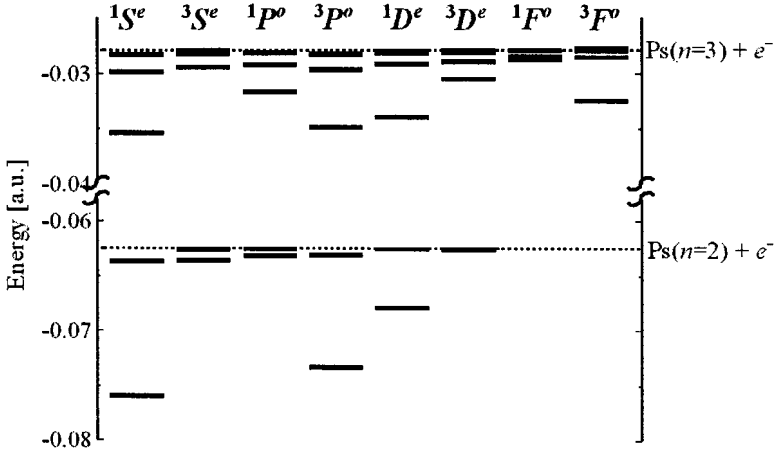

Figure 1. Energy levels of Ps^- resonances.

Table 1. Resonance parameters, (E_R, Γ) [a.u.], of several Ps^- resonances

State	SVM+CSM	References
$^1S^e$	$(-0.07603043 \quad , 4.302\times10^{-5})$	$(-0.0760304 \quad , 4.3\times10^{-5})$[9]
		$(-0.07595 \quad , 4.25\times10^{-5})$[10]
		$(-0.076029875, 4.308\times10^{-5})$[11]
$^3S^e$	$(-0.0635373462, 1.9\times10^{-9})$	$(-0.06353 \quad , 5\times10^{-6})$[9]
		$(-0.0635 \quad , 3\times10^{-9})$[10]
$^3D^e$	$(-0.062588550 \quad , 3\times10^{-9})$	$(-0.0625878 \quad , 6.4\times10^{-6})$[12]

4. Resonances of Ps_2

The Hamiltonian of Ps_2 is invariant with respect to the exchanges of electrons, positrons or charges. Thus, the symmetry is classified by D_{2d} point group[3], which has five irreducible representations labeled as A_1, A_2, B_1, B_2 and E. We calculated S-, P- and D resonances for each symmetry. The decay width is not as small as that of Ps^-.

Figure 2 shows 0^+ resonances of Ps_2 as well as bound states.[13] The dotted line denotes a bound state. The result of Ho[14] is also shown, where the complex scaling method with Hyleraas-type basis functions is used but no full exchange symmetry is taken into account; the resonances are mixed states of A_1, B_2 and E symmetry. Thus the bound state with E symmetry was considered a resonance. The level with $E = -0.313$ a.u. predicted by Ho is actually a mixed state of the A_1 state ($E = -0.329$ a.u.) and E state ($E = -0.330$ a.u.) of our result.

Figure 3 displays P- and D resonances of Ps_2. This is the first calculation for resonances with nonzero angular momentum.

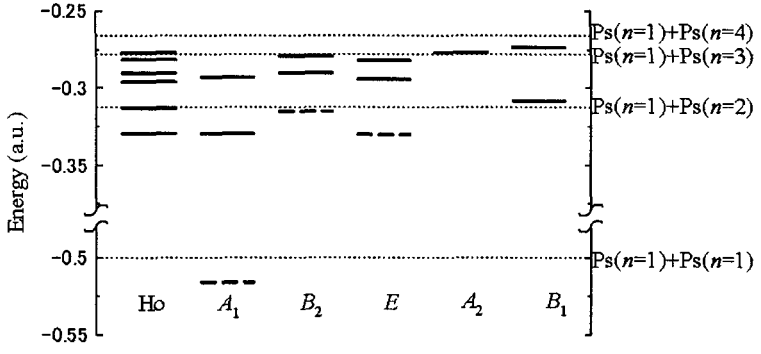

Figure 2. 0^+ resonances of Ps_2 (solid lines). Dashed lines are for bound states.

5. Conclusions

We studied the resonances of positronium complexes. The SVM+CSM with the correlated Gaussian basis is powerful to obtain few-body resonances. It is applicable to more-than-three-body system as well as states with nonzero angular momentum. We located the S-, P-, D-, and F resonances below the threshold of $Ps(n = 3)+e^-$ in Ps^-. We also found nine S-wave, five P-wave and five D-wave resonances in Ps_2.

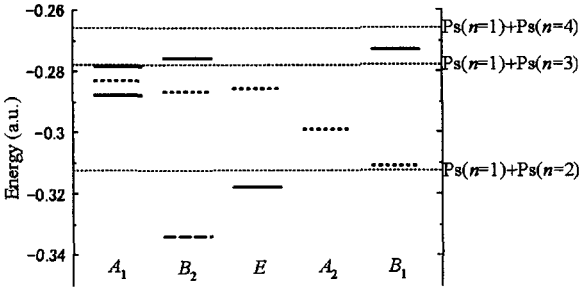

Figure 3. 1^- and 2^+ resonances of Ps_2. Solid lines and dotted lines denotes 1^- and 2^+ resonances, respectively. A dashed line is for 1^- bound state.

Acknowledgments

This work was in part supported by a Grant-in-Aid for Scientific Research (No. 14540249) from the Japan Society for the Promotion of Science.

References

1. A.P. Mills, Jr., *Phys. Rev. Lett.* **46**, 717 (1981).
2. Y. Suzuki and J. Usukura, *Nucl. Instr. and Meth. in Phys. Research* **B171**, 67 (2000).
3. D. B. Kinghorn and R. D. Poshusta, *Phys. Rev.* **A47**, 3671 (1993).
4. K. Varga, J. Usukura and Y. Suzuki, *Phys. Rev. Lett.* **80**, 1876 (1998). J. Usukura, K. Varga and Y. Suzuki, *Phys. Rev.* **A58**, 1918 (1998).
5. J. Aguilar, J.M. Combes, *Commun. Math. Phys.* **22**, 269 (1971); E. Balslev, J.M. Combes, *Commun. Math. Phys.* **22**, 280 (1971); B. Simon, *Commun. Math. Phys.* **27**, 1 (1972).
6. Y. Suzuki, J. Usukura and K. Varga, *J. Phys.* **B31**, 31 (1998).
7. Y. Suzuki and K. Varga, *Stochastic variational approach to quantum-mechanical few-body problem*, Lecture Notes in Physics, Vol. m54 (Springer-Verlag, Berlin Heidelberg, 1998); K. Varga and Y. Suzuki, *Phys. Rev.* **C52**, 2885 (1995); Phys. Rev. **A53**, 1907 (1996).
8. A.U. Hazi and H.S. Taylor, *Phys. Rev.* **1**, 1109 (1970); H.S. Taylor, *Adv. Chem. Phys.* **18**, 91 (1970).
9. Y.K. Ho, *Phys. Lett.* **A102**, 348 (1984).
10. Z. Papp, J. Darai, A. Nishimura, Z.T. Hlousek, C.-Y. Hu and S.L. Yakovlev, *Phys. Lett.* **A304**, 36 (2002).
11. K. Toyota and S. Watanabe, private communication.
12. A.K. Bhatia and Y.K. Ho, *Phys. Rev.* **A48**, 264 (1993).
13. J. Usukura and Y. Suzuki, *Phys. Rev.* **A66**, 010502(R) (2002); Y. Suzuki and J. Usukura, *Nucl. Instr. and Meth. in Phys. Research B*, in press.
14. Y.K. Ho, *Phys. Rev.* **A39**, 2709 (1989).

This page intentionally left blank

Nuclear structure from realistic forces and shell model

This page intentionally left blank

NUCLEAR STRUCTURE – "AB INITIO"

H. FELDMEIER AND T. NEFF
Gesellschaft für Schwerionenforschung mbH
Planckstr. 1, D-64291 Darmstadt, Germany
E-mail: h.feldmeier@gsi.de, t.neff@gsi.de

R. ROTH
Institut für Kernphysik
Schlossgartenstr. 9, D-64289 Darmstadt, Germany
E-mail: robert.roth@physik.tu-darmstadt.de

An ab-initio description of atomic nuclei that solves the nuclear many-body problem for realistic nuclear forces is expected to possess a high degree of predictive power. In this contribution we treat the main obstacle, namely the short-ranged repulsive and tensor correlations induced by the realistic nucleon-nucleon interaction, by means of a unitary correlation operator. This correlator applied to uncorrelated many-body states imprints short-ranged correlations that cannot be described by product states. When applied to an observable it induces the correlations into the operator, creating for example a correlated Hamiltonian suited for Slater determinants. Adding to the correlated realistic interaction a correction for three-body effects, consisting of a momentum-dependent central and spin-orbit two-body potential we obtain an effective interaction that is successfully used for all nuclei up to mass 60. Various results are shown.

1. Introduction

In the last years exact *ab initio* calculations of light nuclei have become feasible with Greens Function Monte Carlo calculations[1] and in the No-Core Shell Model [2]. Here realistic interactions that fit the nucleon-nucleon scattering data and the deuteron properties are used [3,4]. Additional three-body forces are needed and are adjusted to the spectra of nuclei. Chiral perturbation promises to provide a consistent derivation of two- and three-body forces [5,6].

2. The Unitary Correlation Operator Method (UCOM)

Our aim is to perform *ab initio* calculations of larger nuclei with realistic interactions like the Bonn or Argonne potentials in a Hartree-Fock picture or a many-body approach with configuration mixing.

The repulsive core and the strong tensor force of the nuclear interaction induce strong short-range radial and tensor correlations in the nuclear many-body system. These correlations are in the relative coordinates $\boldsymbol{r}_{ij} = \boldsymbol{r}_i - \boldsymbol{r}_j$ and thus can not be represented by products of single-particle states like Slater determinants

$$|\,\Psi\,\rangle = \mathcal{A}\,\{\,|\,q_1\,\rangle \otimes \ldots \otimes |\,q_A\,\rangle\,\} \tag{1}$$

that are usually used as many-body states in Hartree-Fock or a shell-model calculations. $\mathcal{A}$ denotes the antisymmetrization operator and $|\,q_i\,\rangle$ the single-particle states.

Instead we treat the radial and tensor correlations explicitly by a unitary correlation operator C that acts on uncorrelated product states $|\,\Psi\,\rangle$

$$|\,\hat{\Psi}\,\rangle = C\,|\,\Psi\,\rangle \tag{2}$$

such that the many-body state $|\,\hat{\Psi}\,\rangle$ contains the short ranged correlations. For the correlator we make the following ansatz

$$C = C_\Omega \cdot C_r = \exp\Big\{-\mathrm{i}\sum_{i<j} g_{\Omega\,ij}\Big\} \cdot \exp\Big\{-\mathrm{i}\sum_{i<j} g_{r\,ij}\Big\}\,. \tag{3}$$

It is the product of a radial correlator C_r and a tensor correlator C_Ω, both, expressed with a hermitian two-body generator in the exponent.

2.1. *Cluster expansion*

As the ansatz for the correlator contains a two-body operator in the exponent any correlated operator will contain many-body parts. For example a Hamiltonian consisting of one- and two-body parts will turn into

$$\begin{aligned}\hat{H} &= C^\dagger H C = C^\dagger\Big(\sum_i T_i + \sum_{i<j} V_{ij}\Big)C \qquad (4)\\ &= \sum_i T_i + \sum_{i<j} \hat{T}^{[2]}_{ij} + \sum_{i<j<k} \hat{T}^{[3]}_{ijk} + \cdots + \sum_{i<j} \hat{V}^{[2]}_{ij} + \sum_{i<j<k} \hat{V}^{[3]}_{ijk} + \cdots\,,\end{aligned}$$

where the upper script $^{[n]}$ indicates irreducible n-body operators. Here we introduce an approximation by keeping terms only up to two-body operators. This approximation should be good for systems where the range of

the correlator ($g_{r\,ij} = 0$ and $g_{\Omega\,ij} = 0$ for $r_{ij} > R_c$) is short compared to the mean particle distances. In that case the probability to find 3 particles simultaneously within the correlation range R_c is small.

2.2. *Radial correlator*

The radial correlator C_r (described in detail in [7]) shifts a pair of particles in the radial direction away from each other so that they get out of the range of the repulsive core. To perform the radial shifts the generator of the radial correlator uses the radial momentum operator p_r together with a shift function $s(r)$ that depends on the distance of the two nucleons.

$$g_{r\,ij} = \frac{1}{2}\Big(p_{r\,ij}\,s(r_{ij}) + s(r_{ij})p_{r\,ij}\Big) \tag{5}$$

The shift function $s(r)$ is optimized to the potential under consideration. It is large for short distances and will vanish at large distances.

The effect of the transformation $\big|\,\Psi\,\big\rangle \rightarrow C_r\big|\,\Psi\,\big\rangle$ is shown in the upper part of Fig. 1 where the two-body density $\rho^{(2)}_{S,T}$ is displayed as a function of the distance vector $(\boldsymbol{r}_1{-}\boldsymbol{r}_2)$ between two nucleons in ^{4}He. On the l.h.s. $\rho^{(2)}_{S,T}$ is calculated with the shell-model state $\big|\,(1s_{1/2})^4\,\big\rangle$ that is just a product of 4 Gaussians. It has a maximum at zero distance which is in contradiction to the short ranged repulsion of the interaction. This inconsistency is removed by application of the radial correlator C_r that moves density out of the region where the potential is repulsive. The corresponding kinetic, potential and total energies are displayed in the lower part of the figure for three nuclei. The radially correlated kinetic energy $\big\langle\, C_r^\dagger T C_r\,\big\rangle$ increases somewhat compared to $\big\langle\, T\,\big\rangle$ but this is overcompensated by the gain of about -25 MeV per particle in the correlated potential energy. Nevertheless the nuclei are still unbound.

2.3. *Tensor correlator*

The tensor force in the $S=1$ channels of the nuclear interaction depends on the spins and the spatial orientation $\hat{\boldsymbol{r}} = (\boldsymbol{r}_1{-}\boldsymbol{r}_2)/(|\boldsymbol{r}_1{-}\boldsymbol{r}_2|)$ of the nucleons via the tensor operator

$$S_{12}(\hat{\boldsymbol{r}},\hat{\boldsymbol{r}}) = 3(\boldsymbol{\sigma}_1\cdot\hat{\boldsymbol{r}})(\boldsymbol{\sigma}_2\cdot\hat{\boldsymbol{r}}) - (\boldsymbol{\sigma}_1\cdot\boldsymbol{\sigma}_2) = 2\left(3(\boldsymbol{S}\cdot\hat{\boldsymbol{r}})^2 - \boldsymbol{S}^2\right). \tag{6}$$

An alignment of $\hat{\boldsymbol{r}}$ with the direction of the total spin $\boldsymbol{S} = \frac{1}{2}(\boldsymbol{\sigma}_1+\boldsymbol{\sigma}_2)$ is favored energetically. The tensor correlator $C_\Omega = \exp\Big\{-\mathrm{i}\sum_{i<j} g_{\Omega\,ij}\Big\}$,

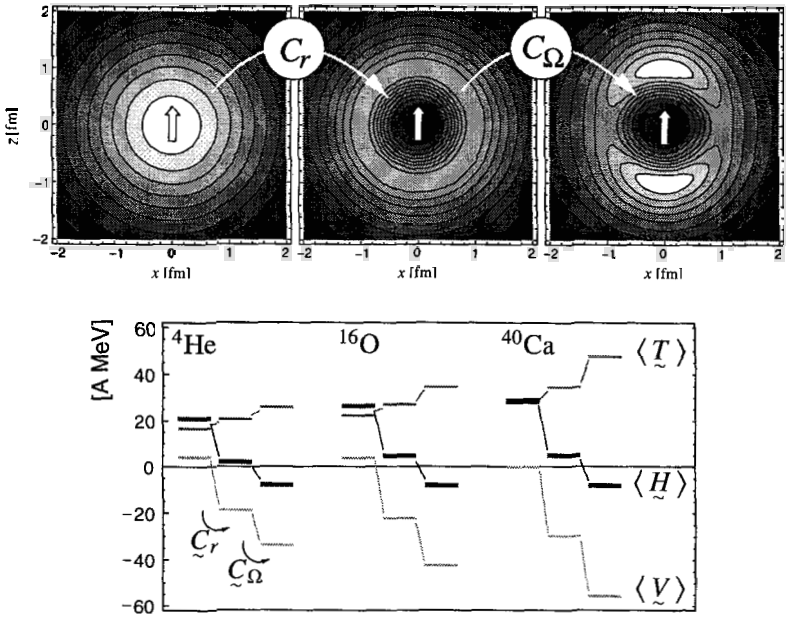

Figure 1. Upper part: Two-body density $\rho^{(2)}_{S,T}(\boldsymbol{r}_1 - \boldsymbol{r}_2)$ of ^{4}He for a pair of nucleons with isospin $T=0$ and parallel spins, $S=M_S=1$. Bright ares denote large probabilities. Arrow indicates spin direction and $(x,y,z) = (\boldsymbol{r}_1 - \boldsymbol{r}_2)$ relative distance vector. Lower part: corresponding kinetic, potential and total energies per particle of ^{4}He, ^{16}O and ^{40}Ca, without, with radial, and with radial and tensor correlations (Bonn-A potential).

defined by the generator

$$g_{\Omega\, ij} = \vartheta(r_{ij}) \frac{3}{2} \Big((\boldsymbol{\sigma}_i \boldsymbol{p}_{\Omega\, ij})(\boldsymbol{\sigma}_j \boldsymbol{r}_{ij}) + (\boldsymbol{\sigma}_i \boldsymbol{r}_{ij})(\boldsymbol{\sigma}_j \boldsymbol{p}_{\Omega\, ij}) \Big) \,, \tag{7}$$

achieves this alignment by shifts perpendicular to the relative orientation $\hat{\boldsymbol{r}}_{ij}$. For that the generator of the tensor correlator uses a tensor operator constructed with the orbital part of the relative momentum operator $\boldsymbol{p}_{\Omega\, ij} = \boldsymbol{p}_{ij} - \boldsymbol{p}_{r\, ij}$. The r-dependent strength and the range of the tensor correlations is controlled by $\vartheta(r)$. For details see [8].

The application of the tensor correlator C_Ω leads to the two-body density depicted in the right hand contour plot of Fig. 1. One may visualize the action of C_Ω as a displacement of probability density from the 'equator' to both 'poles', where the spin of the $S=1$ component of the nucleon pair defines the 'south-north' direction. Again this costs kinetic energy but now the many-body state is in accord with the tensor interaction and one gains the binding needed to end up with about -8 MeV per particle.

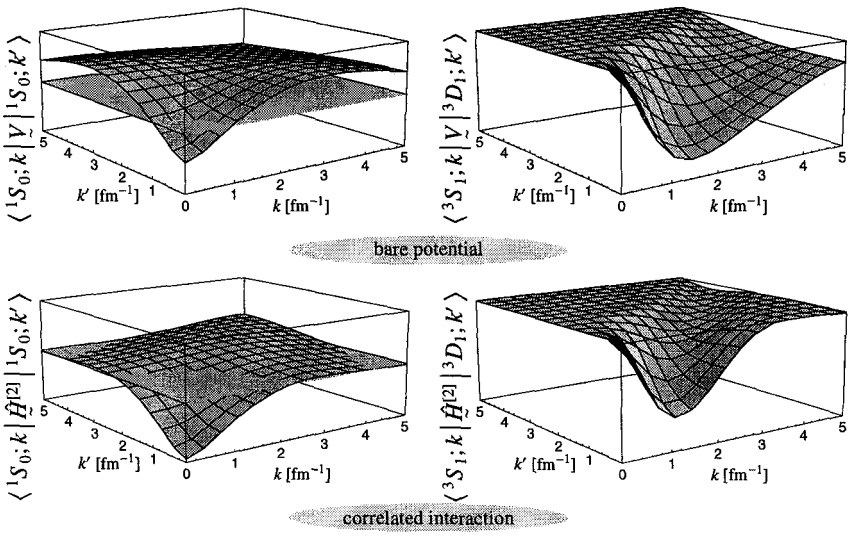

Figure 2. Bare and correlated Argonne V8' interaction in momentum-space. Matrix elements range from -2 to +2 fm^{-1} on the l.h.s. and from -1.5 to 0 fm^{-1} on the r.h.s.

3. Interaction in momentum-space

The inclusion of the short-range correlations achieves a *pre-diagonalization* of the nuclear hamiltonian that is illustrated in Fig. 2. On the l.h.s. the effect of the radial correlations is shown in the ${}^1S_0$ channel. The correlated interaction evaluated in momentum-space is more attractive and does not possess the large off-diagonal matrix elements of the bare interaction. Also the tensor components of the correlated Hamiltonian do not connect to high momenta as is illustrated with the matrix elements between the ${}^3S_1$ and the ${}^3D_1$ channel. The correlated interaction is therefore a low-momentum interaction very similar to the V_{low-k} [9].

4. Effective interaction

To test the two-body approximation we performed no-core shell model calculations with the correlated AV8' interaction for ^{4}He and compared with exact results [10,11]. It turned out that neglecting the $n = 3$- and 4-body parts $\hat{T}^{[n]}$ and $\hat{V}^{[n]}$ of the correlated Hamiltonian leads to an overbinding which is of the same order as the contribution from genuine 3-body forces. Because of the low-momentum nature of the correlated Hamiltonian $\hat{H}^{C2} = T + \hat{T}^{[2]} + \hat{V}^{[2]}$ it can be used directly with simple model spaces

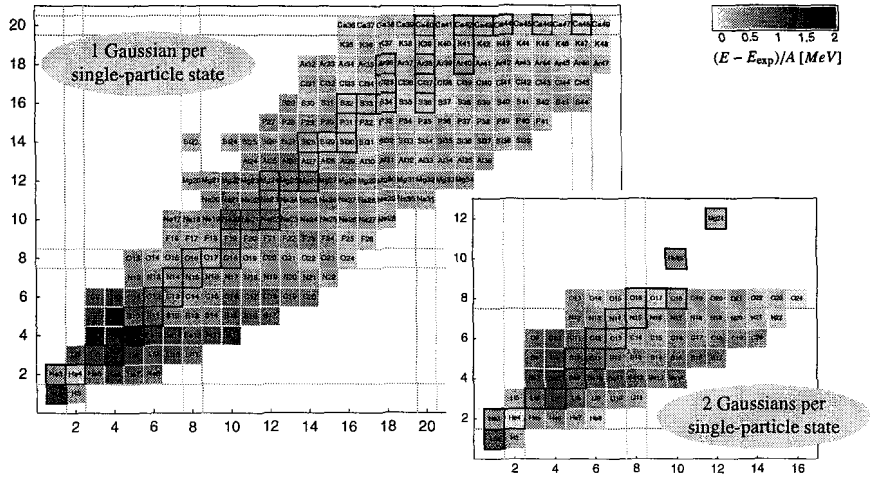

Figure 3. Deviation of mean-field binding energies from measured ones.

built of Slater determinants. The effects of missing higher-order contributions to the correlated interaction and of genuine three-body forces is for now effectively described by a momentum-dependent central and spin-orbit correction H_{corr} with four parameters adjusted to four doubly magic nuclei. The resulting effective interaction $\hat{H}_{eff} = \hat{H}^{C2} + H_{corr}$ is used for all nuclei up to mass number 60. The expectation value of H_{corr} is typically 15% of the correlated interaction energy.

5. Hartree-Fock calculations

For the nuclei listed in the nuclear chart Fig. 3 we minimized the expectation value $\langle \Psi | \hat{H}_{eff} - T_{cm} | \Psi \rangle / \langle \Psi | \Psi \rangle$ with respect to all parameters of the single-particle states

$$\langle \boldsymbol{x} | q \rangle = \sum_i c_i \exp\left\{ -\frac{(\boldsymbol{x} - \boldsymbol{b}_i)^2}{2a_i} \right\} | \chi_i \rangle \otimes | \xi \rangle \tag{8}$$

that are contained in the Fermionic Molecular Dynamics [12] state $| \Psi \rangle$ (Eq. (1)). The summation is either for one or for two independent Gaussians per single-particle state.

The inclusion of a second Gaussian improves the masses of p-shell nuclei substantially (inset of Fig. 3). The largest deviations occur for nuclei with an α-cluster structure like ^{8}Be or ^{12}C or for intrinsically deformed nuclei at

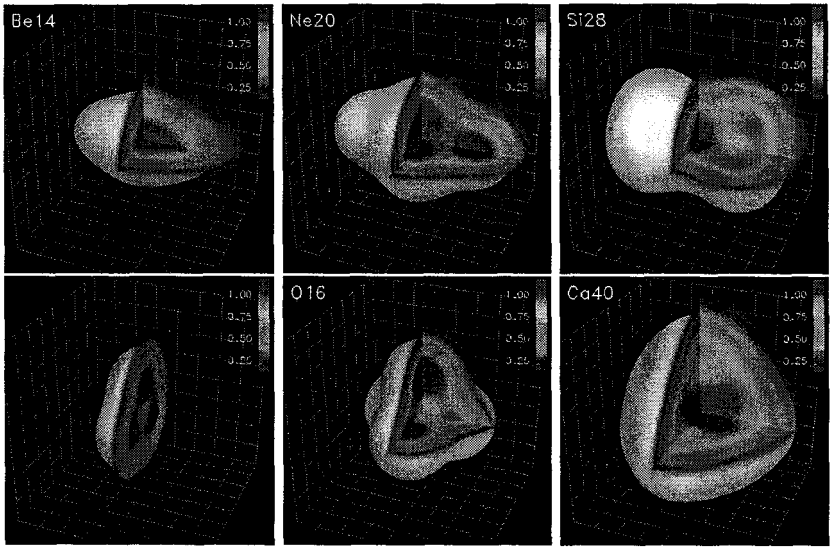

Figure 4. One-body densities of intrinsic states. Upper part: PAV calculation ^{14}Be, ^{20}Ne, ^{28}Si (local minimum); lower part: VAP calculation ^{12}C, ^{16}O, ^{40}Ca.

the middle of the *sd*-shell. Some examples of intrinsic shapes are displayed in the upper half of Fig. 4. In ^{14}Be the extra six neutrons have pulled together the well localized pair of α's that form ^{8}Be. The peanut like shape for ^{28}Si is a local minimum.

6. Projection after variation and variation after projection

To improve the many-body Hilbert space we project on spin and parity after variation (PAV). We also perform variation after projection (VAP) calculations in the sense of the generator coordinate method. The intrinsic state is minimized here with constraints on radius, dipole moment, quadrupole or octupole moment.

With the above described effective interaction ^{16}O gains in a VAP calculation about 5 MeV in binding by forming α-clusters (see lower part of Fig. 4) compared to the spherical closed-shell configuration which represents the energy minimum in the PAV case. Even for ^{40}Ca VAP leads to a deformation towards a tetrahedron of ten α's which however are much more amalgamated than in ^{16}O (Fig. 4).

In a next step the different intrinsic shapes obtained in the VAP process can be used to perform multiconfiguration calculations.

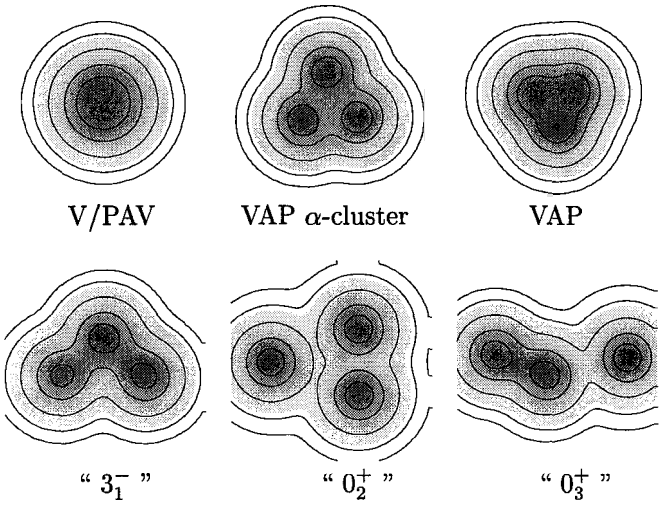

Figure 5. One-body densities of intrinsic ^{12}C states.

A very interesting nucleus is ^{12}C for which the shell-model configuration $(1s_{1/2})^4(1p_{3/2})^8$ is competing with the 3-α cluster structure [13,14]. Like in ^{16}O the PAV ground state of ^{12}C turns out to be a spherical shell-model state (Fig. 5, V/PAV). However, variation after projection leads to a triangular shape made of three α's (Fig. 5, VAP) and 7.2 MeV of additional binding as indicated in Table 1. A pure α-cluster configuration obtained in a VAP calculation has larger distances between the α-clusters and is 4.3 MeV less bound than the shell-model configuration. The difference to the full VAP is due to the polarization of the α-clusters. The description of this polarization is significantly improved by using two Gaussians per single-particle state.

The description of the excited states requires an enlarged Hilbert space. Multiconfiguration calculations with the configurations shown in the lower part of Fig. 5 show only a small increase in binding for the groundstate

	E_b [MeV]	r_{charge} [fm]	$B(E2)$ [e^2fm^4]
V/PAV	84.7	2.33	-
VAP α-cluster	80.4	2.66	56.3
VAP	91.9	2.38	24.7
Multiconfig	93.4	2.50	40.0
Exp	92.2	2.47	39.7 ± 3.3

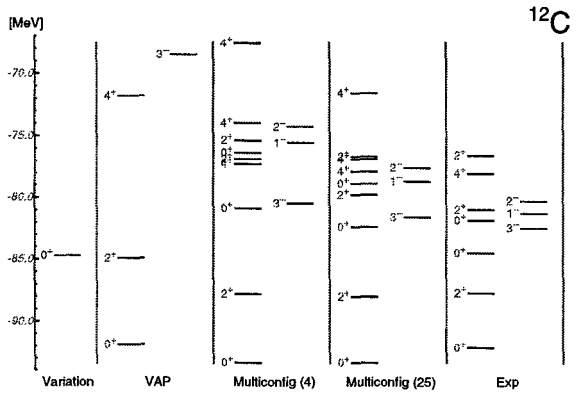

Figure 6. Calculated and experimental level scheme for ^{12}C.

but have a significant effect on the radius and the $B(E2)$ value for the $0_1^+ \longrightarrow 2_1^+$ transition. The additional configurations have been chosen to give lowest energies for the 3_1^- and the second and third 0^+ states. We find 3 α-cluster structures for the 0_2^+ state and ^{8}Be + α-cluster structures for the 0_3^+ state. For an improved description of these states a larger number of configurations with greater distances between the α's is needed. This is consistent with an assumed Bose condensed state[15] for the 0_2^+ state.

References

1. S.C. Pieper, R.B. Wiringa, *Ann. Rev. Nucl. Part. Sci.* **51**, 53 (2001).
2. P. Navratil, W.E. Ormand, *Phys. Rev.* **C68** 034305 (2003).
3. R. Machleidt, *Phys. Rev.* **C63** 024001 (2001).
4. R. Wiringa, V. Stoks, R. Schiavilla, *Phys. Rev* **C51** 53, 2001.
5. D.R. Entem, R. Machleidt, *Phys. Rev.* **C68** 041001 (2003).
6. W. Glöckle et al., *in these proceedings*
7. H. Feldmeier, T. Neff, R. Roth, J. Schnack, *Nuc. Phys.* **A632**, 61 (1998).
8. T. Neff, H. Feldmeier, *Nuc. Phys.* **A713**, 311 (2003).
9. S.K. Bogner, T.T.S. Kuo and A. Schwenk, *Phys. Rept.* **386**, 1 (2003).
10. T. Neff, H. Feldmeier, *Proc. of the International Workshop XXXI on Nuclear Structure and Dynamics at the Limits, Hirschegg, Austria, January 12-18, 2003*
11. H. Kamada et al., *Phys.Rev.* **C64** 044001 (2001).
12. H. Feldmeier and J. Schnack, *Rev. Mod. Phys.* **72**, 655 (2000).
13. Y. Kanada-En'yo, *Phys. Rev. Lett.* **81** 5291 (1998).
14. N. Itagaki et al., *Nuc. Phys.* **A719**, 205c (2003).
15. Y. Funaki, A. Tohsaki, H. Horiuchi, P. Schuck, G. Röpke, *Phys. Rev.* **C67** 051306 (2003).

SHELL STRUCTURES IN OXYGEN ISOTOPES DESCRIBED WITH MODERN NUCLEON-NUCLEON INTERACTIONS

S. FUJII

Department of Physics, University of Tokyo
Tokyo 113-0033, Japan
E-mail: sfujii@nt.phys.s.u-tokyo.ac.jp

R. OKAMOTO AND K. SUZUKI

Department of Physics, Kyushu Institute of Technology
Kitakyushu 804-8550, Japan

Shell structures in the $N \simeq Z$ nucleus ^{17}O and the neutron-rich oxygen isotopes ^{23}O and ^{25}O are microscopically described by calculating single-particle energies with modern nucleon-nucleon interactions within the framework of the unitary-model-operator approach. It is found that the effect of three-body cluster terms on the single-particle energy is more important in ^{23}O and ^{25}O than ^{17}O.

1. Introduction

The shell structure which is closely related to the single-particle level is one of the fundamental properties in nuclei. Recently, it has been argued that the shell structure in neutron or proton-rich nuclei is different from that in stable nuclei, and thus, some magic numbers disappear and new magic numbers arise in nuclei near the drip lines.[1,2] When we calculate the energies of single-particle levels in neutron- or proton-rich nuclei, it would be desirable that the calculation formalism is based on the particle basis. Advantages of the particle-basis formalism are that the Coulomb force can be treated accurately for the *pp* channel and effects of charge dependence in realistic nuclear forces are taken into account in structure calculations. In the particle-basis formalism, one can obtain the energy differences between proton and neutron levels for not only $N \simeq Z$ nuclei but also neutron- or proton-rich nuclei in the same way.

As one of the methods for solving nuclear many-body problems, we have developed a many-body theory, the unitary-model-operator approach (UMOA).[3] In the UMOA, an energy-independent and Hermitian effective

interaction is derived through a unitary transformation of an original Hamiltonian. The unitary transformation for the construction of the Hermitian effective interaction has also been performed in the no-core shell-model calculation.[4] Recently, we have extended the formulation of the UMOA from the isospin basis to the particle one, and actually applied to the calculations of binding energies and single-particle energies of the neutron and proton in nuclei around the $N = Z$ nucleus ^{16}O with modern nucleon-nucleon interactions.[5] In that work, the effect of two-particle one-hole ($2p$-$1h$) excitation from the ground state of ^{16}O has been taken into account in the calculation of single-particle energies in ^{17}O and ^{17}F, but higher-order many-body correction terms such as three-body cluster (3BC) terms have not been evaluated.

In the present study, we apply the extended UMOA to neutron-rich oxygen isotopes in addition to ^{17}O, and calculate single-particle energies with the 3BC correction terms. As far as we know, the present study is the first attempt to clarify the 3BC effect on the single-particle energy in neutron-rich nuclei with a realistic nucleon-nucleon interaction. In the present work, we use the CD-Bonn potential[6] as the realistic nucleon-nucleon interaction. In the following, after the calculation procedure is briefly presented, the calculated results are shown.

2. Calculation procedure

Since the methods for determining the effective interaction and calculating the single-particle energy have been given in detail in the previous work,[5] we here outline the calculation procedure. The harmonic-oscillator (h.o.) wave functions are used as the basis states in the calculations. We consider a model space for each of the nn, np, and pp channels specified by a boundary number ρ_1 which is given with the sets of h.o. quantum numbers $\{n_a, l_a\}$ and $\{n_b, l_b\}$ of two-body states by

$$\rho_1 = 2n_a + l_a + 2n_b + l_b. \tag{1}$$

The value of ρ_1 is taken as large as possible so that the calculated results do not depend on this value. In the present study, we take as $\rho_1 = 12$ as a sufficiently large value. As for the value of the h.o energy $\hbar\omega$ we use the optimal value for each nucleus, which has been discussed in the previous work.[5]

In the large model space, we calculate the two-body effective interaction self-consistently with the single-particle potential. The two-body effective interaction in the large model space is determined so that there are no

vertices which induce $2p$-$2h$ excitation. Using the two-body effective interaction, we calculate the unperturbed ground-state energy. Furthermore, the $2p$-$1h$ ($1p$-$1h$) effect on a nucleus having a single-particle structure (a closed-shell nucleus) is obtained by the diagonalization of the unitarily transformed Hamiltonian which contains the kinetic and single-particle potential energies and the two-body effective interaction. The ground-state energy is given by the sum of the unperturbed ground-state energy and the correlation energy. In the present study, we further evaluate the 3BC effects both on the single-particle system and the closed-shell nucleus, and then the energy of the 3BC effect is added to the ground-state energy. The full details of the 3BC terms for the closed-shell nucleus and the single-particle state based on the particle basis will be shown in a separated paper. The single-particle energy for the ground state is expressed as the difference of the ground-state energies of a nucleus having the single-particle structure and the corresponding closed-shell nucleus. Note that the values of $\hbar\omega$ for these two nuclei are, in general, different from each other since we search for the optimal $\hbar\omega$ for each nucleus.

3. Results and discussion

In the left side of Fig. 1, the calculated results of single-particle energies for the ground states of ^{17}O, ^{23}O, and ^{25}O using the CD-Bonn potential are illustrated. The results are shown separately for the cases with and without the 3BC effect. It is seen that the 3BC effect has significant contributions repulsively to the single-particle energies and becomes larger as the mass number becomes larger. The strong repulsive effect is favorable for the neutron-rich nuclei ^{23}O and ^{25}O to reproduce the experimental values. On the contrary, the result for ^{17}O becomes worse in comparison with the experimental value when the 3BC effect is taken into account. We have also observed that the results for the N^{3}LO potential[7] based on chiral perturbation theory show the same tendency with those for the CD-Bonn potential.

It should be noted that a genuine three-body force is not included in the present calculation. The genuine three-body force would show attractive effects on the single-particle energies, and would have different contributions between the $N \simeq Z$ and neutron-rich nuclei because of the isospin and density dependences. We should include the genuine three-body force in the structure calculation to obtain more reliable results.

In order to discuss the importance of the 3BC contribution to the single-

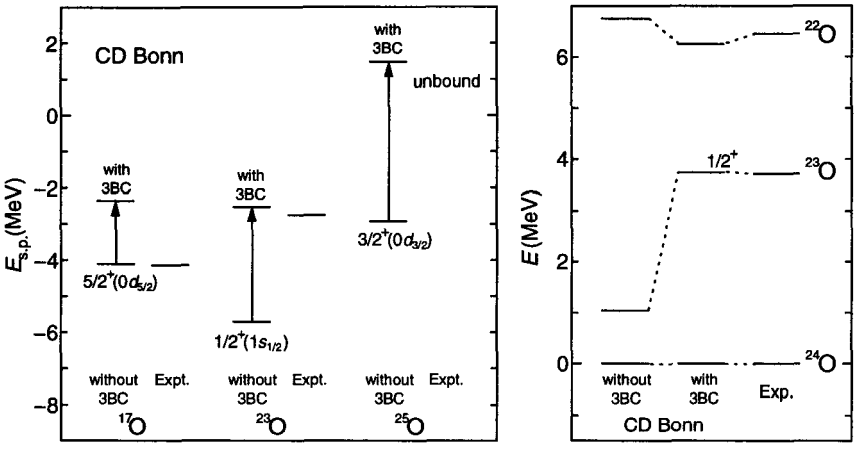

Figure 1. Calculated and experimental single-particle energies for the ground-states of ^{17}O, ^{23}O, and ^{25}O (left figure), and the energies of the ground states of ^{22}O, ^{23}O, and ^{24}O relative to ^{24}O (right figure). The CD-Bonn potential is employed.

particle energy in neutron-rich oxygen isotopes, in the right side of Fig. 1, the energies of the ground-states of ^{22}O, ^{23}O, and ^{24}O relative to the ground state of ^{24}O are exhibited. At the lowest order, ^{22}O and ^{24}O are considered to be the closed-shell nuclei in which the $0d_{5/2}$ and $1s_{1/2}$ states of the neutron are the uppermost occupied states, respectively. We evaluate the 3BC effect on these closed-shell nuclei. The ground state of ^{23}O can be described as the one neutron plus the ground state of ^{22}O at the lowest order. The 3BC terms for the single-particle state of the neutron are calculated. We see that the 3BC effects on the closed-shell nuclei ^{22}O and ^{24}O do not show significant contributions to the relative energy between ^{22}O and ^{24}O. The calculated results for ^{22}O and ^{24}O are in good agreement with the experimental values for both the cases with and without the 3BC effect. On the other hand, as for ^{23}O, the 3BC effect on the single-particle state is considerably large, and then the good agreement with the experimental value is observed when the 3BC effect is taken into account.

4. Conclusions

We have applied the extended UMOA based on the particle basis to the calculation of the single-particle energies of the ground states in oxygen isotopes with the CD-Bonn potential. We have evaluated the 3BC effects on closed-shell nuclei and single-particle states. The calculated results have

shown that the 3BC effect on the single-particle energy is repulsive and more important in neutron-rich oxygen isotopes than ^{17}O. The strong repulsive effect is favorable for the neutron-rich nuclei ^{23}O and ^{25}O to reproduce the experimental values. We conclude that the 3BC effect is indispensable for the microscopic description of the single-particle energies in neutron-rich oxygen isotopes, as far as the present particle-hole formalism is employed. The detailed results of the 3BC effect in oxygen isotopes will be reported elsewhere in the near future.

Acknowledgments

One of the authors (S. F.) acknowledges the Special Postdoctoral Researchers Program of RIKEN. This work is supported by a Grant-in-Aid for Scientific Research (C) from Japan Society for the Promotion of Science (JSPS) (No. 15540280).

References

1. A. Ozawa, T. Kobayashi, T. Suzuki, K. Yoshida, and I. Tanihata, *Phys. Rev. Lett.* **84**, 5493 (2000).
2. T. Otsuka, R. Fujimoto, Y. Utsuno, B. A. Brown, M. Honma, and T. Mizusaki, *Phys. Rev. Lett.* **87**, 082502 (2001).
3. K. Suzuki and R. Okamoto, *Prog. Theor. Phys.* **92**, 1045 (1994).
4. P. Navrátil, J. P. Vary, W. E. Ormand, and B. R. Barrett, *Phys. Rev. Lett.* **87**, 172502 (2001).
5. S. Fujii, R. Okamoto, and K. Suzuki, *nucl-th*/0311053.
6. R. Machleidt, F. Sammarruca, and Y. Song, *Phys. Rev.* **C53**, R1483 (1996).
7. D. R. Entem and R. Machleidt, *Phys. Rev.* **C68**, 041001(R) (2003).

Nuclear shapes and rotation

This page intentionally left blank

TRIAXIAL SUPERDEFORMATION AND WOBBLING MODE IN LU-HF ISOTOPES

WENCHAO MA

Department of Physics, Mississippi State University, Mississippi State, MS 39762, U. S. A. (mawc@ra.msstate.edu)

Triaxial strongly deformed and superdeformed (TSD) structures have been observed in Lu-Hf nuclei. Wobbling motion, a characteristic excitation mode of triaxial nuclei, has been established in odd-Z even-N ^{163,165,167}Lu. The aligned $i_{13/2}$ proton plays a crucial role to realize $\Im_x > \Im_y$ in positive-γ shapes and allowing the wobbling motion compete energetically with other excitations. No evidence for wobbling exists, up to date, for even-even system that was originally predicted. Theoretical calculations successfully predicted the existence of an island of TSD structures in Lu-Hf isotopes, but face great challenges regarding the wobbling mechanism and the calculated proton and neutron shell gaps.

A low-lying collective excitation uniquely related to the rotational motion of a triaxial deformed nucleus is the wobbling mode [1], characterized by a sequence of wobbling bands with increasing number of wobbling quanta, n_w= 0, 1, 2, ... The wobbling mode was predicted about thirty years ago and was only successfully observed in the past several years through extensive experimental studies. The search was concentrated in Lu-Hf isotopes following theoretical investigations [2,3] and later more systematic calculations [4,5] using the "Ultimate Cranker" code [6] which indicated local minima in the potential energy surface with a large quadrupole deformation ($\epsilon_2 \sim 0.4$) and substantial triaxiality ($\gamma \sim \pm 20°$) for nuclei near Z$\sim$72 and N$\sim$94 as shown, for example, in Fig. 1(a). The $\pi i_{13/2}$intruder orbital plays a crucial role in the large deformation. The triaxiality likely results from a shell gap at $N = 94$ with $\gamma \sim 20°$ [5].

In the past several years TSD bands have been reported in six Lu and three Hf isotopes as summarized in Fig. 2. They are ^{161,162}Lu [7], ^{163}Lu [8,9,10], ^{164}Lu [11], ^{165}Lu [5,12], ^{167}Lu [13], ^{168}Hf [14], ^{170}Hf [15], and ^{174}Hf [16]. As an indication of large deformation the dynamical moments of inertia of these bands, as shown in Fig. 1(b). are substantially larger than that of normal deformed (ND) bands, which are less than 50 and 60 in Lu and Hf

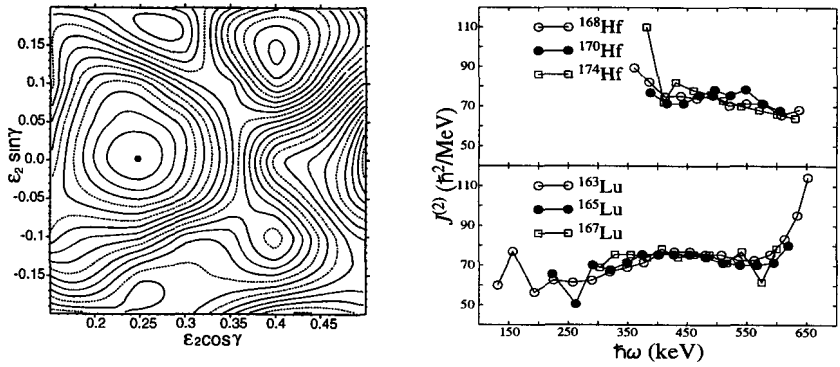

Figure 1. (a) Left: Potential energy surface at $I = 50\hbar$ for the lowest configuration of $(\pi, \alpha) = (+, 0)$ in ^{168}Hf calculated with "Ultimate Cranker" code. The energy difference between the contour lines is 0.2 MeV. (b) Right: Comparison of dynamical moments of inertia for some TSD bands in Lu and Hf isotopes.

Z \ N	90	91	92	93	94	95	96	97	98	102
71	1(0) ^{161}Lu	3(0) ^{162}Lu	4(4)10^{-1} ^{163}Lu	8(2)10^{-1} ^{164}Lu	3(2)10^{-2} ^{165}Lu	^{166}Lu	4(3)10^{-2} ^{167}Lu	^{168}Lu	^{169}Lu	^{173}Lu
72	^{162}Hf	^{163}Hf	^{164}Hf	^{165}Hf	^{166}Hf	^{167}Hf	3(0)10^{-3} ^{168}Hf	^{169}Hf	1(0)10^{-3} ^{170}Hf	4(0)10^{-2} ^{174}Hf

Figure 2. Overview of searches and results for TSD bands in Lu and Hf nuclei. In each square the three parameters A(B)C denote the number of TSD bands observed for that nuclide, the number of these which could be linked to the normal deformed (ND) structures, and the order of the population strength compared with that of the yrast structure.

isotopes, respectively. The large deformation has been further confirmed by the measured large quadrupole moments through lifetime experiments in $^{163-165}$Lu [17,18], ^{168}Hf [14], and ^{174}Hf [19]. In ^{163}Lu an average value of $Q_t \sim 8.4\ eb$ ($\varepsilon_2 \sim 0.36$) was observed, as compared to $\sim 5\ eb$ for ND structures. But a larger $Q_t \sim 11.4\ eb$ and $\sim 13.5\ eb$ ($\varepsilon_2 \sim 0.46$) were obtained in ^{168}Hf and ^{174}Hf.

The critical experimental proof of triaxiality is the wobbling mode which has been established in ^{163}Lu [20,21], ^{165}Lu [12], ^{167}Lu [13], and possibly in ^{161}Lu [22]. The measured large B(E2) values of the decay-out transitions from the excited TSD bands to the lower TSD bands, in competition with the $\Delta I = 2$ in-band transitions, agree well with calculations using the particle-

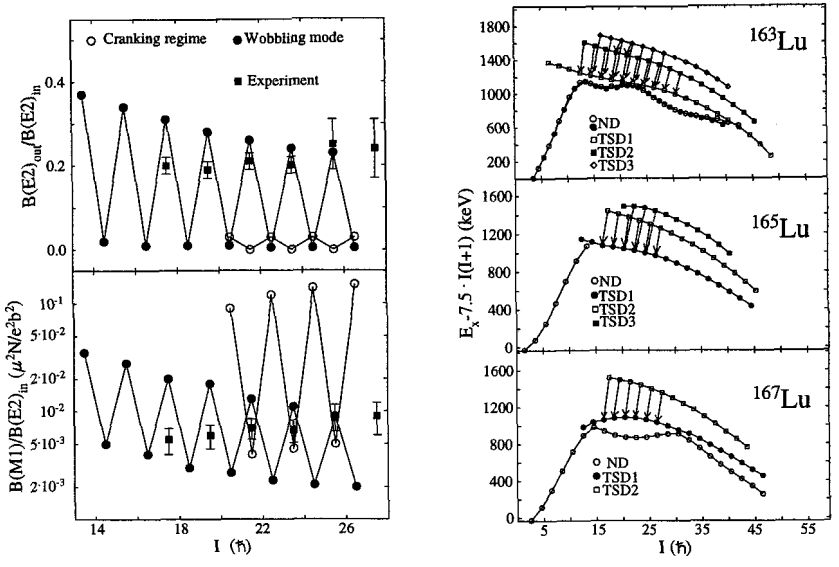

Figure 3. Left: Experimental $B(E2)_{out}/B(E2)_{in}$ and $B(M1)/B(E2)_{in}$ ratios for the $I \longrightarrow I-1$ transitions from TSD2 to TSD1 in ^{163}Lu together with the values calculated by the particle-rotor model. Right: Excitation energy minus a rigid-rotor reference for the bands in ^{163,165,167}Lu. Phonon numbers $n_w = 0$, 1, and 2 for bands TSD1, TSD2, and TSD3, respectively.

plus-rotor model [23,24], see Fig. 3. In cranking regime for a rotational band built on an aligned particle, the core rotates about the shortest axis-X of the nucleus, while the single particle is rotation aligned. Thus both angular momenta from collective rotation and the single particle are aligned in X-direction. In wobbling mode, however, the angular momentum from the collective rotation of the core is tilted away from the X-axis. This tilted "wobbling angle" increases with the phonon number. An alternative approach using cranked shell model plus random phase approximations [25,26] further reproduced the observed experimental spin dependence of the wobbling frequency $\hbar\omega_{wob}$. The calculations indicate that it is crucial to t! ake into account the direct contribution to the moments of inertia from the aligned $i_{13/2}$ proton so as to realize $\Im_x > \Im_y$ in positive-γ shapes and allow wobbling to compete energetically with other excitations.

Other suggested TSD bands in this region were based on their similarities with bands for which quadrupole moments were measured or the wobbling mode was confirmed, and were inferred from comparisons of mea-

sured spectroscopic information with theoretical calculations.

While the wobbling mode was first predicted for even-even systems [1], so far it has only been observed in odd-Z even-N Lu isotopes but not in any Hf (Z=72) isotopes. None of the suggested TSD bands in ^{168,170,174}Hf was linked to known ND structures. Therefore, the exact excitation energy and the spin/parity of these bands remain unknown, and definitive configuration assignments could not be made. The bands in Hf isotopes are much weaker than the bands in Lu isotopes. The role of the aligned particles in the description of wobbling excitations in an even-even system will most likely be different from that of the single $i_{13/2}$ proton in the Lu isotopes. It is questionable if wobbling can exist without the presence of aligned particle.

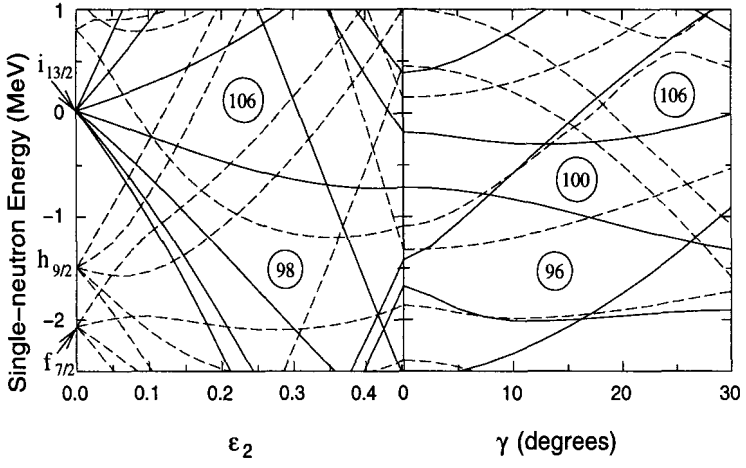

Figure 4. Left panel: single-neutron energy as a function of ϵ_2 from UC calculations. Three "intruder" orbitals from $i_{11/2}$ (solid lines) and two from $j_{15/2}$ states (dashed lines), appearing at large deformation, are strongly down-sloping in energy. Right panel: single-neutron energy as a function of γ, where $\epsilon_2 = 0.453$ and $\epsilon_4 = 0$, see Ref.16.

Earlier theoretical studies [2,3,5,4] predicted the lighter Hf isotopes ^{164,166}Hf to be the best candidates to show TSD shapes. However, TSD bands have only been reported in ^{168,170,174}Hf. Note that ^{174}Hf (N=102) is far away from the predicted neutron shell gap. Recent calculations [16,27] suggest that the larger deformation in heavier Hf TSD bands results from a higher occupancy of the intruder $\nu i_{11/2}$ and $\nu j_{15/2}$ orbitals which originate above N=126 spherical shell gap, thus producing large TSD shell gaps at N=96 and 100 with $\gamma \geq 15^o$, see Fig. 4. Since the positions of these intruder

orbitals are poorly known, the location and magnitude of the neutron shell gap cannot be calculated well. Only the continued experimental investigation of TSD bands can eventually give the spectroscopic information needed to determine the position of these intruder subshells definitively, as well as that of the prolate driving $\pi i_{13/2}$, $\pi h_{9/2}$, and $\nu i_{13/2}$ orbitals.

The author is grateful to his collaborators on the research related to the triaxial deformation and the wobbling mode in Lu-Hf isotopes. This work is supported in part by U.S. DOE grant DE-FG02-95ER40939.

References

1. A. Bohr and B.R. Mottelson, Nuclear Structure (Benjamin, New York, 1975), Vol. II, Chapter 4, p. 190.
2. S. Åberg, Nucl. Phys. A **520** (1990) 35c.
3. I. Ragnarsson, Phys. Rev. Lett. **62** (1989) 2084.
4. R. Bengtsson, www.matfys.lth.se/~ragnar/ultimate.html
5. H. Schnack-Petersen *et al.*, Nucl. Phys. A **594** (1995) 175.
6. T. Bengtsson, Nucl. Phys. **A 512** (1990) 124.
7. P. Bringel *et al.*, Eur. Phys. J. A **A 16** (2003) 155.
8. W. Schmitz *et al.*, Phys. Lett. B **303** (1993) 230.
9. J. Domscheit *et al.*, , Nucl. Phys. A **660** (1999) 381.
10. D.R. Jensen *et al.*, Nucl. Phys. A **703** (2002) 3.
11. S. Törmänen *et al.*, Phys. Lett. B **454** (1999) 8.
12. G. Schönwaßer *et al.*, Phys. Lett. B **552** (2003) 9.
13. H. Amro *et al.*, Phys. Lett. B **553** (2003) 197.
14. H. Amro *et al.*, Phys. Lett. B **506** (2001) 39.
15. A. Neußer *et al.*, Eur. Phys. J. **A 15** (2002) 439.
16. M. Djongolov *et al.*, Phys. Lett. B **560** (2003) 24.
17. G. Schönwaßer *et al.*, Eur. Phys. J. A **15** (2002) 435.
18. A. Görgen *et al*, to be published.
19. M. Djongolov *et al*, to be published.
20. S. Ødegård *et al.*, Phys. Rev. Lett. **86** (2001) 5866.
21. D. R. Jensen *et al.* Phys. Rev. Lett. **89** (2002) 142503.
22. P. Bringel *et al.*, to be published.
23. I. Hamamoto, Phys. Rev. **C 65** (2002) 044305.
24. I. Hamamoto and G. Hagemann, Phys. Rev. **C 67** (2003) 064306.
25. M. Matsuzaki, Y. Shimizu, and K. Matsuyanagi, Phys. Rev. **C 65** (2002) 041303(R).
26. Y.R. Shimizu and M. Matsuzaki, Nucl. Phys. A **588** (1995) 559.
27. R. Bengtsson and H. Ryde, private communication.

TRIAXIAL DEFORMATION AND CHIRAL BANDS IN NUCLEI AROUND MASS 130

N. YOSHINAGA AND K. HIGASHIYAMA

Department of Physics, Saitama University,
Saitama City, 338-8570, Japan
E-mail: yoshinaga@phy.saitama-u.ac.jp

We report on pair-truncated shell-model calculations of low-lying yrast and quasi-γ bands of nuclei around mass 130 using phenomenological effective interactions of pairing plus quadrupole type, where the strengths of interactions are gradually changed as functions of numbers of valence nucleons. The calculations start with even-even nuclei of low-lying states, which exhibit typical features of γ-instability. The model reproduces well experimental energy levels and $E2$ transition rates. We calculate energy levels of odd-A nuclei, where the effective interactions identical to those obtained from the calculations of the even-even nuclei are employed. The agreement between the theoretical values and the experimental observations is rather well.

1. Introduction

Nuclei around mass 130 have many interesting features such as high-spin isomers, backbending phenomena, soft triaxial deformation and recently those features noted by "chiral bands". Moreover, the beta-decays and electron-captures in this region provide us necessary information for predicting the abundance of nuclei in the occasion of super-nova explosions. The nuclei around this region are neither vibrational nor rotational. Thus it is very difficult to treat them in terms of conventional mean field theories. To overcome this difficulty we construct many-body states in terms of collective nucleon pairs which have angular momenta zero (S) and two (D). The model is called an SD version of the pair-truncated shell model (PTSM)[1]. The purpose of this work is to understand many seemingly different features around this region in a self-consistent and a unified way in terms of the PTSM. Because of page limit, we discuss here only Ba isotopes. For odd-odd nuclei we ask readers to refer to the proceeding paper by K. Higashiyama in this volume.

2. Even-even nuclei

In Xe, Ba and Ce isotopes several valence proton particles and neutron holes are coupled to a double magic ^{132}Sn core. In this region the valence proton particles and neutron holes occupy the $0g_{7/2}$, $1d_{5/2}$, $1d_{3/2}$, $0h_{11/2}$ and $2s_{1/2}$ orbitals and we take into account the $50 \leq N(Z) \leq 82$ configuration space for both neutrons and protons, where valence neutrons (protons) are treated as holes (particles). The adopted single-particle energies are the same as given in Ref. 1.

In order to understand systematics we introduce effective interactions which vary according to neutron and proton numbers smoothly. The strengths of the effective interactions are gradually changed as functions of numbers of valence nucleons as follows (in MeV),

$$
\begin{aligned}
G_{0\nu} &= 0.140 - 0.0050\ \bar{N}_\nu, \\
G_{2\nu} &= 0.000 + 0.0025\ \bar{N}_\nu + 0.0015\ N_\pi, \\
\kappa_\nu &= 0.050 + 0.0025\ \bar{N}_\nu, \\
G_{0\pi} &= 0.150 - 0.0050\ N_\pi, \\
G_{2\pi} &= 0.018 - 0.0010\ N_\pi + 0.0010\ \bar{N}_\nu, \\
\kappa_\pi &= 0.030 + 0.0025\ N_\pi, \\
\kappa_{\nu\pi} &= 0.070.
\end{aligned}
$$

Here $\bar{N}_\nu$ represents the number of neutron-holes, and N_π, the number of proton-particles. If we assume that the interactions between neutrons depend solely on the number of neutrons and interactions between protons depend only on the number of protons, it is quite difficult to obtain a good description of the experimental level scheme. Here the definitions of interactions and their detailed descriptions are given in Ref. 1.

Energy spectra for Ba isotopes are shown in Fig. 1. We have obtained a good agreement with experiment up to spin 6 except $N = 80$. For $N = 80$ a higher spin pair seems necessary because the quadrupole collectivity is not so dominant near the closed shell. The first 8^+ states are not well reproduced, which implies the effect of higher spin pairs originating from the $0h_{11/2}$ orbital. The experimental odd-even energy staggering for the quasi-γ band, which indicates γ-instability, is well reproduced theoretically. The figure shows that theoretical quasi-γ-band energies decrease as a function of the number of neutron-hole increases, but they cease to decrease at $N = 74$, which reproduces the experimental trend well.

The $E2$ transition operator is defined as $T(E2;\mu) = e_\nu Q_{\nu\mu} + e_\pi Q_{\pi\mu}$,

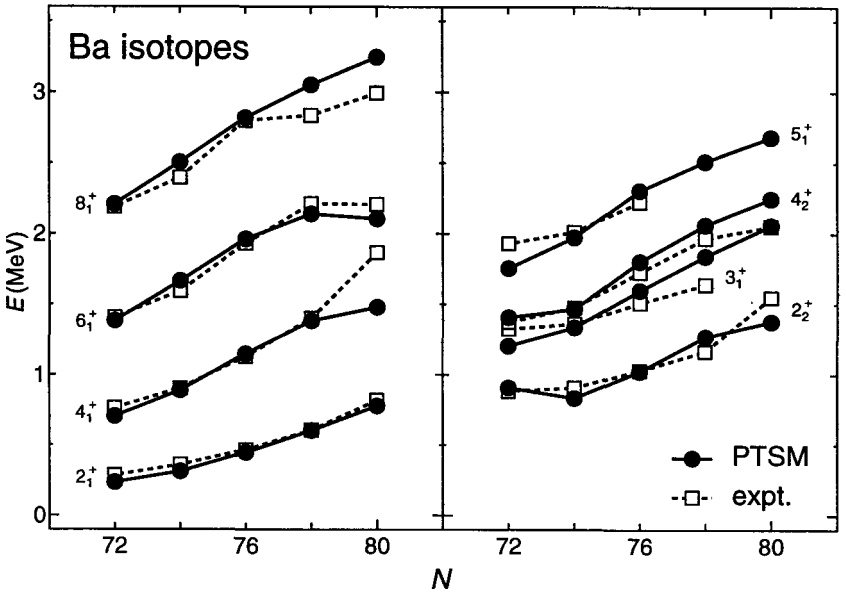

Figure 1. Energy spectra of the yrast and quasi-γ bands for Ba isotopes as a function of neutron number N. Experimental data are taken from Ref. 2.

where e_τ $(\tau = \pi, \nu)$ represents effective charges of a proton and an neutron hole, and the operator $Q_{\tau\mu}$ is the quadrupole operator with the oscillator parameter $b = 1.005A^{1/6}$ fm. The effective charges are assumed to follow the conventional relation[3] $e_\nu = -\delta e$ and $e_\pi = (1+\delta)e$, and the adopted values are $\delta = 0.70 + 0.05(\bar{N}_\nu + N_\pi)$.

Table 1 shows relative $B(E2)$ values between low-lying states for ^{134}Ba, ^{132}Ba and ^{130}Ba. It is seen that the theoretical results reproduce very well the experimental data, which simulate the O(6) limit prediction of the interacting boson model (IBM). Especially, transitions from the 5_1^+ state to others are quite important for the appearance of the O(6) symmetry.

3. Odd-mass nuclei

For a description of odd nucleon systems, we add an unpaired particle to the SD pair states and consider an SD pair+1 particle state. We use the same strengths of the interactions as used for even-even isotopes. Fig. 2 shows energy spectra of the odd Ba isotopes. For ^{131}Ba and ^{133}Ba the energy levels of $7/2_1^+$ and $9/2_1^+$ states are predicted too high in energy, but other states are reproduced well. The smooth change of ordering is seen for

Table 1. Comparison of relative $B(E2)$ values between theory and experiment in low-lying states for ^{134}Ba, ^{132}Ba, and ^{130}Ba. The last column gives the IBM predictions for the O(6) limit. Experimental data are taken from Refs. 4, 5, 6.

	^{134}Ba		^{132}Ba		^{130}Ba		O(6)
$J_i^\pi \to J_f^\pi$	SD	expt.	SD	expt.	SD	expt.	
$2_2^+ \to 2_1^+$	100	100	100	100	100	100	100
$\to 0_1^+$	0.17	0.9(2)	0.063	2.7(4)	4.9	6.2(7)	0
$3_1^+ \to 2_2^+$	100	100	100	100	100	100	100
$\to 4_1^+$	15	$\geq$2.6	30	38(6)	36	22(3)	40
$\to 2_1^+$	0.29	1.1	2.7	2.6(4)	14	4.5(6)	0
$4_2^+ \to 2_2^+$	100	100	100	100	100	100	100
$\to 3_1^+$	21		1.3	$\leq$50(11)	9.9		0
$\to 4_1^+$	24	73	65	73(10)	79	54(10)	91
$\to 2_1^+$	23	2.4	1.6	1.8(3)	0.25	2.3(4)	0
$5_1^+ \to 3_1^+$	100	100	100	100	100	100	100
$\to 4_2^+$	67		42	$\leq$45(7)	43		46
$\to 6_1^+$	9.1		17		33		45
$\to 4_1^+$	1.8		0.49	$\leq$2.2(3)	6.8		0
$0_2^+ \to 2_2^+$	100	100	100	100	100	100	100
$\to 2_1^+$	194	3.5	0.068	$\leq$0.7(1)	0.87	3.3(2)	0

the $3/2_1^+$ and $1/2_1^+$ states. Although reproducing energy levels of odd-A nuclei is much more difficult compared to even-even nuclei, the agreement is rather well, considering the fact that the effective interactions are solely determined for even-even nuclei and no further adjustment is made for odd-A nuclei.

4. Conclusion

In conclusion we have applied the PTSM to Xe, Ba and Ce isotopes around mass 130. The effective interactions are determined to reproduce overall energy spectra of the yrast and quasi-γ bands, which has gradual number dependence. It is found that energy spectra of the yrast state bands and γ-bands of Xe, Ba and Ce isotopes are nicely reproduced along with inter- and intra-band $E2$ transitions, which simulate the typical feature of the O(6) limit of the IBM.

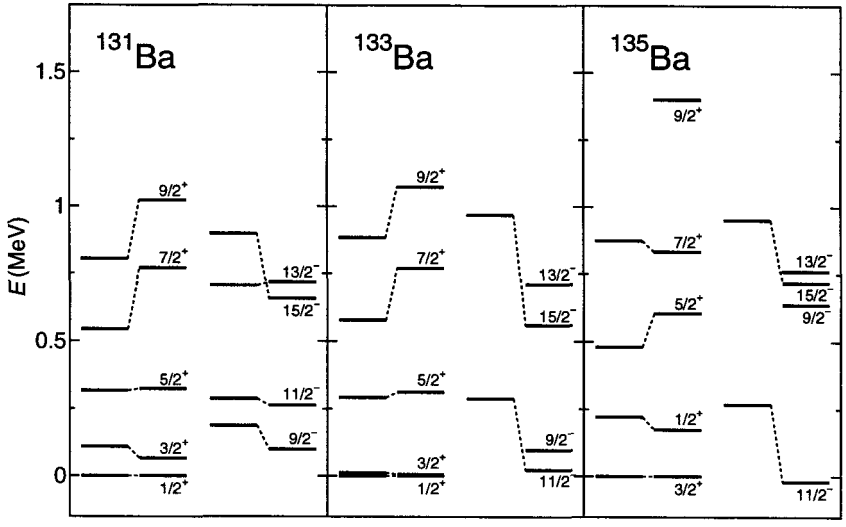

Figure 2. Spectra of odd-A Ba isotopes. Left hand shows experiment and Right hand shows theory. Experimental data are taken from Ref. 2.

For a description of odd-A nuclei we need to extend our model space to include an odd particle in addition to the even-even core and for odd-odd nuclei we need both an odd proton and an odd neutron. Energy spectra of odd-A nuclei of Xe, Ba and Ce isotopes are found to be quite well reproduced by this simple extension of the model.

References

1. K. Higashiyama, N. Yoshinaga and K. Tanabe, *Phys. Rev.* **C67**, 044305 (2003).
2. NUDAT database, National Nuclear Data Center, http://www.nndc.bnl.gov/nndc/nudat/
3. A. Bohr and B. Mottelson, *Nuclear Structure* (Benjamin, New York, 1975) Vol. 1.
4. A. M. Kleinfeld, A. Bockisch, and K. P. Lieb *Nucl. Phys.* **A283**, 526 (1977).
5. A. Gade, I. Wiedenhover, H. Meise, A. Gelberg, and P. von Brentano, *Nucl. Phys.* **A697**, 75 (2002).
6. K. Kirch, G. Siems, M. Eschenauer, A. Gelberg, R. Luhn, A. Mertens, U. Neuneyer, O. Vogel, I. Wiedenhover, P. von Brentano, and T. Otsuka, *Nucl. Phys.* **A587**, 211 (1995).

DEVELOPMENT OF UNSTABLE NUCLEAR BEAM ^{17}N TO SEARCH FOR HIGH-SPIN ISOMERS IN N=51 ISOTONES

A. ODAHARA

Nishinippon Institute of Technology,
1-11, Aratsu, Kanda-tyou, Miyako-gun, Fukuoka-ken, 800-0394, JAPAN
E-mail: odahara@nishitech.ac.jp

Y. GONO, Y. WAKABAYASHI, N. HOKOIWA AND M. KIBE

Department of Physics, Kyushu University, JAPAN

T. FUKUCHI, T. TERANISHI, S. KUBONO, M. NOTANI, S. MICHIMASA, J.J. HE, S. SHIMOURA AND E. IDEGUCHI

Center for Nuclear Study (CNS), University of Tokyo, JAPAN

Y. YANAGISAWA, H. WATANABE, T. KISHIDA, S. NISHIMURA AND M. NISHIMURA

RIKEN, JAPAN

H. BABA

Department of Physics, Rikkyo University, JAPAN

H. IWASAKI

Department of Physics, University of Tokyo, JAPAN

J.Y. MOON

Department of Physics, Chung-Ang University, KOREA

S. KATO

Department of Physics, Yamagata University, JAPAN

H. SAGAWA

Center for Mathematical Sciences, University of Aizu, JAPAN

In order to search for high-spin isomers in N=51 isotones, an unstable nuclear beam ^{17}N was developed using the low-energy radioisotope beam separator(CRIB) of the Center for Nuclear Study(CNS), University of Tokyo, in RIKEN.
High-spin isomers in N=83 isotones have been systematically studied. These isomers are of stretch coupled configurations and oblate shape. High-spin isomers of N=51 isotones are expected to be stemmed from the same isomerism appeared in N=83 isotones.
Since the nuclei with Z <40 of N=51 isotones are close to the stability line, it is difficult to produce high-spin states in these nuclei using reactions by combinations of stable beams and targets. Therefore, it is very effective to use the radioisotope beam. Experiment was carried out by means of the γ spectroscopy method, Seven γ-rays emitted from Nb nuclei which were produced by the secondary fusion reaction of ^{82}Se + ^{17}N were observed.

1. Introduction

High-spin isomers in N=83 isotones have been systematically studied[1]. Their spin-parities are $49/2^+$ and 27^+ for odd and odd-odd nuclei, respectively. Life times of these isomers range between ~10ns and ~μs. Configurations of high-spin isomers are deduced experimentally and theoretically to be $[\nu(f_{7/2}h_{9/2}i_{13/2})\pi h_{11/2}{}^2]_{49/2}{}^+$ for odd nuclei and $[\nu(f_{7/2}h_{9/2}i_{13/2})\pi(d_{5/2}h_{11/2}{}^2)]_{27}{}^+$ for odd-odd nuclei. These isomers have stretch coupled configuration and have oblate shape.

Search for high-spin isomers in N=51 isotones have been started. These isomers are expected to be stemmed from the same origin of isomerism appeared in N=83 isotones. Configurations of these isomers in N=51 isotones are considered to be $[\nu(d_{5/2}g_{7/2}h_{11/2})\pi g_{9/2}{}^2]_{39/2}{}^-$ for odd nuclei and $[\nu(d_{5/2}g_{7/2}h_{11/2})\pi(p_{1/2}g_{9/2}{}^2)]_{20}{}^+$ for odd-odd nuclei.

High-spin isomer of ^{93}Mo was observed for the first time in N=51 region using stable beam produced by cyclotron of Tohoku University[2]. Excitation energy of this isomer is 9.5 MeV and life time is 1.1μs. Spin-parity was assigned tentatively to be $(39/2^-)$.

Since the nuclei with Z <40 of N=51 isotones are close to the stability line, it is difficult to produce high-spin states in these nuclei using reactions by combinations of stable beams and targets. Therefore high-spin isomer search was carried out using unstable nuclear beam ^{17}N, by means of the γ spectroscopy method. Nuclei of ^{90}Y, ^{89}Sr and ^{88}Rb can be produced by the α5n, αp5n and 2α3n reaction channels of the secondary fusion of ^{82}Se+^{17}N, respectively.

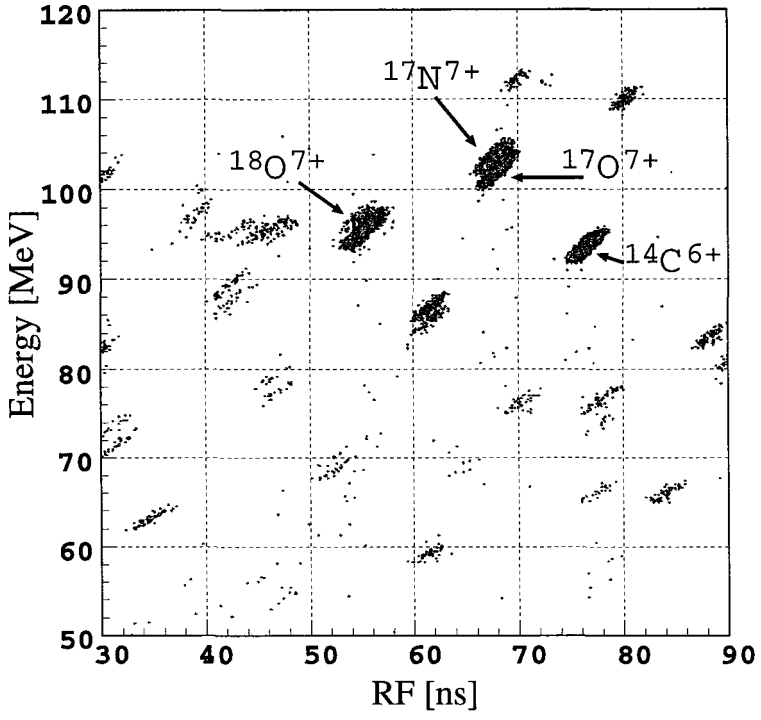

Figure 1. Plots of energies of reaction products vs time differences between signals of RF and F2-PPAC.

2. Experimental procedure and results

A secondary ^{17}N beam was produced by using CRIB[3] which consists of two dipole(D1, D2), three quadrupole(Q1, Q2, Q3) and small correction magnets(M1, M2). A ^{9}Be primary target of 2.3mg/cm^2 was bombarded by a $^{18}O^{8+}$ primary beam of 126.4MeV to obtain a ^{17}N beam. A O^{6+} beam was accelerated by the AVF cyclotron in RIKEN. The beam intensity was 0.4pμA at the primary target position.

A parallel plate avalanche counter(PPAC) was set at a dispersive focal plane(F1) for beam monitoring. In order to identify reaction products, a PPAC and a Si detector of 1.5mm thick were placed at an achromatic focal plane(F2). These detectors were located at 681 and 731mm downstream of Q3, respectively. Secondary target of ^{82}Se of 4.9mg/cm^2 thick was set at 1251mm downstream of Q3. Two clover Ge detectors were located at 40mm apart from the secondary target to measure γ-rays emitted from

nuclei which were produced by the secondary fusion reaction. A plastic scintillator was placed at 597mm down stream from the secondary target position in order to detect the secondary beam.

The acceptance solid angle was set to 5.6msr, which was a maximum setting, by a slit at F0. The energy of ^{17}N recoiling out of a primary target was 109.1±0.8MeV. A $B\rho$ value of D1 was set to be 0.886Tm to select a $^{17}N^{7+}$ beam. Momentum acceptance was restricted to 2.2% by a rectangular slit at F1. The ^{18}O primary beam was stopped by the slit at F1.

Particle identification was made by using energies of reaction products and time differences of RF and F2-PPAC signals, as shown in fig. 1. Energy of $^{17}N^{7+}$ was deduced to be 104±2MeV. As Si detector was moved out during the measurement of γ-rays, particles of $^{17}N^{7+}$ and $^{17}O^{7+}$ could not be separated. The intensity and fraction of ^{17}N and ^{17}O mixed beam were 1.5×10^5 particles/s and 33%.

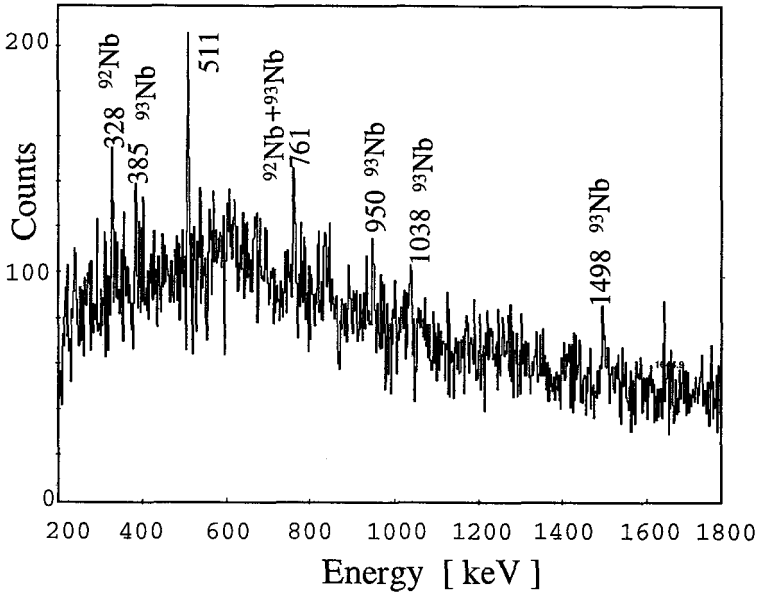

Figure 2. Projection spectrum of $\gamma\gamma$ coincidence. Background γ-rays were subtracted using time informations of $\gamma\gamma$ as well as RF-γ.

After moving out the Si detector at F2, measurement of γ-ray was carried out for 2.4 days. The total events of 2.1×10^8 were stored. Trigger

condition of data taking was made by signals of F2-PPAC and one Ge detector. In order to select the events of secondary fusion reaction, signals of plastic detector were used as veto. During data taking, particle identification was performed using time difference between signals of F2-PPAC and RF. Signals of a cocktail beam of ^{17}N and ^{17}O were added to trigger condition by circuit.

Seven transitions belonging to ^{92}Nb and ^{93}Nb were observed, although the background level caused by the thermal neutron capture γ-rays was 200 times higher than counts of peaks coming from secondary fusion reaction. Nuclei of ^{92}Nb and ^{93}Nb were produced by 7n and 6n channels of the ^{82}Se+^{17}N secondary fusion reaction. Figure 2 shows the projection spectrum of $\gamma\gamma$ coincidence detected by two clover detectors. Background γ-rays are subtracted using time informations of $\gamma\gamma$ as well as RF-γ.

3. Conclusion

Search for high-spin isomers in N=51 isotones has been started using an unstable nuclear beam ^{17}N. We succeeded to measure seven γ-rays emitted from secondary fusion reaction, although the background level caused by the thermal neutron capture γ-rays was high.

Acknowledgments

We would like to thank for the staffs of accelerator group in RIKEN. We also would like to acknowledge for D.C. Radford and his software of data analysis.

References

1. Y. Gono et al., *Eur. Phys. J.* **A13**, 5 (2002) and references therein.
2. T. Fukuchi et al., *Phys. Rev.* **C** to be submitted.
3. Y. Yanagisawa et al., *RIKEN Accel. Prog. Rep.* **34**, 183 (2001).

COULOMB EXCITATION OF STABLE EVEN-EVEN ZN ISOTOPES

M. KOIZUMI[A], A. SEKI[A,B], Y. TOH[A], M. OSHIMA[A], A. OSA[A], Y. UTUNO[A], A. KIMURA[A], Y. HATSUKAWA[A], T. HAYAKAWA[A], T. SHIZUMA[A], J. KATAKURA[A], M. MATSUDA[A], M. SUGAWARA[C], T. MORIKAWA[D], H. KUSAKARI[E], T. CZOSNYKA[F]

[A] *Japan Atomic Energy Research Institute, Tokai, Ibaraki 319-1195, Japan*
[B] *Ibaraki University, Bunkyo 2-1-1, Mito, Ibaraki 310-8512, Japan*
[C] *Chiba Institute of Technology, Narashino, Chiba 275-0023, Japan*
[D] *Kyushu University, Hakozaki, Fukuoka 812-8581, Japan*
[E] *Chiba University, Inage-ku, Chiba 263-8522, Japan*
[F] *Heavy Ion Lab., Warsaw University, Pasteura 5a, 02-093 Warszawa, Poland*

Multiple Coulomb excitation of ^{66,68}Zn was carried out. The experimental data were analyzed with the least-squares search code GOSIA. $E2$ matrix elements and quadrupole moments of 2_1^+ states were obtained. The ground band structures are explained to some extent with the asymmetric rotor model (ARM) and the interacting boson model (IBM) in O(6) limit. Potential energy surfaces (PES) calculated with the Nilsson-Strutinsky model show γ-unstability for ^{66}Zn and shallow two minima for ^{68}Zn. According to the experimental results and induction from the theoretical calculations, it seems that ^{66,68}Zn would be explained with such a model with soft triaxial potential.

1. Introduction

Zn nuclei have two extra protons outside the $Z = 28$ closed shell. Although the pattern of the excitation energy of ^{62,64,66,68}Zn looks like that of collective vibrational nuclei characterized by a 2_1^+ state and a triplet of 0_2^+, 2_2^+, and 4_1^+ states at about twice the energy of the 2_1^+ state as seen in Fig. 1, those isotopes cannot be treated as typical vibrational nuclei. For ^{62,64,66}Zn, enhancement of $E2$ transition probabilities was found between the states of the ground state band and between the states of the band built on the 2_2^+ state, while the inter-band transitions are weak. The low-lying states of those nuclei were, therefore, interpreted as quasi-rotational bands.[1]

In contrast to the 2_1^+, 2_2^+, and 4_1^+ states, the behavior of the 0_2^+ states

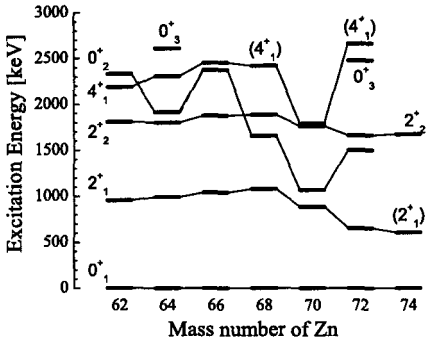

Figure 1. Low-lying states of even-even Zn isotopes.

is quite surprising. The excitation energy of the 0_2^+ states decreases as the neutron number increases until $N = 40$ (^{70}Zn), where also the excitation energy of 2_1^+ starts decreasing.

Coulomb excitation is a useful technique for the measurement of $B(E2)$s and quadrupole moments of low-lying states. Because the excitation process is purely electromagnetic, those values can be derived model-independently.[2] Nowadays, a combination of a 4π γ-ray detector array and position-sensitive detectors, covering the wide range of the scattering angles, has been proven to be useful to get necessary information of particle-γ correlation.[3] Those technical developments open the possibility of studying electromagnetic properties of nuclear states having rather high excitation energies.

In this study, we carried out a projectile multiple Coulomb excitation experiment of ^{66,68}Zn at the tandem-booster accelerator facility of Tokai site of Japan Atomic Energy Research Institute (JAERI). The experimental data were analyzed with the least-square search code GOSIA,[4] and $E2$ reduced transition matrix elements and quadrupole moments of 2_1^+ states were obtained.

2. Experiment and Analysis

^{66,68}Zn nuclei were Coulomb excited on a 1.8-mg/cm^2-thck self-supporting ^{nat}Pb target. The energies of the Zn projectiles were about 270 MeV, which do not exceed the safe energies of head-on collisions. In the experiments, the Ge detector array, GEMINI,[5] and the position sensitive detector array, LUNA,[6] have been used: GEMINI consists of 12 HPGe detectors with BGO anti-Compton suppressors (BGOACS), and LUNA consists of four po-

sition sensitive photomultipliers covered with plastic scintillator. In 2002, GEMINI and LUNA were modified and reinstalled. The new Ge detector array GEMINI-II consists of 16 Ge detectors with BGOACSs, and three low energy gamma detectors (LEPS), and LUNA-II consists of six photomultipliers. The total detection efficiency was increased by a factor of two.

The data acquisition system took event-by-event data of particle-γ coincidence, consisting of the γ-energy, particle position, and time difference between the particle and the γ-ray signal. After a 3-day beam-time for each nucleus with an average beam current of about one pnA, we obtained $5 \sim 10 \times 10^7$ events. Doppler shift of observed γ-energy was corrected event by event using the particle scattering angle and the Ge detector position.

In the analysis, the position sensitive particle detectors were divided into segments along the scattering angle. For each Ge detector, a data set of γ-yields in coincidence with each slice of detected particle angle was constructed. In addition to the γ-yields, spectroscopic data, such as lifetimes, branching ratios, and mixing ratios, were also used as data points to be fitted.

Those data points were analyzed with the least-squares search code GOSIA,[4] which searches the standard χ^2 minimum by changing the matrix elements so as to reproduce the experimental data points. The errors of the matrix elements were determined from the χ^2 distribution in the vicinity of the minimum. Cross-correlation effects are also taken into account. The errors result from requiring the range of the total probability of a parameter set is within confidence limit of 68.3%.

Figure 2 shows some yield data points of ^{66}Zn observed with one of the Ge detectors, for example. The solid and dashed lines connect calculated values of $Y(I_i \to I_f, \theta)/Y(2_1^+ \to 0_1^+, \theta)$ with a function of GOSIA, demonstrating how the diagonal matrix element influences the yield pattern. Note that the M_{ij} is defined by $< I||E2||J >$. It can be seen that the yield ratios of the $2_2^+ \to 2_1^+$ transition are sensitive to $M_{2_1^+,2_1^+}$, while those of the $4_1^+ \to 2_1^+$ transition are insensitive.

The $B(E2)$s and quadrupole moments obtained with GOSIA are given in Table 1. (Further details of the GOSIA analysis are given in references.[7,8] Results of a shell model (SM) calculation carried out with a $(2p_{3/2}, 1f_{5/2}, 2p_{1/2})$ model space with a ^{56}Ni core[9] are also listed in comparison.

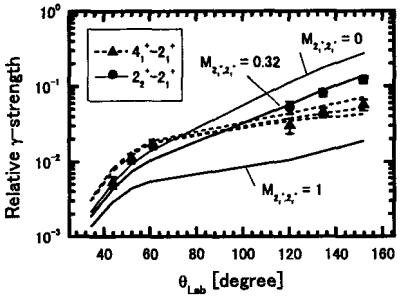

Figure 2. A comparison between experimental and simulated relative γ-strengths of ^{66}Zn for a Ge detector placed at $\theta = 90°$. The horizontal axis is the angle of the center of each particle detector segment in laboratory frame. The vertical axis is the γ-strengths divided by $2_1^+ \rightarrow 0_1^+$ γ-strengths for each scattering angle. The circular and triangular plots indicate experimental values of relative γ-strengths of $2_2^+ \rightarrow 2_1^+$ and $4_1^+ \rightarrow 2_1^+$ transition, respectively. The solid and dashed lines connect calculated relative γ-strengths.

Table 1. Experimental $B(E2)$s [e^{2}fm^4] and quadrupole moments [efm^2] derived from the present Coulomb excitation experiment. A shell model (SM) calculation is also listed in comparison.

		^{66}Zn		^{68}Zn	
		Exp.[7]	SM[9]	Exp.[8]	SM[9]
B(E2)	$2_1^+ \rightarrow 0_1^+$	228 (18)	270 (4)	258 (16)	270 (40)
	$2_2^+ \rightarrow 0_1^+$	0.06 (28)	0.5 (10)	9.5 (8)	8 (5)
	$2_3^+ \rightarrow 0_1^+$			2.3 (4)	
	$0_2^+ \rightarrow 2_1^+$			83 (13)	29 (4)
	$2_2^+ \rightarrow 2_1^+$	650 (230)	260 (40)	300 (60)	350 (50)
	$2_3^+ \rightarrow 2_1^+$			160 (50)	10 (3)
	$4_1^+ \rightarrow 2_1^+$	278 (11)	330 (50)	216 (7)	280 (40)
	$2_2^+ \rightarrow 0_2^+$			125 (90)	1.2 (4)
	$2_3^+ \rightarrow 0_2^+$			287 (23)	
	$4_1^+ \rightarrow 2_2^+$			110 (30)	9.4 (13)
Q	2_1^+	+24 (8)	-19	+9 (3)	-62 (17)

3. Discussion

For the interpretation of the experimental data one can also use the asymmetric rotor model (ARM).[11] From the experimental quadrupole moment $Q(2_1^+)$ and the $B(E2; 2_1^+ \rightarrow 0_1^+)$, the triaxiality can be deduced to be $\gamma = 36^{+8}_{-3}°$ for ^{66}Zn and $\gamma = 32 \pm 1°$ for ^{68}Zn, which clearly deviate from $\gamma = 60°$ (oblate shape). ARM calculation with $\gamma = 30°$ reproduces rather well the $B(E2)$ ratios defined by $R_{B(E2)} \equiv \frac{B(E2;4_1^+ \rightarrow 0_1^+)}{B(E2;2_1^+ \rightarrow 0_1^+)}$, and the excitation energy ratios defined by $R_E \equiv E(4_1^+)/E(2_1^+)$; for ^{66}Zn, the experimental

values are $R_{B(E2)} = 1.2$ and $R_E = 2.4$, and for ^{68}Zn, $R_{B(E2)} = 0.84$ and $R_E = 2.2$, where the calculated values are $R_{B(E2)} = 1.4$ and $R_E = 2.7$. The interacting boson model (IBM) in O(6) limit also reproduced those experimental values to some extent, giving $R_{B(E2)} = 1.4$ and $R_E = 2.5$.

In order to investigate the shape, potential energy surface (PES) calculation was carried out with the Nilsson-Strutinsky model.[12] As seen in Fig. 3, a γ-unstable character at the potential minimum was found for ^{66}Zn, and shallow two minima were found for ^{68}Zn. As seen in the PES of ^{68}Zn, the first minimum is located at $\beta_2 \sim 0.1$ and $\gamma = 60°$, and the second minimum is located at $\beta_2 \sim 0.2$ and $\gamma \sim 40°$; the energy difference between the two minima is less than 500 keV, which is lower then the excitation energy of 2_1^+ state. The shallowness of the minima suggests unstableness of these nuclear shapes.

It would be interesting to examine how the influence of Nilsson orbits appears. Figure 4 shows neutron single-particle energies used for the PES calculation. As seen in the plot of $\gamma = 0°$, the single particle energy of the lowest Nilsson orbit with parentage in $1g_{9/2}$ decreases as the deformation increases. Irrespective of deformation, the energy of the lowest $1g_{9/2}$ orbit is higher then the Fermi surface for the neutron number 38 with $\beta_2 = 0.10$, while that comes below the Fermi surface with $\beta_2 = 0.18$. Since the orbits with different parity do not mix, the nuclear states on the first minimum of the PES of ^{68}Zn ($\beta_2 \sim 0.10$) are not influenced by the $1g_{9/2}$ orbit, while those on the second minimum ($\beta_2 \sim 0.18$) are influenced. For the neutron number 36 (in the case of ^{66}Zn), the lowest $1g_{9/2}$ orbit is higher then the Fermi surface even with the deformation of $\beta_2 \sim 0.18$. Accordingly, the γ-unstable minimum of the PES of ^{66}Zn are not influenced by the $1g_{9/2}$

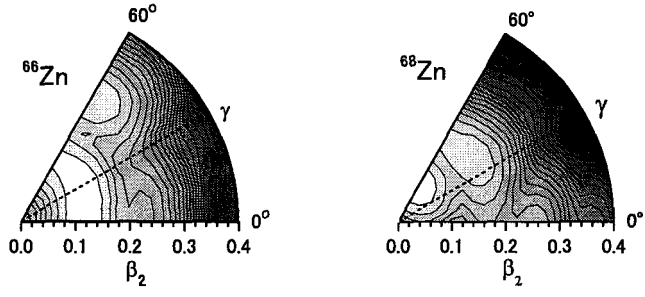

Figure 3. PESs of ^{66}Zn and ^{68}Zn calculated with the Nilsson-Strutinsky model.[11] Harmonic oscillator was used for the single particle energy calculation. The energy difference between the contour lines is 250 keV. The dashed line indicate $\gamma = 30°$.

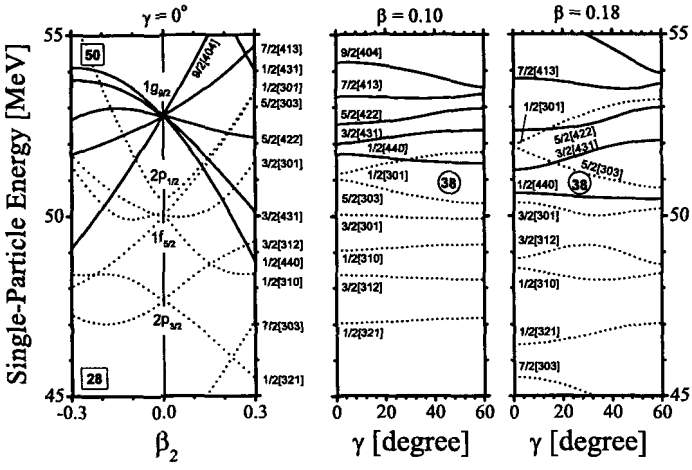

Figure 4. Neutron single-particle energies used for the PES calculation. The assignment of shell orbit and $\Omega[Nn_zL]$ configuration are given according to the reference.[13] Solid lines indicate positive parity orbits, and dashed lines negative parity orbits. The numbers in squares and circles indicate gaps of neutron magic numbers and the neutron number $N = 38$. In order to distinguish the orbits in the plots of $\beta_2 = 0.10$ and $\beta_2 = 0.18$, labels for the Nilsson configurations at $\gamma = 0°$ are used.

orbit.

As seen in Table 1, the SM calculation could not reproduce the experimental $B(E2)$ values of ^{68}Zn relating to the 0_2^+ and 2_3^+ states. The excitation energies of the 0_2^+ and 2_3^+ states of ^{68}Zn are not reproduced by the SM calculation as well.[9] Since the SM calculation do not include the $1g_{9/2}$ orbit, we could consider the discrepancy in ^{68}Zn is due to the omission of the orbit. This means that the 0_2^+ and 2_3^+ states are strongly influenced by the $1g_{9/2}$ orbit, while the other states are not. As a consequence of the SM and the Nilsson-Strutinsky model calculation, the ground state band of ^{68}Zn is constructed on the first minimum of the PES and the intruder band (the 0_2^+ and 2_3^+ states) on the second.

4. Summary

Multiple Coulomb excitation experiment with a ^{66,68}Zn projectile beam was carried out at the tandem-booster accelerator facility of Tokai/JAERI. The obtained data was analyzed with the least-square search code GOSIA. Quadrupole moments of 2_1^+ states and $B(E2)$ values are obtained.

PESs calculated with the Nilsson-Strutinsky model show γ-unstability

for ^{66}Zn, and two shallow minima for ^{68}Zn, in which an influence of the $1g_{9/2}$ orbit emerges as the second minimum. The shallowness of the minima suggests unstableness of these nuclear shapes. The SM calculation suggests that the intruder states of 0_2^+ and 2_3^+ of ^{68}Zn are strongly influenced by the $1g_{9/2}$ orbit. They should be constructed on the second minimum of the PES.

Although the ARM or IBM in O(6) limit reproduced the grand state band structures to some extent, those simple models could not completely explain the features of those transitional nuclei. However, the structure of those nuclei may be explained with such a model with soft triaxial potential.

References

1. D.N. Simister et al., *J. Phys.* **G4**, 1127 (1978); B. Crowell et al., *Phys. Rev* **C50**, 1321 (1994); J.F. Bruandet et al., *Phys. Rev.* **C12**, 1739 (1975); D.P. Ahalpara et al., *Nucl. Phys.* **G8**, 1565 (1982); L. Mulligan et al, *Phys. Rev.* **C19**, 1295 (1979); N.J. Ward et al., *J. Phys.* **G7**, 815 (1981); A. Passoja et al., *Nucl. Phys.* **A438**, 413 (1985); A.N. Wilson et al., *Eur. Phys. J.* **A9**, 183 (2000); J.F. Bruandet et al., *Phys. Rev.* **C14**, 103 (1976).
2. K. Alder and A. Winther, Coulomb Excitation, Academic, New York, (1966); K. Alder, and A. Winther, Electromagnetic Excitation - Theory of coulomb excitation with heavy ions -, North-Holland Publishing co., 1975; D. Cline, Ann. Rev. Nucl. Part. Sci. **36**, 683 (1986).
3. Y. Toh et al., *J. Phys.* **G27**, 1475 (2001); Y. Toh et al., *Eur. Phys. J.* **A9**, 353 (2000); M. Sugawara et al., *Eur. Phys. J.* **A16**, 409 (2002); A. Osa et al., *Phys. Lett.* **B546**, 48 (2002); M. Zielinska et al., *Nucl. Phys.* **A712**, 3 (2002); M. Zielinska et al., *Acta Physica Polonica* **B 33**, 515 (2002); T. Hayakawa et al., *Phys. Rev.* **C67**, 064310 (2003).
4. T. Czosnyka et al., *Nucl. Phys.* **A458**, 123 (1986); T. Czosnyka et al., *Bull. Am Phy. Soc.* **28**, 745 (1983).
5. K. Furuno, M. Oshima, et al., *Nucl. Instr. Meth.* **A421**, 211 (1999).
6. Y. Toh, M. Oshima, T. Hayakawa, et al., *Rev. Sci. Instrum.* **73**, 47(2002).
7. M. Koizumi, A. Seki, Y. Toh, et al., *Eur. Phys. J.* **A18**, 87 (2003).
8. M. Koizumi, A. Seki, Y. Toh, A. Osa, et al., *to be published in Nucl. Phys. A.*
9. J.F.A. Van Hienen, W. Chung and B. H. Wildenthal, *Nucl. Phys.* **A269**, 159 (1976).
10. A.S. Davydov and G.F. Filippov, *Nucl. Phys.* **8**, 237 (1958); A.S. Davydov and V.S. Rostovsky, *Nucl. Phys.* **12**, 58 (1959).
11. F. Iachello and A. Arima, The interacting boson model, Cambridge Univ. press, 1987.
12. T. Bengtsson et al, in Computational Nuclear Physics 1, ed. K. Langanke et al, (Springer-Verlag, 1991) p 51.
13. R. B. Firestone, *Table of Isotopes, 8th ed.* (1996).

APPLICATION OF THE HIGH-SPIN ISOMER BEAMS TO SECONDARY FUSION REACTION AND MEASUREMENT OF G-FACTOR

H. WATANABE, K. ASAHI, T. KISHIDA, H. UENO, W. SATO*, A. YOSHIMI, Y. KOBAYASHI, M. ISHIHARA

RIKEN (The Institute of Physical and Chemical Research), 2-1 Hirosawa, Wako, Saitama 351-0198, Japan
E-mail: hiroshi@rarfaxp.riken.go.jp

D. KAMEDA, H. MIYOSHI

Department of Physics, Tokyo Institute of Technology, Tokyo 152-8551, Japan

Y. GONO, T. FUKUCHI†, Y. WAKABAYASHI, M. KIBE, N. HOKOIWA

Department of Physics, Kyushu University, Fukuoka 812-8581, Japan

A. ODAHARA

Nishinippon Institute of Technology, Kanda, Fukuoka 800-03, Japan

B. CEDERWALL, K. LAGERGREN

Department of Physics, Royal Institute of Technology, Stockholm 10405, Sweden

ZS. PODOLYÁK

Department of Physics, University of Surrey, Guildford GU2 7XH, UK

A technique for providing high-spin isomers as probes of fusion reaction and measurement of g-factor has been worked out at RIKEN. In the study of the secondary fusion reaction $^{12}C(^{145m}Sm,xn)^{157-x}Er$, the γ rays emitted from the fusion-evaporation residue ^{154}Er have been successfully observed. The nuclear g-factor of the $T_{1/2} = 28$ ns high-spin isomer in ^{149}Dy has been measured with the γ-ray TDPAD method.

*Present address: Graduate School of Science, Osaka University, 1-1 Machikaneyamacho, Toyonaka, Osaka 560-0043, Japan

†Present address: Center for Nuclear Study (CNS), University of Tokyo, RIKEN campus, 2-1 Hirosawa, Wako, Saitama 351-0198, Japan

1. Introduction

The spectroscopic study of nuclear high-spin states has progressed markedly through the development of heavy ion beams available for nuclear reactions. Among all known reaction mechanisms, the most favorable situation for the production of high-spin states arises in a collision of two heavy ions occurring at the largest impact parameter leading simultaneously to a complete fusion. It is found from a classical approach [1] that the maximum orbital angular momentum brought in is larger in a symmetric combination of the projectile and the target nucleus than in an asymmetric one when the same compound nucleus is produced at an equal excitation energy. In the symmetric case, however, the compound nucleus is supposed to be highly excited immediately after its production because of the large Coulomb barrier between two interacting heavy ions. The probability of fission event occurring remarkably increases at such a high excitation energy. This problem can be overcome by using high-spin isomers as a projectile or a target of the fusion reaction, where the angular momentum distribution in the compound nucleus is expected to extend toward the higher region due to the sum of the large isomeric spin and the orbital angular momentum involved in the collision. Then the excitation energy of the compound nucleus should additionally increase only by that of the isomeric state. Therefore, it may be possible to produce the nucleus in the lower energy - higher spin region, namely near the yrast line, and to restrain competition from fission. In the present paper, the development of the high-spin isomer beam (HSIB) of ^{145m}Sm and its application to a secondary fusion reaction are described. A preliminary result of the ^{12}C(^{145m}Sm,xn)$^{157-x}$Er reaction is given. Furthermore, the g-factor of the high-spin isomer in ^{149}Dy has been measured by combining the production technique of the HSIB and the γ-ray TDPAD method. We also report on this result.

2. Secondary fusion reaction with the HSIB

The HSIB has been developed at RIKEN Accelerator Research Facility (RARF) in collaboration between RIKEN and Kyushu University [2]. Figure 1 shows a schematic layout of the beam line for the HSIB experiment. The secondary beams produced using a windowless gas target [3] are transported to the secondary target position at F3 through a superconducting solenoid and the following doubly achromatic spectrometer called RIPS (RIKEN projectile-fragment separator) [4]. The production of the isomeric beams is based on fusion-evaporation reactions of inverse kinematics. In

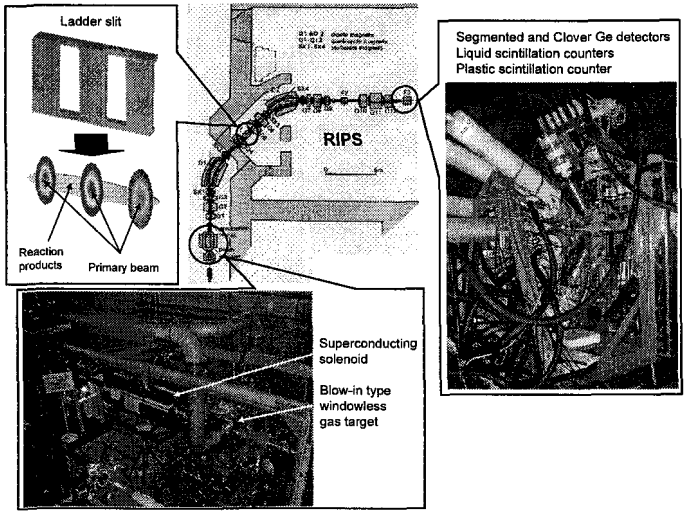

Figure 1. Schematic layout of the beam line for the HSIB experiment.

the present work, the HSIB of ^{145m}Sm ($T_{1/2}$ = 0.95 μs, I^{π} = 49/2^{+} [5]) has been produced via the ^{16}O(^{136}Xe,7n)^{145m}Sm reaction at 7.6 MeV/nucleon. Then the kinetic energy of the ^{145m}Sm beam was estimated to be about 5.5 MeV/nucleon. In this beam condition, unfortunately, the charge state distribution of ^{136}Xe overlapped that of ^{145m}Sm. In order to get rid of the ^{136}Xe component from the secondary beams, a ladder-type slit of variable widths and positions was placed at the dispersive focal plane F1. As illustrated in fig.1, the primary beam certainly makes clear-cut spots at F1 while the reaction products are probably broadened along the transverse axis by their momentum distributions formed in the production process. The ladder slit effectively prevented the ^{136}Xe from passing without reducing the ^{145m}Sm beam intensity by using these properties. The purity of the HSIB was considerably improved by the use of this devise, and more than 10^5 /s of ^{145m}Sm could be obtained on the secondary target from the ^{136}Xe beam intensity of about 50 pnA.

The γ-ray spectra measured with the ^{12}C(^{145m}Sm,xn)$^{157-x}$Er reaction are shown in fig.2. According to a statistical model calculation, it seems that the production of ^{154}Er is the most dominant channel over the beam energy including an energy loss of ^{145m}Sm within the ^{12}C target of 1 mg/cm^2 thickness (see the inset in fig.2). In spite of the existence of numerous contaminant γ rays from the Nd isotopes produced through the fusion re-

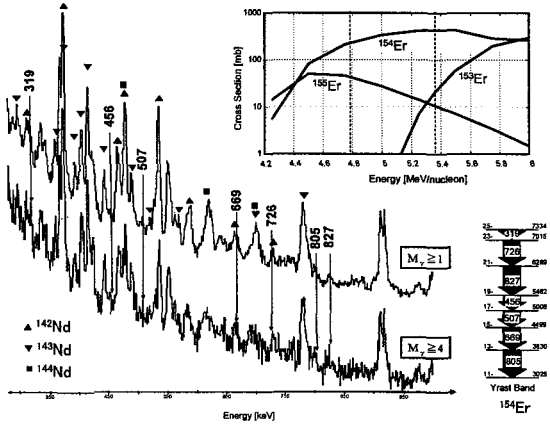

Figure 2. γ-ray spectra measured with the $^{12}C(^{145m}Sm,xn)^{157-x}Er$ reaction. In the figure of cross section calculated by a statistical model code, the energy range enclosed by dashed lines indicates an energy loss of the ^{145m}Sm beam within the ^{12}C target of 1 mg/cm^2 thickness. A partial level scheme of ^{154}Er is also shown.

action with the ^{136}Xe component, we have managed to observe the γ rays which are members of the yrast γ cascade in ^{154}Er. These γ lines seem to be prominent as the number of coincidence fold (M_γ) increases. This is a preliminary result, and the data analysis is now in progress.

3. Measurement of the g-factor of the high-spin isomer in ^{149}Dy

The same kind of high-spin isomers as observed in ^{145}Sm have been systematically discovered in $N = 83$ isotones with $60 \leq Z \leq 66$ [5]. It is very interesting to investigate the mechanism producing these high-spin isomers. More detailed information of the isomeric states can be acquired by measuring nuclear moments. Among these high-spin isomers, however, both the magnetic dipole and electric quadrupole moment have been measured only for ^{147}Gd so far [6,7]. In this work, the nuclear g-factor of the $T_{1/2} = 28$ ns high-spin isomer in ^{149}Dy [8] has been measured using the γ-ray TDPAD technique. This isomeric state was produced by the inverse-kinematic fusion reaction induced by a pulsed beam of ^{132}Xe bombarding a natural Mg target. The details of the experimental setup are described in ref. [9]. The oscillating pattern functions measured with an external magnetic field $B_{ext} = 1.5$ T at two different temperatures are displayed in fig. 3. For each temperature, a g-factor could be deduced from the Larmor

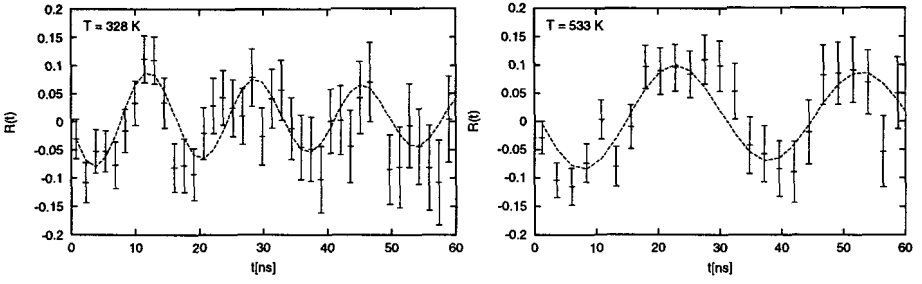

Figure 3. The oscillating pattern functions $R(t)$ obtained from the γ-ray time spectra for the 984.9 keV ($29/2^+ \rightarrow 27/2^-$) transition deexciting the $T_{1/2} = 28$ ns isomer in ^{149}Dy measured at $T = 328$ K (left) and 533 K (right) with $B_{ext} = 1.504$ T.

frequency $\omega_L = g\mu_N B_{ext}\beta(T)/\hbar$, where $\beta(T)$ denotes the temperature dependent paramagnetic correction factor. We have calibrated the $\beta(T)$ with the known g-factor of the isomeric state in ^{152}Dy ($T_{1/2} = 9.9$ ns, $I^\pi = 21^-$, $g = 0.55 \pm 0.06$ [10]), which was produced concurrently with the ^{149}Dy. By taking a weighted average of the g_{exp} measured at the respective temperatures, we have finally obtained the most reliable value, $\langle\, g_{exp} \,\rangle = 0.41 \pm 0.06$, which was in good agreement with the expectation value for a fully aligned multi-quasiparticle configuration $\pi(h^2_{11/2}) \otimes \nu(f_{7/2}h_{9/2}i_{13/2}(d^{-2}_{3/2})_0)$. This result indicates that only neutron particle-hole excitations across the $N = 82$ shell-closure occur at this isomeric state.

Acknowledgments

We wish to acknowledge staff members who belong to the RIKEN Accelerator Research Facility (RARF) for the provision of high quality beams during our experiments.

References

1. R. Bass, *Nucl. Phys.* **A231**, 45 (1974).
2. T. Kishida et al., *Nucl. Instr. Meth.* **A484**, 45 (2002).
3. T. Kishida et al., *Nucl. Instr. Meth.* **A438**, 70 (1999).
4. T. Kubo et al., *Nucl. Instr. Meth.* **B70**, 309 (1992).
5. A. Odahara et al., *Nucl. Phys.* **A620**, 363 (1997).
6. O. Häusser et al., *Phys. Rev. Lett.* **42**, 1451 (1979).
7. O. Häusser et al., *Nucl. Phys.* **A379**, 287 (1982).
8. Y. Gono et al., *Eur. Phys. J.* **A13**, 5 (2002).
9. H. Watanabe et al., *Nucl. Phys.* **A728**, 365 (2003).
10. J. C. Merdinger et al., *Phys. Rev. Lett.* **42**, 23 (1979).

This page intentionally left blank

Light exotic nuclei

This page intentionally left blank

THRESHOLD AND CONTINUUM STRUCTURES IN EXOTIC NUCLEI

I.J. THOMPSON, B.V. DANILIN*, J. MORTIMER,
T. TARUTINA† AND J.A. TOSTEVIN
Department of Physics, University of Surrey, Guildford GU2 7XH, U.K.

The role of continuum states in nuclei is considered, along with use of breakup theories of stripping and diffractive dissociation in probing nuclear structure. In the breakup of three-body nuclei such as Borromean halo systems, both three-body and two-body continuum final states need to be modelled and measured.

1. Few- and many-body dynamics

Nuclei typically show few-body behaviour just below and above the cluster separation thresholds. Many exotic nuclei have just one or a few bound states, and show pronounced cluster dynamics even in their ground states. Probing more details of these structures may follow from elastic scattering or cluster transfers, but breakup cross sections are typically the largest. This makes breakup experiments particularly attractive for spectroscopy with weak beams of exotic nuclei.

Breakup mechanisms lead to continuum states, and the *continuum* has many roles in nuclear structure physics. It appears in several ways, as (a) part of the expansion of bound states; e.g. in RPA for weakly bound states; or (b) dominated by resonances, as 'unbound states' to be identified e.g. with shell model eigenstates above threshold; or (c) in non-resonant continuum; e.g. in breakup reactions. *All* of these features are important parts of nuclear structure.

I therefore review the structure information that is present in breakup amplitudes, as well as bound structure details that can be extracted from different classes of breakup reactions.

*Permanent address: Russian Research Center "The Kurchatov Institute", 123182 Moscow, Russia
†Current address: Departamento de Física Nuclear, Instituto de Física da Universidade de São Paulo, Caixa postal 66318, 05315-970 São Paulo, Brazil

2. Knockout to bound final states

Stripping processes (inelastic breakup) proceed by the removal of a surface nucleon in a high-energy interaction with a target, and can reveal the spectroscopic factors for a wide range of final states. These states may be identified by measurement of coincident γ-rays.

The eikonal reaction theory for breakup by the removal of one or two neutrons or protons is now extensively recognised [1,2] as a useful tool in probing single-particle structures. Contributions from both stripping and diffractive dissociation need to be calculated from the eikonal theory, which gives the integrated cross sections for these two removal mechanisms.

Recent applications of such analyses have been to

- The ^{9}Be(^{17}C,^{16}Cγ) reaction at 60 MeV/u [3], where γ-coincidences allow the extraction of spectroscopic factors for the first three levels in ^{16}C. Shell-model calculations predict a very small parentage of the ^{16}C(0^+) in the ^{17}C$(3/2^-)_{gs}$, while a 20% branch into ^{16}C(0^+) was measured: this may indicate a need for higher order processes in an improved reaction theory.
- The N=8 neutron shell closure in ^{12}Be has been examined [4], by measuring the production of different ^{11}Be final states after one-neutron stripping.
- The ground state structure of ^{8}B has been examined by proton removal from ^{8}B measured at the GSI [5] with γ coincidences, where a 15% branch is seen from the excited ^{7}Be($1/2^-$) core component in the ^{8}B wave function.

Systematic reviews [6,1] of the extracted spectroscopic factors show values that are significantly less than shell-model values (with a 'reduction factor' $R \sim 0.6$) for deeply bound states. The results are in agreement with those from $(e,e'p)$ electron knockout reactions on stable targets, and are believed to reveal correlations from mechanisms not included in the shell model effective interactions, and which couple to configurations outside the assumed model space. These include the short-range correlations from the nucleon-nucleon repulsive core, tensor correlations, and clustering effects. This explanation is supported by noting that the reduction factor is nearer to unity ($R \sim 0.9$) for weakly-bound initial states, such as those in ^{8}B, ^{9}C and ^{15}C.

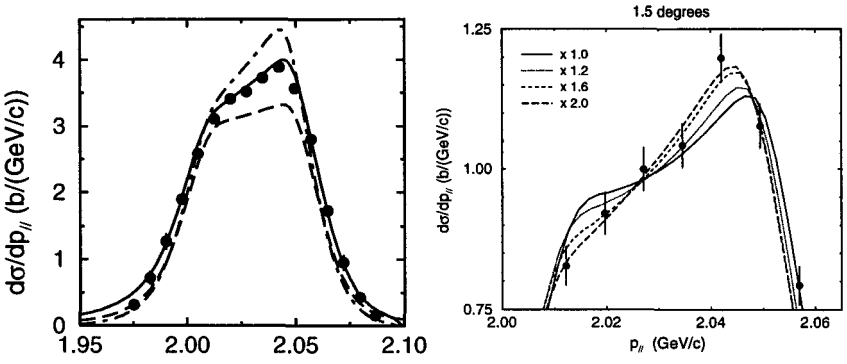

Figure 1. ^{8}B + ^{208}Pb $\rightarrow$ ^{7}Be parallel momentum distributions at 44 MeV/u. (Left) with a 3.5° transverse aperture. Dot-dashed: semiclassical Coulomb; solid: Coulomb+nuclear DWBA; dashed: CDCC coupled channels cross sections. (Right) CDCC calculations with scaled E2 amplitudes, for the same reaction with a 1.5° aperture.

3. Diffractive dissociation to unbound two-body states

Diffraction dissociation (elastic breakup), in which the projectile is dissociated by elastic interactions of the projectile fragments with the target remaining in its ground state, probes *continuum* excited states. For nuclei near the dripline, with few discrete states, these breakup reactions are the principal probe of excited states.

To measure the E1 and E2 multipole breakup of ^{8}B, for example, we need spectroscopy of the non-resonant continuum. This nucleus has a one-proton bound state at -0.137 MeV with dominant structure $[^{7}\mathrm{Be}(3/2^{-}) \otimes (0p_{3/2} + 0p_{1/2})]_{2+}$, as reported above. To find the B(E1) and B(E2) distributions, the transitions $p \rightarrow s, d$ need to be accurately known. These E1 and E2 amplitudes interfere in the $p_{||}(^{7}\mathrm{Be})$ parallel momentum distribution, giving a forward-backward asymmetry [7].

The accurate calculation of these asymmetries therefore requires full treatment of possible quantal effects, nuclear+Coulomb interference, and higher-order processes [8]. It is known that higher-order $(\mathrm{E1})^{2}$*E2 interference *reduces* the observed asymmetries, as shown by the all-order CDCC calculation (dashed curve) in the left part of Fig. 1.

The puzzle that now arises is that the higher-order effects reduce the calculated asymmetry to *less* than is manifest by the data of [7], requiring, as shown in right part of Fig. 1, that the E2 amplitudes be *increased* to fit the data [8]. There is a need for further work in structure models to see whether these properties of the *non-resonant* breakup continuum

may be microscopically reproduced, or whether the ^{7}Be$(1/2^-)$ excited core component needs to be included in the breakup mechanism.

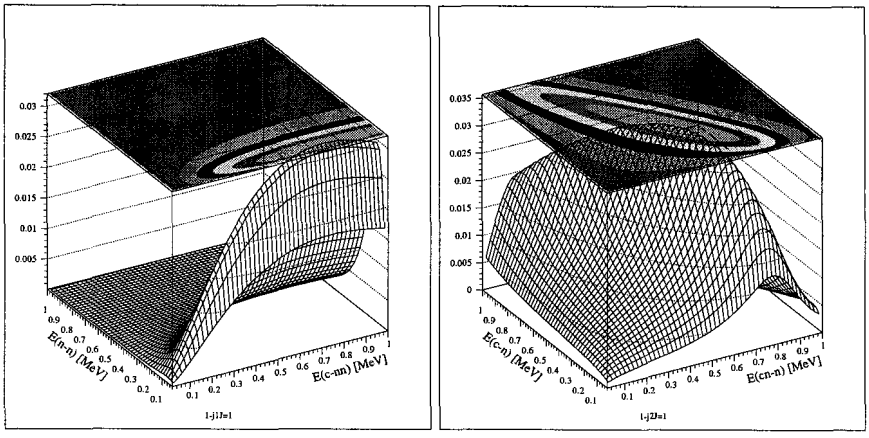

Figure 2. Three-body scattering wave functions averaged over angles, as functions of two Jacobi energies. (Left) Effect of the n-n virtual state. (Right) Effect of hypothetical n-n higher energy esonance

4. Diffractive dissociation to unbound three-body states

Similar questions arise in the breakup of *three-body* systems, where now the distinctions between resonant and non-resonant continua become more complicated, and more interesting. In probing the three-body continuum of Borromean systems (those having no bound binary subsystems), possible experimental signatures may be the energy correlations in the continuum scattering.

Using the continuum states of ^{6}He as an example, we plot in Fig. 2 the scattering wave functions averaged over the angles of the relative motion. The left part shows the correlations obtained from the n-n virtual state, with a strong amplification at low E_{nn} values that is independent of E_{c-nn}. The right part shows the effect of a hypothetical n-n esonance at higher energy in E_{c-n}, E_{cn-n} energy coordinates, where there is now a uniform distribution between these energies.

We now calculate these correlation plots using our three-body models of excited ^{6}He continuum states [9]. The left part of Fig. 3 shows the well known 2^+ resonance at 1.8 MeV (0.9 MeV above the breakup threshold), showing clear resonant energy distributions across both the Jacobi energy

variables shown. In the right part, by contrast, we plot the results of our continuum calculations for dipole 1^- states. Here, there are no clear resonant peaks, either in individual or in summed energy variables. The dipole response is amplified because of attractive dynamical correlations, but not sufficiently to produce a recognisable resonance.

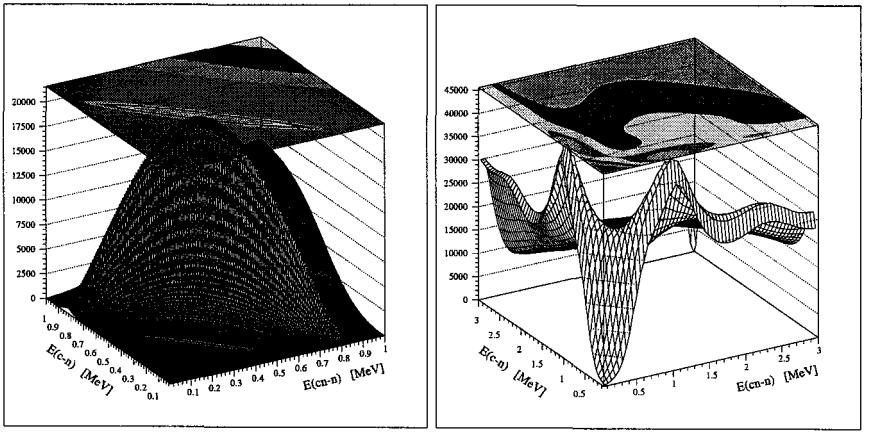

Figure 3. Energy correlation plots (as in Fig. 2) of excited ^{6}He continuum states. (Left) The well known 2^+ resonance at 1.8 MeV. (Right) Dipole 1^- states.

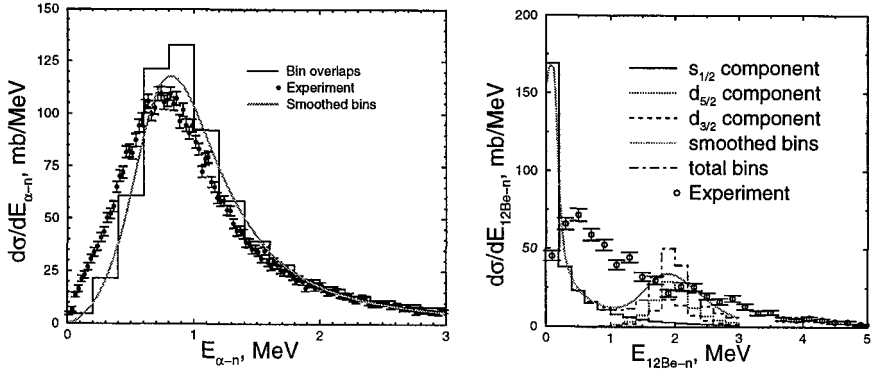

Figure 4. (Left) Nucleon removal cross sections at 240 MeV/u to ^{5}He* from the ^{6}He three-body ground state. The data are from [10]. (Right) to ^{13}Be* from the ^{14}Be g.s. The data are from [13].

5. Knockout producing unbound subsystems

There is also the possibility of probing continuum states of Borromean subsystems by removal of one nucleon. The removal of a neutron from ^{6}He, ^{11}Li or ^{14}Be, for example, populates states of ^{5}He, ^{10}Li or ^{13}Be, respectively.

Experiments have measured the decay spectra of ^{5}He (= ^{4}He + n), ^{13}Be (= ^{12}Be + n), etc., so we calculate these energy correlations within eikonal reaction theory, using good 2-body and 3-body structure models of the A+1 or the A+2 nuclei, respectively. For the ^{6}He case, we first calculate the overlaps $\langle ^{5}\mathrm{He}(E_{\alpha-n})|^{6}\mathrm{He}_{\mathrm{gs}}\rangle$ for a range of $^{5}\mathrm{He}(E_{\alpha-n})$ bin states, then smooth the histogram of the calculated eikonal cross sections with the experimental energy resolutions. In the left part of Fig. 4 we compare theoretical predictions with the GSI data [10]. The total nucleon removal cross sections are calculated [11] to be σ_{str}=137 mb and σ_{diff}=38 mb which compare very favourably with the measured values of 127±14 mb and 30±5 mb respectively.

These good agreements lead us to try the method for the $^{14}\mathrm{Be} \rightarrow {}^{13}\mathrm{Be}$ knockout reaction. In ^{13}Be, initial models [12] require a low-lying s-wave virtual state alongside a d-wave resonance at $\sim$ 2 MeV. The integrated cross sections obtained with such a model are σ_{str}=109 mb and σ_{diff}=109 mb, compared with the measured values [13] of 125±19 mb and 55±19 mb respectively, and the energy spectrum is shown in right part of Fig. 4. For the nucleon removal from this nucleus, we see that the experimental energy spectrum is smoother than that predicted theoretically, with no pronounced virtual-s and resonant-d state peaks. More recent models [11] with core excitation are expected to predict similar energy distributions. We conclude that either there are further sources of experimental energy smoothing, or that the simplified eikonal reaction mechanism is not adequate, which assumes that the produced ^{13}Be* unbound states are spectators and do not undergo mixing and energy sharing during the reaction.

6. Conclusions

Near-threshold states give rise to cluster dynamics and strong coupling to breakup channels. Many of the new, exotic nuclei near the driplines have only one bound state. The modelling and measurement of continuum states, as well as of the mechanisms which produce them, are therefore necessary in order to probe spectroscopic structures in the new era of nuclear structure physics. Spectroscopy of states in the continuum is as important as the spectroscopy of discrete states, whether those are bound states or discrete

resonances.

Acknowledgments

This work was supported by EPSRC grants GR/R25514 and GR/M82141 (U.K.). One of the authors, T.T., would like to acknowledge partial support of FAPESP, Brazil.

References

1. P.G. Hansen and J.A.Tostevin, Ann. Rev. Nucl. Part. Sci **53**, 219 (2003).
2. J. Tostevin, proceedings of RNB6.
3. V. Maddalena et al., Phys Rev C **63**, 024613 (2001).
4. A. Navin et al., Phys. Rev. Lett. **85**, 266 (2000).
5. D. Cortina-Gil et al., Phys Lett B **529**, 36 (2002), Nucl. Phys. **A720**, 3 (2003).
6. B.A. Brown et al. Phys Rev C **65**, 061601(R) (2002)
7. B. Davids *et al.*, Phys. Rev. Lett. **86**, 2750 (2001)
8. J. Mortimer et al., Phys Rev C **65**, 64619 (2002).
9. B.V. Danilin et al, Nucl. Phys. **A632**, 383 (1998).
10. D. Alexandrov et al, Nucl. Phys. **A 633**, 234 (1998).
11. T. Tarutina, Ph.D. thesis, University of Surrey (Sept 2001).
12. I.J. Thompson and M.V. Zhukov, Phys. Rev. **C53**, 708 (1996)
13. H. Simon, private communication

HALO STRUCTURE OF ^{17}B STUDIED VIA ITS REACTION CROSS SECTION

Y.YAMAGUCHI, T.SUZUKI*, T.OHTSUBO, T.IZUMIKAWA,
W.SHINOZAKI, M.TAKAHASHI, R.KOYAMA, S.WATANABE
Department of Physics, Niigata University, Niigata 950-2181, Japan
E-mail: yamaguch@rarfaxp.riken.go.jp

C.WU, A.OZAWA†, T.OHNISHI, D.Q.FANG‡, T.SUDA, R.KANUNGO,
H.JEPPESEN, I.TANIHATA
RI beam science, The Institute of Physical and Chemical Research (RIKEN), Saitama 351-0198, Japan

M.FUKUDA
Department of Physics, Osaka University, Osaka 560-0043, Japan

N.IWASA
Department of Physics, Tohoku University, Miyagi 980-8578, Japan

The reaction cross section for the neutron-rich nucleus ^{17}B on a carbon target has been measured at an energy of 77 AMeV by a transmission method. A large enhancement of ^{17}B reaction cross section at low energy was observed. The density distribution of ^{17}B was deduced through the energy dependence of the reaction cross section together with high-energy data using a finite-range Glauber-model calculation under an optical-limit approximation. It is confirmed that the neutron-tail in the density distribution is necessary for ^{17}B in order to reproduce the measured reaction cross sections. Based on the assumption of a core (^{15}B) plus valence two-neutron picture, the mixture of $\nu(2s_{1/2})$ and $\nu(1d_{5/2})$ was studied without treating the correlation between two neutrons.

*Present address: Department of Physics, Saitama University, Saitama 338-8570, Japan
†Present address: Institute of Physics, University of Tsukuba, Ibaraki 305-8571, Japan
‡Present address: Shanghai Institute of Nuclear Research, Chinese Academy of Sciences, Shanghai 201800, China

1. Introduction

The investigation of unstable nuclei has been extended with rapid progress involving a radioactive ion-beam technique during the last few decades. After the neutron halo structure in ^{11}Li was discovered for the first time,[1] the existence of a neutron halo structure in some neutron-rich light nuclei was observed. Recently, ^{17}B has been suggested to be a two-neutron halo nucleus due to its weak binding energy of the valence two-neutron (S_{2n}=1.39 $\pm$ 0.14 MeV)[2], the large root-mean-square matter radius ($\tilde{r}_m$=2.90 $\pm$ 0.06 fm)[3], and the narrow momentum distribution for ^{15}B fragments (Γ=80 $\pm$ 10 MeV/c)[4] from the breakup of ^{17}B. Therefore, it is interesting to study the density distribution of ^{17}B. In order to deduce the density distribution, we measured the reaction cross section at an energy of 77 AMeV by a transmission method.

2. Experiment

The experiment was performed at RIken Projectile fragment Separator (RIPS).[5] An incident primary beam of ^{22}Ne with 110 AMeV, accelerated by the RIKEN Ring Cyclotron (RRC), was used to impinge on a Be or Ta production target to produce ^{17}B as a secondary beam through the fragmentation reaction. The RIPS was operated in an achromatic mode with an Al wedge degrader and a momentum acceptance of 1.0%. Particle IDentification (PID) was carefully performed event by event. The PID before the C reaction target (377 mg/cm^2 thickness), which was placed at the F2 achromatic focal plane of RIPS, was performed by the Bρ-ΔE-TOF standard method. The magnetic rigidity (Bρ) was determined by position information from Parallel Plate Avalanche Counter (PPAC). The magnetic fields at the two dipole magnets were monitored by NMR probes. The energy loss (ΔE) was measured using a silicon detector (50 $\times$ 50 $\times$ 0.15 mm^3) placed at F2. The Time-Of-Flight (TOF) information before the reaction target was determined by using the rf-signal and the timing signal of a plastic scintillator (0.5 mm thickness) placed at F2. The background contamination of other particles was estimated to be 10^{-4} in an offline analysis. PID after the reaction target was performed by the TOF-ΔE-E method, which is described in Ref.[6]. TOF information was obtained between two plastic scintillators at F2 and F3. The ΔE was measured by an ion chamber[7] placed at F3. The total energy (E) was measured by a 3$''\phi$ $\times$ 6 cm NaI(Tl) detector, which was placed at the end of the beam line with a reaction suppressor.[8]

3. Results and discussion

The reaction cross section of ^{17}B was determined by

$$\sigma_R = -\frac{1}{t}\ln(\frac{R_{in}}{R_{out}}), \quad (1)$$

where t denotes the thickness of the reaction target in units of atom/cm^2; R_{in} and R_{out} are the ratios of the number of outgoing un-reacted ^{17}B particles to that of incident ^{17}B particles with and without the reaction target, respectively. It should be noted here that the outgoing particles include both the inelastic events of ^{17}B and the un-reacted ^{17}B, as well as the reacted ^{17}B. The inelastic events should be deducted from the number of outgoing particles in order to obtain the reaction cross section. Therefore, we carefully estimated the inelastic events by using TOF information.

We did find a large enhancement of the reaction cross section for ^{17}B , compared with that of the predicted value by a phenomenological formula proposed by Kox *et al*[9]. Kox's formula can reproduce the reaction cross section for stable nuclei well. The measured reaction cross sections are shown in Fig. 1 together with the expected value from Kox's formula. At the low-energy region, the enhancement of the reaction cross section is much larger than that at the high-energy region. This effect suggests the existence of a low-density tail at a large distance from the center of the nucleus. The finite-range Glauber-model calculation under an optical-limit

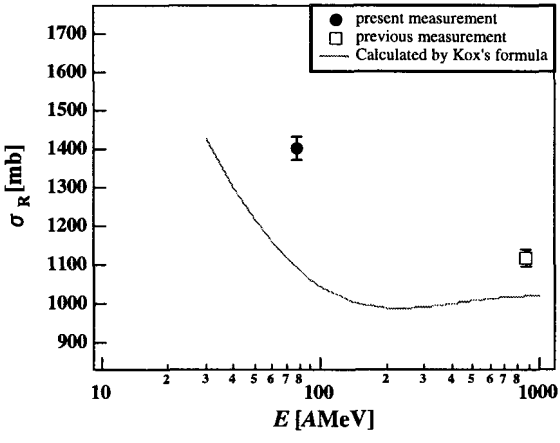

Figure 1. Measured reaction cross sections plotted together with the expected value from Kox's formula as a function of the incident beam energy. The closed circle shows the present measurement and the open square shows a previous measurement, which is taken from Ref.[3].

approximation[10] was performed to deduce the density distribution of ^{17}B. The finite-range parameter in the profile function is parameterized by fitting the energy dependence of ^{12}C+^{12}C reaction.[11] The density distribution of ^{17}B was assumed as a HO-type density for core (^{15}B) plus a Yukawa-square tail,

$$\rho_p(r) = HOtype \qquad \rho_n(r) = \begin{cases} HOtype & (r \leq r_c) \\ C\exp(-\lambda r)/r^2 & (r > r_c) \end{cases} \tag{2}$$

in which r_c is the radius, where the HO-type density crosses with the Yukawa-square tail and λ is the slope of the tail. The r_c value was determined by normalization process for neutrons. The width parameter of the HO-type density, determined to be 1.679 fm so as to reproduce the reaction cross section of ^{15}B, is common for both protons and neutrons. The Yukawa-square tail function is a good approximation to the shape of a single-particle density at the outer region of the core with the centrifugal and Coulomb barriers. By using a χ^2-fitting procedure to the measured reaction cross sections with a free-parameter (λ), we deduced the density distribution of ^{17}B. In Fig. 2, the density distribution of the best fitting to the experimental data is shown. The neutron-tail is necessary to reproduce the measured reaction cross sections.

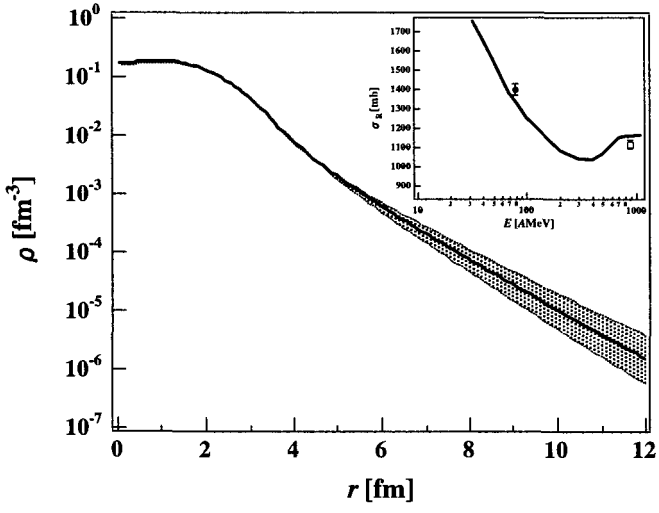

Figure 2. Density distribution of ^{17}B. The hatched area shows the error, upper and lower limit of the error corresponding to the low-energy data and the high-energy data, respectively. The energy dependence of the reaction cross section for ^{17}B+^{12}C is in the inset together with a χ^2 best-fit line.

By assuming the picture of a "core plus valence two-neutron", we again attempted to fit the following equations to the measured data:

$$\begin{cases} \rho_{core}(r) = HOtype(^{15}B, 0^+) \\ \rho_{v2n}(r) = 2 \times [f \times \phi_{2s_{1/2}}(r)^2 + (1-f) \times \phi_{1d_{5/2}}(r)^2] \quad (f \leq 1), \end{cases} \tag{3}$$

where $\rho_{core}(r)$ and $\rho_{v2n}(r)$ are the density distribution of the core (^{15}B) and that of the valence two-neutron, respectively. We did not take the correlation between the two neutrons into consideration this time. The wave functions $\phi_{2s_{1/2}}(r)$ and $\phi_{1d_{5/2}}(r)$ were determined by solving the eigenvalue problem of the Schrödinger equation in a Woods-Saxon potential for a given value of $S_{2n}/2$, with the diffuseness parameter set to be 0.7 fm and a radius parameter of $1.2A^{1/3}$ fm. The s-wave spectroscopic factor (f) was found to be $29 \pm 8\%$ by using a χ^2-fitting procedure under an optical-limit approximation. However, the result obtained from the momentum-distribution measurement is $69 \pm 20\%$ using a few-body Glauber-model. The difference of the optical-limit approximation and the few-body treatment gives different values of the spectroscopic factor. As suggested by the Surrey group, a few-body Glauber-model[12] is more suitable to describe weakly bound systems, like halo nuclei. Thus, another approach to the spectroscopic factor as well as the density distribution using the few-body Glauber-model is now in progress.

Acknowledgments

The authors gratefully acknowledge all of the staff at the RIKEN Ring Cyclotron for their stable operation of the accelerator during the experiment.

References

1. I. Tanihata, H. Hamagaki, et al., *Phys. Lett.* **B160**, 380 (1985); P.G. Hansen and B. Jonson, *Europhys. Lett.* **4**, 409 (1987).
2. G. Audi, O. Bersillon, et al., *Nucl. Phys.* **A624**, 1 (1997).
3. T. Suzuki, R. Kanungo, et al., *Nucl. Phys.* **A658**, 313 (1999).
4. T. Suzuki, Y. Ogawa, et al., *Phys. Rev. Lett.* **89**, 012501-1 (2002).
5. T. Kubo, M. Ishihara, et al., *Nucl. Instrum. Methods* **B70**, 309 (1992).
6. T.Zheng, T.Yamaguchi, et al., *Nucl. Phys.* **A709**. 103 (2002)
7. Y. Yamaguchi, K. Kimura, et al., *RIKEN Accel. Prog. Rep.* **36**, 161 (2003).
8. T. Suda, M. Chiba, et al., *RIKEN Accel. Prog. Rep.* **35**, 171 (2002).
9. S. Kox, A. Gamp, et al., *Phys. Rev.* **C35**, 1678 (1987).
10. Y. Ogawa, K. Yabana, et al., *Nucl. Phys.* **A543**, 722 (1992).
11. M. Fukuda, et al., *Private communication*
12. Y. Ogawa, T. Kido, et al., *Prog. Theor. Phys. Suppl.* **142**, 157 (2001).

HIGHER-ORDER RESOLUTION OF THE TIME-DEPENDENT SCHRÖDINGER EQUATION

D. BAYE, P. CAPEL, G. GOLDSTEIN

Physique Quantique, CP165/82,
Physique Nucléaire Théorique et Physique Mathématique, CP229,
Université Libre de Bruxelles, B-1050 Brussels, Belgium

The breakup of halo nuclei can be studied in a semi-classical approximation by solving the time-dependent Schrödinger equation. The resolution is performed numerically. A high accuracy is required to extract the breakup component. A fourth-order algorithm is proposed and tested. The Coulomb breakup of ^{15}C on a lead target is analyzed and compared with existing data.

1. Introduction

Coulomb breakup is a valuable tool to study properties of weakly-bound systems such as halo nuclei. The halo nucleus is broken in the Coulomb field of a heavy nucleus and information about its structure is obtained by measuring fragment distributions.

For theory, the problem consists in describing a multiparticle reaction. This implies accurately treating the breakup mechanism and finding a good model of the nucleus. Among techniques of calculation of Coulomb breakup, the semi-classical approximation leads to a time-dependent Schrödinger equation that we solve numerically. The resolution is performed on a three-dimensional mesh in spherical coordinates.[1,2,3,4] It requires an accurate time propagation of the wave function which is usually performed with a second-order algorithm.[4] In order to save computer time, we propose a fourth-order algorithm which allows using a larger time step.

The ^{15}C breakup on ^{208}Pb is chosen as an example and compared with existing data.

2. Breakup by a time-dependent method

We consider the breakup of a projectile composed of two clusters with relative coordinate $\boldsymbol{r}$, the core c (with charge $Z_c e$) and the fragment f (with

charge $Z_f e$), impinging on a target T (with charge $Z_T e$). The relative motion between the target and projectile is described by a classical trajectory.

In the projectile reference frame, the interaction between the fast-moving target and the constituents of the projectile induces a varying potential $V(t)$. The time-dependent Schrödinger equation reads

$$i\hbar\frac{\partial}{\partial t}\Psi(t) = [H_0 + V(t)]\,\Psi(t). \tag{1}$$

The Hamiltonian of the projectile (with reduced mass μ) is given by

$$H_0 = -\frac{\hbar^2}{2\mu}\Delta + V_0(\boldsymbol{r}). \tag{2}$$

The time-dependent potential contains Coulomb and nuclear parts,

$$V(t) = V_{cT}^{C+N}(r_{cT}) + V_{fT}^{C+N}(r_{fT}) - \frac{(Z_c + Z_f)Z_T e^2}{R}, \tag{3}$$

where the core-target (r_{cT}), fragment-target (r_{fT}) and projectile-target (R) coordinates depend on time. The classical trajectory $\boldsymbol{R}(t)$ can be a straight line, a Coulomb trajectory, ...The last term of Eq. (3) avoids double counting the projectile-target Coulomb interaction.

The bound and scattering projectile wave functions $\phi_{ljm}(E, \boldsymbol{r})$ are eigenstates of H_0. The time-dependent Schrödinger equation is solved with the projectile initially in its ground state (l_0, j_0, m_0) for the different m_0 values (i.e. different initial orientations). The breakup probability reads

$$\frac{dP}{dE}(E,b) = \frac{1}{2j_0+1}\sum_{m_0}\sum_{ljm}\left|\langle\phi_{ljm}(E,\boldsymbol{r})|\Psi^{(m_0)}(\boldsymbol{r},+\infty)\rangle\right|^2. \tag{4}$$

The breakup cross section is given by

$$\frac{d\sigma_{\mathrm{bu}}}{dE}(E) = 2\pi\int_0^\infty \frac{dP}{dE}(E,b)\,b\,db. \tag{5}$$

3. Higher-order treatment of time evolution

The breakup of halo nuclei requires solving the time-dependent Schrödinger equation (1). Numerical solutions of this equation are usually based on a time propagation with a small time step Δt

$$\Psi(t + \Delta t) = U(t + \Delta t, t)\Psi(t) \tag{6}$$

involving an approximate evolution operator U.

Numerical efficiency requires a separation of H_0 and $V(t)$ in the approximation of U. An often used second-order algorithm[4] reads, with $\hbar = 1$,

$$U(t+\Delta t,t) = e^{-i\frac{1}{2}\Delta t\, V(t+\frac{1}{2}\Delta t)} e^{-i\,\Delta t\, H_0} e^{-i\frac{1}{2}\Delta t\, V(t+\frac{1}{2}\Delta t)} + O(\Delta t^3). \quad (7)$$

The exponentials of operators can be calculated with a Padé approximation.

If they share the simplicity of Eq. (7), higher-order approximations may become extremely useful to speed up the techniques of resolution. Here we propose a new factorization at order Δt^5. It contains five exponentials in place of three in Eq. (7). The Magnus expansion[5] for Eq. (1) reads

$$U(t+\Delta t,t) = e^{-i\Delta t(H_0+W_1)-\Delta t^3[H_0,W_2]+O(\Delta t^5)} \quad (8)$$

with the definitions

$$W_n = \frac{1}{\Delta t^{2n-1}} \int_t^{t+\Delta t} dt_1 (t+\tfrac{1}{2}\Delta t - t_1)^{n-1} V(t_1). \quad (9)$$

A Baker-Campbell-Haussdorff[5] factorization leads to

$$U = e^{i\Delta t^2 W_2} e^{-i\Delta t(H_0+W_1)} e^{-i\Delta t^2 W_2} + O(\Delta t^5).$$

Using a symmetric factorization,[6] one obtains at order Δt^5,

$$U \approx e^{-i\frac{1}{6}\Delta t W_1 + i\Delta t^2 W_2} e^{-i\frac{1}{2}\Delta t H_0} e^{\frac{2}{3}\Delta t \widetilde{W}_1} e^{-i\frac{1}{2}\Delta t H_0} e^{-i\frac{1}{6}\Delta t W_1 - i\Delta t^2 W_2}. \quad (10)$$

The double commutator $[W_1,[H_0,W_1]]$ has been replaced by the gradient term $\widetilde{W}_1 = W_1 - \Delta t^2(\nabla W_1)^2/48\mu$. Consistent Simpson approximations are used for integrals W_1 and W_2.

Expressions (7) and (10) have the merits of preserving the norm and of separating the time-independent Hamiltonian H_0 and the time-dependent potential $V(t)$, which can then both be treated in an optimal way.

The validity of this new approximation has been tested on a solvable problem, i.e. the time evolution of a forced one-dimensional harmonic oscillator, affected by an electric-field pulse.[7] The spatial part of the Schrödinger equation is discretized on a Lagrange mesh.[8] Figure 1 shows that, at given accuracy, significant reductions of the computing time are obtained with the higher-order algorithm.

This algorithm is now being implanted in the breakup code of Ref. 4.

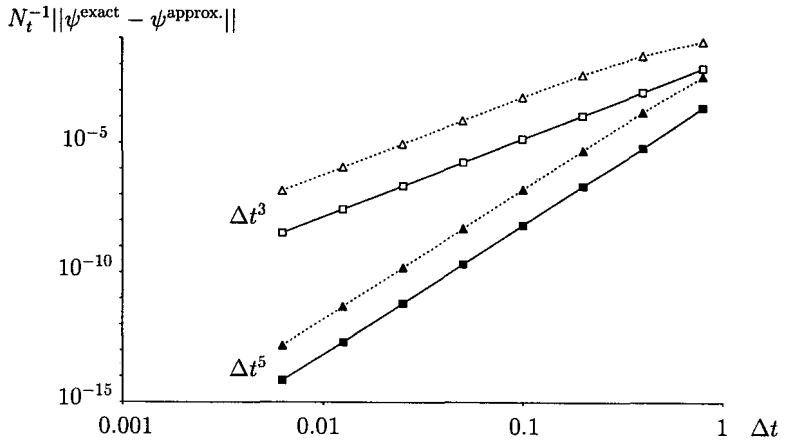

Figure 1. Average accuracy per time step after $N_t = 4/\Delta t$ time steps Δt in different algorithms: second order (open symbols) and fourth order (full symbols); exact exponentials (squares) and Padé approximants (triangles).

4. Coulomb breakup of ^{15}C

The ^{15}C halo nucleus possesses two weakly bound states: $1/2^+$ ($l = 0$) at -1.218 MeV and $5/2^+$ ($l = 2$) at -0.478 MeV. We study its breakup on a ^{208}Pb target with straight-line trajectories. Optical potentials are used for the n + ^{208}Pb and ^{14}C + ^{208}Pb interactions (see Ref. 4). The ^{14}C + n potential is a sum of Saxon-Woods and spin-orbit terms fitting the bound-state energies. It is l and j dependent. The ^{15}C + ^{208}Pb $\rightarrow$ ^{14}C + n + ^{208}Pb breakup cross section at a projectile energy 68 A MeV is displayed in Fig. 2 as a function of the relative energy E between core and fragment. The calculation is performed without any parameter. The results[4] agree fairly well with the preliminary results of Nakamura *et al.*[9] The overestimation of the pure Coulomb-breakup data for $b > 30$ fm seems to indicate that the spectroscopic factor is slightly smaller than unity.

5. Conclusions

We have presented a time-dependent model of the breakup of two-cluster nuclei based on an accurate resolution of the time-dependent Schrödinger equation on a 3D mesh in spherical coordinates. Both nuclear and Coulomb interactions with the target are easily included. Since the main difficulty is the duration of computation, we have developed a new fourth-order evolution algorithm. The model has been applied to the breakups of ^{11}Be

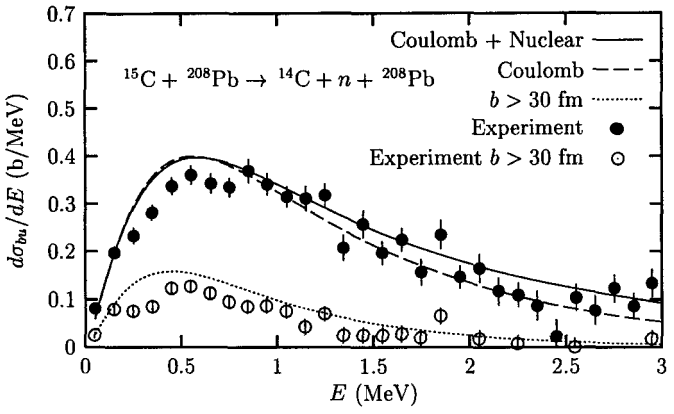

Figure 2. Calculated breakup cross sections[4] of ^{15}C on ^{208}Pb compared with preliminary RIKEN data.[9]

(Refs. 1, 3, 4), ^{15}C (Ref. 4) and ^{17}F (Ref. 2).

In the present approach, we accurately describe the reaction mechanism but the model description of the projectile is too simple. In order to improve it, we still need to reduce computation times without losing accuracy. This would allow more elaborate models including the effect of core excitation or even a microscopic cluster description of the projectile. A longer-range goal is to study in this way the breakup of two-neutron halo nuclei.

Acknowledgments

This text presents research results of the Belgian program P5/07 on interuniversity attraction poles of the Belgian Federal Science Policy Office.

References

1. V.S. Melezhik and D. Baye, *Phys. Rev. C* **59**, 3232 (1999).
2. V.S. Melezhik and D. Baye, *Phys. Rev. C* **64**, 054612 (2001).
3. P. Capel, D. Baye and V.S. Melezhik, *Phys. Lett. B* **552**, 145 (2003).
4. P. Capel, D. Baye and V.S. Melezhik, *Phys. Rev. C* **68**, 014612 (2003).
5. R.M. Wilcox, *J. Math. Phys.* **8**, 962 (1967).
6. M. Suzuki, *Phys. Lett. A* **146**, 319 (1990).
7. D. Baye, G. Goldstein and P. Capel, *Phys. Lett. A* **317**, 337 (2003).
8. D. Baye and P.-H. Heenen, *J. Phys. A: Math. Gen.* **19**, 2041 (1986).
9. Nakamura *et al*, *Nucl. Phys. A* **722**, 301c (2003).

A SEMICLASSICAL APPROACH TO FUSION REACTIONS*

M. S. HUSSEIN

Instituto de Física, Universidade de São Paulo
CP 66318, 05389-970, São Paulo SP, Brazil
E-mail: hussein@fma.if.usp.br

L. F. CANTO AND R. DONANGELO

Instituto de Física, Universidade Federal do Rio de Janeiro,
CP 68528, 21941-972, Rio de Janeiro RJ, Brazil
E-mail: canto@if.ufrj.br, donangelo@if.ufrj.br

The semiclassical method of Alder and Winther is generalized to study fusion reactions. As an illustration, we evaluate the fusion cross section in a schematic two-channel calculation. The results are shown to be in good agreement with those obtained with a quantal Coupled-Channels calculation. We suggest that in the case of coupling to continuum states this approach may provide a simpler alternative to the Continuum Discretized Coupled-Channels method.

1. Introduction

The importance of Coupled-Channels effects on the fusion cross section has been investigated by several authors[1]. These studies have established that the main effect of the coupling of the entrance channel with other bound channels is to produce a pronounced enhancement of the fusion cross section at sub-barrier energies. A more complicated situation arises when the reaction involves weakly bound nuclei. In such cases, the elastic channel is strongly coupled with the breakup channel, which corresponds to states of three or more bodies in the continuum. The total fusion cross section, σ_F, is then the sum of different processes: the complete fusion cross section, σ_{CF}, where all projectile's and target's nucleons merge into a compound system, and incomplete fusion cross sections, σ_{ICF_i}, where only

*This work was supported in part by the brazilian agencies CNPq, FAPESP, FAPERJ and the Instituto do Milênio de Informação Quântica-MCT, Brazil.

the i^{th} fragment of the projectile fuses with the target while the remaining ones come out of the interaction region.

A recent review of the experimental and theoretical work on the fusion of unstable or weakly bound nuclei can be found in ref.[2]. The first theoretical studies[3,4,5] used schematic models, which stress particular aspects of the fusion process. More recently, sophisticated quantum Coupled-Channels calculations have been performed[6,7]. These calculations approximate the continuum by a discrete set of states, according to the Continuum Discretized Coupled-Channels method (CDCC). Those calculations led to the conclusion that in collisions with very heavy targets the coupling to the continuum has a strong influence on the complete fusion cross section, The progress in the experimental study of these collision is more recent, since only recently unstable beams at barrier energies became available[8,9,10,11]. Besides, measurements at sub-barrier energies are very hard to perform, owing to the low intensity of the unstable beams. Although some recent measurements of the fusion cross section in collisions of unstable beams from heavy targets show an enhancement at sub-barrier energies[8,11], more data are needed for a final conclusion. On the other hand, data on the fusion cross section in reactions induced by light weakly bound stable projectiles have been available for a longer time[12].

The importance of the details of the CDCC basis in calculations of the fusion cross section, pointed out in ref.[7], indicates that a simple approximation for the breakup channel can only be used for very qualitative estimates, like that of ref.[13]. A reasonable alternative is the use of the semiclassical method of Alder-Winther (AW)[14]. This method was originally proposed to study Coulomb excitation of collective states and it was latter generalized to other nuclear reactions, including the excitation of the breakup channel[15]. More recently, it has been used to study the breakup of ^{8}B in the ^{8}B + ^{58}Ni collision[16] for a comparison with the CDCC calculations of Nunes and Thompson[17]. The discretization of the continuum space was carried out in the same way as in ref.[17] and the results obtained with the AW approximation were shown to be in good agreement with those of the CDCC method. In the present work, we show how the AW method can be used to evaluate the complete fusion cross section in collisions of weakly bound projectiles and discuss its validity in a schematic two-channel example.

This paper is organized as follows: in section 2 we introduce the Alder-Winther method and show how it can be used to evaluate the complete fusion cross section. An application to a schematic model that mimics the ^{6}He + ^{238}U is made. In section 3 we present the conclusions of this work.

2. The Alder-Winther method

Let us consider a collision described by the projectile-target separation vector, $\mathbf{r}$, and the relevant intrinsic degrees of freedom of the projectile, represented by ξ. For simplicity, we neglect the internal structure of the target. The projectile's Hamiltonian is

$$h = h_0(\xi) + \mathcal{V}(\mathbf{r}, \xi), \tag{1}$$

where $h_0(\xi)$ is the intrinsic Hamiltonian and $V(\mathbf{r}, \xi)$ represents the projectile-target interaction. The eigenvectors of $h_0(\xi)$ are given by

$$h_0 \ |\phi_\alpha\rangle = \varepsilon_\alpha \ |\phi_\alpha\rangle \, . \tag{2}$$

The Alder-Winther method is implemented as follows. First, one uses classical mechanics for the variable $\mathbf{r}$. In its original version, a Rutherford trajectory $\mathbf{r}_l(t)$ was used. The trajectory depends on the collision energy, E, and the angular momentum, l. In our case, we use the solution of the classical equation of motion with the potential $V(\mathbf{r}) = \langle\phi_0| \, \mathcal{V}(\mathbf{r}, \xi) \, |\phi_0\rangle$, where $|\phi_0\rangle$ is the ground state of the projectile. Using the trajectory, the coupling interaction becomes a time-dependent interaction in the ξ-space. That is, $\mathcal{V}(\xi, t) \equiv \mathcal{V}(\mathbf{r}_l(t), \xi)$. Then the dynamics in the intrinsic space is treated as a time-dependent quantum mechanics problem, according to the Schrödinger equation

$$h \ \psi(\xi, t) = [h_0(\xi) + \mathcal{V}(\xi, t)] \ \psi(\xi, t) = i\hbar \ \frac{\partial \psi(\xi, t)}{\partial t}. \tag{3}$$

Expanding the wave function in the basis of intrinsic eigenstates,

$$\psi(\xi, t) = \sum_\alpha a_\alpha(l, t) \ \phi_\alpha(\xi) \ e^{-i\varepsilon_\alpha t/\hbar}, \tag{4}$$

and inserting the expansion in eq.(3), one obtains the Alder-Winther equations

$$i\hbar \ \dot{a}_\alpha(l, t) = \sum_\beta \ \langle\phi_\alpha| \, \mathcal{V}(\xi, t) \, |\phi_\beta\rangle \ e^{i(\varepsilon_\alpha - \varepsilon_\beta)t/\hbar} \ a_\beta(l, t). \tag{5}$$

These equations should be solved with initial conditions $a_\alpha(l, t \to -\infty) = \delta_{\alpha 0}$, which means that before the collision ($t \to -\infty$) the projectile was in its ground state. The final population of channel α in a collision with angular momentum l is $P_l(\alpha) = |a_\alpha(l, t \to +\infty)|^2$ and the cross section is

$$\sigma_\alpha = \frac{\pi}{k^2} \ \sum_l (2l + 1) \ P_l(\alpha). \tag{6}$$

A similar procedure can be used to derive angular distributions.

The AW method can be extended to evaluate the fusion cross section as follows. The starting point is the general expression for the fusion cross section in multi-channel scattering

$$\sigma_F = \sum_\alpha \sigma_F^{(\alpha)}; \quad \sigma_F^{(\alpha)} = \frac{\pi}{k^2} \sum_l (2l+1)\ P_l^F(\alpha), \tag{7}$$

with the fusion probability for the l^{th}-partial-wave in channel α given by

$$P_l^F(\alpha) = \frac{4k}{E} \int dr\ |u_l(k,r)|^2\ W_\alpha^F(r). \tag{8}$$

Above, $u_l(k,r)$ represents the radial wave function for the l^{th}-partial-wave in channel α and W_α^F is the absolute value of the imaginary part of the optical potential in this channel arising from fusion. To use the AW method to evaluate the fusion cross section, we make the approximation

$$P_l^F(\alpha) \simeq T_l\ |a_\alpha(l, t_{ca})|^2 . \tag{9}$$

In the above equation, T_l is the tunneling probability and $|a_\alpha(l,t_{ca})|^2$ is the probability that the projectile is in the state $|\phi_\alpha\rangle$ when the system reaches closest approach.

We have performed a preliminary calculation for a two-channel case, studying the scattering of ^{6}He projectiles on a ^{238}U target, at near barrier energies. The weakly bound ^{6}He nucleus dissociates into ^{4}He and two neutrons, with threshold energy $B = 0.975$ MeV. The elastic channel is strongly coupled to the breakup channel and this coupling has a strong influence on the fusion cross sections. Here we represent the breakup channel by a single effective channel and evaluate the complete fusion cross section using the semiclassical method mentioned above. In this approximation, the complete fusion cross section corresponds to the contribution from the elastic channel to eq.(7). For simplicity, we neglect the excitation energy and the spin of the effective channel. We adopt a form factor with the radial dependence of the electric dipole coupling and the strength is chosen arbitrarily, in such a way that the coupling modifies the cross section predicted by the one dimension penetration barrier appreciably. In figure 1, we compare results obtained with the AW method with those of a coupled channel calculation and also with those obtained with the neglect of channel coupling. We adopt Wood-Saxon shapes for the real and imaginary potentials, with the parameters: $V_0 = -50\ MeV$, $r_{0r} = 1.25\ fm$, $a_r = 0.65\ fm$, $W_0 = -50\ MeV$, $r_{0i} = 1.0\ fm$, $a_i = 0.65\ fm$. We conclude that the semiclassical results are very close to those of a full coupled-channel calculation.

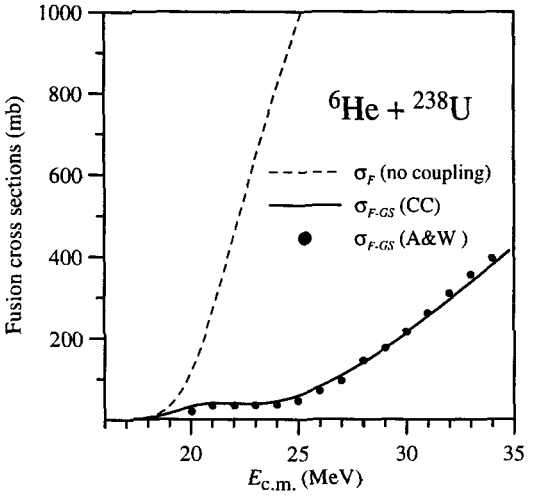

Figure 1. Contribution from the elastic channel to the fusion cross section. Results obtained with the Alder-Winther approximation are represented by solid circles. For comparison, results obtained with a coupled-channel calculation (solid line) and without channel-coupling (dashed line) are also shown.

It should be remarked, however, that this good agreement does not occur at sub-barrier energies. In this energy range the classical trajectory does not reach the barrier radius and therefore the effective barrier lowering that enhances the cross section is not accounted for.

3. Conclusions

The semiclassical Coupled-Channels theory of fusion reactions presented here is a natural extension of what has been done for other reaction channels. As it has been shown in a previous study of the breakup cross section[16], it allows a realistic description of the breakup channel, including continuum-continuum coupling. Although the calculation presented was restricted to a schematic model two-channel model, an extension to a large set of continuum states along the lines of ref.[16] should present no major difficulties.

It should be pointed out that the present model can be extended to calculate the fusion of the fragment that contains all or most of the charge of

the projectile. In a way, it could be considered an improved semi-quantal version of the classical three-body model of Hinde *et al.*[12]. Work is in progress to accommodate both complete and incomplete fusion in the theory and thus supplying a simplified albeit accurate version of the CDCC.

References

1. See, e.g., C.H. Dasso, S. Landowne and A. Winther, *Nucl. Phys.* **A432**, 495 (1985); S.G. Steadman, ed., *Fusion Reactions Below the Coulomb Barrier*, Springer Verlag, Berlin Heidelberg New York Tokyo, 1984.
2. For a recent review see, M.S. Hussein, L.F. Canto and R. Donangelo, *Nucl. Phys.* **A722**, 321c (2003).
3. M.S. Hussein, M.P. Pato, L.F. Canto and R. Donangelo, *Phys. Rev.* **C46**, 377 (1992).
4. N. Takigawa, M. Kuratani and H. Sagawa, *Phys. Rev. C47*, R2470 (1993).
5. C.H. Dasso and A. Vitturi, *Phys. Rev.* **C50**, R12 (1994).
6. K. Hagino, A. Vitturi, C.H. Dasso and S. Lenzi, *Phys. Rev.* **C61**, 037602 (2000).
7. A. Diaz-Torres and I.J. Thompson, *Phys. Rev.* **C65**, 024606 (2002); A. Diaz-Torres, I.J. Thompson and C. Beck, nucl-th/0307021.
8. J.J. Kolata *et al., Phys. Rev. Lett.* **81**, 4580 (1998).
9. K.E. Rehm *et al., Phys. Rev. Lett.* **81**, 3341 (1998).
10. C. Signorini *et al., Eur. Phys. J.* **A5**, 7 (1999).
11. M. Trotta *et al., Phys. Rev. Lett.* **84**, 11 (2000); N. Alamanos *et al., Phys. Rev.* **C65**, 054606 (2002).
12. J. Takahashi *et al., Phys. Rev. Letters* **78**, 30 (1997); M. Dasgupta *et al. Phys. Rev.* **C66**, 041602 (2002); D.J. Hinde *et al., Phys. Rev. Lett.* **89**, 272701 (2002).
13. W.H.Z. Cardenas, L.F. Canto, N. Carlin, R. Donangelo and M.S. Hussein, *Phys. Rev.* **C68**, 054614 (2003).
14. K.Alder and A. Winther, *Electromagnetic Excitations* (North-Holland, Amsterdam, 1975).
15. L.F. Canto, R. Donangelo, N.S. Nikam and P. Ring, *Phys. Lett.* **192B**, 4 (1987); C.A. Bertulani and L.F. Canto, *Nucl. Phys.* **A539**, 163 (1992); L.F. Canto, A. Romanelli, M.S. Hussein and A.F.R. de Toledo Piza, *Phys. Rev. Letters* **72**, 2147 (1994).
16. H.D. Marta, L.F. Canto and R. Donangelo and P. Lotti, *Phys. Rev.* **C66**, 024605 (2002).
17. F.M. Nunes and I.J. Thompson, *Phys. Rev.* **C57**, R2818 (1998); F.M. Nunes and I.J. Thompson, *Phys. Rev.* **C59**, 2652 (1999).

This page intentionally left blank

Light exotic nuclei and clustering

This page intentionally left blank

DIRECT AND RESONANT REACTIONS WITH SECONDARY BEAMS AT LOW ENERGY

W. MITTIG, C.E DEMONCHY, P. ROUSSEL-CHOMAZ, L. GIOT,
H. WANG*, H. SAVAJOLS,
GANIL (DSM/CEA, IN2P3/CNRS), BP 5027, 14076 Caen Cedex 5, France

N. ALAMANOS, A. DROUART, A. GILLIBERT, V. LAPOUX,
E. POLLACCO
CEA/DSM/DAPNIA/SPhN, Saclay, 91191 Gif-sur-Yvette Cedex, France

G.TER-AKOPIAN, A.FOMICHEV, M.S. GOLOVKOV, S.STEPANTSOV,
R.WOLSKI †
FLNR,JINR, Dubna, P. O. Box 79, 101 000 Moscow, Russia

The low to medium energy acceleration of radioactive beams opens up specific possibilities for the study of nuclear reactions and nuclear structure. This energy domain is particularly well suited for the study of direct transfer reactions and resonant scattering. The study of nuclei far from stability interacting with simple target nuclei, such as protons, deuterons, ^{3}He and ^{4}He implies the use of inverse kinematics. The kinematics, together with the low intensities of the beams call for special techniques. We tested a new detector, in which the detector gas is the target, an active target. This allows in principle a 4π solid angle of the detection, and a big effective target thickness without loss of resolution. The detector developped, called Maya, used isobutane C_4H_{10} as gas in the first experiment, and other gases are possible. The multiplexed electronics of more than 1000 channels allows the reconstruction of the events occurring between the incoming particle and the detector gas atoms in 3D. Here we were interested in the reactions induced by ^{8}He on protons at 2-3.5MeV/n. The design of the detector is shown, and some first results are discussed.

*Permament adress: IMP, Lanzhou, China

†and Institute of, Nuclear Physics, Cracow , partially supported by the IN2P3-Poland coll.

1. Introduction

Secondary beams obtained by fragmentation are most efficiently used at velocities near to the primary beam velocity due to the kinematics of this reaction. This leads to secondary beam energies of typically 25-75MeV at Ganil and Dubna, 100-400MeV/n at Riken and MSU, and 200MeV to 1GeV/n at GSI. These energies are best suited for high energy inelastic and quasielastic scattering, knock-out reactions, and one or some nucleon removal reactions. Since 1989 low energy reaccelerated secondary beams are available at LLN, and since more recent dates at Ganil-Spiral , ORNL, Triumf-Isac and Rex-Isolde with energies typically in the 0.1-10MeV/n domain. These energies are ideally suited for the study of resonant reactions, among them those of astrophysical interest, and direct transfer or pick-up reactions. Elastic and inelastic scattering are other reactions of interest at this energy, especially near the Coulomb barrier. In most of these studies the interaction with simple target nuclei, such as protons, deuterons, ^{3}He and ^{4}He is preferred in order to obtain quantitative results. This implies the use of gas targets and of inverse kinematics. In the study of reactions in inverse kinematics, the information of interest can be deduced by measuring either the kinematical characteristics of the heavy residue and/or of the light fragment. In the case of the heavy residue, the detection efficiency is increased by the forward focusing of the reaction, and the large velocity allows for the use of relatively thick targets. A recent revue on this subject can be found in ref[1]. A detector, in which the detector gas is the target, this is, an active target, has in principle a 4π solid angle of detection, and a big effective target thickness without loss of resolution, and is thus ideally suited for the study of reactions induced by secondary beams.

2. Active Targets

Active targets,such as bubble, chambers were developped since a long time in high energy physics. In the domain of secondary beams, the archetype is the detector IKAR [2]. A discussion of the use of this detector for elastic scattering at GSI energies can be found in ref[3]. The use of this detector was limited to H_2 at a pressure of 10atm. Another example can be found in ref[4], where a flash adc readout of wedge signals was used. For the domain of low energies, and for the use of various gases, we developed a new detector called MAYA[5,6] that we will describe here.
If we want to use a thick target without loss of resolution, the locus of the reaction must be determined. A high solid angle together with this con-

sideration implies a tracking of the particles in three dimensions. Typical maximum pressures and associated range of typical reaction products, together with the fact that isotopically enriched gases are considered, lead to dimensions of the order of 30cm. If we want a range resolution of the order of one percent, corresponding to an energy resolution of half a percent, a resolution of the length of the trace of the order 1mm is needed. Charge division of the signal induced allows a resolution of typically a factor 10 of the pad size used. These general considerations lead us to a design of a detector with an active volume of 28(width)*26(length)*20(heigth) cm^3. It can be filled with pressures up to 4atm. The resolution requirement results in a subdivision of about 30*30 pads of the active detector area. The detector is shown schematically on the figure 1.

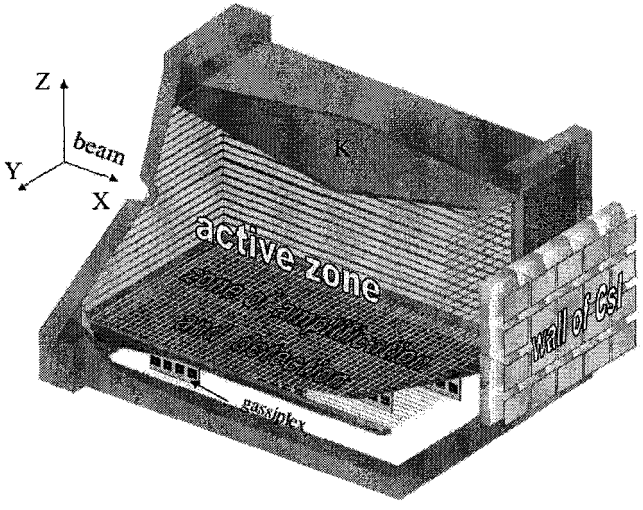

Figure 1. The scheme of the detector MAYA. The secondary beam is incident from the left, the electrons produced by ionising reaction products in the detector gas drift down, and induce a signal after amplification in the anode pattern. These signals are read out by gassiplex electronics below this anode.

For a two body reaction, scattered and recoiling particles are in a plane. The electrons from the ionisation of the gas by the particles are drifting down to the amplifying wires. The wires are parallel to the beam. Therefore their diameter can be different in the region of the beam, to adjust for

different ionisation densities of beam and recoil particles. In the experiment with ^{8}He we obtained a gain of 1/10 in this central region by the use of 20μ instead of 10μ amplifying wires. The spacing of the wires should be quite small, in principle less than the drift straggling of the electrons in order to avoid digitalisation. We used a distance of 3mm. The wires corresponding to a row of pads are connected to the same preamplier. The angle of the reaction plane can be determined by the drift time to the wires. The amplified signal is induced in the pads below. The distance between the wires and the pads determines the width of the induction pattern. A distance of 10mm was chosen in order to have best position resolution that is obtained if the signal of two nearby lateral pads have about half the amplitude of a central pad. A hexagonal structure was choosen for these strips, in order to have best conditions for the reconstruction of the trajectory, independant of the direction. This results in a honeycomb structure. A matrix of 35 by 34 pads, this is, 1190 pads constitues this anode. The pads are arranged in rows below the wires, in order to have a precise time relation between the wire signal and the pad signal. The pads are connected to Gassiplex Asics. These provide a multiplexed readout, limiting the numbers of connections from the detector to the outside. The Gassiplex are mounted on the back of the anode. The Gassiplex need a track and hold signal, that is provided by the wire signal, treated by classical electronics.
As pointed out above, inverse kinematics generate recoil particles in a large energy domain. High energy light particles such as protons cannot be stopped in a reasonable gas volume. For escaping particles, we added a CsI wall of 20*25cm^2, covering about 45 degrees around the beam for events in the middle of the detector. The detector can be characterized as a CPC: Charge Projection Chamber.

3. Some results obtained with a secondary beam of ^{8}He at 3.9MeV/n

A first experiment with this detector was performed in july 2003. The incoming beam was ^{8}He at 3.9MeV/n and the detector was filled with 1atm of isobutane. With this gas density, the beam was stopped in the detector, and thus the energy domain covered is between the incident energy and zero energy. The 3 dimensional determination of the trajectories needed a quite important development of software[6]. First results are given below. As an example we will show some results of the ^{8}He(d,p) reaction. In order to get spectra that allow to identify reactions and final states, a

first condition must be set on the locus of the reaction. A typical range-range correlation of the two reaction partners is shown on figure 2. A particle identification is obtained from the correlation of total charge on a trajectory and the range. From the approximate relation between energy loss and energy $dE/dx \propto MZ^2/E$, the range R is $R \propto E^2/(MZ^2)$, and charge collected is proportional to the energy.

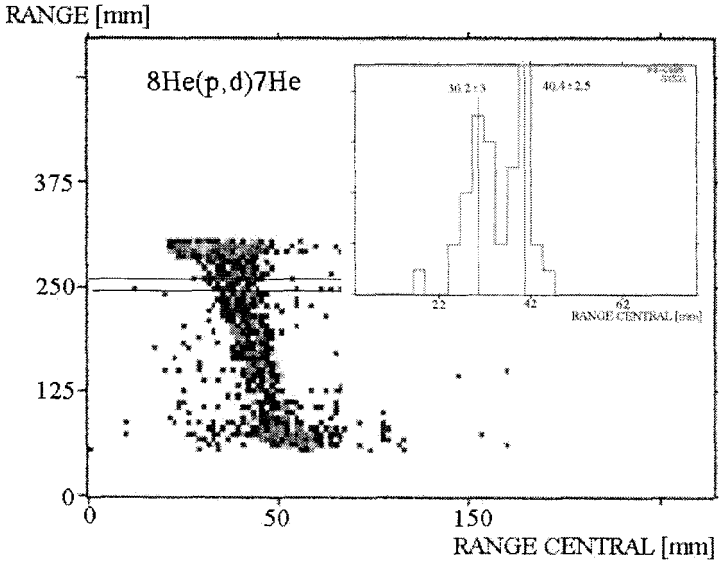

Figure 2. Correlation for the range of reaction partners, conditionned for reactions at (50±1)mm after entrance in the detector, and by the identification of deuterons. As insert is shown the projection on the range of He.

The ground state of ^{7}He is known[7] to be unbound by 440keV, with a width of 150keV. Thus ^{7}He disintegrates in ^{6}He plus neutron, and the remaining ^{6}He has a variable kinetic energy due to recoil. This kinematic pattern is easily recognized on the figure 2 on the insert, the two peaks corresponding to the emission of the neutron in forward and backward direction. It shows that such a detector that measures the two reaction partners is a powerful instrument to determine decay properties at the same time, and illustrates the resolution of the detector.

The range-angle correlation for the light particle is shown on figure 3. The upper line can be identified as being due to protons, a very large condition only being set on the identification in order not to introduce cuts at low

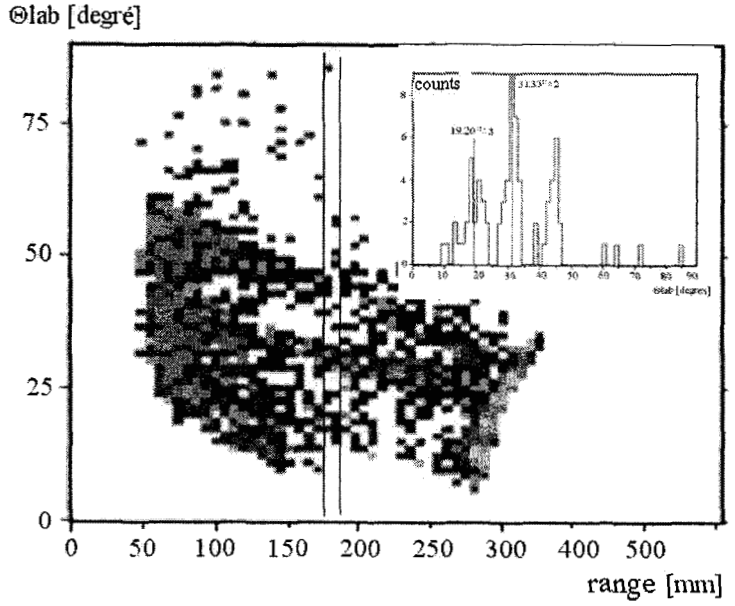

Figure 3. Correlation for the range of the light particle with the angle, conditionned for reactions at (50±1)mm after entrance in the detector with a broad window on the particle identification. As insert is shown the projection on the angle.

energy. The lower lines could be shown, by conditioning the identification by this domain of the theta-range correlation, to correspond to deuterons. In this domain of inverse kinematics, the excitation energy of the final ^{7}He influences kinematically mainly the angle. The insert therefore shows the projection on the angle co-ordinate. Above the ground state, a structure shows clearly up. When the angle is converted by kinematics to excitation energy, this structure corresponds to E_x=1.2MeV above the groundstate. The experimental energy resolution for the ground state is 300keV. In ref[10] an excited state at 2.9MeV was observed. In heavy ion transfer reactions[12], only the ground state of ^{7}He was observed, as well as in recent experiment on the isobaric analogue state[8]. In a fragmentation reaction at GSI[11], evidence for a state at 1.4MeV above ground state was found with a width of 1.2MeV. The structure we observed could correspond to this state, with a width of the order of 500keV. However, due to the low energy of the present experiment, the structure observed could correspond to phase space, and an experiment at somewhat higher energy, about 8MeV/nucleon, should

allow to confirm one of these solutions.

The angular distributions were obtained for maximum energy down to about 2MeV/n. They were analysed using the code Fresco, with an optical potential taken from CH89[9]. Experimental uncertainties of the absolute cross section are of the order of 30% due to efficiency of the reconstruction algorithm. The optical model introduces another uncertainty in the evaluation of this reaction. Nonetheless, the angular distributions agree well, and a spectroscopic factor $C^2S=3\pm1$ is obtained in the analysis. This is close to a simple shell model estimation where one expects $C^2S=4$ for 4 nucleons in the p3/2 shell. A similar result was obtained at much higher energy[10]. Large transfer reaction cross sections have been predicted[13] at low energy for loosely bound systems. This results from the very low Fermi momentum in these systems, that implies highest overlap at very low velocity. To our knowledge this effect has not yet been observed. On figure 4 the angle integrated cross section as a function of energy is shown. The experimental data were integrated using the Fresco angular distributions renormalized on the experimental data.

As can be seen, the cross section is very high, reaching 1barn in the energy

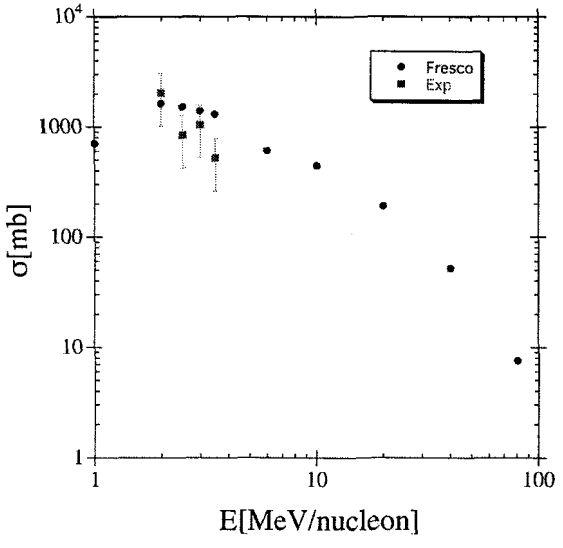

Figure 4. Angle integrated cross section for the $^8He(p,d)^7He_{gs}$ reaction. The theory is given with $C^2S=4$.

domain of the present experiment. The good agreement between the theory and experiment shows that even at this low energy the direct reaction mechanism is dominant.

Elastic scattering and the (p,t) reaction were observed simultaneously. There is not enough space to discuss in more detail these reactions, the reults will be presented elsewhere.

4. Conclusion

We developped a new active target detector, that takes full advantage of modern electronics, using Asics for cheap and compact electronics, and that is particularly well suited for the low energy domain. We think that such type of detectors is an excellent tool for studying the properties of exotic nuclei by low intensity secondary beams, where highest efficiency and good resolution in inverse kinematics is essential.As we have shown, the energy domain below 10MeV/n shows very specific and interesting possibilities. This was illustrated by the study of ^{8}He induced reactions on protons in the domain of 2-3.9MeV/n. Very large cross-sections were observed for direct reactions reaching more than 1barn for the (p,d) reaction. Data were also obtained for the (p,t) reaction and resonant elastic scattering. These results will be presented elsewhere.

References

1. P.Roussel Chomaz and W.Mittig, Nucl.Physics A 693 (2001) 495
2. A.A.Vorobyov et al., NIM 119 (1974) 509 and NIM A270(1988)419
3. P.Egelhof, Proc. Int. Workshop on Physics with Unstable Nuclear Beams, Serra Negra, Sao Paulo Brazil, ed. C.A.Bertulani et al., World Scientific 1997, ISBN981-02-2926-7, page 222
4. Y.Mizoi et al., NIM A431(1999) 112 and Phys.Rev. C62, 065801 (2000)
5. P.Gangnant, C.Spitaels, G.Fremont, P.Bourgault, J.F.Libin report Ganil 27.2002
6. C.E.Demonchy, thesis T 03 06, december 2003, University of Caen, France
7. D.R.Tilley et al, TUNL Manuscript, Energy levels of light nuclei A=7, and Energy levels of light nuclei A=9
8. R.V.Rogachev et al, contribution to the RNB conference 2003, to be published
9. R.L.Varner et al., Phys. Rep. 201,57 (1991)
10. A.A.Korsheninnikov et al,Phys.Rev. Lett. 82, 3581 (1999)
11. M.Meister et al,Phys.Rev. Lett. 88, 102501(2002)
12. W. von Oertzen et al., Nuclear Physics A588, 129 (1995).
13. H.Lenske AND G.Schrieder, Eur.Phys. J. A 2 (1997) 41

RESONATING CLUSTERS*

R. G. LOVAS†, J. ZS. MEZEI AND T. VERTSE
Institute of Nuclear Research of the Hungarian Academy of Sciences, Debrecen, PO Box 51, H-4001, Hungary

Four treatments of resonance states are outlined: direct search of the S-matrix pole, complex scaling, analytic continuation in the coupling constant and Berggren's theory. Examples for the latter two show their feasibility and usefulness.

1. Introduction

In this talk the description of nuclear resonances is reviewed. Resonance states have particular significance for exotic nuclei since these have hardly any bound states. Resonances have to be treated as such; otherwise we may obtain false results. Their description should be a generalization of that of bound states. The more general concept to be used is that of the poles of the S-matrix as a function of the complex energy E or wave number k.

After a classification of discrete states as S-matrix poles, four methods of the description of resonances will be reviewed: direct pole search, complex scaling, analytic continuation in the coupling constant and Berggren's theory as a generalized continuum shell model. A few new and illuminating illustrations will be presented for the latter two.

2. Classification of poles

For simplicity, let us confine ourselves to s-wave motion in a spherical potential. To avoid the ambiguity of $S(E)$ caused by $k \sim \pm\sqrt{E}$, two Riemann sheets are defined by $\mathrm{Im}\, k \geq 0$ (physical sheet) and by $\mathrm{Im}\, k < 0$ (non-physical sheet). The asymptotic form of the wave function looks like $u(r) \sim k^{-1/2}(\mathrm{e}^{-ikr} - S\mathrm{e}^{ikr})$ or, in a renormalized form,

*This work was supported by OTKA grants T029003 and T037991 (Hungary).
†E-mail: rgl@atomki.hu

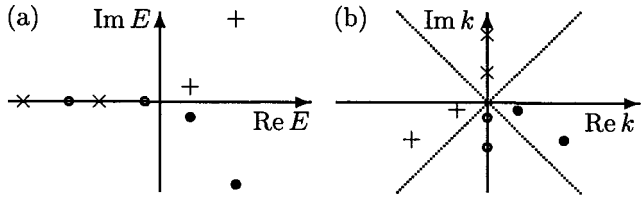

Figure 1. Bound-state (×), resonance (•), antiresonance (+) and virtual-state (○) poles in the complex energy plane (a) and in the complex momentum plane (b).

$u(r) \sim k^{-1/2}(S^{-1}\mathrm{e}^{-ikr} - \mathrm{e}^{ikr})$. At a pole of S, one has $u(r) \sim -k^{-1/2}\mathrm{e}^{ikr}$, thus the asymptotic wave function is just an outgoing wave.

The poles of physical significance are the following (Fig. 1):
(i) bound states: $\bar{E} < 0$; $\bar{k} = i\kappa \sim (\bar{E})^{1/2}$ $(\kappa > 0)$, $u(r) \sim \mathrm{e}^{-\kappa r}$;
(ii) virtual or antibound states: $\bar{E} < 0$; $\bar{k} = -i\kappa$ $(\kappa > 0)$, $u(r) \sim \mathrm{e}^{\kappa r}$;
(iii) resonances: $\bar{E} = E_\mathrm{R} - i\frac{1}{2}\Gamma$, $(E_\mathrm{R}, \Gamma > 0)$, $\bar{k} = \kappa - i\gamma$ $(\kappa, \gamma > 0)$, $u(r) \sim \mathrm{e}^{\gamma r}\mathrm{e}^{i\kappa r}$;
(iv) antiresonances: $\bar{E} = E_\mathrm{R} + i\frac{1}{2}\Gamma$, $\bar{k} = -\kappa - i\gamma$, $u(r) \sim \mathrm{e}^{\gamma r}\mathrm{e}^{-i\kappa r}$.

Resonance and antiresonance states are at conjugate positions $E_\mathrm{R} \pm i\frac{1}{2}\Gamma$, $\pm\kappa - i\gamma$; they are each other's timed-reversed, and their wave functions are related by $u_{-\bar{k}^*}(r) = u_{\bar{k}}^*(r)$. Bound and antibound states also occur pairwise, but there is no such strict correspondence between them.

To interpret resonance states, let us substitute the ansatz $\Psi = \mathrm{e}^{-\frac{i}{\hbar}\bar{E}t}\psi$ in the Schrödinger equation $i\hbar\frac{\partial}{\partial t}\Psi = H\Psi$, and prescribe the outgoing-wave boundary condition $\psi(\mathbf{r}) \propto u(r) \sim \mathrm{e}^{ikr}$. We obtain $\Psi \sim \mathrm{e}^{-\frac{\Gamma}{2\hbar}t}\mathrm{e}^{-\frac{i}{\hbar}E_\mathrm{R}t}\mathrm{e}^{ikr}$. The time dependence of $|\Psi|^2 \propto \mathrm{e}^{-\frac{\Gamma}{\hbar}t}$, with the asymptotic form e^{ikr}, describes exponential decay of a state of width Γ. The exponential increase of the amplitude with r expresses that the decay started an infinitely long time ago and lasts up to infinity. Such a wave function is called a Gamow wave function.

The Hamiltonian H is non-Hermitean in the space of functions satisfying the outgoing-wave boundary condition. The Gamow wave function is not a legitimate quantum mechanical state, but is an approximation to the wave packet that describes decay. It is as good an approximation as is the law of exponential decay for the actual decay process. The Gamow wave function is not normalizable: $\int_0^\infty u^2(r)dr \not\ni$, but a redefined integral, $\lim_{\epsilon\to 0}\int_0^\infty u^2(r)\mathrm{e}^{-\epsilon r^2}dr$ does exist. By an analytic continuation of $u(r)$ one can get alternative definitions [1]:

$$\lim_{\epsilon\to 0}\int_0^\infty u^2(r)\mathrm{e}^{-\epsilon r^2}dr = \lim_{\epsilon\to 0}\int_C u^2(r)\mathrm{e}^{-\epsilon r^2}dr = \int_C u^2(r)dr = \int_{C'} u^2(r)dr,$$

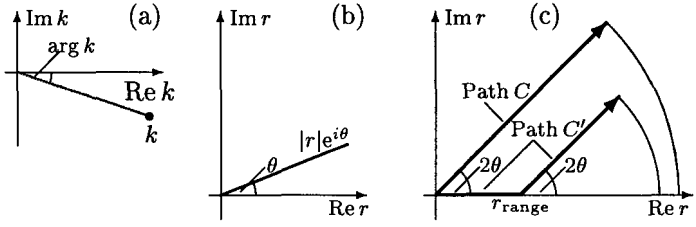

Figure 2. The k-plane (a), path along which $u(r)$ is damped (b), integration paths (c).

where the paths C and C' are defined in Fig. 2, and the equalities hold provided that $\theta > |\arg k|$. The (radial) matrix elements of non-singular operators may be calculated similarly:

$$\lim_{\epsilon \to 0} \int_0^\infty u_1(r) O u_2(r) \mathrm{e}^{-\epsilon r^2} dr = \int_C u_1 O u_2 dr = \int_{C'} u_1 O u_2 dr.$$

The expectation values in resonance states are complex. These imaginary parts, just as Γ, are to be interpreted as the measures of the uncertainty inherent in the definition of a resonance itself.

The Gamow functions form a biorthogonal set: $\langle \tilde{u}_{E_i,k_i} | u_{E_j,k_j} \rangle = \delta_{ij}$, with $\tilde{u}_{E,k} = u_{E^*,-k^*} = u^*_{E,k}$, so that $\tilde{u}^*_{E,k} = u_{E,k}$. In the quantum mechanics of resonance states, a matrix element is only defined between an "incoming" and an "outgoing" state[2]: $\langle \tilde{u} | O | u' \rangle = \int u O u' dr$. Thus it is not the ordinary norm of u that is unity but its overlap with its time-reversed. The tails, which describe decay and buildup, respectively, hardly overlap, and thus have minute effects on matrix elements. With this prescription, the resonance state may be interpreted as the decaying state before decay.

These concepts lead to a generalized orthonormality and completeness relation, which is the core of Berggren's theory[2] (see Fig. 3):

$$1 = \sum_i |\tilde{u}_i\rangle\langle u_i| + \int dE \; |\tilde{u}_E\rangle\langle u_E|.$$

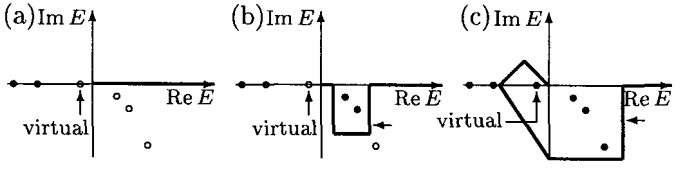

Figure 3. Alternative contours for the completeness relation. The curves off the real axis are in the non-physical Riemann sheet.

The sum may run over the bound states; then the continuum may just be that of the ordinary scattering states. Alternatively, some resonance states may be included in the sum, and then the continuum should embrace them in the unphysical sheet from below. The sum may even include virtual states. Berggren's theory makes it possible to form quantum mechanical bases including discrete unbound states.

3. Description of resonances

3.1. *Direct pole search*

This[3] is a brute-force method and is applicable whenever the resonance problem is formulated as a (multichannel) scattering problem. The scattering formalism can be extended to complex energies, and the resonance on the appropriate Riemann sheet can be located by a pole search. The pole search may just be an iterative procedure for finding the parameters of a truncated Laurent series $S(E) = c_{-1}(E-\bar{E})^{-1}+c_0+\ldots$, starting with a set of first guesses. The procedure usually converges rapidly. The wave function belonging to the resulting energy $\bar{E}$ is just the Gamow wave function.

3.2. *Complex scaling*

A transformation $r \to re^{i\theta}$ performed in H leaves the positions of the poles unchanged. It transforms the Gamow wave functions with $|\arg k| < \theta$ into square-integrable functions and rotates the energy continua by -2θ.

Diagonalization of the rotated Hamiltonian on an L^2 basis thus results in discrete states: the bound states, the resonance states that lie close to the real axis and the discretized continuum (Fig. 4). In principle, the Gamow wave functions can be recovered from the solution of the rotated problem, but that procedure is ill-posed numerically [5]. The matrix elements between Gamow states may rather be calculated from the rotated wave function, with an appropriately rotated operator.

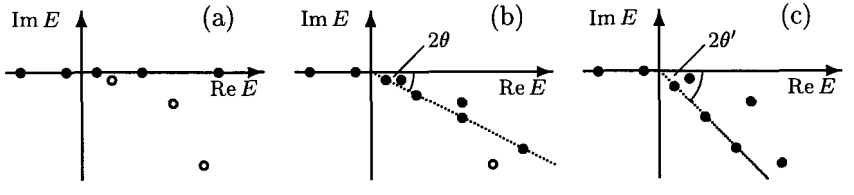

Figure 4. Energies (•) obtained by L^2-diagonalization without rotation (a) and with rotation by θ (b) and by θ' (c). Some poles not obtainable are denoted by ○ .

3.3. *Extrapolation of bound states*

Resonances can be located by extrapolation of bound states to the unbound-state region. The method is called the analytic continuation in the coupling constant (ACCC) [6,7]. When the potential strength is varied, the poles move along trajectories like those shown in Fig. 5. From a number of bound-state pole positions known as a function of a potential strength λ ('coupling constant'), one can calculate the position of the pole in the unbound-state region as well. The extrapolation should be performed as a function of $x = (\lambda - \lambda_0)^{1/2}$, where λ_0 is the value of λ at the bifurcation. The extrapolation (see Fig. 5b) can be done, e.g., by a Padé approximation formula.

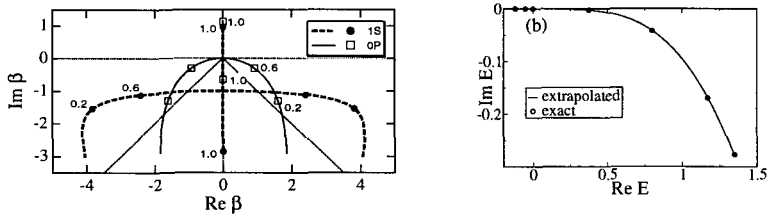

Figure 5. S- and p-wave pole trajectories in the $\beta = ka$-plane in a square well of radius a, with some λ-values displayed [7]. The dotted lines mark $\mathrm{Im}\,\beta = \pm\mathrm{Re}\,\beta$ (a). Exact and extrapolated s-wave pole trajectories (the latter calculated in a Gaussian basis) in the E-plane generated by the potential $V(r) = -3.2\lambda e^{-0.16r^2} + 2e^{-0.04r^2}$ a.u. (b).

In principle, the Gamow wave function can be produced by analytic continuation of bound states, but, as Fig. 6a shows, its tail cannot be recovered in this way. When, however, the asymptotic form is known, one can write $u(r) = \varphi(r)u_{\mathrm{as.}}(r)$, where $u_{\mathrm{as.}}(r)$ is smooth, with $u_{\mathrm{as.}}(0) = 0$ and

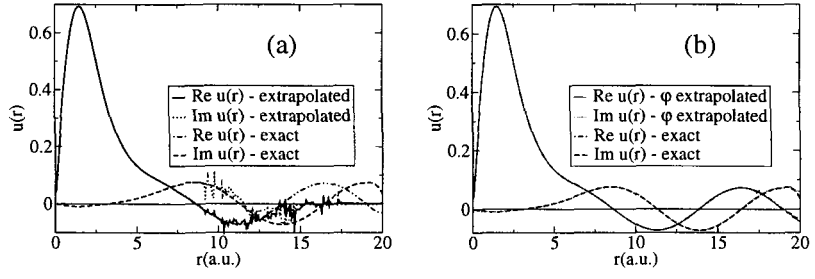

Figure 6. Exact and continued (Gaussian basis) Gamow functions generated by the potential given in the caption of Fig. 5b; (a) full extrapolation, (b) extrapolation of $\varphi(r) = u(r)/u_{\mathrm{as.}}(r)$.

Table 1. Exact and extrapolated energies and r.m.s. radii (a.u.) of the model problem.

λ	1		0.5	
	Exact	Extrapolated	Exact	Extrapolated
$\bar{E}$	0.37618-i0.003025	0.37618-i0.003024	1.734+i0.1697	1.729+i0.1690
$\langle r^2\rangle^{1/2}$	2.11206+i0.13797	2.11205+i0.13793	2.248+i1.012	2.247+i1.018

$u_{\text{as.}}(r) \to e^{i\bar{k}r}$. Then $\varphi(r)$ is more easily tractable (Fig. 6b). Quite agreeable results can be obtained even for higher-energy and broader resonances.

Since it may not be easy to formulate the asymptotic form, it seems more practical to extrapolate matrix elements directly. Table 1 shows that the extrapolation may be very accurate even for broad resonances.

A calculation for the α+α relative motion shows that its rms radius is very well defined, 5.970+i0.079 fm. Folded with the α-particle radii, this results in $\langle r^2\rangle^{1/2}$=3.42 fm for the nucleus ^{8}Be, which is much larger than the values obtained in recent bound-state-like models[9,10] (2.07–2.3 fm). This indicates that no bound-state-like model can be fully realistic for an unbound state.

3.4. *Berggren's theory*

Berggren's theory is useful, e.g., in the shell model when no bound s.p. states exist. We discuss just one aspect of the structure of ^{11}Li. Several realistic calculations[11,12] show that the halo contains an ~50% $(1s_{1/2})^2$ component[12], and that is often attributed to the near-theshold virtual neutron s.p. state in the ^{9}Li+n relative motion.

We have explored the effect of this virtual state. We used[13] a basis of the type of Fig. 3b for the $p_{1/2}$, $d_{5/2}$ and $d_{3/2}$ waves, and of Fig. 3a or c for the s-wave. With the residual force adjusted to the experimental two-neutron separation energy, we obtained 43.4% for the weight of the $(s_{1/2})^2$ configuration. With real s-wave continuum we found that the [0, 0.1 MeV] interval is responsible for half of the $(s_{1/2})^2$ component.

To see whether that is due to the virtual state, we used a basis of the type of Fig. 3c for the s-wave (Table 2). As a test, we excluded the virtual state with the contour kept unchanged, and then omitted the contour but included the virtual state. One may expect that the energy gets enhanced, with a drop of the s-wave component in both cases. What happened was just the opposite. Finally, we restored the correct binding in both cases by varying the residual force. One then expects that the looser binding reduces the weight of the s^2 component. This expectation was not met either.

One can reconcile oneself with these results by recalling that the *anti-*

Table 2. Energy and weights in calculations with distorted contours

Calculation	Energy (MeV)	$(s_{1/2})^2$	$(p_{1/2})^2$	d^2
full	−0.295	0.434+i0.003	0.484−i0.003	0.082
no virtual	−2.691	0.773	0.128	0.099
no $l = 0$ contour	−1.567	0.768	0.150	0.082
no virtual, NN fitted	−0.295	0.982	0.015	0.003
no $l = 0$ contour, NN fitted	−0.295	0.979	0.018	0.003

bound state moves opposite to a change in the s.p. potential depth. Moreover, the properly normalized virtual state is imaginary, which makes any expectation value to have a sign opposite to the usual sign. The s^2 component thus results from complicated interference effects between the complex continuum and the antibound state.

4. Conclusion

Discrete unbound states can be treated via the S-matix poles they belong to. There are efficient tools for locating them and calculating their properties. In particular, an extrapolation technique has been shown to be suitable for calculating physical properties. Berggren's theory has been used to analyse how the virtual state affects the g.s. of ^{11}Li. It has been found to show antibinding and to exert its effect through complicated interference with the continuum.

References

1. B. Gyarmati and T. Vertse, *Nucl. Phys.* **A160**, 523 (1971).
2. T. Berggren, *Nucl. Phys.* **A109**, 265 (1968).
3. B. G. Giraud, M. V. Mihailović, R. G. Lovas and M. A. Nagarajan, *Ann. Phys.* (N. Y.) **140**, 29 (1982).
4. J. Aguilar and J. M. Combes, *Commun. Math. Phys.* **22**, 269 (1971).
5. A. Csótó, B. Gyarmati, A. T. Kruppa, K. F. Pál and N. Moiseyev, *Phys. Rev.* **A41**, 3469 (1990).
6. V. I. Kukulin and V. M. Krasnopol'sky, *J. Phys.* **A10**, 33 (1977).
7. N. Tanaka, Y. Suzuki, K Varga and R. G. Lovas, *Phys Rev.* **C59**, 1391 (1999).
8. S. Ali and A. R. Bodmer, *Nucl. Phys.* **80**, 99 (1966).
9. Xinhua Bai and Jimin Hu, *Phys. Rev.* **C56**, 1410 (1997).
10. P. Navrátil and B. R. Barrett, *Phys. Rev.* **C57**, 3119 (1998).
11. I. J. Thompson and M. V. Zhukov, *Phys. Rev.* **C49**, 1904 (1994).
12. Y. Suzuki, R. G. Lovas, K. Yabana and K. Varga: Stucture and Reactions of Light Exotic Nuclei, pp. 446–456 (Taylor & Francis, London, 2003).
13. R. Id Betan, R. J. Liotta, N. Săndulescu and T. Vertse, submitted to *Phys. Lett.* **B** (2003).

STUDY OF BE ISOTOPES BASED ON THE GENERALIZED TWO-CENTER CLUSTER MODEL

MAKOTO ITO

Institute of Physics, University of Tsukuba, 305-8571 Tsukuba, Japan
E-mail: itom@nucl.ph.tsukuba.ac.jp

KIYOSHI KATŌ

Division of Physics, Graduate School of Science, Hokkaido University, 060-0810 Sapporo, Japan

KIYOMI IKEDA

RI Beam Science Laboratory, RIKEN(The institute of Physical and chemical Research), Wako, Saitama 351-0198, Japan

A generalized two-center cluster model (GTCM), including various partitions of the valence nucleons around two α-cores, is proposed for studies on the exotic cluster structures of Be isotopes. This model is applied to the ^{10}Be=$\alpha+\alpha+2n$ and the ^{12}Be=$\alpha+\alpha+4n$ systems. The adiabatic energy surfaces for $\alpha-\alpha$ distances are calculated. It is found that this model naturally describes the formation of the molecular orbitals as well as that of asymptotic cluster states depending on their relative distance.

1. Introduction

In recent studies, much attention has been concentrated on Be isotopes in which a motion of valence neutrons couples to the two-α structure of ^{8}Be. Based on the molecular orbital model (MOM), Itagaki *et al.* has extensively studied the low-lying states of Be isotopes [1]. The molecular orbitals, such as π and σ orbitals associated with the covalent bonding of atomic molecules, have been shown to give a good description for the low-lying states of Be-isotopes [1].

Furthermore, recent experiments by Freer *et al.*, [2] revealed the existence of the interesting resonant states, which dominantly decay to ^{6}He$_{g.s.}$+^{6}He$_{g.s.}$ and α+^{8}He$_{g.s.}$ channels in the excited states of ^{12}Be. Similar resonant states have also been observed in ^{10}Be [2] and ^{14}Be [3]. Since the

energies for the two neutron separation is small in both ^{6}He and ^{8}He, it is properly considered that the valence neutron of ^{6}He and ^{8}He are associated with companion clusters when they approach each other, which is similar to the covalent bonding of valence neutrons in the low-lying states.

Therefore, it is important to study the molecular structures in low-lying and high-lying states of Be-isotopes in a unified way by taking into account couplings between a valence neutron's motion and the α clustering. To achieve this purpose, we propose a new framework of a generalized two-center cluster model (GTCM) where we can describe atomic-orbital motions of valence neutrons around individual α clusters on the same footing with molecular orbitals, being a single-particle motion around two α-cores. We apply this model to ^{10}Be and ^{12}Be and discuss its applicability on systematic studies of Be-isotopes.

2. Generalized two-center cluster model

The basis functions of GTCM for ^{10}Be are given as

$$\Phi^{J^\pi K}_{m,n}(S) = \hat{P}^J_K \hat{A} \{\psi_L(\alpha)\ \psi_R(\alpha)\varphi(m)\varphi(n)\} \tag{1}$$

$$\Phi^{J^\pi}_K(^{10}\mathrm{Be};\ S) = \sum_{m,n} C^{J^\pi K}_{m,n}(S)\ \Phi^{J^\pi K}_{m,n}(S)\ . \tag{2}$$

The α-cluster wave function $\psi_i(\alpha)$ $(i{=}L, R)$ is given by the $(0s)^4$ configuration in the harmonic oscillator (HO) potential with the relative distance-parameter S. The position of an α-cluster is explicitly specified as the left (L) or right (R) side. A single-particle state for valence neutrons around one of α clusters is given by an atomic orbitals, $\varphi(i, p_n, \tau)$ with the subscripts of a center i $(=L$ or $R)$, a direction p_n $(n{=}x, y, z)$ of $0p$-orbitals and a neutron spin τ $(=\uparrow$ or $\downarrow)$. In Eqs. (1) and (2), the index $m(n)$ is an abbreviation of the atomic orbital (i, p_n, τ). The basis function $\Phi^{J^\pi K}_{m,n}(S)$ with the parity π is projected to the eigenstate of the total spin J and its intrinsic angular projection K by the projection operator $\hat{P}^J_K$. Various linear combinations of $\Phi^{J^\pi K}_{m,n}(S)$ can reproduce the molecular orbital configurations as well as the cluster-model states of $[\alpha{+}^6\mathrm{He}]$ and $[^5\mathrm{He}{+}^5\mathrm{He}]$.

The coefficients $C^{J^\pi K}_{m,n}(S)$ are determined by solving a coupled channel GCM (Generator Coordinate Method) equation [4]:

$$\int dS' \sum_{\beta' K'} C^{J^\pi K'}_{\beta'}(S') \times \left\langle \Phi^{J^\pi K}_{\beta}(S) \mid H - E^{J^\pi} \mid \Phi^{J^\pi K'}_{\beta'}(S') \right\rangle = 0 \ . \quad (3)$$

with $\beta = (m, n)$. When we set $C^{J^\pi K}_{\beta}(S')$ to be $D^{J^\pi K}_{\beta} \cdot \delta(S - S')$, Eq. (3) is reduced to the equation at a fixed S. In such a case, the eigenvalue E^{J^π} depends on S, and then we call the energies and the wave functions "adiabatic energy surfaces" and "adiabatic eigenstates", respectively.

3. Results

In the present calculation, we adopted the Volkov No.2 with the Majorana parameter m=0.576 and without the Bartlett and Heisenberg exchanges for the nucleon–nucleon interaction. We also employed the G3RS interactions for the spin-orbit parts. The radius parameter b of HO for α clusters and valence neutrons is taken as 1.44 fm^{-1}.

The calculated adiabatic energy surfaces for ^{10}Be with J^π=0$^+$ state are shown by open circles in the left panel of Fig. 1. In this panel, the thick-solid and thick-dotted curves are the expectation values $< H >$ of the $[^4\mathrm{He}+^6\mathrm{He}(I)]_L$ and $[^5\mathrm{He}(I_1)+^5\mathrm{He}(I_2)]_{IL}$ cluster-states, respectively, in which individual clusters have intrinsic spins $(\mathbf{I_1}, \mathbf{I_2})$, the channel spin I $(\mathbf{I} = \mathbf{I_1} + \mathbf{I_2})$ and the relative one L. From Fig. 1, we can see that in $S \geq$ 6 fm, the calculated energy surfaces are completely the same as those of cluster states.

On the other hand, in $S \leq 6$ fm, the energies for the cluster states deviate from the adiabatic energy surfaces. To see the intrinsic structure at a short S, we take the overlaps between the molecular orbitals and the adiabatic eigenstates. In Fig. 1, the adiabatic eigenstates connected by the thin-solid curves at the internal region have the common dominant-component of a molecular orbital.

Therefore, the cluster states become a good basis state for describing the system at the external region, while the molecular orbtials at the internal region. At an intermediate region (S=5$\sim$6 fm), we find that the eigenstate has an intermediate character between the molecular orbitals and the cluster states.

Finally, the GCM equation (3) is solved by employing the basis states ranging from S = 1 fm to S = 9 fm with the mesh of 0.5 fm. The lowest three GCM solutions have energy gains of about 1$\sim$2 MeV, and the

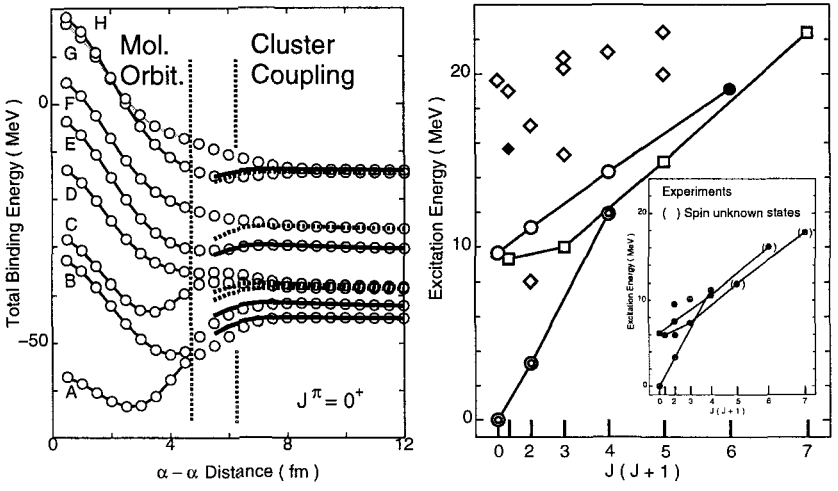

Figure 1. (Left panel) Adiabatic energy surfaces for ^{10}Be with $J^\pi = 0^+$. In the right part, the solid and dotted curves show the energies of the α+^{6}He and ^{5}He+^{5}He cluster states, respectively. In the left part, the surfaces of A, B, C and D have a dominant component of $(\pi^-_{3/2})^2$, $(\sigma^+_{1/2})^2$, $(\pi^-_{1/2})^2$ and $(\pi^+_{3/2})^2$, respectively, while E, F, G and H $(\pi^+_{1/2}\sigma^+_{1/2})$ and $(\pi^-_{1/2}\sigma^-_{1/2})$, $(\sigma^-_{1/2})^2$ and $(\pi^+_{1/2})^2$, respectively. (Right panel) Band structures in ^{10}Be. The bands shown by the double circles and the white squares have $(\pi^-_{3/2})^2$ and $(\pi^-_{3/2}\sigma^+_{1/2})$, respectively, while that with the white circles does $(\sigma^+_{1/2})^2$. The inset is a same figure but for the observed states[2,7]. The spins for the states in parentheses are tentatively suggested in Ref. [2].

dominant amplitudes around the respective local minimums in the adiabatic energy surfaces A, B and C. Therefore, these solutions of the 0^+_1, 0^+_2 and 0^+_3 states are concluded to have the molecular-orbitals configuration of $(\pi^-_{3/2})^2$, $(\sigma^+_{1/2})^2$ and $(\pi^-_{1/2})^2$, respectively [1].

To see band structures in ^{10}Be, we solve GCM Eq. (3) for other spins with a natural parity. The calculated bands are shown in the right panel of Fig. 1. The moment of inertia of individual bands is well reproduced. Furthermore, our model predicts the existence of the higher spin states which were suggested by a recent experiment [2]. In the states shown by the solid diamond and the solid circle, we find the enhancement of the $[\alpha$+$^6\mathrm{He}_{g.s.}]_{L=1}$ and $[\alpha$+$^6\mathrm{He}(2^+_1)]_{L=4}$ state, respectively. In addition to the three bands, we identify the several excited states in the higher energy region (white diamonds). The quantitative analysis on such states including their decay width will be given in forthcoming papers.

We have also calculated the adiabatic energy surfaces of ^{12}Be with

$J^\pi=0^+$ and compared them with the surfaces of the cluster states of α+^{8}He, ^{5}He+^{7}He, ^{6}He+^{6}He. We find that, in $S \geq 6$ fm, the calculated energy surfaces are completely the same as those of cluster states, while they deviate from the cluster's surfaces. In the third excited surface, however, the component of the $^6\mathrm{He}_{g.s.}$+$^6\mathrm{He}_{g.s.}$ cluster state is enhanced even if the distance S becomes small.

4. Summary and discussion

In summary, we proposed a generalized two-center cluster model (GTCM) and discussed its application to the ^{10}B and ^{12}Be. The adiabatic energy surfaces depending on the α–α distance were calculated. The adiabatic eigenstates have the molecular orbital configuration at an internal region, while they becomes the cluster states at an external one. The middle distances correspond to the transitional region having an intermediate coupling-scheme between the internal regions and the external ones.

Finally, we solved the coupling between the relative motions of clusters and the intrinsic motion of valence neutrons. The calculated bands of ^{10}Be reproduce the moment of inertia of the observed bands. In addition, our model predicts the possible appearance of the $[\alpha+^6\mathrm{He}(0_1^+)]_{L=1}$ and $[\alpha+^6\mathrm{He}(2_1^+)]_{L=4}$ cluster-structures in the excited 1_2^- and the lowest 6^+ states, respectively, which have not been discussed in previous studies [1,5,6].

In conclusion, we can say that GTCM well describes the low-lying molecular orbitals obtained by other theoretical models [1,5,6]. Furthermore, this model naturally reproduce the asymptotic cluster states in an equal footing. These results indicate that the present GTCM is applicable to the study of low-lying and high-lying states in Be-isotopes. A systematic studies of Be isotopes are now under progress.

References

1. N. Itagaki and S. Okabe, Phys. Rev. C **61**, 044306 (2000) ; N. Itagaki, S. Okabe and K. Ikeda, Phys. Rev. C **62**, 034301 (2000), and references therein.
2. M. Freer *et al.*, Phys. Rev. Lett. **82**, 1383 (1999); Phys. Rev. C **63**, 034301 (2001), and references therein.
3. A. Saito *et al.*, Suppl. Prog. Theor. Phys., **146**, 615 (2003).
4. H. Horiuchi *et al.*, Suppl. Prog. Theor. Phys. 62, 1 (1977) and references therein.
5. Y. Kanada-En'yo, H. Horiuchi and A. Dote Phys. Rev. C **60**, 064304 (1999).
6. Y. Ogawa *et al.*, Nucl. Phys. **A673**, 122 (2000).
7. J. A. Liendo *et al.*, Phys. Rev. C **65**, 034317 (2002).

Heavy exotic nuclei

This page intentionally left blank

FRONTIERS OF NUCLEAR STRUCTURE RESEARCH AT GSI — SOME NEW DEVELOPMENTS

G. MÜNZENBERG

Gesellschaft für Schwerionenforschung (GSI) mbH, Planckstr. 1, 64291 Darmstadt, Germany
and Johannes Gutenberg - Universität Mainz, D-55128 Mainz, Germany
E-mail: g.muenzenberg@gsi.de

In this contribution one example of challenging new experimental developments will be presented: direct mass measurements in the GSI experimental storage ring. The exploration of the nuclear mass surface in exotic regions gives first information on the location and persistence of nuclear shells far-off stability and isospin effects e.g. on the pairing strength. An outline of the the recently approved GSI project for an extended new synchrotron facility including an overview over the experimental program, new experimental developments, and the perspectives for nuclear structure research is given.

1. INTRODUCTION

GSI research is based on a system of accelerators for heavy ions of all chemical elements of the periodic table ranging from protons to uranium[1]. The UNIversal Linear ACcelerator (UNILAC) is used for near Coulomb-barrier energies and as injector for the heavy-ion synchrotron (SIS). The energy limit for uranium is above 1 AGeV. A unique instrument is the Experimental Storage Ring (ESR) which can store and cool heavy ions.

The advantage of the storage ring compared to ion traps is the ability to store beams of a large number of different nuclides in various ionic charge states[2]. Direct mass measurements in storage rings are the ideal tool for systematic studies e.g. mapping of the mass surface to get a first overview on the evolution of nuclear structure towards the limits of nuclear stability, best suited to explore isospin effects.

2. DIRECT MASS MEASUREMENTS IN THE STORAGE RING

The nuclides of interest are produced by fragmentation of relativistic heavy ions in peripheral collisions or by fission of relativistic ^{238}U. Typical projectile energies for storage-ring experiments are 600 AMeV to 900 AMeV. The nuclides of interest are separated in-flight by the FRS and injected into the experimental storage ring with their full energy. Optionally beam cocktails with definite number of isotopes or mono isotopic beams can be provided[4]. After injection into the ring the nuclei are stored and electron-cooled to momentum spreads of the order of 10^{-6}. The quality of the cooling finally determines the mass resolution[5]. The revolution frequency of the coasting ions is $10^6/s$. The Schottky noise signal is measured and Fourier transformed to obtain the mass (or more precisely, the mass over charge ratio). The cooling time of about 10 s limits this method to long-lived species[2]. Operating the storage ring in a different ion optical mode, so that the beam trajectories become isochronuous, permits to use the ring as a large time-of-flight spectrometer. The flight time of the ions which make 100 to 1000 turns is measured with pickups using thin carbon foils and secondary-electron detection[3]. Half-lives of the order of microseconds become accessible. An overview over the measured nuclides is displayed in Fig. 1. Nuclei which have been measured for the first time at GSI are indicated. They extend the region of known masses by more than 10%.

Schottky mass spectroscopy permits the measurement even of single ions as shown in the inset. The precision is of the order of 30 keV. Masses of 350 nuclides have been determined with a precision of 30 keV for the first time. Fig. 2 shows as an example a portion of a mass spectrum obtained with electron cooled fragments produced by fragmentation of ^{209}Bi. Known and unknown masses are well mixed to guarantee a precise calibration. First experiments with the time-of flight method gave resolutions which are lower by about one order of magnitude.

3. COMPARISON TO PREDICTIONS

The wealth of the GSI data allows a large-scale comparison between experiment and prediction. Fig. 3 shows as an example the comparison between experiment and prediction over a large part of the nuclear chart[7]. The example shows a self consistent Hartree-Fock BCS calculation[8] using the Skyrme force MSk7. The averaged precision taking only our 310 new or improved masses is 960 KeV. Please note that the figure shows the absolute

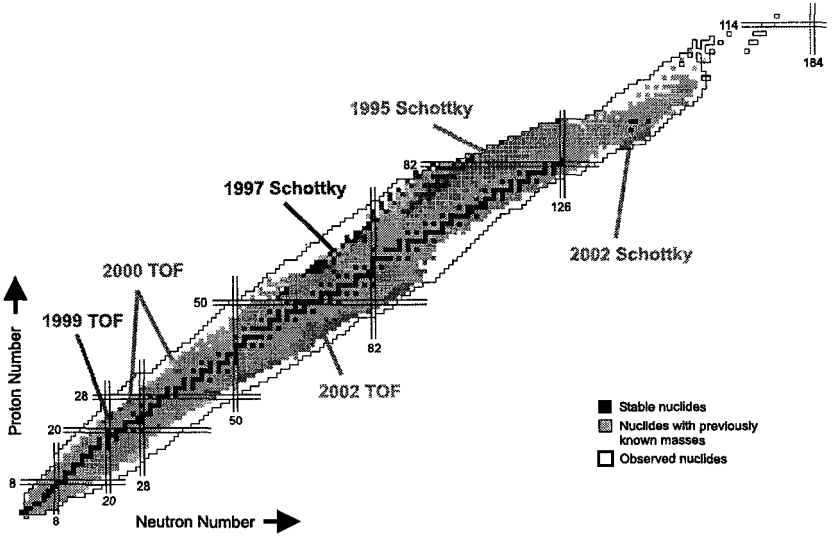

Figure 1. The nuclear chart with the new masses obtained from the FRS-ESR experiments.

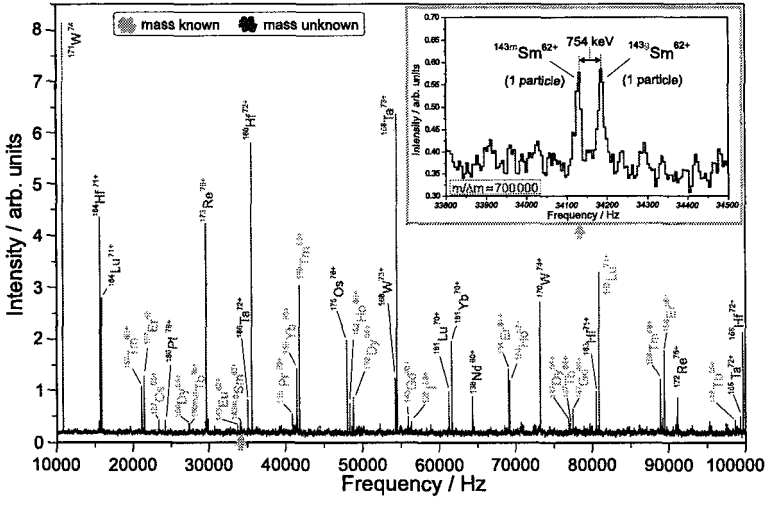

Figure 2. Portion of a mass spectrum of electron cooled projectile fragments stored in the ESR. The inset demonstrates the resolving power of this method.

deviations. Large discrepancies are observed near the $Z = 82$ proton shell. They are as big as +2 MeV. Deviations up to - 2 MeV, of opposite sign,

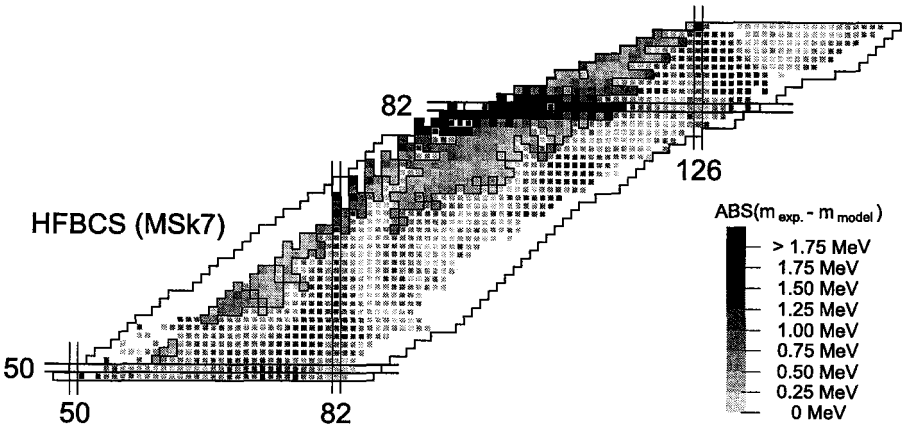

Figure 3. Comparison of the experimental masses to the prediction of a self-consistent model. The masses measured at GSI are marked with with squares, the gray tone indicates the absolute value of the deviation from theory.

are observed in the Ytterbium region ($Z = 70$) more close to stability in the transition region between the N = 82 and N = 126 shell closures.

Fig. 4 shows an investigation of the strength of the lead proton shell from beyond the neutron shell closure at $N = 126$ towards the proton dripline. The shell strength has been obtained from the double differential two - proton separation energies δ_{2p} according to Koopman's rule. The value for δ_{2p} drops by a factor of two from more than 6 MeV at the closed neutron shell $N = 126$ to below 3 MeV for $N = 100$, which suggests a shell quenching[9]. A theoretical investgation[10] however shows that the data can be reproduced with a constant shell gap of close to -10 MeV as seen in the figure. The reason for the decrease in separation energies in presence of an almost constant shell gap is that the nuclear structure in this region changes fast.

Very recently the isospin dependence of the neutron and proton pairing strength has been investigated. The pairing strength for neutrons as well as for protons increases strongly towards the proton dripline, an effect not predicted by theoretical models[11] as shown in Fig. 6, where the data for the doubly even hafnium isotopes are compared to the Finite Rage Liquid Drop Model (FRLDM)[12] and to Hartree-Fock Bogolubov (HFB) and HFBCS calculations. It is interesting to note that both, the neutron as well as the proton pairing increase strongly towards the proton dripline. Neither the

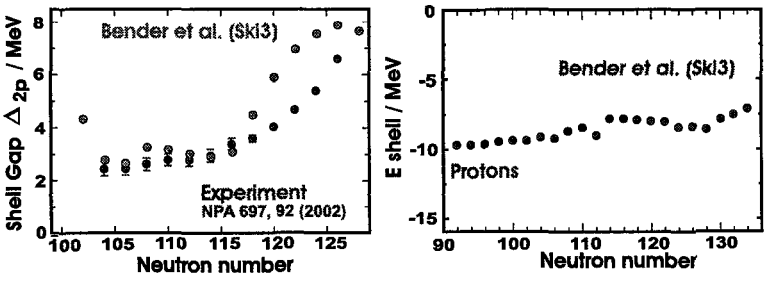

Figure 4. The lead proton shell. Left panel: Comparison of experiment (black dots) and theory (grey dots). Right panel: Calculated shell corrections of Pb isotopes.

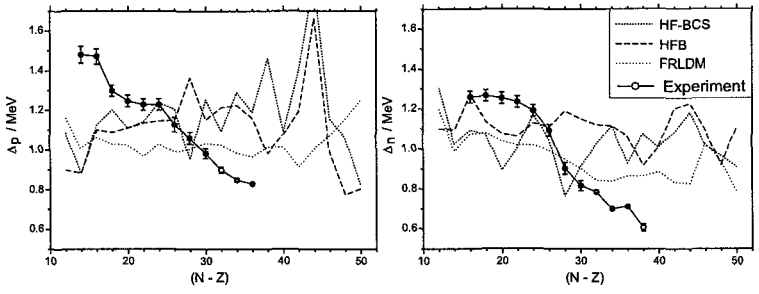

Figure 5. The pairing gap energies for doubly even hafnium isotopes. The experimental data (dots) are compared to macroscopic - microscopic and self-consistent Hartree-Fock calculations. Left panel: proton gap, right panel: neutron gap.

macroscopic-Microscopic calculations nor the self consistent models contain any isospin dependence of the pairing gap energy[7].

In forthcoming experiments regions around closed shell as well as along the cosmic nucleosynthesis paths including the rp- the r- process will be measured.

4. THE NEXT GENERATION FACILITY

The prerequisite to access more exotic species and to approach the limits of nuclear stability is a new generation of powerful heavy-ion accelerators which can deliver intense beams of all stable isotopes - including the rare ones - of all natural chemical elements. The future GSI facility will be a multipurpose facility, using the experience in parallel operation for several experiments gained with the existing SIS18. The accelerator system is

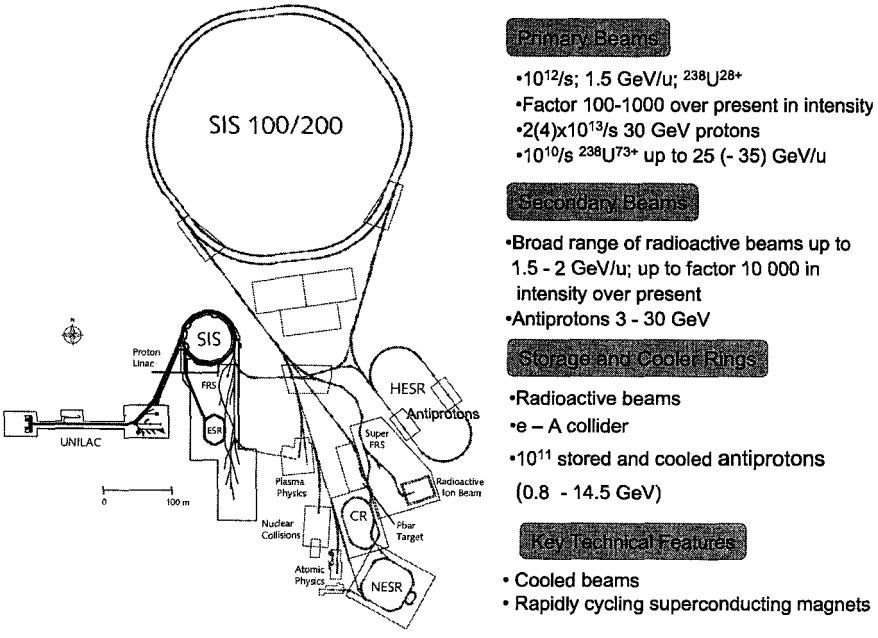

Figure 6. The proposed GSI facility with the double-ring synchrotron, the storage ring complex and the super FRS for nuclear structure research. The existing UNILAC-SIS18 serve as injector

based on a super conducting double-ring synchrotron system of 100 Tm and 200 Tm[13]. The 100 Tm synchrotron is fast cycling to achieve a high duty factor providing intense beams for the production of unstable nuclei for structure research. The 200 Tm machine can be used as stretcher ring to provide large duty factors for slow extraction.

For exotic beam production the new facility will provide beam intensities of the order of 10^{12}/s for all natural elements of the periodic table at energies around 1 AGeV. The high primary beam intensity is required to access exotic new regions, to allow for detailed structure studies of sufficiently exotic species, and to open the new field of reaction studies with unstable nuclei in storage rings. The high beam energy is necessary for clean separation of heavy elements and fission products. An improved multi-stage super conducting fragment separator of large acceptance adapted to the

large phase space of fission fragments, the "Super FRS", provides beams for three experimental areas[14] as shown in Fig. 6:

- A low energy branch for decay and in-beam studies,
- A high energy branch for reaction studies at full energy,
- A ring branch for the storage-cooler ring system.

The storage-ring system comprises an accumulator for in-flight separated projectile- and fission fragments with fast stochastic cooling, an experimental storage ring, an internal target for reactions at with low momentum transfer and highest precision, and a small intersecting electron ring for structure studies.

This next generation facility will allow to proceed further to the limits of the existence of nuclear matter. New experimental methods for structure research will allow to investigate the many facets of nuclear structure. New probes will give new access to hitherto unknown and new facets of the atomic nucleus. Systematic studies of selected and most relevant features of the atomic nucleus, starting from the light few-body systems to the heavy multi-nucleon systems will help us to understand it as the building block of elementary matter.

References

1. www.gsi.de
2. T. Radon, H. Geissel, G. Münzenberg et al., *Nucl. Phys. A* **677**, 75 (2000)
3. M. Matos, Thesis Univ. Giessen, under preparation
4. H. Geissel, G. Münzenberg and K. Riisager, *Ann. Rev. Nucl. Part. Sci.* **45**, 163 (1995)
5. M. Steck et al., *Phys. Rev. C* **77**, 3808 (1996)
6. P. Ring, priv. comm. 2003
7. Yu. A. Litvinov, thesis Univ Giessen and GSI report, 2003
8. S. Goriely et al., *At. Data Nucl. Data Tables* **77**, 311 (2001)
9. Yu. A. Novikov et al., *Nucl. Phys. A* **697**, 92 (2002)
10. M. Bender et al., *Eur. Phys. J. A* **14**, 23 (2002)
11. Yu. A. Novikov, priv. comm 2003 *Atomic Data Nuclear Data Tables* **39**, 213 (1988)
12. P. Möller and. J. R. Nix, *J. Phys. G* **20**, 1681 (1994)
13. Conceptual design report for "An International Accelerator Facility for Ions and Antiprotons", GSI, Darmstadt 2002, WWW.gsi.de available as CD-rom
14. H. Geissel et al., *Nucl. Instr. Meth. B* **204**, 71 (2003)

STRUCTURE OF EXOTIC NUCLEI

J. DOBACZEWSKI[1-3], N. MICHEL[2-4], W. NAZAREWICZ[1-3],
M. PŁOSZAJCZAK[5], M.V. STOITSOV[2-4,6]

[1] *Institute of Theoretical Physics, Warsaw University, ul. Hoża 69, PL-00681, Warsaw, Poland*

[2] *Department of Physics and Astronomy, The University of Tennessee, Knoxville, Tennessee 37996*

[3] *Physics Division, Oak Ridge National Laboratory, P.O. Box 2008, Oak Ridge, Tennessee 37831*

[4] *Joint Institute for Heavy Ion Research, Oak Ridge, Tennessee 37831*

[5] *Grand Accélérateur National d'Ions Lourds (GANIL), CEA/DSM - CNRS/IN2P3, BP 55027, F-14076 Caen Cedex 05, France*

[6] *Institute of Nuclear Research and Nuclear Energy, Bulgarian Academy of Sciences, Sofia-1784, Bulgaria*

The progress in the modeling of exotic nuclei with an extreme neutron-to-proton ratio is discussed. Two topics are emphasized: (i) the quest for the universal microscopic nuclear energy density functional and (ii) the progress in the continuum shell model.

1. Introduction

The goal of nuclear structure theory is to build a unified microscopic framework in which bulk nuclear properties (including masses, radii, and moments, structure of nuclear matter), nuclear excitations (including a variety of collective phenomena), and nuclear reactions can all be described. While this goal is extremely ambitious, it is no longer a dream. Indeed, hand in hand with experimental developments in the radioactive nuclear beam (RNB) experimentation, a qualitative change in theoretical modeling is taking place. Due to the influx of new ideas and the progress in computer technologies and numerical algorithms, nuclear theorists have been

quite successful in solving various pieces of the nuclear puzzle.

During recent years, we have witnessed substantial progress in many areas of theoretical nuclear structure. The Effective Field Theory (EFT) has enabled us to construct high-quality NN and NNN bare interactions consistent with the chiral symmetry of QCD[1,2]. New effective interactions in the medium have been developed which, together with a powerful suite of *ab-initio* approaches, provide a quantitative description of light nuclei[3,4,5,6,7]. For heavy systems, *global* modern shell-model approaches[8,9,10,11] and self-consistent mean-field methods[12,13,14] offer a level of accuracy typical of phenomenological approaches based on parameters *locally* fitted to the data. By exploring connections between models in various regions of the chart of the nuclides, nuclear theory aims to develop a comprehensive theory of the nucleus across the entire nuclear landscape.

From a theoretical point of view, short-lived exotic nuclei far from stability offer a unique test of those aspects of the many-body theory that depend on the isospin degrees of freedom[15]. The challenge to microscopic theory is to develop methodologies to reliably calculate and understand the origins of unknown properties of new physical systems, physical systems with the same ingredients as familiar ones but with totally new and different properties. The hope is that after probing the limits of extreme isospin, we can later go back to the valley of stability and improve the description of normal nuclei.

2. Towards the Universal Nuclear Energy Density Functional

For medium-mass and heavy nuclei, a critical challenge is the quest for the universal energy density functional, which will be able to describe properties of finite nuclei (static properties, collective states, large-amplitude collective motion) as well as extended asymmetric nucleonic matter (e.g., as found in neutron stars). Self-consistent methods based on the density functional theory (DFT) have already achieved a level of sophistication and precision which allows analyses of experimental data for a wide range of properties and for arbitrarily heavy nuclei. For instance, self-consistent Hartree-Fock (HF) and Hartree-Fock-Bogoliubov (HFB) models are now able to reproduce measured nuclear binding energies with an impressive rms error of $\sim$700 keV [12,16,17]. However, much work remains to be done. Developing a universal nuclear density functional will require a better understanding of the density dependence, isospin effects, and pairing, as well

as an improved treatment of symmetry breaking effects and many-body correlations.

2.1. *Density Functional Theory and Skyrme HFB*

The density functional theory[18,19] has been an extremely successful approach for the description of ground-state properties of bulk (metals, semiconductors, and insulators) and complex (molecules, proteins, nanostructures) materials. It has also been used with great success in nuclear physics[20,21,22,23]. The main idea of DFT is to describe an interacting system of fermions via its densities and not via its many-body wave function. The energy of the many body system can be written as a density functional, and the ground state energy is obtained through the variational procedure.

The nuclear energy density functional appears naturally in the Skyrme-HFB theory[24,25], or in the local density approximation (LDA)[22,26], in which the functional depends only on local densities, and on local densities built from derivatives up to the second order. In practice, a number of local densities are introduced: nucleonic densities, kinetic densities, spin densities, spin-kinetic densities, current densities, tensor-kinetic densities, and spin-current densities. If pairing correlations are considered, the number of local densities doubles since one has to consider both particle and pairing densities.

In the case of the Skyrme effective interaction, as well as in the framework of the LDA, the energy functional is a three-dimensional spatial integral of local energy density that is a real, scalar, time-even, and isoscalar function of local densities and their first and second derivatives. In the case of no proton-neutron mixing, the construction of the most general energy density that is quadratic in one-body local densities can be found in Ref.[27]. With the proton-neutron mixing included, the construction can be performed in an analogous manner[28].

2.2. *From finite nuclei to bulk nucleonic matter*

In the limit of the infinite nuclear matter, the density functional is reduced to the nuclear equation of state (EOS). The EOS plays a central role in nuclear structure and in heavy-ion collisions. It also determines the static and dynamical behavior of stars, especially in supernova explosions and in neutron star stability and evolution. Unfortunately, our knowledge of the EOS, especially at high densities and/or temperatures, is very poor. Many insights about the density dependence of the EOS, in particular the den-

sity dependence of the symmetry energy, can be obtained from microscopic calculations of neutron matter using realistic nucleon-nucleon forces[29,30,31]. Those results will certainly be helpful when constraining realistic energy density functionals. Another constraint comes form measurements of neutron skin and radii[32,33]. Recently, a correlation between the neutron skin in heavy nuclei and the derivative of the neutron equation of state has been found[34,33,35], which provides a way of giving a stringent constraint on the EOS if the neutron radius of a heavy nucleus is measured with sufficient accuracy.

A serious difficulty when extrapolating from finite nuclei to the extended nuclear matter is due to the diffused neutron surface in neutron-rich nuclei. As discussed in Ref.[36], the nuclear surface cannot simply be regarded as a *layer of nuclear matter at low density.* In this zone the gradient terms are as important in defining the energy relations as those depending on the local density.

2.3. *The First Step: Microscopic Mass Table*

Microscopic mass calculations require a simultaneous description of particle-hole, pairing, and continuum effects – the challenge that only very recently could be addressed by mean-field methods. A new development[14] is the solution of deformed HFB equations by using the local-scaling point transformation [37,38]. A representative example of deformed HFB calculations, recently implemented using the parallel computational facilities at ORNL, is given in Fig. 1. By creating a simple load-balancing routine that allows one to scale the problem to 200 processors, it was possible to calculate the entire deformed even-even mass table in a single 24 wall-clock hour run (or approximately 4,800 processor hours).

Future calculations will take into account a number of improvements, including (i) implementation of the exact particle number projection before variation[39]; (ii) better modeling of the density dependence of the effective interaction by considering corrections beyond the mean-field and three-body effects[40], the surface-peaked effective mass[41,17], and better treatment of pairing[36]; (iii) proper treatment of the time-odd fields [42]; and (iv) inclusion of dynamical zero-point fluctuations associated with the nuclear collective motion [43,44,45]. As far as the density dependence is concerned, many insights can be obtained from the EFT[46]. The resulting universal energy density functional will be fitted to nuclear masses, radii, giant vibrations, and other global nuclear characteristics.

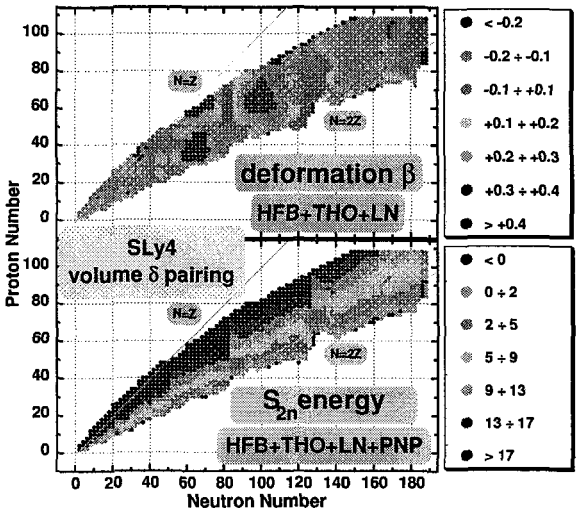

Figure 1. Quadrupole deformations β (upper panel) and two-neutron separation energies S_{2n} in MeV (lower panel) of particle-bound even-even nuclei calculated within the HFB+THO method with Lipkin-Nogami correction followed by exact particle number projection. The Skyrme SLy4 interaction and volume contact pairing were used. (From Ref. [14].)

Finally, let us remark that a realistic energy density functional does not have to be related to any given effective force. This creates a problem if a symmetry is spontaneously broken. While the projection can be carried out in a straightforward manner for energy functionals that are related to a two-body potential, the restoration of spontaneously broken symmetries of a general density functional poses a conceptional dilemma[47,48].

3. Continuum Shell-Model

The major theoretical challenge in the microscopic description of nuclei, especially weakly bound ones, is the rigorous treatment of both the many-body correlations and the continuum of positive-energy states and decay channels. The importance of continuum for the description of resonances is obvious. Weakly bound states cannot be described within the closed quantum system formalism since there always appears a virtual scattering into the continuum phase space involving intermediate scattering states. The consistent treatment of continuum in multi-configuration mixing calculations is the domain of the continuum shell model (CSM) (see Ref.[49] for a review). In the following, we briefly mention one recent development in the

area of the CSM, the so-called Gamow Shell Model.

3.1. *Gamow Shell Model*

Recently, the multiconfigurational CSM in the complete Berggren basis, the so-called Gamow Shell Model (GSM), has been formulated [50,51]. The s.p. basis of GSM is given by the Berggren ensemble [52] which contains Gamow states (or resonant states and the non-resonant continuum). The resonant states are the generalized eigenstates of the time-independent Schrödinger equation which are regular at the origin and satisfy purely outgoing boundary conditions. They correspond to the poles of the S matrix in the complex energy plane lying on or below the positive real axis.

There exist several completeness relations involving resonant states [53]. In the heart of GSM is the Berggren completeness relation:

$$\sum_n |u_n\rangle\langle\tilde{u}_n| + \int_{L_+} |u_k\rangle\langle\tilde{u}_k| dk = 1 \quad , \tag{1}$$

where $|u_n\rangle$ are the Gamow states (both bound states and the decaying resonant states lying between the real k-axis and the complex contour L_+) and $|u_k\rangle$ are the scattering states on L_+. (For neutrons, $l = 0$ resonances do not exist and, sometimes, one has to include the anti-bound $l = 0$ state in the Berggren completeness relation [54,55]. This implies a modification of the complex contour L_+, which has to enclose this pole.) As a consequence of the analytical continuation, the resonant states are normalized according to the squared radial wave function and not to the modulus of the squared radial wave function. In practical applications, one has to discretize the integral in (1). Such a discretized Berggren relation is formally analogous to the standard completeness relation in a discrete basis of L^2-functions and, in the same way, leads to the eigenvalue problem $H|\Psi\rangle = E|\Psi\rangle$. However, as the formalism of Gamow states is non-hermitian, the matrix H is complex symmetric.

One of the main challenges in the CSM is the determination of many-body resonances because of a huge number (continuum) of surrounding many-body scattering states. A practical solution to this problem has been proposed in Refs.[50,51]. It is based on the fact that resonances have significant overlap with many-body states calculated in the pole approximation in which the Hamiltonian is diagonalized in a smaller basis consisting of s.p. resonant states only. The eigenstates representing the non-resonant background tend to align along regular trajectories in the complex energy plane. As discussed in Refs. [56,54], the shapes of these trajectories directly reflect

the geometry of the contour in the complex k-plane. In the two-particle case, this information can be directly used to identify the resonance states. However, this is no longer the case if more than two particles are involved.

In the shell-model calculations with Gamow states, only radial matrix elements are treated differently as compared to the standard shell model. This means that the angular momentum and isospin algebra do not change in the GSM. However, expectation values of operators in the many-body GSM states have both real and imaginary parts. As discussed in Refs.[57,58,59], the imaginary part gives the uncertainty of the average value. It is also worth noting that, in most cases, the real part of the matrix element is influenced by the interference with the non-resonant background.

Contrary to the traditional shell model, the effective interaction of GSM cannot be represented as a single matrix calculated for all nuclei in a given region. The GSM Hamiltonian contains a real effective two-body force expressed in terms of space, spin, and isospin coordinates. The matrix elements involving continuum states are strongly system-dependent and they fully take into account the spatial extension of s.p. wave functions.

In the first applications of the GSM, a schematic zero-range surface delta force was taken as a residual interaction. As a typical example, the calculated level scheme of ^{19}O is displayed in Fig. 2 together with the selected E2 transition rates. It is seen that the electromagnetic transition rates involving unbound states are complex.

The first applications of the GSM to the oxygen and helium isotopes look very promising[50,51]. The beginning stages of a broad research program has begun which involves applications of GSM to halo nuclei, particle-unstable nuclear states, reactions of astrophysical interest, and a variety of nuclear structure phenomena. The important step will be to develop effective finite-range interactions to be used in the GSM calculations. One would also like to optimize the path of integration representing the non-resonant continuum. In order to optimize the GSM configuration space, we intend to carry out GSM calculations in the Hartree-Fock basis. To this end, a Hartree-Fock program in the Gamow basis has been developed (GHF) [60]. The GHF method will also be applied to describe nuclear vibrational states in the continuum RPA (or QRPA) framework.

4. Conclusions

The main objective of this presentation was to discuss the opportunities in nuclear structure that have been enabled by studies of exotic nuclei with

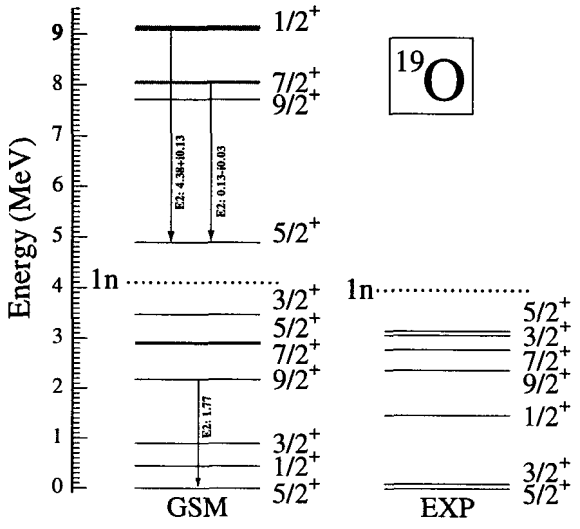

Figure 2. The GSM level scheme of ^{19}O calculated in the full *sd* space of Gamow states and employing the discretized (10 points) $d_{3/2}$ non-resonant continuum. The dashed lines indicate experimental and calculated one-neutron emission thresholds. As the number of states becomes large above the one-neutron emission threshold, only selected resonances are shown. Selected E2 transitions are indicated by arrows and the calculated E2 rates (all in W.u.) are given (from Ref. [51]).

extreme neutron-to-proton ratios. New-generation data will be crucial in pinning down a number of long-standing questions related to the effective Hamiltonian, nuclear collectivity, and properties of nuclear excitations.

One of the major challenges is to develop the "universal" nuclear energy density functional that will describe properties of finite nuclei as well as extended asymmetric nucleonic matter as found in neutron stars. This quest is strongly driven by new data on nuclei far from stability, where new features, such as weak binding and altered interactions, make extrapolations of existing models very unreliable.

Another major task is to tie nuclear structure directly to nuclear reactions within a coherent framework applicable throughout the nuclear landscape. From the nuclear structure perspective, the continuum shell model is the tool of choice that will be able to describe new phenomena in discrete/continuum spectroscopy of exotic nuclei.

Acknowledgments

This work was supported in part by the U.S. Department of Energy under Contract Nos. DE-FG02-96ER40963 (University of Tennessee) and DE-AC05-00OR22725 with UT-Battelle, LLC (Oak Ridge National Laboratory), by the Polish Committee for Scientific Research (KBN), and by the National Science Foundation Contract No. 0124053 (U.S.-Japan Cooperative Science Award).

References

1. D.R. Entem and R. Machleidt, Phys. Rev. C **68**, 041001 (2003).
2. W. Gloeckle et al., nucl-th/0312063; and these proceedings.
3. S.C. Pieper, K. Varga, and R.B. Wiringa, Phys. Rev. **C66**, 044310 (2002).
4. R.B. Wiringa and S.C. Pieper, Phys. Rev. Lett. **89**, 182501 (2002).
5. B.R. Barrett, P. Navratil, and J.P. Vary, Nucl. Phys. A **704**, 254c (2002).
6. P. Navratil and W.E. Ormand, Phys. Rev. C **68**, 034305 (2003).
7. K. Kowalski et al., nucl-th/031008.
8. E. Caurier, F. Nowacki, and A. Poves, Eur. Phys. J. A **15**, 145 (2002).
9. M. Honma et al., Phys. Rev. C **65**, 061301 (2002); Nucl. Phys. A **704**, 134c (2002).
10. K. Langanke and G. Martinez-Pinedo, Nucl. Phys. A **704**, 154c (2002).
11. K. Langanke, D.J. Dean, and W. Nazarewicz, Nucl. Phys. A **728**, 109 (2003).
12. S. Goriely et al., Phys. Rev. C **66**, 024326 (2002).
13. M. Bender, P.-H. Heenen, and P.-G. Reinhard, Rev. Mod. Phys. **75**, 121 (2003).
14. M.V. Stoitsov et al., Phys. Rev. C **68**, 054312 (2003).
15. J. Dobaczewski and W. Nazarewicz, Phil. Trans. R. Soc. Lond. A **356**, 2007 (1998).
16. M. Samyn et al., Nucl. Phys. A **700**, 142 (2002).
17. S. Goriely et al., Phys. Rev. C **68**, 054325 (2003).
18. P. Hohenberg and W. Kohn. Phys. Rev. B **76**, 6062 (1964); M. Levy. Proc. Nat. Acad. Sci. **76**, 6062 (1979).
19. W. Kohn, L.J. Sham, Phys. Rev. A **140**, 1133 (1965).
20. A.B. Migdal, *Theory of Finite Fermi Systems and Applications to Atomic Nuclei* (Interscience, New York, 1967).
21. J.W. Negele, Phys. Rev. **C1**, 1260 (1970).
22. J.W. Negele and D. Vautherin, Phys. Rev. **C5**, 1472 (1972).
23. M. Brack and R.K. Bhaduri, *Semiclassical Physics* (Addison Wesley, Reading 1997).
24. T.H.R. Skyrme, Nucl. Phys. **9**, 615 (1959).
25. D. Vautherin and D.M. Brink, Phys. Rev. **C5**, 626 (1972).
26. P. Ring and P. Schuck, *The Nuclear Many-Body Problem* (Springer-Verlag, Berlin, 1980).
27. J.Dobaczewski and J.Dudek, Acta Phys. Pol. **B27**, 45 (1996).

28. E. Perlińska et al., nucl-th/0310005; accepted to Phys. Rev. **C**.
29. B.A. Friedman and V.R. Pandharipande, Nucl. Phys. **A361**, 502 (1981).
30. J. Morales, V.R. Pandharipande, and D.G. Ravenhall, Phys. Rev. C **66**, 054308 (2002).
31. J. Carlson et al., nucl-th/0302041 (2003).
32. C. Horowitz and J. Piekarewicz, Phys. Rev. Lett. **86**, 5647 (2001).
33. R.J. Furnstahl, Nucl. Phys. A **706**, 85 (2002).
34. S. Typel and B.A.Brown, Phys. Rev. C **64**, 027302 (2001).
35. A.E.L. Dieperink, D. Van Neck, Y. Dewulf, and V. Rodin, nucl-th/0312012.
36. J. Dobaczewski, W. Nazarewicz, and M. V. Stoitsov, Eur. Phys. J. A **15**, 21 (2002).
37. M.V. Stoitsov, W. Nazarewicz, and S. Pittel, Phys. Rev. **C58**, 2092 (1998).
38. M.V. Stoitsov et al., Phys. Rev. **C61**, 034311 (2000).
39. J.A. Sheikh and P. Ring, Nucl. Phys. A **665**, 71 (2000); J.A. Sheikh et al., Phys. Rev. C **66**, 044318 (2002).
40. T. Duguet and P. Bonche, Phys. Rev. C **67**, 054308 (2003).
41. M. Farine, J.M. Pearson, and F. Tondeur, Nucl. Phys. A **696**, 396 (2001).
42. M. Bender et al., Phys. Rev. **C65**, 054322 (2002).
43. P.-G. Reinhard, Z. Phys. **A285**, 93 (1978).
44. P.-G. Reinhard and K. Goeke, Rep. Prog. Phys. **50**, 1 (1987).
45. P.-G. Reinhard et al., Phys. Rev. **C60**, 014316 (1999).
46. S.J. Puglia, A. Bhattacharyya, and R.J. Furnstahl, Nucl. Phys. A **723**, 145 (2003).
47. A. Görling, Phys. Rev A **47**, 2783 (1993).
48. J.P. Perdew, A. Savin, and K. Burke, Phys. Rev A **51**, 4531 (1995).
49. J. Okołowicz, M. Płoszajczak, and I. Rotter, Phys. Rep. **374**, 271 (2003).
50. N. Michel et al., Phys. Rev. Lett. **89**, 042502 (2002).
51. N. Michel et al., Phys. Rev. **C67**, 054311 (2003).
52. T. Berggren, Nucl. Phys. **A109**, 265 (1968).
53. P. Lind, Phys. Rev. C **47**, 1903 (1993).
54. R. Id Betan et al., nucl-th/0307060.
55. G. Hagen, M. Hjorth-Jensen, and J.S. Vaagen, nucl-th/0303039.
56. R. Id Betan et al., Phys. Rev. Lett. **89**, 042501 (2002).
57. T. Berggren, Phys. Lett. **B373**, 1 (1996).
58. C.G. Bollini et al., Phys. Lett. **B 382**, 205 (1996).
59. O. Civitarese, M. Gadella, and R.I. Betan, Nucl. Phys. **A660**, 255 (1999).
60. N. Michel et al., invited talk at the XXVIISymposium on Nuclear Physics, Jan. 5-8, 2004, Taxco, Guerrero, Mexico.

PROTON RADIOACTIVITY

LÍDIA S. FERREIRA

Centro de Física das Interacções Fundamentais, and Departamento de Física, Instituto Superior Técnico, Av. Rovisco Pais, P-1049-001 Lisboa, Portugal, email: flidia@ist.utl.pt

ENRICO MAGLIONE

Dip. di Fisica "G. Galilei" and INFN, Via Marzolo 8, I-35131 Padova, Italy, email: maglione@pd.infn.it

Proton radioactivity from deformed drip–line nuclei is discussed. It is shown how it is possible to describe all experimental data currently available for decay from ground and isomeric states, and fine structure of odd-even and odd–odd nuclei, within a consistent theoretical approach.

1. Introduction

Proton emission from exotic nuclei lying beyond the proton drip-line has been observed in recent experiments[1,2] in the region of $50 < Z < 82$, where the Coulomb barrier is very high. The emitted proton is trapped by the barrier in a resonance state which will decay by tunneling through the barrier for almost 80 fm, thus leading to quite narrow decay widths. Since the escape energy of the emitted proton is also very small, these resonances lie very low in the continuum, and correspond essentially to single particle excitations, in contrast with what happens in stable nuclei.

From the experimental point of view, proton radioactivity provides measurements of the separation energy of the proton, important to test mass formulae, and to map the proton drip-line. Using tagging techniques with the proton, it is possible to measure the decay spectrum of the decaying nucleus, data which is very difficult to obtain otherwise. On the theoretical side, it is a quite important tool to study nuclear structure on exotic nuclei far away from the stability valley.

Spherical[3] as well as deformed proton radioactive nuclei, even with large deformations[4] were observed, decaying mainly from the ground state, but

decay from isomeric excited states of the parent nucleus and fine structure[5] have also been observed.

Due to the single particle character of this decays, and the large potential energy barrier a simple WKB calculations can already give a good estimate of the experimental data for spherical nuclei. The purpose of this work is to show how decay from deformed nuclei can be studied as decay from a Nilsson resonance in a deformed system[6,7]. The parent nucleus can be treated in the strong coupling limit of the particle-rotor model[8], as a first approach. The inclusion[9] of Coriolis mixing, requires a proper treatment of the pairing residual interaction, leading to a unified interpretation of all available data on these emitters.

2. Decay widths for deformed proton emitters

2.1. *Adiabatic approach: the strong coupling limit*

The partial decay width can be determined from the overlap between the initial and final states. Since nuclei on the drip–line have a Fermi level very close or even immersed in the continuum, decay of odd–Z even–N nuclei has been interpreted, as decay from a single particle Nilsson resonance of the unbound core–proton system. The states close to the Fermi surface are the most probable ones for decay to occur. The wave function of the decaying proton, can than be obtained from the exact solution of the Schrödinger equation with a deformed mean field with deformed spin–orbit, imposing outgoing wave boundary conditions, as discussed in Ref[10,11]. The simplest approach to determine the wave function of the parent nucleus is to impose the strong coupling limit[8], where the nucleus behaves as a particle plus rotor with infinite moment of inertia.

Within these assumptions, if decay occurs to the ground state, only the component of the s.p. wave function with the same angular momentum as the ground state contributes, and the decay width becomes,

$$\Gamma_{l_p j_p}(r) = \frac{\hbar^2 k}{\mu(j_p + 1/2)} \frac{|u_{l_p j_p}(r)|^2}{|G_{l_p}(kr) + iF_{l_p}(kr)|^2} u^2_{K_i}, \qquad (1)$$

where F and G are the regular and irregular Coulomb functions, respectively, and $u_{l_p j_p}$ the component of the wave function with momentum j_p, equal to the spin of the decaying nucleus. The quantity $u^2_{K_i}$ is the probability that the single particle level in the daughter nucleus is empty, evaluated in the BCS approach.

In case of decay to the ground state of the daughter nucleus, angular momentum conservation leads to $j_p = J_i = K_i$, only one component of

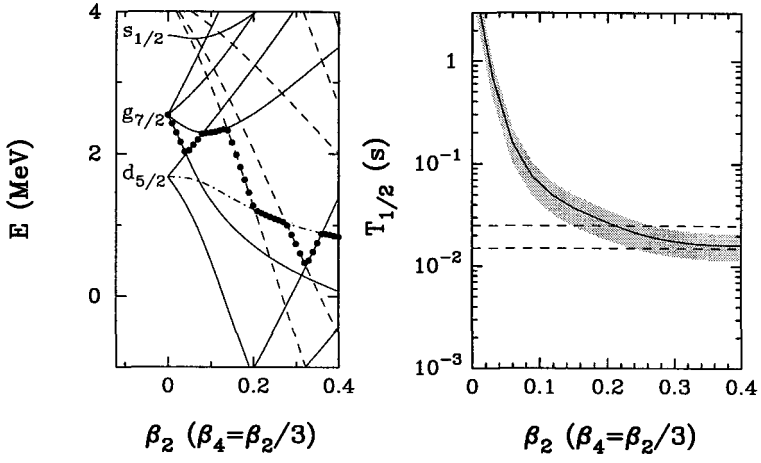

Figure 1. Proton Nilsson levels in ^{117}La (left part). The full circles represent the Fermi surface, the dashed lines the negative parity states, and the dashed-dotted line, the decaying state. A hexadecapole deformation $\beta_4 = \beta_2/3$ was included. Half-life for decay from the ground state of ^{117}La as a function of deformation (right side). The experimental value[12] is within the dashed lines.

the wavefunction is tested, and could even be very small. Decay to excited states, allow few combinations for $l_p j_p$ according to angular momentum coupling rules, and consequently different components of the parent wave function are then tested. Similar calculations were done within the coupled-channel Green's function model[4].

The decay width obtained from Eq. 1 depends on deformation, and is very sensitive to the wave function of the decaying state. Therefore, if it is able to reproduce the experimental value, will give clear information on the deformation and properties of the decaying state. The method is illustrated in Figure 1 for the proton emitter ^{117}La. The state $K = 3/2^+$ reproduces the experimental half-life for a deformation $\beta_2 \approx .2 - .3$, with a small hexadecapole contribution $\beta_4 = .1$, in close agreement with the theoretical predictions of Ref. [13].

Emission from deformed systems with an odd number of protons and neutrons can be discussed in a similar fashion[7]. However, in contrast with decay to ground state of odd-even nuclei where the proton is forced to escape with a specific angular momentum, many channels will be open due to the angular momentum coupling of the proton and daughter nucleus, $\vec{J}_d + \vec{j}_p$, giving the total width for decay as a sum of partial widths allowed by parity and momentum conservation. This dependence on the quantum numbers of

the unpaired neutron, gives to the neutron the important role of "influential spectator" contributing significantly with its angular momentum to the decay, thus allowing a determination of the neutron s.p. level.

We have applied[6,7,14,15] our model to all measured deformed proton emitters including isomeric decays. The experimental half-lives are perfectly reproduced by a specific state, with defined quantum numbers and deformation, thus leading to unambiguous assignments of the angular momentum of the decaying states. Extra experimental information provided by isomeric decay observed in ^{117}La, ^{141}Ho and ^{151}Lu, and fine structure in ^{131}Eu can also be successfully accounted by the model. The experimental half–lives for decay from the excited states were reproduced in a consistent way with the same deformation that describes ground state emission.

2.2. *Effect of Coriolis mixing and pairing residual interaction: the non–adiabatic quasi-particle approach*

As we have discussed, calculations within the strong coupling limit were able to reproduce the experimental results. According to this model, the rotational spectrum of the daughter nucleus collapses into the ground state.

The effect of a finite moment of inertia of the daughter nucleus on proton decay, was studied within the non-adiabatic coupled channel[16], and coupled-channel Green's function[17] methods, but the excellent agreement with experiment found in the adiabatic context was lost. The results differ by factors of three or four from the experiment, and even the branching ratio for fine structure decay is not reproduced[16,17,18]. The use of spherical spin–orbit in Ref.[16,18]is a strong handicap of their model. Decay rates in deformed nuclei, are extremely sensitive to small components of the wave function. The Coriolis interaction mixes different Nilsson wave functions, and can be responsible for strong changes in the decay widths. A correct treatment [9]of the pairing residual interaction in the BCS approach, can modify this mixing of states which should be considered between quasi-particle states instead of particle ones as used in Refs.[16,17,18]. Such non-adiabatic treatment of the Coriolis coupling, brings back the perfect agreement with data observed in the strong coupling limit.

3. Conclusions

We have shown how proton radioactivity from deformed nuclei can be well understood, as decay from single particle Nilsson resonances, evaluated exactly using single particle potentials that fit large sets of data on nuclear

properties. The rotational spectra of the daughter nucleus and the pairing residual interaction, are taken into account, leading to a treatment of the Coriolis coupling in terms of quasi–particles. All available experimental data on even–odd and odd–odd deformed proton emitters from the ground and isomeric states and fine structure, were accurately and consistently reproduced, identifying the decay level and deformation of the decaying nucleus, and also supporting previous predictions on nuclear structure properties of the emitter. For decay from odd–odd deformed nuclei, an important finding was the dependence of the final decay width on the quantum numbers of the unpaired neutron state which cannot be considered only a spectator, but contributes significantly with its angular momentum to the decay.

Acknowledgments

This work was supported by the Fundação de Ciência e Tecnologia (Portugal), Project: POCTI-36575/99.

References

1. P. J. Woods and C. N. Davids, Annu. Rev. Nucl. Part. Sci. **47** (1997) 541.
2. A. A. Sonzogni, Nuclear Data Sheets **95** (2002) 1.
3. S. Åberg, P. B. Semmes and W. Nazarewicz, Phys. Rev. **C56** (1997) 1762.
4. C. N. Davids, *et al.*, Phys. Rev. Lett. **80** (1998) 1849.
5. A. A. Sonzogni, *et al.*, Phys. Rev. Lett. **83** (1999) 1116.
6. E. Maglione, L. S. Ferreira and R. J. Liotta, Phys. Rev. Lett. **81** (1998) 538; Phys. Rev. **C59** (1999) R589.
7. L. S. Ferreira and E. Maglione, Phys. Rev. Lett. **86** (2001) 1721.
8. D. D. Bogdanov, V. P. Bugrov and S. G. Kadmenskii, Sov. J. Nucl. Phys. **52** (1990) 229.
9. G. Fiorin, E. Maglione and L. S. Ferreira, Phys. Rev. **C67** (2003) 054302.
10. L. S. Ferreira, E. Maglione and R. J. Liotta, Phys. Rev. Lett. **78** (1997) 1640.
11. L. S. Ferreira, E. Maglione, and D. Fernandes, Phys. Rev. **C65** (2002) 024323.
12. F. Soramel, *et al.*, Phys. Rev. **C63** (2001) 031304(R).
13. P. Möller, *et al.*, At. Data Nucl. Data Tab. **59** (1995) 185; ibd. **66** (1997) 131.
14. L. S. Ferreira and E. Maglione, Phys. Rev. **C61** (2000) 021304(R).
15. E. Maglione and L.S. Ferreira, Phys. Rev. **C61** (2000) 47307.
16. A. T. Kruppa, B. Barmore, W. Nazarewicz and T. Vertse, Phys. Rev. Lett. **84** (2000) 4549; B. Barmore, A. T. Kruppa, W. Nazarewicz and T. Vertse, Phys. Rev. **C62** (2000) 054315.
17. H. Esbensen and C. N. Davids, Phys. Rev. **C63** (2001) 014315.
18. W. Królas, *et al.*, Phys. Rev. **C65** (2002) 031303(R).

Mean-field methods and effective interactions

This page intentionally left blank

SOLUTION OF THE HFB CONTINUUM PROBLEM ON A 2-D LATTICE: NEUTRON-RICH AND DRIPLINE NUCLEI

V. E. OBERACKER, A.S. UMAR AND A. BLAZKIEWICZ

Department of Physics and Astronomy, Vanderbilt University, Nashville, Tennessee 37235, USA
E-mail: volker.e.oberacker@vanderbilt.edu

E. TERÁN

Physics Department, San Diego State University, San Diego, California 92182, USA

The Skyrme-HFB equations are solved in coordinate space on a 2-D lattice for deformed axially symmetric nuclei. Using B-Spline techniques, we focus on an accurate representation of the HFB continuum states for neutron-rich exotic nuclei. Results are presented for the sulfur isotope chain $^{34-52}S$ up to the two-neutron dripline. We also study the g.s. properties of neutron-rich heavier nuclei ($^{102,104}Zr$,^{152}Ce,^{156}Nd, and $^{158,160}Sm$) some of which exhibit very large prolate quadrupole deformations.

1. Introduction

We solve the Skyrme-HFB equations in coordinate space on a 2-D lattice for deformed neutron-rich exotic nuclei. The coordinate space method has the advantage that well-bound, weakly bound and (discretized) continuum states can be represented with the same numerical accuracy. Early 1-D calculations for spherical nuclei[1] have demonstrated that one needs continuum states with an equivalent single-particle energy up to 60 MeV to describe the ground state properties near the neutron dripline. Recently, we have solved for the first time the HFB continuum problem in two dimensions using Basis-Spline methods[2,3]. The novel feature of our HFB code is that it generates very accurately high-energy continuum states in 2-D which will be important for future lattice-based QRPA calculations of collective excited states. Alternatively, an expansion in a transformed harmonic oscillator basis has been used[4]. Current 3-D HFB codes in coordinate space[5,6] utilize an expansion of the quasiparticle wavefunctions in a truncated HF-basis

which is limited to continuum states up to about 5 MeV.

2. HFB equations in coordinate space

In coordinate space representation, the Skyrme-HFB Hamiltonian and the quasiparticle wavefunctions depend on the distance vector $\mathbf{r}$, spin projection $\sigma = \pm\frac{1}{2}$, and isospin projection $q = \pm\frac{1}{2}$

$$\begin{pmatrix} (h^q - \lambda) & \tilde{h}^q \\ \tilde{h}^q & -(h^q - \lambda) \end{pmatrix} \begin{pmatrix} \phi^q_{1,n} \\ \phi^q_{2,n} \end{pmatrix} = E_n \begin{pmatrix} \phi^q_{1,n} \\ \phi^q_{2,n} \end{pmatrix} \quad . \tag{1}$$

There are two types of quasiparticle spinor wavefunctions, ϕ_1 and ϕ_2, which determine the normal density and the pairing density.

Using cylindrical coordinates, we introduce a 2-D lattice (r_α, z_β). Via an expansion in B-Splines of order $M = 7$ or $M = 9$ we represent wavefunctions and derivative operators with high accuracy[7,8] on a relatively coarse grid with a lattice spacing of about 0.8 fm. While our current 2-D lattices are linear, an extension to nonlinear lattices is possible. The numerical solution of the HFB equations results in a set of quasiparticle wavefunctions at the lattice points. The corresponding quasiparticle energy spectrum E_n contains both bound and (discretized) continuum states. We diagonalize the HFB Hamiltonian separately for fixed isospin projection q and fixed angular momentum projection $j_z = 1/2, 3/2, ..., 21/2$.

In all calculations we utilize the Skyrme (SLy4) effective N-N interaction in the p-h channel and a delta interaction in the p-p channel (pairing strength $V_0 = -170.0\ MeVfm^3$), with an equivalent s.p. energy cutoff parameter $\epsilon_{max} = 60$ MeV.

3. Quasiparticle energies and spectral distribution of pairing density

In fig.1 we show the quasiparticle energy spectrum for sulfur-50 at $j_z = 1/2$ up to 60 MeV, and the equivalent s.p. energy spectrum. Fig.2 depicts the spectral distribution of the neutron pairing density

$$\tilde{\rho}(\mathbf{r}) \;=\; -\sum_{E_n>0}^{\infty} \sum_{\sigma=-\frac{1}{2}}^{+\frac{1}{2}} \phi_2(E_n, \mathbf{r}\sigma)\ \phi_1^*(E_n, \mathbf{r}\sigma) \tag{2}$$

for ^{104}Zr. The pairing density describes the probability of *correlated* nucleon pair formation with opposite spin projection, and it determines the pair transfer formfactor.

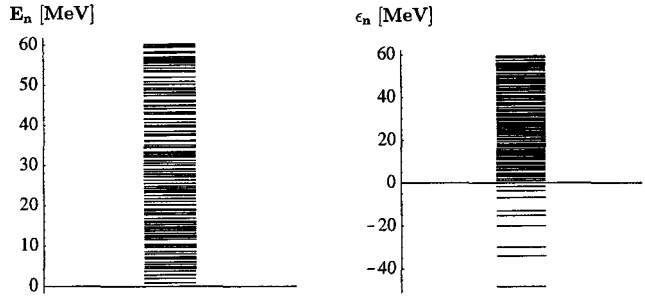

Figure 1. Left: quasiparticle energy spectrum for sulfur-50 at $j_z = 1/2$. Right: equivalent s.p. energy spectrum.

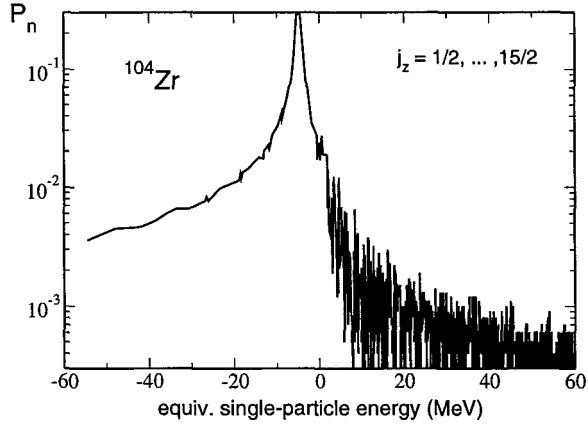

Figure 2. Equivalent s.p. energy spectrum of the neutron pairing density for ^{104}Zr.

4. Strongly deformed neutron-rich Zr, Ce, Nd and Sm isotopes

Recently, experiments have been carried out with Gammasphere at LBNL[11] which have determined quadrupole deformations of neutron-rich medium/heavy mass nuclei with $N/Z \approx 1.6$. Furthermore, laser spectroscopy has yielded precise rms-radii in this region. Table 1 presents a comparison of our HFB results with experimental data. The theoretical quadrupole deformations of the proton charge distributions agree very well with the data of ref.[11], and the calculated proton rms-radius for ^{102}Zr is in good agreement with laser spectroscopic data (see Fig.4 of ref.[12]). Theoretical HFB predictions are also given for the neutron density distributions.

Table 1. HFB results for neutron-rich zirconium, cerium, neodymium, and samarium isotopes. The first column lists the neutron-to-proton ratio N/Z. Subsequent columns display quadrupole deformations $\beta_2(p), \beta_2(n)$ and rms-radii r_p, r_n of protons and neutrons. Experimental data are taken from ref.[11,12].

	N/Z	$\beta_2(p)$	$\beta_2^{exp}(p)$	$\beta_2(n)$	r_p (fm)	r_p^{exp} (fm)	r_n (fm)
^{102}Zr	1.55	0.43	0.42(5)	0.43	4.47	4.54	4.65
^{104}Zr	1.60	0.45	0.45(4)	0.45	4.49		4.70
^{152}Ce	1.62	0.32	0.30(3)	0.33	5.01		5.22
^{156}Nd	1.60	0.37		0.36	5.08		5.27
^{158}Sm	1.55	0.38	0.46(5)	0.37	5.14		5.27
^{160}Sm	1.58	0.38		0.37	5.13		5.31

5. Sulfur isotope chain up to the two-neutron dripline

The sulfur isotopes ($Z = 16$) have been investigated several years ago by Werner et al.[9]: both Skyrme-HF and relativistic mean field (RMF) model calculations were carried out using a "constant pairing gap" approximation. Within the single-particle shell model, one would expect nuclei such as $^{44}_{16}S_{28}$ with "magic" neutron number $N = 28$ to be spherical. But the mean field theories predict, in fact, deformed intrinsic shapes as a result of "intruder" states. Fig.3 shows theoretical and experimental two-neutron

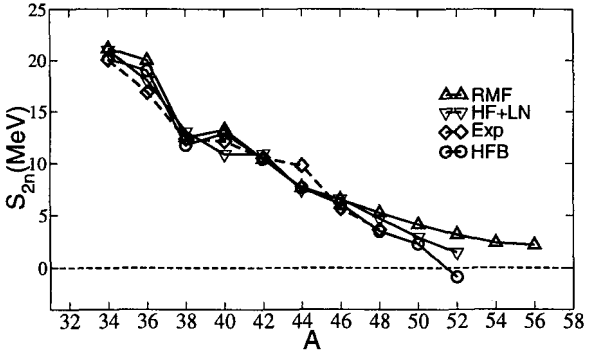

Figure 3. Two-neutron separation energies for the even sulfur isotopes.

separation energies. We compare our HFB and HF+LN (Lipkin/Nogami

pairing) calculations to the RMF (relativistic mean field with BCS pairing) calculations by Lalazissis et al.[10]. Both HFB and RMF calculations agree with available experimental data, but there are dramatic differences near the two-neutron dripline: Our HFB calculations predict ^{50}S to be the last isotope which is stable against two neutron emission. By contrast, RMF predicts $S_{2n}(Z,N) > 0$ at least up to ^{56}S.

Intermediate energy Coulomb excitation experiments[13,14] yield the following quadrupole deformations for the even sulfur isotopes $^{38-44}S$: $|\beta_2^{exp}| = 0.246(16),\ 0.284(16),\ 0.300(24),\ 0.258(36)$; our corresponding Skyrme-HFB theory results are $\beta_2^{HFB} = 0.16,\ 0.26,\ 0.25,\ 0.29$. Both HFB and RMF calculations reveal shape coexistence in this region[3].

Acknowledgments

This work has been supported by the U.S. Dept. of Energy, grant No. DE-FG02-96ER40963, with Vanderbilt University. The numerical calculations were carried out at the IBM-RS/6000 SP supercomputer at NERSC.

References

1. J. Dobaczewski, W. Nazarewicz, T.R. Werner, J.F. Berger, C.R. Chinn and J. Dechargé, *Phys. Rev.* **C 53**, 2809 (1996).
2. E. Terán, V.E. Oberacker, and A.S. Umar, *Phys. Rev.* **C 67**, 064314 (2003).
3. V.E. Oberacker, A.S. Umar, E. Terán, and A. Blazkiewicz, *Phys. Rev.* **C 68**, in print (Dec. 2003).
4. M.V. Stoitsov, J. Dobaczewski, P. Ring and S. Pittel, *Phys. Rev.* **C 61**, 034311 (2000).
5. J. Terasaki, P.-H. Heenen, H. Flocard and P. Bonche, *Nucl. Phys.* **A 600**, 371 (1996).
6. M. Yamagami, K. Matsuyanagi, and M. Matsuo, *Nucl. Phys.* **A 693**, 579 (2001).
7. A.S. Umar, J. Wu, M.R. Strayer and C. Bottcher, *J. Comp. Phys.* **93**, 426 (1991).
8. D.R. Kegley, V.E. Oberacker, M.R. Strayer, A.S. Umar and J.C. Wells, *J. Comp. Phys.* **128**, 197 (1996).
9. T.R. Werner, J.A. Sheikh, W. Nazarewicz, M.R. Strayer, A.S. Umar, and M. Misu, *Phys. Lett.* **B 333**, 303 (1994).
10. G.A. Lalazissis, S. Raman, and P. Ring, *At. Data Nucl. Data Tables* **71**, 1 (1999).
11. J.K. Hwang, et al., subm. to *Phys. Rev.* **C**.
12. P. Campbell *et al.*, *Phys. Rev. Lett.* **89**, 082501 (2002).
13. H. Scheit *et al.*, *Phys. Rev. Lett.* **77**, 3967 (1996).
14. T. Glasmacher *et al.*, *Phys. Lett.* **B 395**, 163 (1997).

MEAN-FIELD APPROACH WITH M3Y-TYPE INTERACTION

H. NAKADA

Department of Physics, Chiba University, Chiba 263-8522, Japan
nakada@faculty.chiba-u.jp

M3Y-type interactions are developed and applied to mean-field calculations. By comparing results of an M3Y-type interaction on the uniform nuclear matter with those of the Skyrme and the Gogny interactions, we find a remarkable difference in the spin-isospin properties, to which the one-pion-exchange potential gives significant contribution. Correlating to variation of the shell structure, these spin-isospin properties play a certain role in the new magic numbers near drip lines such as $N = 16$ and $N = 32$.

1. Introduction

Mean-field calculations are useful to study basic characters of effective interactions for low-energy nuclear structures. The Hartree-Fock calculations have successfully been used to describe the saturation and the shell structure for stable nuclei. On the other hand, structures of unstable nuclei provide us with significant information on the nuclear effective interaction which is complementary to our knowledge obtained from stable nuclei. While most effective interactions (or parameter-sets) have been devised to describe the structures of stable nuclei, they do not necessarily reproduce the properties of unstable nuclei. An important question will be whether or not the irregular behavior of nuclear radii and the exotic magic numbers in unstable nuclei [1] can be treated well in the mean-field calculations, if the effective interaction is properly chosen. It is also of interest what aspects of unstable nuclei are related to the equation of state in the asymmetric nuclear matter, reflecting characters of effective interactions.

By introducing a density-dependent contact term, we have explored M3Y-type interactions applicable to the mean-field calculations [2]. Using these interactions, shell structures and their variation in the *sd*- and the *pf*-shells are investigated, in connection to the new magic numbers far from the β-stability.

2. M3Y-type interactions

We have developed M3Y-type interactions,

$$v_{12} = v_{12}^{(\mathrm{C})} + v_{12}^{(\mathrm{LS})} + v_{12}^{(\mathrm{TN})} + v_{12}^{(\mathrm{DD})}\,; \tag{1}$$

$$v_{12}^{(\mathrm{C})} = \sum_n (t_n^{(\mathrm{SE})} P_{\mathrm{SE}} + t_n^{(\mathrm{TE})} P_{\mathrm{TE}} + t_n^{(\mathrm{SO})} P_{\mathrm{SO}} + t_n^{(\mathrm{TO})} P_{\mathrm{TO}})\, f_n^{(\mathrm{C})}(r_{12})\,,$$

$$v_{12}^{(\mathrm{LS})} = \sum_n (t_n^{(\mathrm{LSE})} P_{\mathrm{TE}} + t_n^{(\mathrm{LSO})} P_{\mathrm{TO}})\, f_n^{(\mathrm{LS})}(r_{12})\, \mathbf{L}_{12} \cdot (\mathbf{s}_1 + \mathbf{s}_2)\,,$$

$$v_{12}^{(\mathrm{TN})} = \sum_n (t_n^{(\mathrm{TNE})} P_{\mathrm{TE}} + t_n^{(\mathrm{TNO})} P_{\mathrm{TO}})\, f_n^{(\mathrm{TN})}(r_{12})\, r_{12}^2 S_{12}\,,$$

$$v_{12}^{(\mathrm{DD})} = t^{(\mathrm{DD})}(1 + x^{(\mathrm{DD})} P_\sigma)[\rho(\mathbf{r}_1)]^\alpha\, \delta(\mathbf{r}_{12})\,, \tag{2}$$

where $f_n(r_{12}) = e^{-\mu_n r_{12}}/\mu_n r_{12}$. The longest-range part of $v_{12}^{(\mathrm{C})}$ is fixed to be the one-pion-exchange potential, which will be denoted by $v_\pi^{(\mathrm{C})}$. Although in the original M3Y interaction the coupling constants (t) are fitted to the G-matrix at a certain density [3], the non-relativistic G-matrix approach has not yet successfully reproduced the saturation properties. For this reason we introduce $v_{12}^{(\mathrm{DD})}$ and modify t's in a phenomenological manner, except the $v_\pi^{(\mathrm{C})}$ part, by fitting to the properties of the nuclear matter and several doubly magic nuclei. In the present study we use a parameter-set called 'M3Y-P2'. For details of the interaction, see Ref. [2].

3. Basic characters of interactions

To be applied to many nuclei in a wide range of mass region, effective interactions should reproduce the nuclear matter properties, particularly those around the saturation point. In Table 1, the Fermi momentum (k_{F0}), the energy per nucleon ($\mathcal{E}_0$), the effective mass (M^*), the incompressibility ($\mathcal{K}$) and the volume symmetry energy (a_t) at the saturation point are listed. Moreover, we also show the Landau parameters relevant to the spin and spin-isospin responses (g_0, g_1, g_0' and g_1'). These values obtained with the M3Y-P2 interaction are compared with those of the Skyrme SLy5 and the Gogny D1S interactions.

Whereas all the three interactions give similar results for k_{F0}, $\mathcal{E}_0$, $\mathcal{K}$, M^* and a_t, significant differences are found in g_ℓ and g_ℓ'. This is apparently because these properties have not been taken care of when the interactions are developed. An appropriate comparison with experiments [4] indicates $g_0 \ll g_0' \approx 1$, which favors M3Y-P2 but does not SLy5 and D1S. It is emphasized that contribution of $v_\pi^{(\mathrm{C})}$ is quite important in the g_0' value in

Table 1. Nuclear matter properties at the saturation point.

		M3Y-P2	SLy5	D1S
k_{F0}	(fm)	1.340	1.334	1.342
$\mathcal{E}_0$	(MeV)	−16.14	−15.98	−16.01
$\mathcal{K}$	(MeV)	220.4	229.9	202.9
M^*/M		0.652	0.697	0.697
a_t	(MeV)	30.61	32.03	31.12
g_0		0.113	1.123	0.466
g_1		0.273	0.253	−0.184
g_0'		1.006	−0.141	0.631
g_1'		0.202	1.043	0.610

M3Y-P2. Explicit inclusion of $v_\pi^{(C)}$ makes it easy to obtain the reasonable spin-isospin properties.

We have also confirmed that the M3Y-P2 interaction reproduces the binding energies and the rms matter radii of doubly magic nuclei with a similar accuracy to the other interactions [2].

4. Z-dependence of $N = 16$ and $N = 32$ shell gaps

It has been suggested [5] that the spin-isospin degrees-of-freedom contained in the effective interactions may be relevant to the new magic numbers far from the β-stability. Using the above effective interactions, we shall discuss influence of the spin-isospin properties on the shell evolution.

A new magic number $N = 16$ around $Z \approx 8$ has been reported [6], which seems subject to the $n1s_{1/2}$-$n0d_{3/2}$ shell gap. We investigate the single-particle energies (ε) from nucleus to nucleus by the spherical Hartree-Fock calculations. In Fig. 1, the Z-dependence of $\Delta\varepsilon(n0d_{3/2}) = \varepsilon(n0d_{3/2}) - \varepsilon(n1s_{1/2})$ is depicted for the $N = 16$ nuclei with several effective interactions. The effective single-particle energies in the shell model space with the 'USD' matrix elements are also evaluated.

We find that USD and M3Y-P2 give larger $\Delta\varepsilon(n0d_{3/2})$ for decreasing Z. In the M3Y-P2 result, we have confirmed that this trend comes primarily from $v_\pi^{(C)}$ [7]. On the other hand, SLy5 and D1S show quite different Z-dependence. Therefore, as pointed out in Ref. [5], the spin-isospin property plays a certain role in the new magic number $N = 16$, and should be taken into account appropriately in describing the shell evolution. In a quantitative sense, however, major difference among the interactions is present in the β-stable region, rather than in the neutron-rich region. Hence careful investigation on low-energy structure of the β-stable nuclei may also

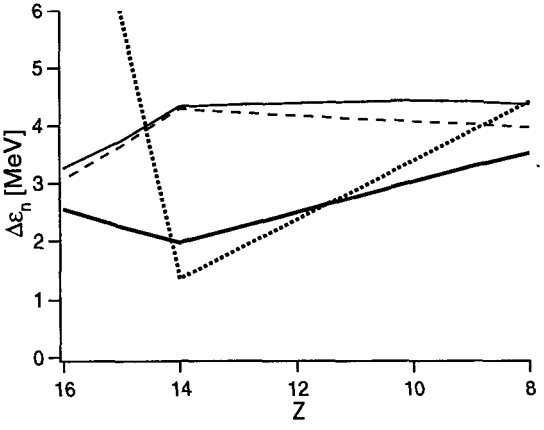

Figure 1. Z-dependence of $\Delta\varepsilon(n0d_{3/2})$ for the $N = 16$ isotones. The thick solid, dotted, thin solid and dashed lines correspond to the results with the M3Y-P2, USD, D1S and SLy5 interactions, respectively.

help clarifying effects of the spin-isospin degrees-of-freedom on the shell evolution.

There is experimental evidence,[8] on the new magic number $N = 32$ around $Z \approx 20$Relevant to this problem, the Z-dependence of $\Delta\varepsilon(n1p_{1/2}) = \varepsilon(n1p_{1/2}) - \varepsilon(n1p_{3/2})$ and $\Delta\varepsilon(n0f_{5/2}) = \varepsilon(n0f_{5/2}) - \varepsilon(n1p_{3/2})$ in the $N = 32$ isotones is illustrated in Fig. 2. Significant difference among the interactions is found in $\Delta\varepsilon(n0f_{5/2})$. The slope of $\Delta\varepsilon(n0f_{5/2})$ correlates well to the g'_0 value in Table 1. The strong Z-dependence with M3Y-P2 has been confirmed to be carried by $v_\pi^{(C)}$. Therefore the spin-isospin properties play a certain role again in forming the $N = 32$ new magic number. It is also noted that M3Y-P2 reproduces the inversion of $0f_{5/2}$ and $1p_{1/2}$, which is clearly observed in the $N = 29$ nuclei, without corrections due to the core-polarization. There is an argument[9] that $N = 34$ could also be an magic number around $Z \approx 20$. However, this depends on the position of the $n1p_{1/2}$ orbit as well as on the Z-dependence of $\Delta\varepsilon(n0f_{5/2})$. In the M3Y-P2 result the $n1p_{1/2}$-$n0f_{5/2}$ gap does not seem large enough to make $N = 34$ a magic number.

5. Summary

M3Y-type interactions have been developed and applied to mean-field calculations. Basic characters of effective interactions are investigated via the

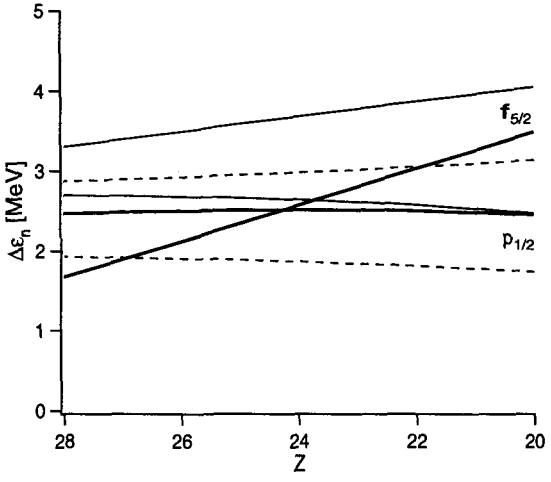

Figure 2. Z-dependence of $\Delta\varepsilon(n1p_{1/2})$ and $\Delta\varepsilon(n0f_{5/2})$ for the $N = 32$ isotones. The thick solid, thin solid and dashed lines correspond to the results with the M3Y-P2, D1S and SLy5 interactions, respectively.

nuclear matter properties; results of an M3Y-type interaction are compared with those of the Skyrme and the Gogny interactions. A remarkable difference is found in the spin-isospin properties, to which the one-pion-exchange potential gives significant contribution. The spin-isospin properties are relevant to variation of the shell structure, playing a certain role in the new magic numbers far from the β-stability such as $N = 16$ and $N = 32$. Careful study is also desired on some β-stable nuclei, to establish how the spin-isospin degrees-of-freedom influence the shell evolution.

References

1. I. Tanihata, *Nucl Phys.* **A654**, 235c (1999).
2. H. Nakada, *Phys. Rev.* **C68**, 014316 (2003).
3. G. Bertsch *et al.*, *Nucl. Phys.* **A284**, 399 (1977);
   N. Anantaraman, H. Toki and G. F. Bertsch, *Nucl. Phys.* **A398**, 269 (1983).
4. M. Bender *et al.*, *Phys. Rev.* **C65**, 054322 (2002).
5. T. Otsuka *et al.*, *Phys. Rev. Lett.* **87**, 082502 (2001).
6. A. Ozawa *et al.*, *Phys. Rev. Lett.* **84**, 5493 (2000).
7. H. Nakada, *Nucl. Phys.* **A722**, 117c (2003).
8. I. Prisciandaro *et al.*, *Phys. Lett.* **B510**, 17 (2001);
   R. Kanungo and I. Tanihata, *Phys. Lett.* **B528**, 58 (2002).
9. R. V. F. Janssens *et al.*, *Phys. Lett.* **B546**, 55 (2002).

DENSITY AND ISOSPIN DEPENDENCIES IN RELATIVISTIC MEAN FIELD MODELS

M. SERRA

Department of Physics, University of Tokyo, Hongo, Bunkyo-ku, Tokyo, Japan
mserra@tkyntm.phys.s.u-tokyo.ac.jp

T. OTSUKA

Department of Physics, University of Tokyo, Hongo, Bunkyo-ku, Tokyo,
CNS/University of Tokyo, RIKEN, Wako-shi, Japan

Y. AKAISHI

KEK, Oho, Tsukuba-shi, Ibaraki, Japan,

S. HIROSE

Department of Physics, University of Tokyo, Hongo, Bunkyo-ku, Tokyo, Japan

P. RING

Physics Department, Technical University Munich, Garching, Germany,

We study the connection between relativistic mean field models and the bare nucleon-nucleon interaction. We start from a bare interaction, and by employing a G-matrix formalism we derive a density dependent realistic interaction in the medium. We introduce a one-boson-exchange potential and we extract the masses and the coupling strengths of the meson fields through a fit to the G-matrix potentials. The parameters and their density dependence are compared with those of other one-boson-exchange parametrizations.

1. INTRODUCTION

Relativistic mean field (RMF) models [1] describe atomic nuclei as a system of independent nucleons interacting between themselves by the exchange of a few effective meson fields. In spite of their success in predicting ground state and dynamical properties of stable and unstable nuclei [2,3], these models are fully phenomenological approaches for the solution of the nuclear many-body problem. In this work we look for a connection between RMF

models and the bare nucleon-nucleon (NN) interaction. We concentrate on the role that the tensor force of the NN interaction plays in RMF models. In fact, it is well known from ab-initio calculations [4] that the tensor force is the main responsible for attraction, whereas in RMF models the σ field is the only responsible for it. We start from a nonrelativistic bare NN interaction, the Tamagaki potential [5]. Using the G-matrix formalism developed by S. Nagata et al. [6], we derive a realistic interaction in the medium. It saturates and depends on the density of the medium, or on its Fermi momentum k_F. These properties are due to the renormalization of the tensor force. For simplicity we consider the Fermi gas model with $N = Z$. We show that its medium and long ranges can be described to a good approximation by an effective density dependent one-boson-exchange (OBE) potential. We have extracted the mass and the coupling strength of the meson fields at various k_F determining in such a way the density dependence of the effective fields. A comparison with the bare parameters allows us to study the many-body and multi-scattering effects on their properties. Furthermore, these values result to be rather consistent with the parameters of other RMF phenomenologies. In Section 2 the realistic interaction in the medium and its properties are discussed. In Section 3 our model is presented and results are discussed. Section 4 contains summary and conclusions.

2. REALISTIC INTERACTION IN THE MEDIUM

In Fig. 1 the potentials obtained by the G-matrix calculation are shown as a function of the internucleon distance for the Fermi momenta $k_F = 1.8$ (dashed line), 1.4 (solid line) and 1.0 (long-dashed line) fm^{-1}. The density dependence of the realistic interaction in the medium is different in each channel. In panel (a) the pure central potential V_0 is shown: it is repulsive at short distance and becomes attractive for $r \gtrsim 0.7$ fm. The density dependence is rather strong in the intermediate range. In panel (b) the spin central potential V_σ is displayed. It is positive for $r \gtrsim 1.0$ fm and it is almost density independent. Panel (c) shows the isospin central potential V_τ: it is negative at short range, it becomes positive for $r \geq 0.6$ fm.It shows a rather strong density dependence. In panel (d) the spin-isospin potential $V_{\sigma\tau}$ is positive for $r \gtrsim 0.5$ fm. Panel (e) displays the tensor potential in the triplet-even state V_T. It is attractive for $r \geq 0.5$ fm and it is rather strongly density dependent. In panel (f) V_{ls} is negative and for $r \gtrsim 0.6$ fm it increases rapidly to zero. It is almost independent of the Fermi momentum.

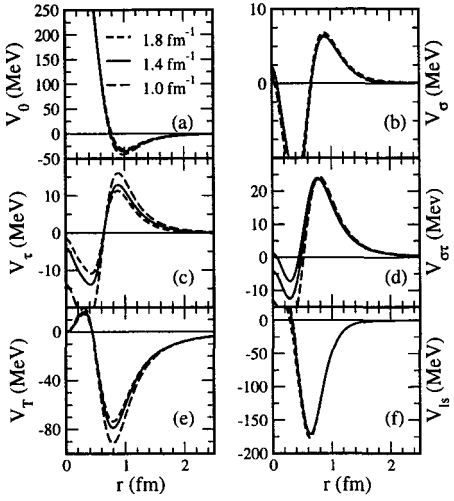

Figure 1. Potentials obtained by the G-matrix calculation as a function of the inter-nucleon distance for the Fermi momenta $k_F = 1.8$ (dashed line), 1.4 (solid line), 1.0 (long-dashed line) fm^{-1}. (a) Pure central potential V_0; (b) spin central potential V_σ; (b) spin central potential V_τ; (d) spin-isospin potential $V_{\sigma\tau}$; (e) tensor potential in the triplet-even state V_T; (f) spin-orbit potential in the triplet-odd state V_{ls}.

3. ONE-BOSON-ECHANGE POTENTIAL

In order to describe the G-matrix potentials, we have introduced a OBE potential based on a isoscalar scalar σ-field, a isoscalar vector ω-field (vector coupling only), a isovector scalar δ-field, a isovector vector ρ-field (vector and tensor couplings), and a pseudoscalar pion field (pseudo-vector coupling) π. The fit parameters of the OBE potential are the masses m and the coupling constants g of the fields σ, ω, δ, ρ. In this study, $m_\pi = 137$ MeV and $f_\pi^2/4\pi = 0.081$, and for the coupling of the ρ-field tensor term we have chosen $f_\rho/g_\rho = 6.1$. The eight free parameters have been adjusted so that the OBE model reproduces the G-matrix potentials as much as possible in the intermediate and long ranges. In Figures 2 (left) and 3 (right) the masses and the coupling constants of the fields σ, ω, δ, and ρ are shown as a function of k_F. The filled symbols correspond to the value of k_F at which the OBE potentials have been fitted to the G-matrix ones. In the left upper panel of Fig. 2, m_σ (circles) has been found to be independent of the density and its value is about 7% smaller than in relativistic Hartree (RH) parametrizations. In the upper panel on the right, m_δ (diamonds) is plotted. We have found that m_δ and g_δ are mainly determined by V_τ. m_δ shows

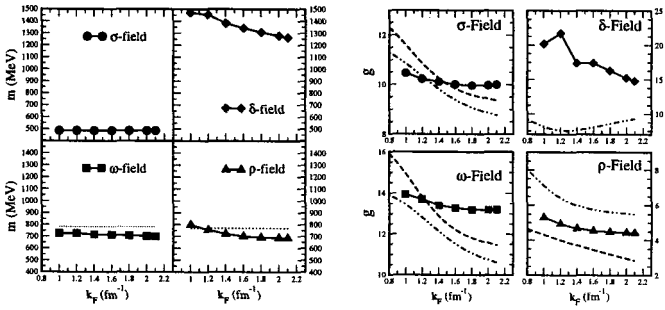

Figure 2. Density dependent masses of the fields σ (circles), ω (squares), δ (diamonds), and ρ (triangles) as a function of the Fermi momentum k_F.

Figure 3. Density dependent couplings of the fields σ (circles), ω (squares), δ (diamonds), and ρ (triangles) as a function of the Fermi momentum k_F in the case of FIT 1. The dashed and the dot-dashed lines represents the density dependent couplings of the RHB model of Ref. [10] and of the density dependent hadron field theory of Ref. [9].

a very strong dependence on k_F, it is very large and therefore it seems completely unrelated to the resonance at 983 MeV. The enhancement of this channel is due to the second order effect of the tensor force. In the lower part of the figure, we show m_ω and m_ρ. On the left, m_ω (squares) decreases with the k_F. On the right, the triangles show m_ρ that also decreases with the density. The dotted line represents the bare masses of the fields. The decreasing behavior is consistent with the requirements of chiral symmetry and with the results of many-body theories [7] and QCD oriented models [8]. We find that the ratio between the in-medium and the bare masses of ω and ρ is almost the same for $k_F \geq 1.4$ fm^{-1}. In Fig. 3 the coupling constants of the fields are displayed as a function of k_F. In addition to our results shown by filled symbols, the dot-dashed line displays the parameters of the density dependent hadron field theory by Hofmann et al. [9] and the dashed line shows the parameters of the fully phenomenological density dependent relativistic Hartree-Bogoliubov (RHB) model by T. Niksic et al. [10]. In the upper part of the figure, on the left g_σ (circles) is found to be a rather weakly decreasing function of the density. The density dependence of the hadron field theory and of the RHB model is much stronger. We notice an agreement between our parameters and those of the other calculations in the region of the densities close to saturation. On the right panel, g_δ (diamonds) has a strong density dependence. A comparison with the density dependent hadron field theory results [9] shows very different behavior and strength. In the lower part of the figure, g_ω (squares) is displayed in the

left panel. Its decrease is analogous to the one observed for the g_σ. The other relativistic calculations show a much stronger density dependence. Similarly to the σ-field, the agreement among the density dependences of the various models is better in the region around saturation. On the right panel the ρ-field coupling, g_ρ is displayed. g_ρ decreases with the density. Its strength is rather consistent with the other two parametrizations. In particular, it shows an almost exponential dependence on k_F, which is very similar to the calculations of Ref. [9], while the RHB model of Ref. [10] has a more linear dependence.

4. CONCLUSIONS

In summary, starting from a bare interaction and by employing a G-matrix formalism, we have derived a density dependent realistic interaction in the nuclear medium. We have introduced a OBE potential and by extracting the masses and couplings of the fields from a fit to the G-matrix potentials, we have been able to establish a connection of RMF models to the underlying bare NN interaction. We have studied the density dependence of the parameters. We have found that the tensor force of the NN interaction is essential for explaining the σ-field dominance for attraction and that the extracted parameters are rather consistent with other density dependent parametrizations [9,10]. As for the density dependence of the effective OBE potential, we have found that the mean field density dependence enforces saturation, i.e. the masses (apart from m_σ) and the coupling strengths decrease with an increasing k_F. In particular, the decreasing of m_ω and m_ρ is consistent with chiral symmetry requirements and QCD oriented models [7,8]. We have found that m_ω and m_ρ scale at the same rate.

One of the authors (M.S.) acknowledges the postdoctoral fellowship from JSPS.

References

1. B.D. Serot and J.D. Walecka, Int. J. Mod. Phys. **E6**, 515 (1997)
2. P. Ring, Progr. Part. Nucl. Phys. **37**, 193 (1996)
3. Y.Sugahara and H. Toki, Nucl. Phys. **A579**, 557 (1994)
4. B.S. Pudliner, V.R. Pandharipande, J. Carlson, S.C. Pieper and R.B. Wiringa, Phys. Rev. **C56**, 1720 (1997)
5. R. Tamagaki and T. Takatsuka, Prog. Theor. Phys. **105**, 1059 (2001)
6. S. Nagata, H. Bando and Y. Akaishi, Prog. Theor. Phys. Suppl. **65**, 10 (1979)
7. G. E. Brown, H. Müther and M. Prakash, Nucl. Phys. **A506**, 565 (1990).
8. T. Hatsuda and T. Kunihiro, Phys. Lett. **B185**.
9. F. Hofmann, C. M. Keil, H. Lenske, Phys. Rev. **C64** (2001) 034314.
10. T. Niksic, D. Vretenar, P. Finelli, P. Ring, Phys. Rev. **C66** (2002) 024306.

HARTREE-FOCK MEAN FIELD MODEL WITH A SEPARABLE NUCLEON-NUCLEON INTERACTION APPLIED TO CALCULATION OF CHARGE DENSITY DISTRIBUTION AND GROUND STATE BINDING ENERGIES OF SELECTED EVEN-EVEN NUCLEI.

J. RIKOVSKA STONE
University of Oxford
Department of Physics,
Oxford OX1 3PU, England
and
University of Maryland
Department of Chemistry and Biochemistry,
Collage Park, MD 20742
E-mail: j.stone@physics.ox.ac.uk

W. B. WALTERS
University of Maryland
Department of Chemistry and Biochemistry,
College Park, MD 20742
E-mail: ww3@umail.umd.edu

The Hartree-Fock + BCS model with a separable monopole nucleon-nucleon interaction is applied to calculate the charge density distribution in selected even-even nuclei. The charge r.m.s. of $^{40-48}$Ca isotopes and binding energies of even-even Cd nuclei are discussed. The Q_β value for ^{130}Cd $\rightarrow$ ^{130}In is calculated, giving good agreement with experiment.

1. Introduction

The main objective of the theory effort described is the development and application of a many-body perturbation model with a novel density dependent separable monopole (SMO) effective two-body nucleon-nucleon interaction. The lowest order of the model is formally equivalent to the better known Hartree-Fock +BCS mean field calculation with Skyrme or Gogny effective potentials. There is however a major difference between the physics contained in the SMO and earlier models.

The Skyrme (Gogny) potential is of zero (finite but short) range. As a consequence of this limited range it follows that when these potentials are used in perturbation theory, designed to account for correlations beyond the mean field and calculate corrections to energies, radii and other observables, results obtained are strongly divergent. The presence of correlations beyond the mean field in nuclei is generally accepted but so far no general treatment is available. For example, the RPA technique exists but it does not self-consistently use the potential which generates the mean field and, furthermore, is applicable only to 1p-1h excitations.

The SMO potential with its indefinite range has been designed to overcome this fundamental problem. A basic description of the model is given in Ref. 1. Stevenson et al.[1] showed that when used in perturbation theory up to 4th order, it produced converging results for spherically symmetric nuclei. Very recently, a more general derivation has been made, applicable to spherical and axially symmetric deformed nuclei[2]. The computer code based on this theory is under test with encouraging preliminary results.

Successful application of the first two parametrisations of the separable interaction, SMO1[1] to spherical nuclei and SMO2[3,4] to axially deformed nuclei, nuclear matter and neutron stars has been reported. Both parametrisations, like the other phenomenological effective interactions used in mean field theories, have their adjustable parameters chosen by fitting properties of closed shell nuclei. We stress that, because we do not know the true functional form of the nucleon-nucleon potential, all the nuclear physics is really absorbed in the fitted parameters. The isospin and density dependence of the parameters is however also unknown and it is therefore uncertain how well parameters optimized at the stability line will represent real nuclei at the nucleon drip-line and beyond.

We addressed this problem during the design of a new SMO parametrisation, SMO3, developed in the last two months and reported here. We discuss the conceptual differences between SMO3 and the previous SMO1 and SMO2 models and illustrate results obtained with SMO3 on charge density distributions, mean square radii and nuclear binding energies.

2. The SMO3 interaction

The potential is a sum of attractive and repulsive parts which have identical functional form but differ in fitted parameters. Each part is a sum of separable density dependent, volume, isospin and surface terms. Standard Coulomb and one-body spin-orbit terms are added. The total potential

is employed in derivation of Hartree-Fock equations which are solved self-consistently. Finally, a density dependent surface pairing interaction is included following the method of Bender et al.[6] with an appropriate cutoff[7]. In SMO3 the isospin term has been rearranged so that contributions of isospin-isospin interaction between like and unlike nucleons are formally separated.Also the surface term has been improved. The explicit form the the SMO3 potential will be published elsewhere[8]. These changes allow more definitive identification of the fitted parameters with individual processes in the nucleus. Should a local adjustement of the parameters be required SMO3 can do this simply.

In fitting the SMO3 parameters a novel approach has been adopted. Properties of infinite asymmetric nuclear matter were used to fix the parameters of the volume term and the like-nucleon isospin term. These parameters were kept fixed when SMO3 was applied to finite nuclei. The physics of finite asymmetric nuclear matter confined by a defined surface was described by the strengths of the unlike-isospin, surface, spin-orbit and pairing terms fitting ground state properties of doubly-closed shell nuclei across the nuclear chart. In this way we use two extreme scenarios to fit SMO3 parameters: (i) doubly closed shell nuclei with the ratio $N/Z \approx 1$ and (ii) asymmetric beta-equilibrium nuclear matter, as is taken to exist in cold neutron stars, with $N/Z \approx 4 - 9$. Thus neutron heavy nuclei at the neutron drip-line and beyond, with $N/Z \approx 1.7$ shold be more realistically described using SMO3 than with the previous parametrisations. There are a total of seven fitted constants, six of them are adopted with no local adjustments of any kind. One of them, the strength of the isospin-isospin interaction between like nucleons, gives potentially better results if allowed a slight N,Z dependence. This feature will be discussed elsewhere in more detail[8].

3. Applications of the SMO3 Model

We briefly summarise three areas in which the new SMO3 parametrisation has given very encouraging results.

In Fig. 1 we show calculated and experimental charge density distributions, as a function of radial distance from the centre of the nucleus for nine even-even nuclei (see Ref. 5 and references therein) . The deviations of the calculated values from the experiment at small values of r can be attributed to the fact that no short range correlations are included in the model at present. The global overall agreement is very encouraging.

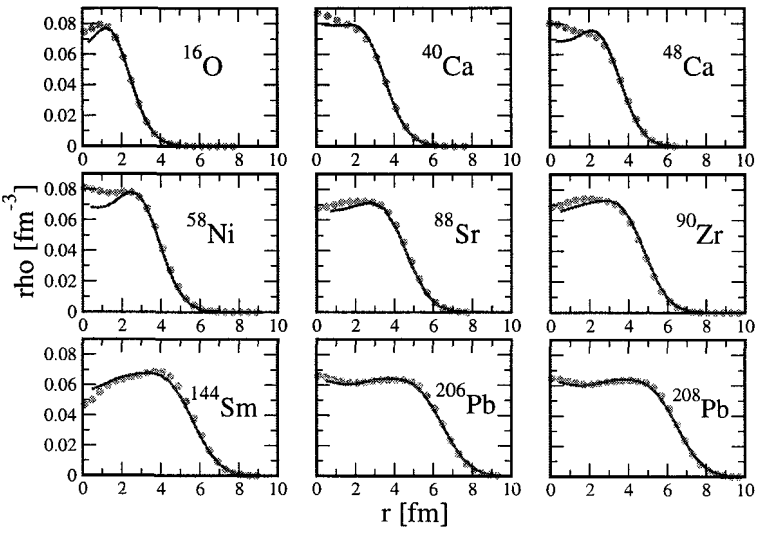

Figure 1. Experimental and calculated charge density distributions

To further test the validity of the SMO3 model we calculated of the neutron number dependence of the charge root-mean-square radius for $^{40-48}$Ca, a known 'problem' system for mean-field models. The experimental data reflect the presence of the excited 0^+ intruder states in $^{40-44}$Ca which may not be spherical but will mix with the ground state. Our model is sensitive to this mixing and correctly reproduces the trend of the experimental r.m.s., as shown in Fig. 2. Results of the Relativistic Mean Field model[9] and the HF+BCS non-relativistic model with the MSk7[10] Skyrme interaction are added for comparison. Finally, Q_β (^{130}Cd - ^{130}In) has recently become a focus of interest. The half-life of this β decay is important for understanding solar system r-process abundances in the $A = 130$ region as ^{130}Cd is a well known 'waiting point' nucleus[11]. To calculate this quantity, binding energies of even-even $^{100-130}$Cd isotopes were used to test the precision of the SMO3 model. The mean deviation between experiment and SMO3 theory for $^{100-128}$Cd was less than 300 keV. SMO3 then predicts the binding energy of ^{130}Cd to be 1073.3(3) MeV, yielding Q_β 8.4±0.3 MeV (taking the experimental mass of ^{130}In). This compares very well with the recent experimental value of 8.34±0.15 MeV. Other mass models seriously underestimated this this quantity[12] and to obtain agreement with experiment needed to invoke substaintial neutron shell quenching. Our result has been achieved using standard parameters of the model with no special

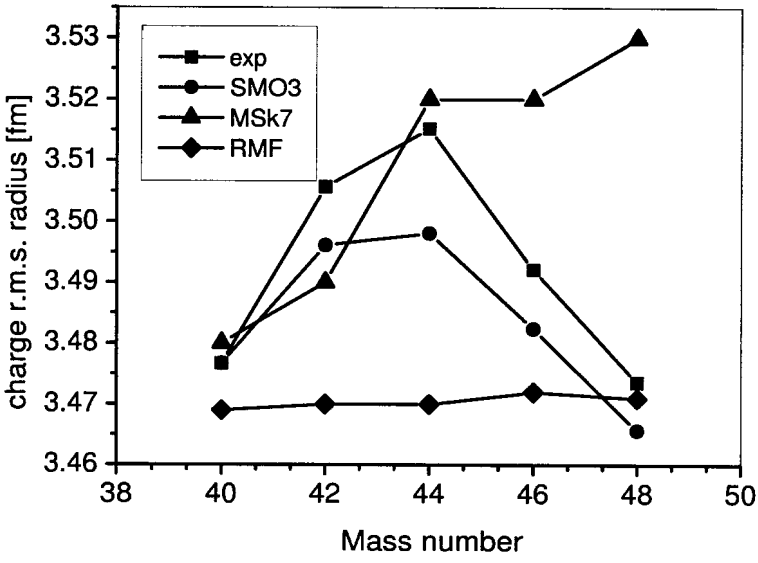

Figure 2. Calculated charge r.m.s of $^{40-48}$Ca isotopes in comparison with experiment and some other model calculations

adjustments.

Acknowledgments

Support by the US DOE grant No. DE-FG02-94-ER40834 is gratefully acknowledged.

References

1. P. D. Stevenson et al., *Phys. Rev.* **C65**, 1729 (2001).
2. Ch. Kirst, J. Rikovska Stone and D. M. Brink, in preparation.
3. P. D. Stevenson et al., *Phys. Lett.* **B545** , 291 (2002).
4. J. Rikovska Stone et al., *Phys. Rev.* **C65**, 064312 (2002).
5. B. A. Brown, *Phys. Rev.* **C67**, 034317 (2003)
6. M. Bender et al., *Eur.Phys.J.* **A8**, 59 (2000)
7. S. J. Krieger et al., *Nucl. Phys.* **A517**, 275 (1990).
8. J. Rikovska Stone et al., in preparation
9. G. A. Lalazissis et al., *At.Data Nucl. Data Tables* **71**, 1 (1999)
10. S. Goriely et al., *At.Data Nucl. Data Tables* **77**, 311 (2001)
11. K.-L. Kratz et al., *Z.Phys.* **A325** 489 (1986)
12. I. Dillmann et al., *Phys. Rev. Lett.* **91** 162503 (2003)

Shell structure in exotic nuclei

This page intentionally left blank

PERSPECTIVES OF THE SHELL MODEL

TAKAHARU OTSUKA

Department of Physics and Center for Nuclear Study, University of Tokyo, Hongo, Bunkyo-ku, Tokyo, 113-0033, Japan and RIKEN, Hirosawa, Wako-shi, Saitama, 351-0198, Japan

The evolution of shell structure in exotic nuclei is discussed. There are two major aspects of this shell evolution : one is related to the spin-isospin dependent central part of the nucleon-nucleon interaction, while the other is the tensor interaction. I shall mainly discuss the latter case, since the former one has been discussed to some detail. It will be suggested that the tensor interaction can change the shell structure, for instance, by varying the spin-orbit splitting considerably as a function of N and Z.

1. Introduction

I shall discuss, in this talk, on the single-particle structure of exotic nuclei, indicating that the shell structure can be varied in going from stable to exotic nuclei and such changes can be strongly related to certain properties of the nucleon-nucleon (NN) interaction. This paradigm, referred to as shell evolution [1,2], should play one of the key roles in determining structure of exotic nuclei.

The nuclear shell model has been conceived by Mayer and Jensen by identifying its magic numbers and their origin [3]. The study of nuclear structure has been advanced on the basis of the shell structure thus proposed. In stable nuclei, the magic numbers suggested by Mayer and Jensen remain valid, and the shell structure can be understood well in terms of the harmonic oscillator potential with a spin-orbit splitting. Recently, studies on exotic nuclei far from the β-stability line have been started owing to development of radioactive nuclear beams, as discussed extensively in the this conference.

If single-particle energies are calculated by the Woods-Saxon potential, they change as the proton number (Z) or the neutron number (N) varies. In this case, the single-particle energies are shifted basically in parallel, keeping their relative energies (or mutual differences of the energies) almost

unchanged. This kind of change is due to the variation of the potential radius depending on $A(= N + Z)$ and/or the shift of the potential depth associated with N/Z asymmetry. Note that, even with the Woods-Saxon potential, the relative energies can be changed near drip lines owing to varying influences of the centrifugal potential, but such changes are not the subject of this talk.

The shell evolution suggested in [1,2] means that, as N and/or Z changes, such relative energies can vary rather significantly due to the NN interaction, without approaching the dripline. If this energy change becomes sufficiently significant, even the shell gap can nearly disappear or a spin-orbit splitting may be reduced.

2. Proton-neutron spin-flip interaction and the shell evolution

The shell evolution has been discussed in the p-shell and sd-shell already [1]. In order to understand it, we use effective single-particle energies (ESPE's) which include monopole effects from valence nucleons [4,5,6]. Usually, the naive filling configuration is assumed to calculate ESPE's. If relevant ESPE's change significantly, it is called the shell evolution. The shell evolution discussed so far is shown to occur due to a common mechanism related to the spin-isospin dependent NN interaction, i.e., a strong attraction between a proton and a neutron in the spin-flip partner orbits [1]. To be more concrete, if a proton is in $j_>= l + 1/2$ and a neutron is in $j_<= l - 1/2$ (or vive versa), they attract each other. This means that, as the proton $j_>$ orbit is filled, the neutron $j_<$ orbit is lowered and its ESPE becomes smaller.

The major origin of this interaction is the $\tau\tau\sigma\sigma$ part of the central potential, $V_{\tau\sigma}$, which contains a large contribution from the one-pion exchange process [1,2]. The G-matrix interaction should maintain basic features of meson exchange processes, and, in fact, existing G-matrix interactions (with proper renormalization of core polarization) generally have quite large matrix elements for proton-neutron spin-flip interaction [1,7].

It has been pointed out [2] that, since the $V_{\tau\sigma}$ interaction affects spin-isospin properties of nuclei, the shell evolution of this kind should be linked to the Gamov-Teller (GT) and magnetic properties. Along this line, Suzuki, Fujimoto and myself have shown recently that GT and magnetic moments of p-shell nuclei can be much better described if the interaction is improved so as to describe the shell evolution around N=8 [8].

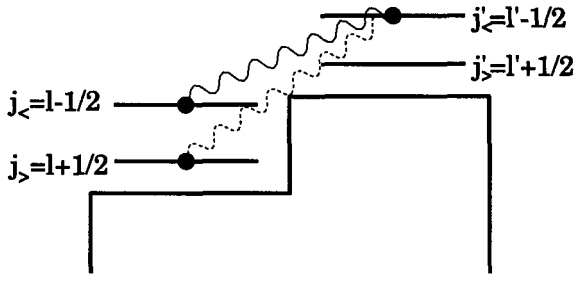

Figure 1. Schematic picture of the monopole interaction produced by the tensor interaction. The solid and dotted wavy lines are monopole interactions with opposite signs.

3. Tensor interaction and the shell evolution

Besides the mechanism discussed above, I would like to present, in this talk, the second mechanism of the shell evolution. As well-known, the one-pion exchange process produces the other important interaction, a tensor interaction. The tensor interaction can be written as

$$V_T = ([\vec{s_1}\vec{s_2}]^{(2)} \cdot Y^{(2)}) f(r), \tag{1}$$

where $\vec{s}_{1,2}$ denotes the spin of nucleon 1 and 2, $[\,]^{(L)}$ means the coupling of two operators in the brackets to an angular momentum (or rank) L, Y implies the spherical harmonics for the relative orientation, and the symbol $(\cdot)$ means a scalar product.

Here, $f(r)$ is a function of the relative distance, r between the two nucleons. For the one-pion exchange process, the function $f(r)$ has been well-known.

We investigate how the (spherical) single-particle levels are shifted by the tensor interaction as other orbits are occupied. Since these single-particle levels are spherical ones, the monopole component of the interaction is responsible. In other words, we extract the following two-body matrix elements from a general interaction (similarly to the first type of the shell evolution [1]):

$$V^T_{j_1,j_2} = \frac{\sum_J (2J+1) < j_1\, j_2 | V | j_1\, j_2 >_{JT}}{\sum_J (2J+1)}, \tag{2}$$

where $< j_1\, j_2 | V | j_1'\, j_2' >_{JT}$ stands for the matrix element of coupled to an angular momentum J and an isospin T. Here, J takes only values satisfying antisymmetrization. We then construct a two-body interaction,

called V_M which is comprised of two-body matrix elements defined by the above equation. Apparently, this interaction, V_M, is monopole, and it represents the angular-averaged, i.e., monopole property of the original interaction, V, which is the tensor interaction in the present case.

In this talk, I discuss situations shown in Fig. 1. Namely, protons are in either $j_> = l + 1/2$ or $j_< = l - 1/2$, while neutrons are in either $j'_> = l' + 1/2$ or $j'_< = l' - 1/2$. We further assume that proton and neutron orbits are of opposite parities. In Fig. 1, neutrons are in the shell just above the proton shell. The generalization of this is straightforward, but we remain in this situation.

With V being the tensor interaction, I found the following identiy,

$$(2j_> + 1)\, V^T_{j_> j'} + (2j_< + 1)\, V^T_{j_< j'} = 0, \quad for\ T = 0\ and\ 1, \tag{3}$$

where j' is either $j'_>$ or $j'_<$. Note that $V^{T=0}_{jj'} = 3 \times V^{T=1}_{jj'}$.

This identity means that the tensor monopole interaction between proton $j_>$ and neutron $j'_<$ has the opposite effect to that between proton $j_<$ and neutron $j'_<$ (See Fig. 1). The same property holds for other but similar combinations of the orbits. For instance, in the closed (sub-) shell picture, the proton $p_{1/2}$ is empty in C isotopes, whereas fully occupied in O isotopes. In the latter case, this tensor monopole pulls down the neutron $d_{5/2}$ orbit, becoming the major reason for the $s_{1/2}$-$d_{5/2}$ inversion between C and O, and affecting the stability of N=14 subshell.

Here, one needs another argument to determine the sign of the effect. This can be given in an intuitive way. In the case that a nucleon on $j_>$ is colliding another on $j'_<$, due to high relative momentum, the spatial wave function of their relative motion is narrowly distributed in the direction of the collision which is basically the direction of the orbital motion. The spins of two nucleons are parallel, giving rise to S=1 basically. Thus, the spatial distribution is narrower in the direction perpendicular to the composite spin S=1. From the analogy to the deuteron, the tensor force works attractively. The same mechanism holds for two nucleons in $j_<$ and $j'_>$. On the other hand, the tensor produces a repulsive effect for two nucleons in $j_>$ and $j'_>$ (or vice versa).

After this mechanism had been found, there have been many numerical works to assess the effects with $\pi + \rho$ or G-matrix potential, and several experimental cases have been noticed [9]. These will be published soon [10], although some of them were presented in the talk. I also mention that predictions can be made based upon the above mechanism [10]. For instance,

the spin-orbit splitting of the $d_{5/2}$ and $d_{3/2}$ of protons becomes smaller from ^{40}Ca to ^{48}Ca [11], and similarly those of protons in the pf-shell becomes smaller from ^{68}Ni to ^{78}Ni. It should be mentioned also that the inversion between the neutron $d_{5/2}$ and $s_{1/2}$ orbits in moving between carbon and oxygen isotopes is also largely related to the tensor interaction. A recent shell model calculation for carbon isotopes has succeeded in explaining small $B(E2)$ value of ^{16}C as presented by Imai in this conference, owing partly to this mechanism.

4. Summary and Perspectives

In summary, I discussed two mechanisms of the shell evolution. As the second mechanism of the shell evolution, I mentioned the tensor interaction. The tensor interaction can change crucially the shell structure of exotic nuclei [10]. The significant role of the tensor interaction as rather direct effects of π and ρ mesons seems to be related to the Chiral Perturbation idea of Weinberg [12]. The $1/N_c$ expansion of QCD supports also the importance of the tensor interaction [13]. Although the tensor effect on the mean field was discussed, for instance, in [14] with the δ-function type tensor interaction leading to a rather different conclusion, the finiteness of the interaction should be important.

Acknowledgments

The author acknowledges collaborations with Prof. T. Suzuki, Dr. R. Fujimoto, Prof. H. Grawe, and Prof. Y. Akaishi. This work has been a part of the RIKEN-CNS joint research project on large-scale nuclear-structure calculations. This work was supported in part by a Grant-in-Aid for Specially Promoted Research (13002001) from the MEXT.

References

1. T. Otsuka, R. Fujimoto, Y. Utsuno, B.A. Brown, M. Honma and T. Mizusaki, Phys. Rev. Lett. **87**, 082502 (2001).
2. T. Otsuka, Prog. Theor. Phys. Suppl. **146**, 6 (2002).
3. M.G. Mayer, Phys. Rev. **75** 1969 (1949); O. Haxel, J.H.D. Jensen and H.E. Suess, Phys. Rev. **75** 1766 (1949).
4. R.K. Bansal and J.B. French, Phys. Lett. **11**, 145 (1964).
5. A. Poves and A. Zuker, Phys. Rep. **70**, 235 (1981).

6. Y. Utsuno, T. Otsuka, T. Mizusaki, and M. Honma, Phys. Rev. C **60**, 054315 (1999).
7. M. Hjorth-Jensen, T.T.S. Kuo and E. Osnes, Phys. Rep. **261**, 125 (1995).
8. T. Suzuki, R. Fujimoto and T. Otsuka, Phys. Rev. C **67**, 044302 (2003).
9. H. Grawe et al., Nucl. Phys. A **704**, 211 (2002).
10. T.Otsuka, T. Suzuki, R. Fujimoto, H. Grawe and Y. Akaishi, to be published.
11. P.D. Cottle and K.W. Kemper, Phys. Rev. C **58**, 3761 (1998).
12. S. Weinberg, Phys. Lett. B **251**, 288 (1990).
13. D.B. Kaplan and A.V. Manohar, Phys. Rev. C **56**, 76 (1997).
14. Fl. Stancu, D.M. Brink, and H. Flocard, Phys. Lett. B **68**, 108 (1977).

SPECTROSCOPY OF ^{13}B VIA ^{4}He(^{12}Be,^{13}Bγ) REACTION

S. OTA†, T. MURAKAMI

Department of Physics, Kyoto University, Kyoto 606-8502, Japan
†*E-mail: ota@nh.scphys.kyoto-u.ac.jp*

S. SHIMOURA, S. MICHIMASA, S. KUBONO, T. TERANISHI, M. NOTANI, M. TAMAKI, E. IDEGUCHI AND T. FUKUCHI

Center for Nuclear Study, University of Tokyo, Saitama 351-0198, Japan

H. IWASAKI AND H. SAKURAI

Department of Physics, University of Tokyo, Tokyo 113-0033, Japan

M. KUROKAWA, T. MOTOBAYASHI, Y. YANAGISAWA, T. MINEMURA, S. TAKEUCHI, N. AOI, Z. ELEKES AND M. ISHIHARA

Institute of Physical and Chemical Research (RIKEN), Saitama 351-0198, Japan

N. IWASA

Department of Physics, Tohoku University, Miyagi 980-8578, Japan

T. GOMI, K. YAMADA, A. SAITO, H. BABA, Y. U. MATSUYAMA, S. KANNO, E. TAKESHITA, K. DEMICHI, H. HASEGAWA, AND K. KURITA

Department of Physics, Rikkyo University, Tokyo 171-8501, Japan

A. ODAHARA

Nishinippon Insutitute of Technology, Fukuoka, 800-0394 Japan

K. MILLER

Michigan State University, USA

Excited states in the ^{13}B nucleus were investigated by a measument of the proton transfer reaction (α,t) at 50 MeV per nucleon in the inverse kinematics. From an analysis on the angular distribution of the ^{13}B for the 4.83-MeV excited state, its spin and parity was assigned to be $1/2^{+}$ for the first time.

1. Introduction

Disappearance of regular magic numbers in neutron-rich nuclei is one of the most interesting phenomena in the nuclei far from the stability line. Since the magic numbers relate to the single-particle levels, this phenomenon may provide a new study for changes in the single-particle states in the unstable nuclei. Relating to N=8 magicity in neutron rich nuclei, we focus on the proton-single particle states in the ^{13}B nucleus by using proton transfer reactions to the ^{12}Be which exhibits disappearance of N=8 magicity[1,2,3,4,5].

According to several experimental reports on ^{13}B; ^{11}B(t,p)^{13}B reaction[6], ^{9}Be(^{14}B,^{13}B)X reaction[7], β delayed neutron decay of ^{14}Be[8], and multi-nucleon transfer reaction[9] on ^{16}O and ^{12}C, the excitation energies of several low-lying states in ^{13}B are well known as shown in Table 1. However, their spins and parities are not assigned except for the suggestion of $3/2^+$, $5/2^+$, $1/2^-$ for the 3.48, 3.68, 4.83 MeV states[7,9], respectively.

In the present study, we aim at assigning spins and parities (J^π) of the known states in ^{13}B by analyzing the angular distribution of the ^{13}B in the one-proton transfer reaction, ^{4}He(^{12}Be,^{13}Bγ), which is expected to populate proton single-particle states.

2. Experiment

The experiment was performed at RIKEN Accelerator Research Facility. A secondary ^{12}Be beam was produced by the projectile fragmentation of a 100 MeV per nucleon primary ^{18}O beam which bombarded a 1.85 g/cm^2-thick Be target. The ^{12}Be beam was separated by the RIKEN Projectile-fragment Separator (RIPS)[10]. The intensity and purity of the secondary beam was 2×10^5 particles per second and 88%, respectively. The ^{12}Be nucleus, having 50 MeV per nucleon in front of the experimental target, was identified event-by-event via the TOF-ΔE method with two 1-mm thick plastic scintillators, located at the first achromatic focus and the final focus. The incident angle of the beam was monitored with two PPAC's[11]. The ^{12}Be nucleus bombarded a 120 mg/cm^2-thick liquid helium target where a proton was picked up and then an excited ^{13}B was producted. Outgoing particles were measured by a hodoscope which consists of 13 ΔE and 16 E plastic scintillators and identified via the TOF-ΔE-E method. The TOF was the flight time between the secondary target and the ΔE plastic scintillator located 3.4 m downstream of the secondary target. The position of the outgoing particles at the hodoscope was extracted from the timing information of two PMT's attached to both ends of each plastic and was used

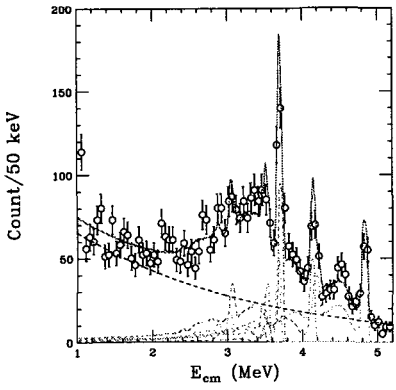

Figure 1. Doppler-corrected gamma-ray energy spectrum obtained in coincidence with ^{13}B.

to determine the scattering angle. The angular acceptance and resolution of the hodoscope was 8.3 degrees and 0.3 degrees (σ), respectively.

Excited states in ^{13}B were identified by de-excition γ rays, which were detected by an array of segmented-Ge detectors[12]. The array consists of six segmented-Ge detectors located at 140 degrees to the beam direction. The detection efficiency of the array are 0.17% for 1.3-MeV γ ray from ^{60}Co standard source. The energy resolution was 16 keV (σ) for the Doppler-corrected 2.1-MeV γ ray from ^{12}Be traveling at $\beta \sim 0.3$.

3. Result

Figure 1 shows a Doppler-corrected γ-ray energy spectrum measured in coincidence with the outgoing ^{13}B. There are peaks corresponding to the six known excited states. The relative intensities of these states was obtained by fitting simulated γ-ray energy spectra to the experimental one. In the simulation, the GEANT4 code[13] was used with assuming all the known excited states and exponential background, taking into account the energy resolution and the angular resolution of each detector. The free parameter was only the normalization factor of each state. The obtained relative intensities are listed in Table 1. The 3.71-MeV and 4.83-MeV excited states were more strongly popublated than the other states. In the other reactions, these states were not strongly populated than the other states. So, these two states may have a single particle nature.

For the highest excited state at 4.83-MeV, we extracted the angular distribution of ^{13}B. The experimental data is indicated by closed circles

Table 1. Relative intensities of excited states measured via four reactions. The error is only statistical one.

Ex (MeV)	Present ^{4}He (^{12}Be,^{13}Bγ)	^{11}B (t,p)^{13}B	^{9}Be (^{14}B,^{13}B)X	^{14}Be β delayed n
3.48	0.06 ± 0.13	0.06	0.6	
3.53	0.31 ± 0.12	0.19		1
3.68	0.48 ± 0.16	0.38	1	
3.71	0.95 ± 0.18	0.25		
4.13	0.59 ± 0.13	1	0.04	
4.83	1	0.03		

Table 2. Optical potentials used in DWBA calculations.

	V_0 (MeV)	r_V (fm)	a_V (fm)	W_0 (MeV)	r_W (fm)	a_W (fm)
^{4}He+^{12}C	75.680	1.277	0.728	13.880	1.885	0.425
^{3}He+^{12}C	108.47	1.020	0.828	18.483	1.171	0.594

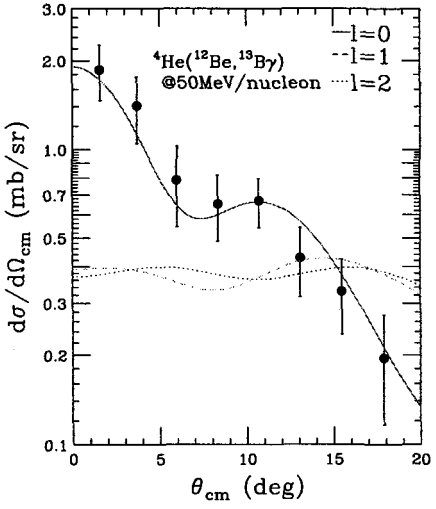

Figure 2. Angular distribution of ^{13}B with DWBA calcuration.

in Fig 2. Since the distribution has a forward peak, transfered angular momentum is expected to be zero. Three curves were obtained via zero-range distorted-wave Born approximation (DWBA) calculations assuming transfered angular momenta l=0, 1, and 2. The set of optical potentials[14,15] used in the calculation is listed in Table 2. The experimental angular distribution is well reproduced by the DWBA calculation with l=0. Since

the ground state of ^{12}Be is 0^+, we assigned $J^\pi=1/2^+$ to the 4.8-MeV excited state.

4. Summary

We measured the proton transfer reaction ^{4}He(^{12}Be,^{13}Bγ) at 50 MeV per nucleon. From the analysis on the angular distribution of the ^{13}B for the 4.83-MeV excited state, we assigned $J^\pi=1/2^+$ to the excited state for the first time. Analysis on the other states is in progress.

The present study shows that the (α,t) reaction in the inverse kinematics at intermediate energy becomes one of the powerful tools for the spectroscopy of neutron-rich nuclei.

Acknowledgements

The authors would like to thank the RIKEN Ring Cyclotron staff members for their support.

References

1. A. Navin *et al.*, Phys. Rev. Lett. **85**, 266 (2000).
2. F. Nunes *et al.*, Nucl. Phys. **A609**, 43 (1996).
3. H. Iwasaki *et al.*, Phys. Lett. **B481**, 7 (2000).
4. H. Iwasaki *et al.*, Phys. Lett. **B491**, 8 (2000).
5. S. Shimoura *et al.*, Phys. Lett. **B560**, 31 (2003).
6. F. Ajzenberg-Selove *et al.*, Phys. Rev. **C 17**, 1283 (1978).
7. V. Guimarães *et al.*, Phys. Rev. **C 61** (2000).
8. N. Aoi *et al.*, Phys. Rev. **C 66** (2002).
9. R. Kalpakchieva *et al.*, Eur. Phys. J. A **7**, 451 (2000).
10. T. Kubo *et al.*, Nucl. Instrum. and Method **B70**, 309 (1992).
11. H. Kumagai *et al.*, Nucl. Instrum. and Method **A470**, 562 (2001).
12. M. Kurokawa *et al.*, IEEE Transactions on Nuclear Science **50**, 1309 (2003).
13. GEANT4 [Online], http://wwwasd.web.cern.ch/wwwasd/geant4/geant4.html.
14. A. Ingemarson *et al.*, Nucl. Phys. **A696**, 3 (2001).
15. A. Ingemarson *et al.*, Nucl. Phys. **A676**, 3 (2000).

This page intentionally left blank

Deformation and shell structure

This page intentionally left blank

ANOMALOUSLY LONG LIFETIME OF 2_1^+ STATE OF ^{16}C

N. IMAI[A], H.J. ONG[B], N. AOI[A], H. SAKURAI[B], K. DEMICHI[C], H. KAWASAKI[C], H. BABA[C], ZS. DOMBRADI[D], Z. ELEKES[A] *, N. FUKUDA[A], ZS. FULOP[D], A. GELBERG[E], T. GOMI[C], H. HASEGAWA[C], K. ISHIKAWA[F], H. IWASAKI[B], E. KANEKO[C], S. KANNO[C], T. KISHIDA[A], Y. KONDO[F], T. KUBO[A], K. KURITA[C], S. MICHIMASA[G], T. MINEMURA[A], M. MIURA[F], T. MOTOBAYASHI[A], T. NAKAMURA[F], M. NOTANI[G], T.K. ONISHI[B], A. SAITO[C], S. SHIMOURA[G], T. SUGIMOTO[F], M.K. SUZUKI,[B], E. TAKESHITA[C], S. TAKEUCHI[A], M. TAMAKI[G], H. WATANABE[A], K. YAMADA[C], K. YONEDA[A] † AND M. ISHIHARA[A]

[A] *RIKEN, Hirosawa 2-1, Wako, Saitama 351-0198, Japan*

[B] *Department of Physics, University of Tokyo, Hongo 7-3-1, Bunkyo, Tokyo 113-0033, Japan*

[C] *Department of Physics, Rikkyo University, Nishi-Ikebukuro 3-34-1, Toshima, Tokyo 171-8501, Japan*

[D] *ATOMKI, H-4001 Debrecen, P.O. Box 51, Hungary*

[E] *Institut für Kernphysik der Universität zu Köln, D-50937 Köln, Germany*

[F] *Department of Physics, Tokyo Institute of Technology, Ookayama 2-12-1, Meguro, Tokyo 152-8551, Japan*

[G] *CNS, University of Tokyo, RIKEN campus, Hirosawa 2-1, Wako, Saitama 351-0198, Japan*

Email: imai@rarfaxp.riken.jp

A new experimental method has been developed to measure the mean-life of the first excited state of ^{16}C. The method uses a concept of the shadow technique with high velocity ($\beta \simeq 0.3$) of the excited nucleus. The mean-life was determined to be $\tau = 77 \pm 14$ (stat) ± 19 (syst) ps. The central value of mean-life corresponds to $B(\mathrm{E2}; 2_1^+ \rightarrow 0_{\mathrm{g.s.}}^+) = 0.63\ e^2\mathrm{fm}^4$, or 0.26 Weisskopf units. This transition strength was found to be anomalously small compared to the empirically predicted value.

*On leave from ATOMKI, Debrecen, Hungary.

†Present address: NSCL, Michigan State University, USA.

1. Introduction

It is known that the neutron-rich carbon isotopes have various unique features. For example, the ground states of odd A nuclei exhibit an irregular sequence of spin-parity; $1/2^+$ for ^{15}C, $3/2^+$ for ^{17}C, and $1/2^+$ for ^{19}C. This is in contrast to the case for the spherical oxygen isotopes with neutron numbers $N = 9$, 11, and 13, for which the spin-parity of $5/2^+$ is favored. Such a phenomenon may be related to a drastic change of nuclear structure such as the modification of shell structure and/or the interplay between different degrees of freedom for the nuclear deformation[1]. Determination of the B(E2) would bring a useful clue to disentangle the exotic nature of the neutron-rich carbon isotopes.

In the present work, the $E2$ transition from the first 2^+ state to the ground 0^+ state in ^{16}C is studied through measurement of the lifetime by a modified recoil shadow method[2]. A standard method for determining B(E2) values of unstable nuclei is the intermediate-energy Coulomb excitation method with unstable nuclear beams[3,4]. However, a fairly large uncertainty remains in B(E2) values determined by this method especially for $Z < 8$ nuclei, since nuclear excitation is comparably strong with Coulomb excitation so that model-independent deduction of the Coulomb contribution becomes difficult. In contrast, the present method is a direct measurement of the lifetime, leading to the determination of B(E2) model-independently.

2. Experiment

The experiment was performed at the RIKEN accelerator research facility. A radioactive beam of ^{16}C was produced by the projectile fragmentation of a 100 AMeV ^{18}O beam. The ^{16}C beam was separated by the RIPS beam line and hit a 370 mg/cm^2 thick Be target to populate the first excited state. A schematic view of the experimental setup is shown elsewhere[5]. The ^{16}C beam had a typical intensity of 2×10^5 particles per second with a purity of about 97%. The average beam energy in the target was 34.6 AMeV. The excited nucleus emerged from the target with a speed of as fast as $\beta = 0.24$. The target was surrounded by a 5 cm-thick lead slab. The slab had an outer frame of 60×60 cm^2 and an inner hole of 6.2 cm ϕ. The inner hole surrounded a beam tube housing the ^{9}Be target. For the sake of later discussion, the upstream surface of the slab was defined as $z = 0.0$ cm. The de-excitation γ rays from the inelastically excited ^{16}C were detected by thirty-two NaI(Tl) scintillation detectors. The NaI(Tl) array was divided

into two rings, R1 and R2. R1 (R2) consisted of 14 (18) detectors with their centers placed at 120 (108) degrees with respect to the beam line. The emittance of projectiles and scattering angles of ejectiles were measured by using three parallel plate avalanche counters. Two of them were placed upstream of the target, while the third was placed downstream of the target. Ejectiles were identified with a plastic scintillator hodoscope located most downstream of the beam line.

The efficiencies of the γ-ray detectors were determined by the geometry of the R1 and R2 detectors with respect to the lead slab, and the γ-ray emission point z. With the velocity of $\beta = 0.24$, a mean-decay length for a mean-life $\tau = 100$ ps is as long as 0.74 cm. When the target is placed at $z = 0.0$ cm, the γ rays emitted in flight between $z = 0.0$ and 2.2 cm can reach the centers of the NaI crystals of R1 without screening by the lead slab ($z = 0.0$ and 0.7 cm for R2). For a τ of as long as a few tens ps, some measured γ rays pass through the lead slab. The intensities of those γ rays attenuate exponentially to the path length in the slab. Since the path length to R2 in the slab will be longer than that to R1 as the emission point is moved further downstream, the relative efficiency of R2 with respect to R1 decreases. This difference between efficiencies results in dependence of the γ-ray yield ratio (R1/R2) on τ. Thus, τ can be determined from the R1/R2 γ-ray yield ratio.

3. Result and Discussion

We measured the de-excitation γ-ray with the target placed at $z = 0.0$ cm. In addition, another measurement was performed with a different target position $z = 1.0$ cm in order to cross-check the deduced τ for each target position. The measured R1/R2 ratios for $z = 0.0$ and 1.0 cm were 1.06 ± 0.03 and 1.70 ± 0.06, respectively. The uncertainties stand for the statistical errors in a standard deviation.

To obtain the relation between the R1/R2 ratio and τ, Monte Carlo simulations were performed using GEANT3 code for both target positions. The simulation took into account the geometry, the beam profile, and the angular distribution of γ-rays. The simulated emission-point and γ-ray energy dependence of R1/R2 ratio were verified by comparison with the measurements using standard sources. The measured emittance and scattering angles were used for the beam profile in the simulation. The angular distribution was calculated using the ECIS79 code with two sets of optical model potential[7,8]. The results of the simulations are exhibited in Fig. 1

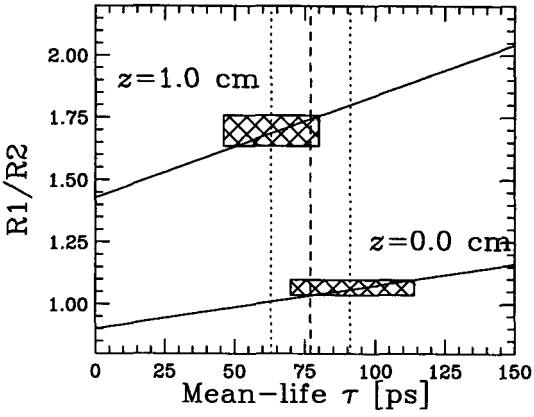

Figure 1. Correlation between the R1/R2 ratio and the mean-life τ. Two solid lines indicate the results of Monte Carlo simulation for the target position $z = 0.0$ and 1.0 cm. Hatched zones indicate the measured R1/R2 ratios (vertical width) and the corresponding mean-lives (horizontal width). Dashed line represents the mean value of the adopted τ, while dotted lines denote the range of statistical error.

together with the measured R1/R2 ratios. From overlapping areas of simulated lines and experimental R1/R2 ratios, the τ were determined to be 92 ± 22 ps and 63 ± 17 ps for the target positions $z = 0.0$ and 1.0 cm, respectively. These two values were statistically consistent. We adopted a weighted average of these values, 77 ± 14 ps, as the final value.

The systematic error derived mainly from the ± 0.5 mm uncertainty of the target position. Due to this uncertainty, the τ changed by $\pm 20\%$. Additionally, due to the choice of the optical model potential sets, the central value of τ changed by 5%. The systematic error was estimated to 25% by adding these two values. As the results, τ was determined to be 77 ± 14 (stat) ± 19 (syst) ps.

The central value of τ corresponds to $B(\mathrm{E2}) = 0.63\ e^2\mathrm{fm}^4$, or 0.26 Weisskopf units. In Weisskopf units, the present $B(\mathrm{E2})$ was found to be the smallest of $B(\mathrm{E2})$ values of all even-even nuclei.

In the frame work of the liquid drop model, $B(\mathrm{E2})$ is inversely proportional to the excitation energy of the 2_1^+ state $E(2_1^+)$[6]. This systematics can be written as $B(E2)_{\mathrm{sys}} = 6.47 \times Z^2 A^{-0.69} E(2_1^+)^{-1}$. In Fig. 2(a), $B(\mathrm{E2})$ and $E(2_1^+)$ for even-even carbon isotopes are shown by a function of neutron number. When the neutron number changes from 8 to 10, $E(2_1^+)$ suddenly decreases from 7.01 to 1.77 MeV. Accordingly, the $B(E2)_{\mathrm{sys}}$ increases from 5.42 to 19.6 $e^2\mathrm{fm}^4$. However, the measured $B(\mathrm{E2})$ of ^{16}C

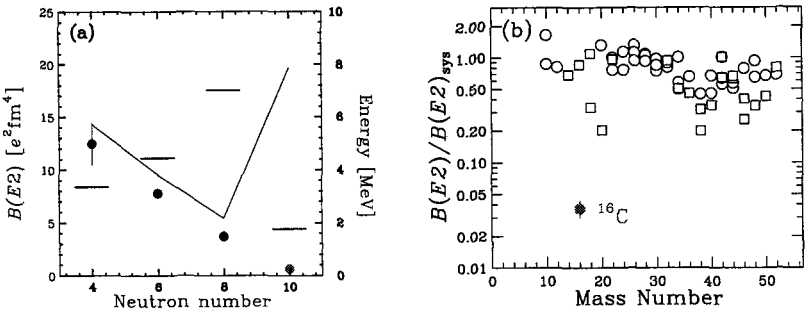

Figure 2. (a) B(E2) and excitation energy of the 2_1^+ state of even-even carbon isotopes. Horizontal bars stand for the excitation energies. Filled circles indicate the experimental B(E2). Solid line exhibits $B(\mathrm{E2})_{\mathrm{sys}}$. (b) Ratios of the experimental B(E2) to $B(\mathrm{E2})_{\mathrm{sys}}$ for the even-even nuclei smaller than $A = 50$. Circle (square) stands for the open (closed)-shell nucleus.

decreases to 0.63 $e^2\mathrm{fm}^4$, exhibiting clear violation of the systematics. This anomaly can be emphasized by comparison with other even-even nuclei as shown in Fig. 2(b). The ratio of the present B(E2) to the corresponding $B(\mathrm{E2})_{\mathrm{sys}}$ is 0.036, being much smaller than those for other nuclei by an order of magnitude. This anomaly is open for challenges of any nuclear theories.

Acknowledgments

The authors would like to thank the RIKEN Ring Cyclotron staff for co-operation. N. I. is grateful for the financial assistance from the Special Postdoctoral Researcher Program of RIKEN. The present work was supported in part by a Grant-in-Aid for Scientific Research (No. 1520417) from Monbukagakusho (Japan) and OTKA 042733 (Hungary).

References

1. Y. Kanada-En'yo and H. Horiuchi, Phys. Rev. C **55**, 2860 (1997).
2. H. Backe, *et al.*, Z. Phys. **A285**, 159 (1978).
3. T. Motobayashi, *et al.*, Phys. Lett. **B346**, 9 (1995).
4. T. Glasmacher, Ann. Rev. Nucl. and Part. Sci. **48**, 1 (1998).
5. N. Imai, *et al.*, Phys. Rev. Lett., in press (2004).
6. S. Raman, C.W. Nestor, Jr., and K.H. Bhatt, Phys. Rev. C **37**, 805 (1988).
7. C.-C. Sahm, *et al.*, Phys. Rev. C **34**, 2165 (1986).
8. Mariá-Ester Brandan, Phys. Rev. Lett. **60**, 784 (1988).

NEW STRUCTURE PROBLEMS IN CARBON ISOTOPES

H. SAGAWA,* X. R. ZHOU †AND X. Z. ZHANG ‡

Center for Mathematical Sciences, University of Aizu
Aizu-Wakamatsu, Fukushima 965-8560, Japan
E-mail: sagawa@u-aizu.ac.jp

TOSHIO SUZUKI

Department of Physics, College of Humanities and Sciences, Nihon University
Sakurajosui 3-25-40, Setagaya-ku, Tokyo 156-8550, Japan

Structure of Carbon isotopes are investigated by deformed Skyrme Hartree-Fock and shell model calculations. We point out that the quadrupole deformations of C−isotopes have a strong isotope dependence as a manifestation of nuclear Jahn-Teller effect. It is shown also that the quadrupole moments and the magnetic moments of the odd C isotopes depend clearly on assigned configurations, and their experimental data will be useful to determine the spin-parities and the deformations of the ground states of these nuclei. The electric quadrupole (E2) transitions in even C isotopes are also studied. The isotope dependence of the E2 transition strength is reproduced properly, although the calculated strength overestimates extremely small observed value in ^{16}C.

1. DEFORMATION OF CARBON ISOTOPES

We investigate the neutron number dependence of deformation properties along the chain of C−isotopes. For this purpose, we perform deformed HF+BCS calculations with a Skyrme interaction SGII. The axial symmetry is assumed for the HF deformed potential. The pairing interaction is taken to be a density dependent pairing interaction in BCS approximation. The pairing strength is taken to be -410 MeV·fm^3 for both neutrons and protons [1]. A smooth energy cut-off is employed in the BCS calculations [2].

*This work is supported in part by the Japanese Ministry of Education, Culture ,Sports, Science and Technology by Grant-in-AID for Scientfic Research under the program number (C(2)) 12640284.

†On leave from Department of Physics, Tsinghua University, Beijing, China

‡On leave from China Institute of Atomic Energy , Beijing, China

Fig. 1 shows the binding energy surfaces for even-mass C isotopes as a function of the quadrupole deformation parameter β_2. The spin–orbit interaction of SGII interaction is reduced to be 60% of the original strength. The energy minimum in ^{12}C appears at oblate deformation with $\beta_2 = -0.32$. The energy minimum becomes spherical in ^{14}C because of the neutron closed shell effect. For heavier C isotopes ^{16}C and ^{18}C, two minima appear both in the prolate and oblate sides. In ^{18}C, the ground state has the largest deformation at β_2=0.36, while the local minimum appears at the oblate side at $\beta_2 \sim -0.3$. The deformation becomes oblate in ^{20}C and ^{22}C. The HF calculations with the original spin-orbit strength gives a spherical shape for ^{22}C.

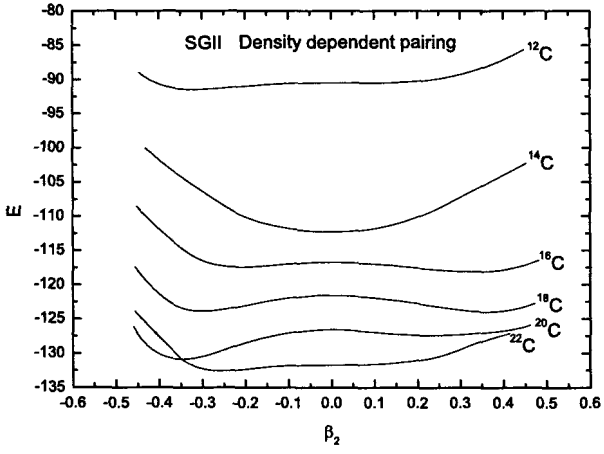

Figure 1. Deformed HF calculations of C isotopes with SGII interaction. The strength of spin–orbit force is modified to be 60% of the original one.

A blocked deformed Skyrme HF+BCS calculation are performed for odd Carbon isotopes. The results shows that the ground state of ^{17}C is prolate with $J^\pi = \frac{3}{2}^+$ while that of ^{19}C is oblate with $J^\pi = \frac{3}{2}^+$. In ^{19}C, the energy minimum of $J^\pi = \frac{1}{2}^+$ is almost degenerate with that of $J^\pi = \frac{3}{2}^+$ with almost the same oblate deformation $\beta_2 \sim -0.36$. These spin-parities of the ground states are consistent with our shell model calculations [1]. The spin of the ground state of ^{17}C has been assigned as $3/2^+$ in the magnetic moment measurement [3]. The spin of ^{19}C is assigned as $1/2^+$ in the Coulomb break-up reactions [4] while there is still controversial argument on the experimental assignment in Ref. [5].

2. Q-MOMENTS, μ-MOMENTS AND E2 TRANSITIONS

We study electromagnetic moments and transitions in C isotopes by the shell model calculations [6]. We first discuss on the Q-moments. The WBP10 interaction is adopted within the $0\hbar\omega$ space with the inclusion of effective charges. State dependent polarization charges, e_{pol}(SA) [7], given by the microscopic particle vibration coupling model (Hartree-Fock + Random Phase Approximation) are used. The polarization charge can be parameterized as

$$e^{II}_{pol}/e = a\frac{Z}{A} + b\frac{N-Z}{A} + (c + d\frac{Z}{A}\frac{N-Z}{A})\tau_z \qquad (1)$$

with a=0.82, b=−0.25, c=0.12 and d=−0.36 to reproduce the values of e_{pol}(SA) for ^{12}C and ^{16}C. Both the neutron (ν) and proton (π) polarization charges decrease as the neutron excess increases.

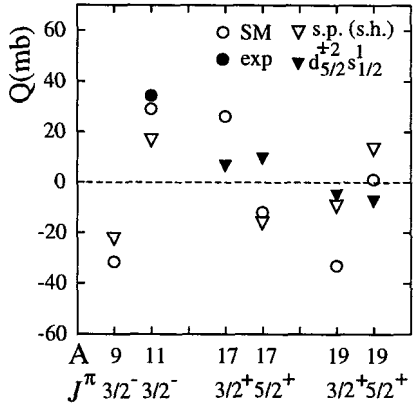

Figure 2. Q-moments for the odd C isotopes. Open circles denote the results of the shell model calculations obtained with the use of $e_{pol}(SA)$. Open triangles denote single-particle or -hole values, while filled triangles give results of the $0d^{\pm 2}_{5/2}1s_{1/2}$ configuration. These values include the effects of the polarization charges, e^{II}_{pol}. The filled circle is the experimental value for ^{11}C [8].

The Q-moments obtained by using these polarization charges are shown in Fig. 2. Open circles denote results of the shell model calculations with the use of e^{SA}_{pol}. Single-particle or -hole values with the use of e^{II}_{pol} are given by open triangles. The configurations for ^{9}C and ^{11}C are $\nu p_{3/2}$ and $\nu p^{-1}_{3/2}$, respectively. The configurations for ^{17}C and ^{19}C are $\nu d_{5/2}1s^2_{1/2}$ and $\nu d^{-1}_{5/2}$ ($\nu d^5_{5/2}$), respectively, for the $5/2^+$ state. For the $3/2^+$ state of ^{17}C, a case for a single particle configuration of $\nu d_{3/2}$ is given.

Filled triangles are obtained for $\nu d_{5/2}^{\pm 2} 1s_{1/2}$ configuration with the use of e_{pol}^{II}. The $\nu d_{5/2}^{2}(J=2)1s_{1/2}$ and $\nu d_{5/2}^{-2}(J=2)1s_{1/2}$ are possible simple configurations for ^{17}C and ^{19}C, respectively, since the $\nu d_{5/2}^{3}$ or $\nu d_{5/2}^{3} 1s_{1/2}^{2}$ configuration corresponding to the middle of the $d_{5/2}$ shell results in the vanishing of the Q-moments. The Q-moments are given by $\mp\frac{2}{5} e_{pol}^{n} Q_{sp}(d_{5/2})$ for $3/2^+$ and $\mp\frac{4}{7} e_{pol}^{n} Q_{sp}(d_{5/2})$ for $5/2^+$ in the case of the $\nu d_{5/2}^{\pm 2}(J=2)1s_{1/2}$ configuration. Here, e_{pol}^{n} is the neutron polarization charge and $Q_{sp}(d_{5/2})$ is the single particle value of the Q-moment for $d_{5/2}$. Note that the signs of the Q-moments for ^{17}C and ^{19}C are opposite.

The shell model values of the Q-moments are obtained by the admixture among these configurations, and their magnitudes are usually enhanced compared to those of the simple configurations. Nevertheless, the difference of the signs between ^{17}C and ^{19}C can be understood from those of the simple configurations.

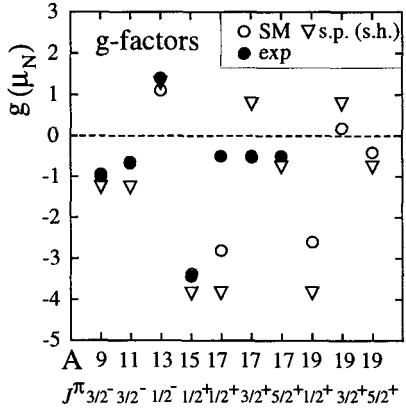

Figure 3. Magnetic moments for the odd C isotopes. Open circles show the results of the shell model calculations, while filled circles give experimental values [9,10,11]. In case of $3/2^+$ state in ^{17}C, the calculated g-factor coincides with the observation [3]. Open triangles denote the single-particle or -hole values.

Calculated values for the magnetic (μ) moments are shown in Fig. 3. Here, $g_s^{eff}/g_s^{free} = 0.9$ is used for neutron. The values of the μ moments are found to be sensitive to the configurations as in the case for the Q-moments, which is useful to find out the spin-parities and the deformations of the ground states of these nuclei.

Let us now discuss on the E2 transitions in the even C isotopes. Calculated and experimental $B(E2)$ values for the $2_1^+ \rightarrow 0_{g.s.}^+$ transitions are

shown in Fig. 4. The shell model values obtained with the use of e^{II}_{pol} are larger than the experimental values except for ^{10}C, for which larger effective charges of $e_p = 1.5$ and $e_n = 0.8$ are needed. For $^{12\sim16}$C, the isotope dependence of the observed values [12,13] are well explained by that of e^{II}_{pol}, but their magnitudes are smaller than the calculation. In particular, the observed $B(E2)$ value is quite small for ^{16}C [13], which suggests some exotic structure yet unknown in the isotopes, for example, the shape coexistence of prolate and oblate deformations expected from the deformed HF calculations. It would be also interesting to find out if the $B(E2)$ value increases for ^{18}C as the calculation predicts. This increase comes from that of the neutron contribution.

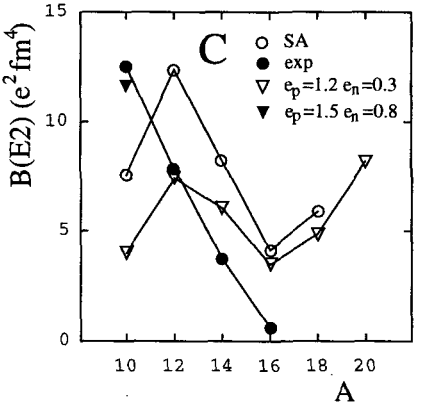

Figure 4. $B(E2)$ values for the $2^+_1 \rightarrow 0_{g.s.}$ transitions in even C isotopes. Open circles show the results of the shell model calculation with the use of the polarization charges e^{II}_{pol} given by Eq. (6). Open and filled triangles are obtained with $e_p = 1.2$, $e_n = 0.3$ and $e_p = 1.5$, $e_n = 0.8$, respectively. Filled circles denote experimental values [12,13].

3. SUMMARY

We have studied the isotope dependence of deformation in C nuclei by using the deformed HF calculations with BCS pairing approximation. We found a clear isotope dependence of the deformation change as a manifestation of nuclear Jahn–Teller effect. The configuration dependence of the Q-moments and μ-moments in the odd C isotopes, which can be attributed to the shell effects, is also pointed out by using the shell model wave functions. This dependence can be used to determine the spin-parities as well as the deformation properties of the ground states of the isotopes. The isotope dependence of the $B(E2)$ values in even C isotopes is reproduced well by

the calculations, while the experimental values are found to be smaller in $^{12\sim16}$C, in particular, in ^{16}C where the observed $B(E2)$ value almost vanishes. This suggests an exotic structure of ^{16}C still to be found out.

References

1. T. Suzuki, H. Sagawa, and K. Hagino, in the Proceedings of the International Symposium on "Frontiers of Collective Motions (CM2002)", (to be published); H. Sagawa, T. Suzuki and K. Hagino, Nucl. Phys. A**722**, 183 (2003).
2. M. Bender, K. Rutz, P.-G. Reinhard, and J.A. Maruhn, Eur. Phys. J. **A8**, 59 (2000).
3. H. Ogawa et al., Euro. Phys. J. A**13**, 81 (2002).
4. D. Bazin et al., Phys. Rev. C**57**, 2156 (1998).
   T. Nakamura et al., Phys. Rev. Lett. **83**, 1112 (1999).
   V. Maddalena et al., Phys. Rev. C**63**, 024613 (2001).
5. Rituparna Kanungo, I. Tanihata, Y. Ogawa, H. Toki and A. Ozawa, Nucl. Phys. A**677**, 171 (2000).
6. E. K. Warburton and B. A. Brown, Phys. Rev. C**46**, 923 (1992); OXBASH, the Oxford, Buenos-Aires, Michigan State, Shell Model Program, B. A. Brown et al., MSU Cyclotron Laboratory Report No. 524, 1986.
7. H. Sagawa and K. Asahi, Phys. Rev. C**63**, 064310 (2001).
8. *Table of Isotopes*, eds. by R. B. Firestone et al., (Wiley, New York, 1996).
9. K. Matsuta et al., Nucl. Phys. A**588**, 153c (1995).
10. P. Raghaven, Atomic Data Nucl. Data Tables **42**, 189 (1989).
11. K. Asahi et al,
12. S. Raman et al, Atomic Data Nucl. Data Tables **36**, 1 (1987).
13. N. Imai et al., these proceedings.

A SELF-CONSISTENT QRPA STUDY OF QUADRUPOLE COLLECTIVITY AROUND ^{32}MG

MASAYUKI YAMAGAMI
Department of Physics, Graduate School of Science,
Kyoto University, Kyoto 606-8502, Japan
E-mail:yamagami@ruby.scphys.kyoto-u.ac.jp

NGUYEN VAN GIAI
Institut de Physique Nucléaire, IN_2P_3-CNRS,
91406 Orsay Cedex, France
E-mail:nguyen@ipno.in2p3.fr

On the basis of the Hartree-Fock-Bogoliubov (HFB) plus quasiparticle random phase approximation method (QRPA) based on the Green's function approach with Skyrme force, we discuss the anomalous E2 properties of the first 2^+ states in neutron-rich nuclei ^{32}Mg and ^{30}Ne. The B(E2) values and the excitation energies of the first 2^+ states are well described within HFB plus QRPA calculations with spherical symmetry. We conclude that pairing effects account largely for the anomalously large B(E2) values and the low excitation energies in ^{32}Mg and ^{30}Ne.

1. Introduction

The observed anomalous E2 properties in ^{32}Mg and ^{30}Ne, the large B(E2) values and the low excitation energies, are clear evidences of the vanishing of the N=20 shell closure.[1,2] Several theoretical studies have shown the importance of the neutron 2p-2h configurations across the N=20 shell gap to describe these anomalous properties (e.g.[3]). The 2p-2h configurations imply deformation of these nuclei, however, it is under great debate whether ^{32}Mg is deformed or not. The observed energy ratios $E(4_1^+)/E(2_1^+)$ is 2.6 in ^{32}Mg [4,5]. This value is in between the rigid rotor limit 3.3 and the vibrational limit 2.0. The B(E2) value (in single-particle units) is 15.0±2.5 in ^{32}Mg, and this value is smaller than in deformed Mg isotopes (21.0±5.8 in ^{24}Mg, 19.2±3.8 in ^{34}Mg [6]). Moreover, in mean-field calculations, irrespective to relativistic or non-relativistic, the calculated ground states in ^{32}Mg have been found to be spherical (e.g.[7]). Generally speaking, the neutron

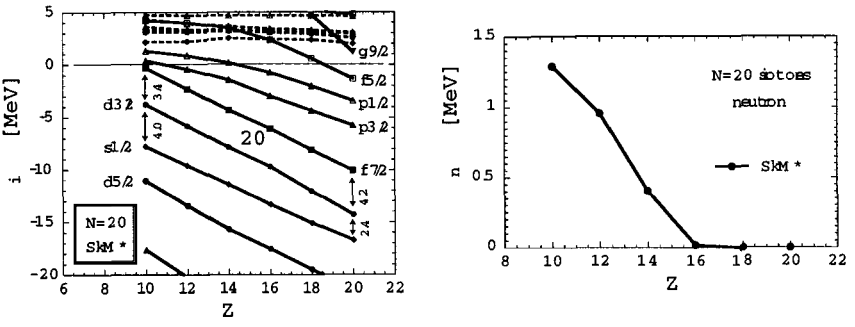

Figure 1. HF neutron single-particle levels and the neutron pairing gaps in N=20 isotones calculated with SkM*. Single-particle levels represented by solid lines correspond to bound and resonance-like states, dashed lines to positive energy discretized states.

2p-2h configurations can originate not only from deformation but also from neutron pairing correlations. In ^{32}Mg these two effects may coexist and help to make the anomalous E2 properties. In the previous studies it is not clear which effect is more essential to describe the anomalous properties.

We have performed HFB plus QRPA calculations with Skyrme force for the first 2^+ states in N=20 isotones.[8] The QRPA equations are solved in coordinate space by using the Green's function method.[8,9] To emphasize the role of neutron pairing correlation, spherical symmetry is imposed. The residual interaction is consistently derived from the hamiltonian density of Skyrme force that has an explicit velocity dependence. A detailed account of the method can be found in Ref.[8]. We obtained a good agreement not only qualitatively but also quantitatively with the experimental results.

2. Ground state properties in N=20 isotones

The ground states are given by Skyrme-HFB calculations. The Skyrme parameter SkM* and the density-dependent pairing interaction, $V_{pair}(\boldsymbol{r},\boldsymbol{r}') = V_{pair}[1-\rho(\boldsymbol{r})/\rho_c]\delta(\boldsymbol{r}-\boldsymbol{r}')$, are adopted. $\rho_c = 0.16$ fm^{-3} is fixed. The strength $V_{pair} = -418$ MeV·fm^{-3} is determined so as to reproduce the experimental neutron pairing gap in ^{30}Ne. The quasiparticle cut-off energy is taken to be $E_{cut} = 50$ MeV. Fig.1 shows the neutron single-particle levels in N=20 isotones calculated in HF. The size of the N=20 shell gaps change slowly, because $2d_{3/2}$ and $1f_{7/2}$ orbits have high centrifugal barriers. On the other hand, the calculated neutron pairing gaps change considerably from 1.26 MeV in ^{30}Ne to zero in ^{38}Ar (Fig.1). The mechanism can be understood by the change of the level density in the fp shell. As close to

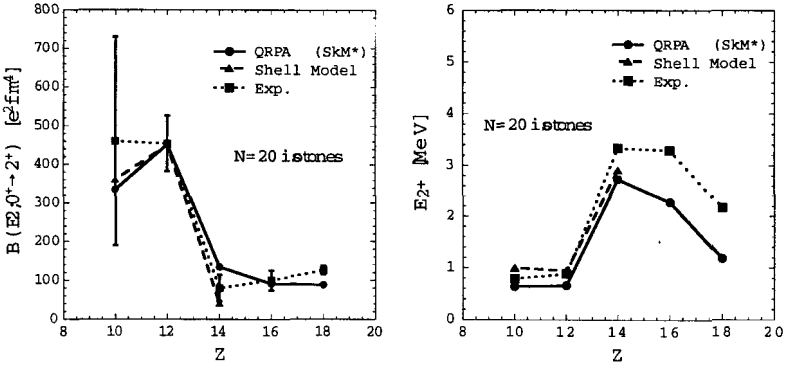

Figure 2. The $B(E2, 0_1^+ \rightarrow 2_1^+)$ transition probabilities and excitation energies of the first 2^+ states in N=20 isotones calculated in QRPA with SkM*. For comparison the available experimental data [1,2] and the results of shell model [3] are shown.

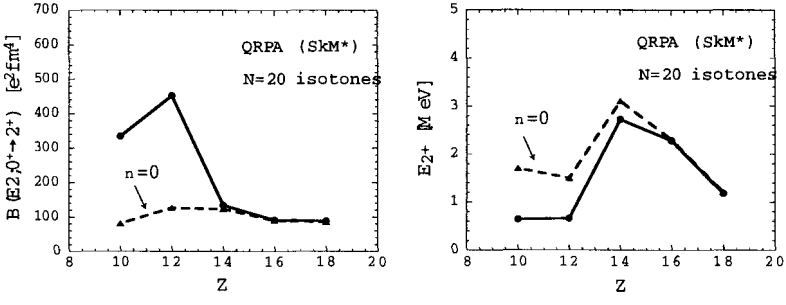

Figure 3. The $B(E2, 0_1^+ \rightarrow 2_1^+)$ values and the excitation energies of the first 2^+ states in N=20 isotones calculated with/without neutron pairing correlations. Proton pairing is included in both cases.

the neutron drip-line, the single-particle energy (SPE) of the high-l orbit $1f_{7/2}$ change almost linearly while the changes of $2p_{3/2}$ and $2p_{1/2}$ SPEs become very slow. Moreover, the spin-orbit splitting of $2p_{3/2}$ and $2p_{1/2}$ states becomes smaller. Because of these different l-dependences of the SPEs, the level density in the fp shell becomes higher in ^{32}Mg and ^{30}Ne. Within HFB calculations with spherical symmetry, the N=20 shell gap is naturally broken by neutron pairing correlations.

3. E2 properties in N=20 isotones

We have calculated the first 2^+ states in N=20 isotones in HFB plus QRPA calculations with spherical symmetry. Our aim is to investigate whether

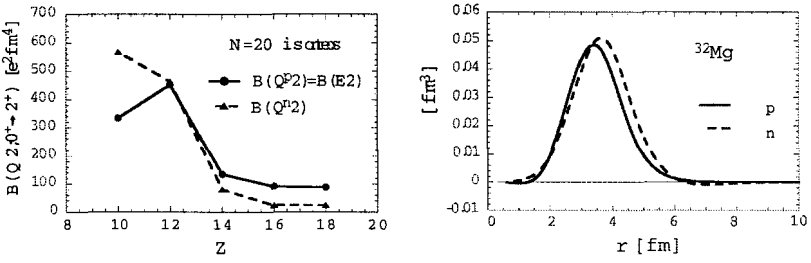

Figure 4. The proton and neutron transition probabilities $B(Q^{\tau}2;0^+ \rightarrow 2^+)$ in N=20 isotones, and the transition densities in ^{32}Mg calculated by QRPA with SkM*.

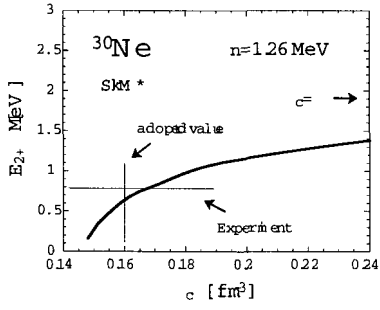

Figure 5. The excitation energy of the first 2^+ state in ^{30}Ne as a function of ρ_c. The pairing strength is determined so as to get the experimental pairing gap $\Delta_n = 1.26$ MeV at each ρ_c. The limit $\rho_c = \infty$ corresponds to the volume-type pairing.

these 2^+ states can be described as vibrational states built on the spherical ground states. In Fig.2 our QRPA results are compared with the available experimental data[1,2] and the results of shell model.[3] The QRPA calculations have been done with SkM* and the fixed pairing strength. The general properties of the first 2^+ states in N=20 isotones, especially large quadrupole collectivity in ^{32}Mg and ^{30}Ne, are well reproduced. Without neutron pairing correlations, we cannot explain the anomalous E2 properties (Fig.3). Under these considerations, we can conclude that the large quadrupole collectivity in ^{32}Mg and ^{30}Ne appears thanks to the neutron pairing correlations. To understand the mechanism that neutron pairing correlations help to make the large B(E2) values, we calculated the neutron transition probability $B(Q^n2)$. If neutron pairing correlations exist, the $B(Q^n2)$ value can be large and the surface of neutron density becomes soft (Fig.4). In this situation, at the first stage, an electric external field makes the proton density of the spherical ground state vibrate in small

amplitude. This proton vibration makes neutrons vibrate by coherence between protons and neutrons. This neutron vibration can be very large, because neutron density is very soft thanks to the neutron pairing correlations. Finally, this large neutron vibration makes protons vibrate again by coherence between protons and neutrons, and this proton vibration becomes very large. The transition density in ^{32}Mg clearly exhibits this situation that the proton and neutron densities vibrate altogether coherently (Fig.4). The peak position of the neutron transition density is slightly outside the nucleus due to the presence of neutron skin. We expect that the nature of this vibrational state is sensitive to the surface properties. Fig.5 shows the excitation energy of the first 2^+ state in ^{30}Ne as a function of ρ_c. This state is very sensitive to ρ_c, and $\rho_c = 0.16$ fm^{-3} gives $E_{2+} = 0.64$ MeV that is close to the experimental observation 0.791(26) MeV.[2] The information of low-lying collective states in neutron-rich nuclei may help to pin down the density dependence of pairing interactions.

4. Conclusions

We have studied the first 2^+ states in N=20 isotones by the HFB plus QRPA with Skyrme force. Because of the different behaviors of the neutron $1f$ and $2p$ orbits around zero energy, the neutron pairing correlations appear. This mechanism breaks the N=20 magicity in ^{32}Mg and ^{30}Ne. Within QRPA calculations with spherical symmetry, the B(E2) values and the excitation energies of the first 2^+ states in N=20 isotones including ^{32}Mg and ^{30}Ne are well described. The existing experimental data are reproduced quantitatively. The important role of the neutron pairing correlations is emphasized. In the real ^{32}Mg nucleus, both neutron pairing and deformation effects may coexist and help to make the large B(E2) value, but our calculation shows that neutron pairing correlations are essential.

References

1. T. Motobayashi, *et al.*, Phys. Lett. 346B (1995) 9.
2. Y. Yanagisawa, *et al.*, Phys. Lett. B 566 (2003) 84.
3. Y. Utsuno, T. Otsuka, T. Mizusaki, M. Honma, Phys. Rev. C60 (1999) 054315.
4. K. Yoneda, *et al.*, Phys. Lett. 499B (2001) 233.
5. D. Guillemaud-Mueller, Eur. Phys. J. A 13 (2002) 63.
6. H. Iwasaki, *et al.*. Phys. Lett. 522B (2001) 227.
7. P. -G. Reinhard, *et al.*, Phys. Rev. C60 (1999) 014316.
8. M. Yamagami, Nguyen Van Giai, preprint nucl-th/0307051.
9. E. Khan, *et al.*, Phys. Rev. C66 (2002) 024309.

G-FACTOR MEASUREMENT FOR ^{19}N

D. KAMEDA, K. ASAHI*, H. MIYOSHI, K. SHIMADA, G. KATO
S. EMORI AND G. KIJIMA

Department of Physics, Tokyo Institute of Technology, 2-12-1 Ookayama, Meguro-ku, Tokyo 152-8550, Japan

H. UENO, A. YOSHIMI, H. WATANABE, T. HASEYAMA, Y. KOBAYASHI,
J. MURATA† AND W. SATO‡

RIKEN, 2-1, Hirosawa, Wako-shi, Saitama 351-0198, Japan

H. OGAWA

Photonics Research Institute, AIST, Umezono 1-1-1, Tsukuba, Ibaraki 305-8568, Japan

The magnetic moment of ^{19}N was measured by using a β-NMR method and a spin-polarized ^{19}N beam from the fragmentation reaction. As a result, the g value for the ^{19}N ground state, $g = 0.61 \pm 0.03$(preliminary), was obtained. The value was compared with those of ^{15}N and ^{17}N. Contrary to shell-mode predictions that the g value should increase with increasing number of neutrons in the *sd* shell, the obtained g for $^{19}N_{g.s.}$ is significantly smaller than the g factor for $^{17}N_{g.s.}$.

1. Introduction

The magnetic moments of odd-mass nitrogen isotopes have an exclusive character which is related to the $p_{1/2}$-valence orbital. In contrast to the well known observation that almost all of the measured nuclear magnetic moments are found inside the Schmidt lines due to the core polarization effect, the magnetic moment of ^{15}N and also that of ^{17}N [2] fall outside the Schmidt lines. These properties can be understood from the Arima-Horie

*also at riken

†present address: *department of physics, rikkyo university, 3-34-1 nishi-ikebukuro, toshima, tokyo 171-8501, japan*

‡present address: *department of chemistry, osaka university, 1-1, machikaneyama, toyonaka, osaka, 560-0043, japan*

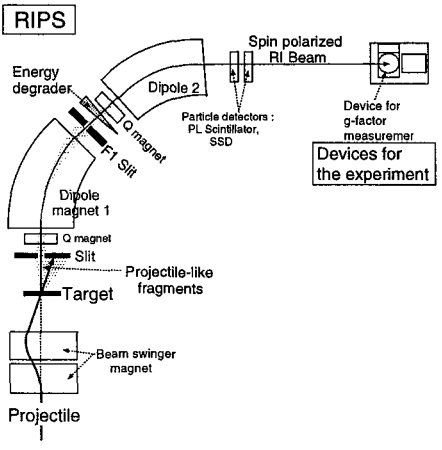

Figure 1.
RIKEN projectile-fragment separator RIPS. The emission angles and momenta were selected in order to obtain the spin polarized RI beam.

formula [1]: the core polarizations should vanish in the case of $p_{1/2}$-valence orbital if the spatial dependence of the residual interactions responsible for the core polarizations are treated as of the δ-function type. The size of deviation in g for a neutron-rich nitrogen isotopes ^{17}N is larger than that for ^{15}N. It is shown in Ref. 2 that the configurations in which two neutrons in the *sd*-shell are coupled to $J^\pi = 2^+$ are the major contributions to the deviation of g in this direction. Considering the increased number of neutrons in the *sd*-shell, the g factor for ^{19}N should be even larger than ^{17}N. Shell model calculations predict, in fact, that the g factor for ^{19}N which should be larger than that of ^{17}N.

2. Experimental Procedure

The nuclear moment measurements in this region have been enabled by combining the β-NMR method with a technique to produce spin-polarized radioactive nuclei via the fragmentation reaction [2-7]. The present experiment was performed at the RIKEN Accelerator Research Facility. The ^{19}N was obtained from the fragmentation reaction of a ^{22}Ne projectile at an energy of 110 MeV/nucleon on a carbon target of 546 mg/cm^2 thickness. By using the projectile-fragment separator RIPS [8], the ^{19}N fragments were separated from the other fragments, as shown in Fig. 1. In order to produce spin polarization in the fragment nuclei, only those with the emission angles $2.6° \sim 6.0°$ and the outgoing momenta $8.18 \sim 8.69$ GeV/c were accepted by RIPS.

To perform a nuclear magnetic resonance (NMR) experiment, the polar-

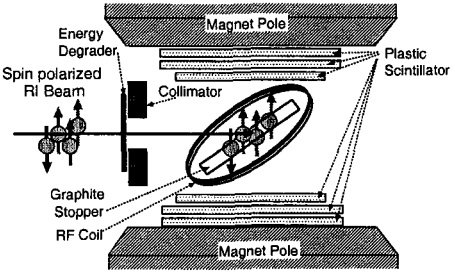

Figure 2.
β-NMR setup. Spin polarized beam of ^{19}N fragments passed through an energy degrader, and were implanted in a graphite stopper. For more details, see the text.

ized ^{19}N fragments were implanted in a graphite stopper to which a static magnetic field $B_0 = 2001.2$ G was applied as shown in Fig. 2. The fact that the spin 1/2 nitrogen polarization is preserved in a graphite stopper was known from the previous ^{17}N($J^\pi = 1/2^-$, $T_{1/2} = 4.173$ s) experiment[2]. An rf field was applied to the stopper in the direction perpendicular to the static field, by using an rf coil wound around the stopper. In the adiabatic fast passage method of the NMR technique[9], the direction of spin was reversed when the frequency of the rf field was swept across the NMR frequency.

To observe the resonance of ^{19}N, an asymmetry change in the β-ray emission from ^{19}N was detected by using plastic scintillator telescopes located above and below the stopper as shown in Fig. 2.

3. Result of the Experiment

The obtained NMR spectrum is shown in Fig. 3. Three data points are shown by filled circles. The vertical axis represents the observed asymmetry change in the β-ray emission. The vertical bar attached to each point shows the statistical error from the β-ray counts. The horizontal bar indicates a sweep width over which the frequency of the rf field was varied for the adiabatic fast passage method. In Fig. 3, the effect of the resonance was observed in the leftmost data point with a deviation of 3.2σ from zero, where σ denotes the standard deviation. The g value was preliminarily determined to be $g = 0.61 \pm 0.03$. The attached error here mainly comes from the sweep width of the frequency.

4. Comparision with Shell Model Calculations

The shell model calculations were performed by using the OXBASH code [10]. Two different sets of effective interactions, the PSDMK and PSDWBT interactions in Ref.10, were used. In these calculations, the bare g factors

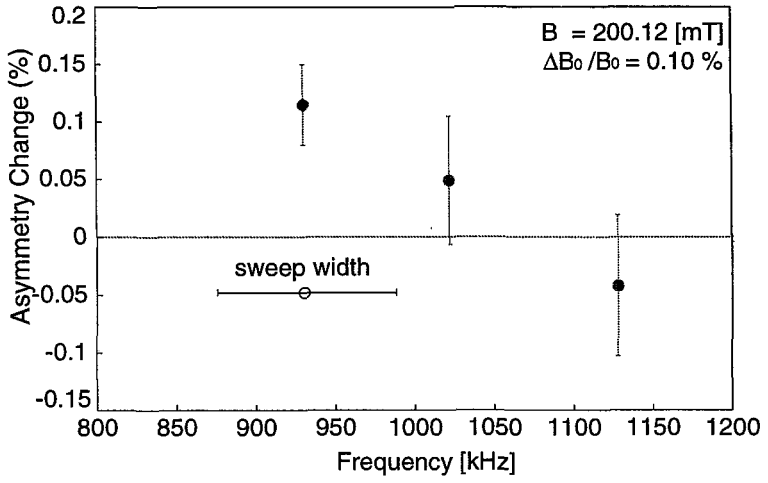

Figure 3. The obtained NMR spectrum for ^{19}N stopped in a graphite stopper. Details are described in the text.

for the nucleon spins and orbital angular momenta were taken for the sake of simplicity. In Fig. 4, the experimental and theoretical $|g|$ factors for the odd-mass neutron-rich N isotopes are shown. A systematic trend is observed: The shell models predict $|g|$ values which monotonously increase with increasing number of neutrons n in the *sd* shell. The experimental $|g|$ certainly follow this trend up to $n = 2$ (i.e.,^{17}N). At $n = 4$ (^{19}N), however, the experimental $|g|$ abruptly decreases.

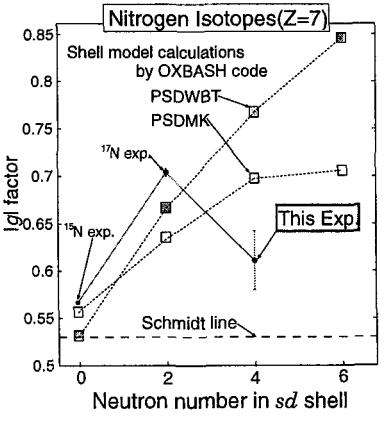

Figure 4.
The experimental (circle with an error bar) and theoretical (square) $|g|$ values for odd-mass N isotopes.

5. Summary

The g factor for the ground state of ^{19}N was measured by using spin-polarized radioactive nuclear beams from the projectile fragmentation reaction. The obtained g value was smaller than both of the shell-model calculations using the PSDMK and PSDWBT interactions. Obviously, more refined understanding of nuclear structure in the region with large neutron excesses is needed.

Acknowledgments

We wish to acknowledge staff members of the RIKEN Accelerator Research Facility (RARF) for the provision of high quality beams during our experiment. One of the authors (D.K.) is grateful to Research Fellowship of the Japan Society for the Promotion of Science for Young Scientists. This work was supported in part by a Grant-in-Aid for Scientific Research from the Ministry of Education, Science and Culture.

References

1. H. Morinaga and T. Yamazaki, *In-Beam Gamma-Ray Spectroscopy (North-Holland Publ. Co., Amsterdam, 1976)*, p120.
2. H. Ueno *et al.*, Phys. Rev. C **53**, 2142 (1996).
3. H. Okuno *et al.*, Phys. Lett. B **354**, 41 (1995).
4. H. Izumi *et al.*, Phys. Lett. B **451**, 11-18 (1999).
5. H. Ogawa *et al.*, Phys. Rev. C **67**, 064308 (2003).
6. H. Miyatake *et al.*, Phys. Rev. C **67**, 014306 (2003).
7. K. Matsuta *et al.*, Hyperfine Interactions **97/98**, 519-526 (1996).
8. T. Kubo *et al.*, Nucl. Instrum. Mehods Phys. Res. B **70**, 309 (1992).
9. A. Abragam, The Principle of Nuclear Magnetism (Clarendon, Oxford, 1961).
10. B. A. Brown, A. Etchengoyen, and W. D. Rae, Computer code OXBASH, MSU Cyclotron Laboratory Report No. 524, 1986.

This page intentionally left blank

Excitation of exotic nuclei

This page intentionally left blank

THE STRUCTURE OF EXOTIC NUCLEI INVESTIGATED VIA SCATTERING EXPERIMENTS WITH FAST FRAGMENTATION BEAMS AT GSI

THOMAS AUMANN

Gesellschaft für Schwerionenforschung mbH (GSI),
Planckstr. 1,
D-64291 Darmstadt, Germany
E-mail: t.aumann@gsi.de

Reactions of secondary beams at energies of several hundred MeV/u are utilized at the GSI radioactive beam facility to explore the structure of unstable nuclei. Scattering of radioactive nuclei can be studied by kinematically complete measurements with the LAND reaction setup. In the present article, experiments concerning inelastic excitations to the continuum will be discussed utilizing the electromagnetic excitation process at high energies. First experiments in this direction were performed for light neutron-rich nuclei. Two aspects are of particular interest: i) Non-resonant transitions to the continuum just above the threshold, which have been established as a spectroscopic tool to study the ground state single-particle structure of the projectile. ii) The dipole excitations of neutron-proton asymmetric systems, in particular collective excitations such as the giant dipole resonance or low-lying soft modes.

1. Introduction

Giant resonances are collective nuclear excitation modes exhausting a large fraction of the respective sum rules. Microscopically, they are understood as a coherent superposition of many particle-hole states across one or two major shells. The isovector giant dipole resonance (GDR) was the first discovered experimentally, about 50 years ago, and has been interpreted as the collective vibration of neutrons against protons. Systematic studies involving almost all stable nuclei available as target material yielded a large data basis and have shown that nearly the complete dipole strength given by the classical energy-weighted Thomas-Reiche-Kuhn (TRK) dipole sum rule is absorbed into this excitation mode. The ultimate proof of the vibrational character of the GDR, however, came only recently with the observation of the second phonon state[1], demonstrating that the GDR is essentially a

harmonic vibration. With the advent of radioactive beams, the possibility of giant resonance studies with unstable nuclei came into reach. Again, it is the GDR which is studied first, also due to experimental reasons.

The question, how the multipole strength functions evolve when going away from stable, almost neutron-proton symmetric nuclei, towards unstable nuclei with large neutron or proton excess has been studied in the past few years theoretically by various approaches, see, e.g., [2,3,4,5,6,7,8]. Concerning the dipole strength function, a stronger fragmentation of the strength, in particular a redistribution of the strength towards lower excitation energies has been predicted consistently by calculations of different kind. Experimentally, such a redistribution of strength was observed recently at GSI for the oxygen isotope chain[9], as will be discussed in the present article. Dipole excitations are most effectively studied using the electromagnetic excitation process at high energy, yielding rather large cross sections. In principle, also magnetic dipole and quadrupole excitations can be investigated, the cross sections being, however, much smaller. A precise angular distribution and/or beam-energy dependence has to be measured with good statistics in order to disentangle such contributions from the dominant dipole excitations. For the two-neutron halo nucleus ^{6}He, low-lying multipole strength other than dipole was observed in a nuclear inelastic excitation experiment[10] using a carbon target. To study quadrupole and monopole excitations in unstable nuclei, new experimental approaches have to be developed, e.g., inelastic alpha scattering in inverse kinematics or electron scattering using storage rings, as envisaged at the planned radioactive beam facility at GSI[11].

The study of the dipole strength function for exotic nuclei has different aspects. Giant resonance parameters were used in the past for stable nuclei to determine effective interactions used in the mean-field calculations. As pointed out by Reinhard[4], the predicted giant resonance strength in exotic nuclei is particularly sensitive to the isospin and density dependent parts of the effective interaction, which are not well determined from the studies with stable nuclei. In turn, the measurement of the strength functions for exotic nuclei might help constraining such effective forces. Another aspect is the appearance of new coherent modes, e.g., the collective dipole vibration of excess neutrons against the core for neutron rich nuclei. Such a soft dipole mode was predicted by various calculations.

So far, experimental information on the multipole response of unstable nuclei is rather limited. Low-lying dipole strength was observed in particular for nuclei exhibiting a halo structure, see, e.g., the $E1$ strength distri-

butions measured for the two-neutron halo nuclei ^{6}He [10] and ^{11}Li [12,13], and for the one-neutron halo nuclei ^{11}Be [14,15] and ^{15,19}C [16,17]. The question of the resonant character of this low-lying strength is to our understanding still open for the two-neutron halo nuclei, while for the one-neutron halo nuclei the strength can be attributed to non-resonant dipole transitions to the continuum and is solely related to the single-particle properties of the weekly bound neutron. Such non-resonant transitions, however, are found to be a promising spectroscopic tool. Here, we discuss the example of a measurement of the dipole response of neutron-rich oxygen nuclei. Concerning Coulomb breakup as a spectroscopic tool, we refer to our recent publications[14,16,18].

2. Experimental Method

The experimental method applied by the LAND collaboration at GSI consists of producing high-energy radioactive beams and a kinematical measurement of breakup products produced in secondary targets. The excitation energy prior to decay is reconstructed by utilizing the invariant-mass method. The measurement is exclusive or kinematically complete in the sense, that all projectile-like decay products are detected, i.e. reaction products with velocities close to the beam velocity. Target-like reaction products are not measured (with the exception of γ-rays).

The experimental results exemplified in the next section utilized radioactive beams, which were produced by fragmentation of a primary ^{40}Ar beam delivered by the synchrotron SIS at GSI, Darmstadt. Fragment beams were selected by the Fragment Separator FRS according to their magnetic rigidity only, thus mixed secondary beams containing isotopes with similar mass-over-charge ratio were transported to the experimental area. The incident projectiles, however, were uniquely identified on an event-by-event basis by utilizing energy-loss and time-of-flight measurements.

In a similar manner, the fragments produced in the reaction target are identified. Here, the magnetic rigidity is determined from three position measurements defining the trajectories of the charged projectile residues in the magnetic field of a large-gap dipole magnet placed behind the target. Additional energy-loss and time-of-flight measurements allow unique identification of the outgoing fragments and determination of their momenta.

Neutrons emitted from the excited projectile or excited projectile-like fragments are kinematically focused in the forward direction and detected with high efficiency (90%) in the LAND neutron detector. The momenta

of the neutrons are determined from the time-of-flight and position information. The angular range for fragments and neutrons covered by the detectors corresponds to a 4π measurement of the breakup in the rest frame of the projectile for fragment-neutron relative energies up to 5.5 MeV (at 500 MeV/u beam energy).

At the high beam energies used, the γ-rays need to be detected with good angular resolution in order to minimize Doppler broadening effects. Two detectors are used alternatively: the Crystal Ball spectrometer, which consists of 160 NaI detectors covering almost the full solid angle, or, a CsI array consisting of 144 submodules. The latter covering only the forward hemisphere, but with better angular resolution. Still, the resolution is limited by the Doppler broadening.

The excitation energy prior to decay is obtained by reconstructing the invariant mass combining the measurements described above. The resolution in excitation energy depends on the relative fragment-neutron kinetic energy and the resolution for measuring the gamma-sum energy (in the projectile rest frame) in case of the population of excited states. It changes from about 200 keV at the threshold to a few MeV in the region of the giant dipole resonance (at excitation energies around 15 MeV). In order to extract the electromagnetic excitation cross section from the measurement with the lead target, the nuclear contribution is determined from a measurement with a carbon target and scaled accordingly before subtraction.

3. Dipole excitations in neutron-rich oxygen isotopes

The evolution of the dipole-strength distribution as a function of neutron-to-proton asymmetry was investigated systematically for the oxygen isotope chain ranging from a neutron excess of $N - Z = 1$ up to $N - Z = 7$. ^{16}O is a strongly bound doubly magic nucleus with a neutron separation energy $S_n = 16$ MeV, while, for the heavier isotopes, the separation energy decreases to $S_n \approx 7$ MeV for the even isotopes with $A = 18$ to 22, and $S_n \approx 4$ MeV for the odd isotopes. Thus, one may expect a decoupling of the valence neutrons from the inert ^{16}O core and the appearance of a collective soft-dipole excitation.

The neutron-decay channels after electromagnetic scattering on a lead target at about 600 MeV/u beam energy was investigated. From the coincident measurement of charged fragments, neutrons, and gamma-rays, the differential cross sections $d\sigma/dE^*$ for electromagnetic excitation were derived and converted to the photoneutron cross sections $\sigma_{(\gamma,xn)}$ by ap-

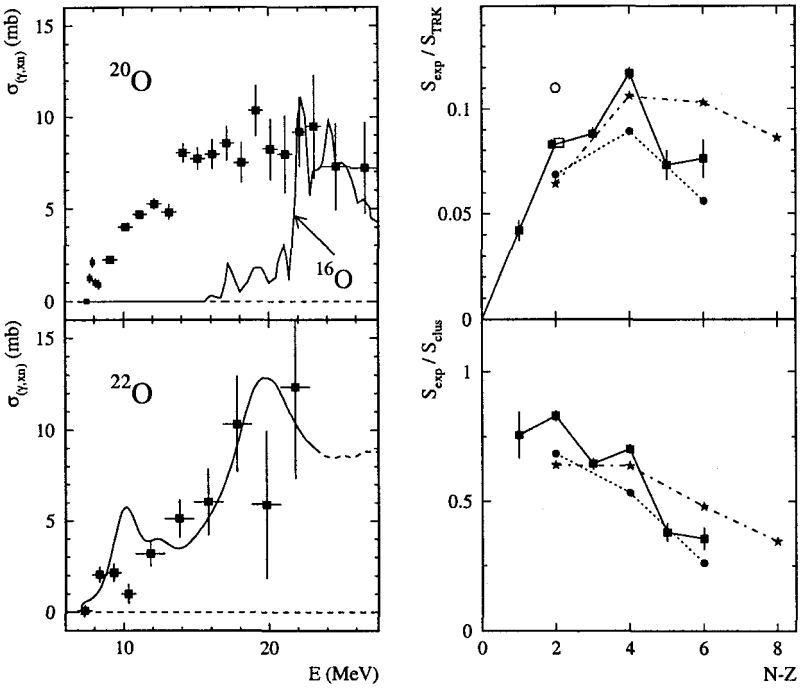

Figure 1. Left panels: Photoneutron cross sections $\sigma_{(\gamma,xn)}$ for the unstable isotopes ^{20}O (upper panel) and ^{22}O (lower panel) as extracted from the measured electromagnetic excitation cross section (symbols). For comparison, the photoneutron cross section for the stable ^{16}O [20] is displayed additionally as the solid curve in the upper panel. Right panels: Evolution of integrated (up to 15 MeV excitation energy) strength S_{exp} in units of the TRK sum rule S_{TRK} (upper panel) and of the cluster-sum-rule limit S_{clus} (lower panel) for oxygen isotopes with neutron excess $N - Z$. For the stable isotope ^{18}O, the values extracted from the real-photon absorption experiments are given as the circle [21] and open square [22]. The values extracted from the electromagnetic-excitation experiment [9] are given by the filled squares. The data are compared to shell-model calculations by Sagawa and Suzuki [5] (stars) and the quasi-particle RPA calculation by Colò and Bortignon[7] (filled circles).

plying semiclassical calculations[19]. Figure 1 shows the (γ, n) cross section for the unstable isotopes ^{20,22}O (left panels) in comparison with the stable nucleus ^{16}O [20] (solid curve overlaid to the cross section for ^{20}O). Evidently, the dipole response changes significantly due to the presence of the valence neutrons. Most noticeable is the sizeable dipole absorption cross section below the giant dipole resonance (GDR) energy region. A clear separation into two energy domains associated with GDR excitations of the core and a soft-dipole mode involving valence neutrons is not observed. For ^{22}O, the

data are compared to a large-scale shell-model calculation[5] after convolution with the experimental resolution (solid curve in the lower left panel). Qualitatively, the shell-model calculations reproduce the experimental observation of a redistribution of the $E1$ strength towards excitation energies below the GDR compared to that of the doubly magic nucleus ^{16}O.

The right part of Figure 1 shows the energy-weighted experimental low-lying dipole strength S_{exp} units of the classical energy-weighted Thomas-Reiche-Kuhn sum rule S_{TRK}. While no dipole strength below 15 MeV is observed for the $N = Z$ nucleus ^{16}O, about 10% of the sum-rule value is exhausted for the neutron-rich isotopes. For ^{20}O, cumulation of dipole strength was also observed below the neutron threshold in the energy range from 5 to 7 MeV as extracted from a virtual-photon scattering experiment[23]. The integrated value of about 0.1 e^2fm^2 [23], however, corresponds to much less than 1% of the TRK sum rule only.

Our results for the integrated low-lying dipole strength are compared in Figure 1 (right panels) to a large-scale shell-model calculation[5] (stars) and a calculation using the quasi-particle random-phase approximation (QRPA)[7]. Both calculations reproduce the amount (about 5% to 12% of the TRK sum-rule value) of dipole strength as found experimentally at low excitation energies. Also, the experimentally observed trend of an increase of the strength as a function of neutron excess up to ^{20}O followed by a decrease for isotopes heavier than ^{20}O is reproduced qualitatively in both calculations. The maximum at $A = 20$ might reflect a shell effect: Both ^{16}O and ^{24}O are doubly closed shell nuclei, implying that the low-lying dipole strength is most pronounced for the mid-shell region. It is interesting to note, that such an effect was observed in relativistic mean field calculations for the tin isotopes [6].

In the lower panel, the same quantity is plotted as fraction of the cluster sum rule limit $S_{\mathrm{clus}}/S_{\mathrm{TRK}} = Z_c/A_c \cdot N_\nu/N$, where the indices refer to core (c) and valence (ν) nucleons. This sum rule results from a decomposition of the dipole strength into excitations of the core, excitations among the valence nucleons (which is zero in the present case), and the dipole strength S_{clus} associated with the relative motion between the core and the valence nucleons. It appears that a large fraction of this sum rule limit of around 0.5 is exhausted, with a clear tendency of values decreasing with neutron number. The question to which extent the observed low-lying dipole strength involves collective excitations was studied theoretically by Vretenar *et al.*[6] within the relativistic mean field approach. According to this calculation, the low-lying strength in the oxygen isotopes is mainly related to single neu-

tron particle-hole excitations, while for heavier neutron-rich nuclei, e.g., for the tin isotopes, a resonance-like structure at low excitation energy resulting from a coherent superposition of particle-hole excitations is predicted. Similarly, Colò and Bortignon[7] found in their QRPA plus phonon coupling calculation only a small number of components in the wave functions of the low-lying structures in the oxygen isotopes. The low-lying dipole strength observed in neutron-rich oxygen nuclei can thus not be attributed to a collective soft dipole ('pygmy') mode.

Acknowledgments

The experiments discussed in this article are the result of a collaborative effort. The author wishes to thank all members of the LAND/FRS collaboration.

References

1. T. Aumann *et al.*, Annu. Rev. Nucl. Part. Sci. **48** (1998) 351.
2. I. Hamamoto and H. Sagawa, Phys. Rev. C **53** (1996) R1492.
3. F. Ghielmetti *et al.*, Phys. Rev. C **54** (1996) R2143.
4. P.G. Reinhard, Nucl. Phys. A **649** (1999) 305c.
5. H. Sagawa and T. Suzuki, Phys. Rev. C **59** (1999) 3116.
6. D. Vretenar *et al.*, Nucl. Phys. A **692** (2001) 496.
7. G. Colò and P.F. Bortignon, Nucl. Phys. A **696** (2001) 427.
8. M. Matsuo, Nucl. Phys. A **696** (2001) 371; Progr. Theor. Phys. Auppl. **146** (2002) 110; contribution to these proceedings.
9. A. Leistenschneider *et al.*, Phys. Rev. Lett. **86** (2001) 5442.
10. T. Aumann *et al.*, Phys. Rev. C **59** (1999) 1252.
11. *An International Accelerator Facility for Beams of Ions and Antiprotons*, Conceptual Design Report, Publisher GSI (2001), http://www.gsi.de/GSI-Future/cdr/.
12. S. Shimoura *et al.*, Phys. Lett. **B348** (1995) 29.
13. M. Zinser *et al.*, Nucl. Phys. A **619** (1997) 151.
14. R. Palit *et al.*, Phys. Rev. C **68** (2003) 034318.
15. T. Nakamura *et al.*, Phys. Lett. B **331** (1994) 296.
16. U. Datta Pramanik *et al.*, Phys. Lett. B **551** (2003) 63.
17. T. Nakamura *et al.*, Phys. Rev. Lett. **83** (1999) 1112.
18. C. Nociforo, K.L. Jones, L.H. Khiem *et al.*, submitted to Physics Letters B.
19. C.A. Bertulani and G. Baur, Phys. Rep. **163** (1988) 299.
20. E.G. Fuller, Phys. Rep. **127** (1985) 187.
21. J.G. Woodworth *et al.*, Phys. Rev. C **19** (1979) 1667.
22. U. Kneissl *et al.*, Nucl. Phys. A **272** (1976) 125.
23. E. Tryggestad *et al.*, Phys. Lett. B **541** (2002) 52.

DI-NEUTRON CORRELATION AND SOFT DIPOLE EXCITATION IN MEDIUM MASS NUCLEI NEAR NEUTRON DRIP-LINE*

MASAYUKI MATSUO, KAZUHITO MIZUYAMA, YASUYOSHI SERIZAWA
Graduate School of Science and Technology, Niigata University, Niigata 950-2181, Japan
E-mail: matsuo@nt.sc.niigata-u.ac.jp

Pair correlation effects on the soft dipole excitation in medium mass nuclei near neutron drip-line are investigated by means of the continuum quasiparticle random phase approximation. The correlation of di-neutron type found in the ground state affects strongly the soft dipole excitation, and enhances the transition amplitude for two-neutron pair transfer.

1. Introduction

The soft dipole excitation is one of the most striking examples of exotic excitation in unstable nuclei near the neutron drip-line. Significant amount of E1 strength observed just above the very low neutron threshold energy in light halo nuclei indicates that weakly bound neutron forming the halo plays important role. However, low lying dipole strength near the neutron threshold energy is recently observed in neutron-rich oxygen isotopes[1]. This suggests that the soft dipole excitation is not specific to halo, but emerge generally in nuclei near neutron drip-line including medium mass region.

Effect of di-neutron correlation on the soft dipole excitation has been one of the central issues since the early discussions[2,3,4] on the two-neutron halo nucleus ^{11}Li. If spin-singlet neutron pair exhibits localized correlation with respect to the relative distance, rather than uniformly correlated around the nuclear center, this may be regarded as the di-neutron correlation. The di-neutron correlation is predicted to influence the soft dipole excitation in ^{11}Li[4] although consistent experimental picture has not been established yet[5]. Since the pair correlation is a generic aspect of the nuclear many-

*Work supported by the JSPS Grant-in-Aid for Scientific Research No. 14540250.

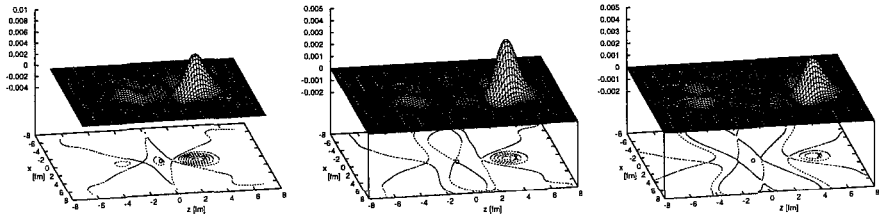

Figure 1. The two-body neutron correlation density $\rho_{corr}(\boldsymbol{r}\uparrow, \boldsymbol{r}'\downarrow)/\rho(\boldsymbol{r}')$ in ^{22}O, ^{54}Ca and ^{82}Ni (from left to right). One neutron is fixed at the nuclear surface (the cross) on the z-axis, and the correlated density of the other neutrons is plotted in the xz-plane.

body correlation, one may expect similar pair correlation effect on the soft dipole excitation also in medium mass and heavier neutron rich nuclei near drip-line. In the present work, we investigate this possibility by means of the continuum quasiparticle random phase approximation (the continuum QRPA), which we have formulated exactly on the basis of the Hartree-Fock-Bogoliubov theory in the coordinate-space representation[6].

2. Di-neutron correlation in the ground state

We first investigate the pair correlation in the ground state described by the coordinate-space HFB theory[7]. The adopted model Hamiltonian consists of a Woods-Saxon potential and the effective pairing interaction, for which we adopt the density-dependent delta force. The force strength is fixed to reproduce an overall values of the experimental neutron pairing gap.

To display the spatial correlation of the spin-singlet neutron pair in the ground state, we evaluate the two-body correlation density

$$\rho_{corr}(\boldsymbol{r}\uparrow, \boldsymbol{r}'\downarrow) = \sum_{i\neq j} \int\int d\boldsymbol{r}_i d\boldsymbol{r}_j \sum_{\sigma_i\sigma_j} \delta(\boldsymbol{r}-\boldsymbol{r}_i)\delta(\boldsymbol{r}'-\boldsymbol{r}_j)\delta_{\sigma_i\uparrow}\delta_{\sigma_j\downarrow} - \rho(\boldsymbol{r})\rho(\boldsymbol{r}') \quad (1)$$

An example is shown Fig.1. The correlation is localized well around the reference position of one neutron (placed at the nuclear surface in this case). This indicates the pair correlation having the di-neutron structure. This feature is seen in oxygen, calcium and nickel cases, suggesting a generality of the di-neutron correlation in nuclei near neutron drip-line.

3. Di-neutron correlation in soft dipole excitation

We describe nuclear excitation against the E1 response by means of the continuum QRPA [6,8]. The present continuum QRPA deals with the quasi-

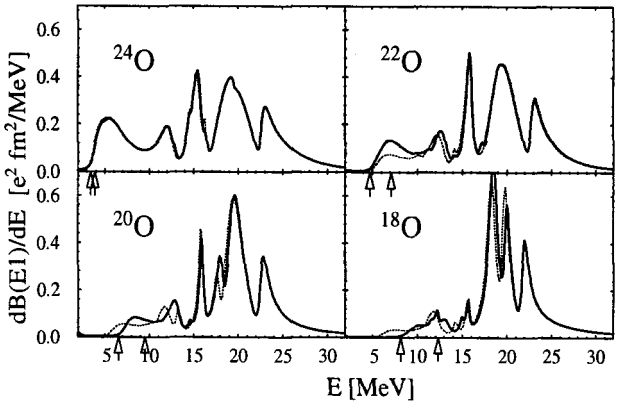

Figure 2. The B(E1) strength function calculated for oxygen isotopes. The thin dotted curve shows the results where a very small pairing force strength is adopted, leading to an essentially zero pairing correlation.

particle states with use of the exact coordinate space representation of the HFB Green function, which satisfies the out-going boundary condition for the continuum orbits. This exact treatment is essentially important for description of the soft dipole excitation, whose strength is distributed just above the neutron threshold, where neutron emission becomes effective. The continuum QRPA takes into account both the particle-hole and the particle-particle correlations among two-quasiparticle excitations, including two continuum channels of one-neutron and of two-neutron escaping. The theory is able to describe the pair correlation among two neutrons, one or both of which are configured in the continuum states.

The dipole strength calculated for oxygen isotopes is shown in Fig.2. It is seen that the soft dipole strength located just above the one-neutron threshold emerges already in ^{18}O, and develops as the drip-line is approached toward ^{24}O. The energy weighted sum below $Ex < 15$ MeV is consistent with the experiment[1] in ^{18,20}O, but overestimates in ^{22}O. In this figure effect of the pair correlation is also displayed by contrasting to a calculation where the pairing correlation is neglected. The pair correlation influences the strength near the threshold energy. Effect is large in ^{22}O, and small in ^{18,22}O, and negligible in ^{24}O.

The transition densities provide with more detailed characteristics of the excitation mode. Here we utilize the pair-add and pair-remove transition densities,

$$P_i^{\rm add}(r) = \langle i|\,\psi^\dagger(r\downarrow)\psi^\dagger(r\uparrow)\,|0\rangle\,, \quad P_i^{\rm rm}(r) = \langle i|\,\psi(r\uparrow)\psi(r\downarrow)\,|0\rangle\,,$$

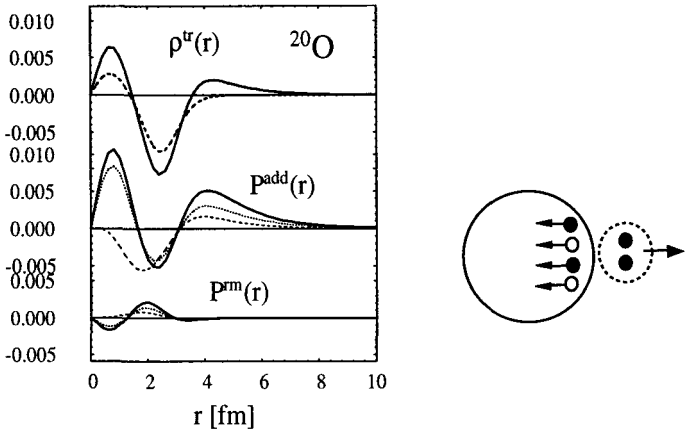

Figure 3. The transition densities for the soft dipole excitation in ^{20}O. The thick solid and dashed curves represent the neutron and proton amplitudes, respectively. For $P^{\rm add}$ and $P^{\rm rm}$, the neutron amlitude without the dynamical pairing effect is shown by the thin dotted curve. The thin dashed curve represents the results where the pair correlations are fully neglected. Right: a schematic picture of the di-neutron correlation in the soft dipole excitation

in addition to the usual particle-hole transition density $\rho_i^{\rm tr}(\boldsymbol{r}) = \langle i|\sum_\sigma \psi^\dagger(\boldsymbol{r}\sigma)\psi(\boldsymbol{r}\sigma)\,|0\rangle$ The pair-add transition density $P^{add}(r)$ represents the amplitude of a spin-singlet nucleon pair at the position r from the ground state of the $A-2$ system to the excited state. On the other hand, the pair-remove transition density $P^{rm}(r)$ corresponds to removing a nucleon pair from the ground state of the $A+2$ system to reach the excited state.

An example for ^{20}O is shown in Fig.3. Focusing on amplitude in the surface and outer regions responsible for the soft dipole excitation, the largest amplitude among the three is carried by the pair-add transition density $P^{\rm add}$. This indicates that the soft dipole excitation in ^{20}O is the mode which has dominantly a particle-particle character, rather than particle-hole character. On the other hand, the pair-remove transition density is very small. The pair correlation is essential to cause the above feature. If we neglect the dynamical pair correlation among neutrons participating in the soft dipole excitation, the pair-add amplitude $P^{\rm add}$ is reduced by a factor of two in the surface and outer regions. Further reduction is caused if we neglect the pair correlation both in the ground state and in the excited state, and the particle-hole character becomes dominant. These observations leads to a picture that in the soft dipole excitation a neutron pair

having the di-neutron correlation is moving against the rest part of nucleus which has strong overlap with the ground state of the $A-2$ system.

The neutron $2s1/2$ orbit plays an important role for the soft dipole excitation in neutron rich oxygen isotopes since the $2s1/2$ orbit has long spatial tail extending out of the nuclear radius. In addition, the pair correlation enhances its role. If one assume a zero neutron pairing in $^{18-22}$O, the $2s1/2$ orbit becomes unoccupied. In this case the $2s1/2$ orbit does not contribute since the soft dipole excitation becomes predominantly a particle-hole excitations from $1d5/2$ orbit to the continuum p orbit. Conversely, when the pairing correlation is taken into account, the $2s1/2$ orbit make significant contribution to the soft dipole mode in $^{18-22}$O since this orbit becomes partially occupied and contributes both in the particle-hole and particle-particle channels. This leads to an strong interplay between the particle-hole and particle-particle correlations. In ^{24}O, on the other hand, the $2s1/2$ is fully occupied as the pairing correlation is weak due to the N=16 subshell. In this case, the soft dipole excitation has dominant component of the neutron particle- hole excitation from $2s1/2$ to the continuum p orbits.

We have also investigated the soft dipole excitation in Ca and Ni isotopes near neutron drip-line[8]. It is found that the results obtained here is not specific to the oxygen isotopes, but rather general features of medium mass nuclei near neutron drip-line.

References

1. A. Leistenschneider, et al., Phys. Rev. Lett. **86**, 5442 (2001).
2. P.G. Hansen, B. Jonson, Europhys. Lett. **4**, 409 (1987).
3. K. Ikeda, Nucl. Phys. **A538**, 355c (1992).
4. G.F. Bertsch, H. Esbensen, Ann. Phys. **209**,327 (1991); Nucl. Phys. **A542**, 310 (1992).
5. D.Sackett, et al.: Phys. Rev. **C48**, 118 (1993); S.Shimoura, et al.: Phys. Lett. **B348**, 29 (1995); M.Zinser, et al.: Nucl. Phys. **A619**, 151 (1997).
6. M. Matsuo, Nucl. Phys. **A696**, 371 (2001); Prog. Theor. Phys. Suppl. **146**, 110 (2002); Proc. Int. Symp. on Frontiers of Collective Motions (World Scientific 2003), ed. H. Sagawa and H. Iwasaki, p.312.
7. J. Dobaczewski, H. Flocard, J. Treiner, Nucl. Phys. **A422**, 103 (1984).
8. M. Matsuo, K. Mizuyama, Y. Serizawa, in preparation; K. Mizuyama, Y. Serizawa, M. Matsuo, in this proceedings.

RESPONSE IN THE CONTINUUM FOR LIGHT DEFORMED NEUTRON-RICH NUCLEI *

TAKASHI NAKATSUKASA†
Department of Physics, Tohoku University, Sendai 980-8578, Japan

KAZUHIRO YABANA
Institute of Physics, University of Tsukuba, Tsukuba 305-8571, Japan

The time-dependent Hartree-Fock calculation with a full Skyrme energy functional has been carried out on the three-dimensional Cartesian lattice space to study $E1$ giant dipole resonances (GDR) in light nuclei. The outgoing boundary condition for the continuum states is treated by the absorbing complex potential. The calculation for GDR in ^{16}O suggests a significant influence of the residual interaction associated with time-odd densities in the Skyrme functional. We also predict a large damping for superdeformed ^{14}Be at the neutron drip line.

1. Time-dependent approach to nuclear response in the continuum

The quantum-mechanical problems are usually solved in the energy (time-independent) representation. Namely, we either solve an energy eigenvalue problem for bound states or, for scattering states, we calculate a wave function with a proper boundary condition at a given energy. However, if one wishes to calculate physical quantities in a wide energy region, the time-dependent approach is very useful because a single time propagation provides information for a certain range of energy. Another advantage may be an intuitive picture provided by the time evolution of the wave function.

In Ref. 1, we have calculated molecular photoabsorption cross sections in the electronic continuum by using the time-dependent and time-independent approaches. The results indicate the capability and efficiency

*This work is supported by Japan Society for the Promotion of Science (1470146 and 14540369).
†Present address: Institute of Physics, University of Tsukuba, Tsukuba 305-8571, Japan.

of the time-dependent method. In the present paper, we will show nuclear response calculations using the same technique, the time-dependent Hartree-Fock (TDHF) method combined with the absorbing boundary condition (ABC).

The TDHF state consists of A-occupied single-particle wave functions, $\{\phi_i(\mathbf{r},t)\}_{i=1,\cdots,A}$, each of which is complex and has two components (spinor). The three-dimensional (3D) Cartesian coordinate, (x,y,z), is discretized in rectangular lattice and derivatives are estimated with the nine-point formula. The time evolution is determined by

$$\phi_i(\mathbf{r},t) = \exp\left(-i\int_0^t dt' h_{\rm HF}[\rho(t')]\right)\phi_i(\mathbf{r},0), \tag{1}$$

where the HF Hamiltonian, $h_{\rm HF}[\rho(t)]$, depends on $\phi_i(\mathbf{r},t)$ and their derivatives. The initial state, $\{\phi_i(\mathbf{r},0)\}_{i=1,\cdots,A}$, is chosen as the HF ground state wave function perturbed by an instantaneous external field, $\phi_i(t=0) = e^{ik\hat{F}}\phi_i^0$. Here, the coupling parameter, k, can be arbitrary but should be small to validate the Fourier analysis (linear response approximation). The time variable is also discretized in a small step Δt and the exponential operator in Eq. (1) is approximated by the fourth-order expansion,

$$\exp\left(-i\int_0^{\Delta t} dt' h_{\rm HF}[\rho(t')]\right) \approx \sum_{n=0}^{4}\frac{1}{n!}\left(h_{\rm HF}[\rho(\Delta t/2])\right)^n. \tag{2}$$

The time evolution of the expectation value of the external field, $\langle\Psi(t)|\hat{F}|\Psi(t)\rangle$, is computed, then we utilize the Fourier transform to obtain the strength function, $S(E) \propto E\sum_n \delta(E-E_n)|\langle n|\hat{F}|0\rangle|^2$.

Next, let us discuss the treatment of the continuum. During the time evolution of the TDHF state, a part of the wave function may escape from the nuclear binding and become an outgoing wave. In the time-dependent approach, it is very difficult to impose the outgoing boundary condition (OBC) explicitly, because the outgoing particles have different energies. Furthermore, the boundary condition for non-spherical systems requires involved computation.[1] Thus, instead of exactly treating the OBC, we use the absorbing boundary condition (ABC) which can be practically identical to the OBC. In the ABC method, the Cartesian coordinate space ($r < R_0$) is divided into two parts: an interacting region ($r < R_c$) and a non-interacting region ($R_c < r < R_0$). We introduce a complex absorbing potential, $-i\tilde{\eta}(r)$, active only in the non-interacting region. Then, we solve the TDHF equation of motion, Eq. (1), with the box boundary condition (BBC) at $r = R_0$, $\phi_i(\mathbf{r},t)|_{r=R_0} = 0$ for all occupied orbitals. This means

that the treatment of the continuum simply requires an addition of the absorbing potential to the HF Hamiltonian.

$$h_{\rm HF}[\rho(t)]\Big|_{\rm OBC\ at\ } {}_{r=R_c} \doteqdot (h_{\rm HF}[\rho(t)] - i\tilde{\eta}(r))\Big|_{\rm BBC\ at\ } {}_{r=R_0}. \qquad (3)$$

We have demonstrated accuracy and practicality of the ABC method both in the time-dependent[1,2,3,4] and the time-independent approaches.[5,6]

2. Applications

2.1. *Giant dipole resonance in* ^{16}O

Giant dipole resonance (GDR) in ^{16}O has been studied extensively.[7] Since ^{16}O is a doubly-closed spherical nucleus, the continuum RPA[8] is applicable. A microscopic calculation with the Skyrme energy functional was done[9] and showed a two-peak structure for GDR in ^{16}O. However, the calculation is not fully self-consistent because the residual Coulomb, spin-orbit, and $\sigma \cdot \sigma$ part of the interaction are neglected. According to the best of our knowledge, the continuum RPA calculation with the Skyrme functional has never been carried out fully self-consistently. Therefore, it is worth while to perform a fully self-consistent TDHF+ABC calculation and to investigate effects of the neglected part of the residual interaction.

We use the Skyrme energy functional of Ref. 10 with the SGII parameter set. The 3D sphere of radius $R_0 = 22$ fm is adopted as a model space. The mesh spacing is $\Delta x \approx \Delta y \approx \Delta z \approx 1$ fm inside the interacting region but gradually increase up to $\Delta \approx 3$ fm in the non-interacting region. After obtaining the HF ground state of ^{16}O, the isovector dipole field, $\hat{F} = z_n - z_p$, is activated instantaneously at $t = 0$. The time evolution is computed up to $T = 30\ \hbar/\mathrm{MeV}$. The result of the Fourier transform is shown in Fig. 1 (b). Apparently, we observe only one peak at $E \approx 20$ MeV, except for small peaks and a shoulder. This is inconsistent with results of the continuum RPA. The disagreement turns out to be due to the fact that the continuum RPA neglects part of the residual interaction. In the real-time calculation, we must use the same density functional as the one to define the HF ground state. Therefore, it is impossible to neglect the residual Coulomb and spin-orbit interaction. However, it is possible to neglect time-odd densities in the functional, because this does not affect the ground state. The calculation without the time-odd densities is shown in Fig. 1 (a). Now, the result becomes very similar to that of the continuum RPA and there are two peaks in the continuum. There are still some discrepancies related to the residual Coulomb and spin-orbit force. Our result indicates an important

role of the time-odd density part of the residual interaction. Since the time-odd part of the Skyrme energy functional is not well determined by the ground-state properties, this might provide a useful constraint.

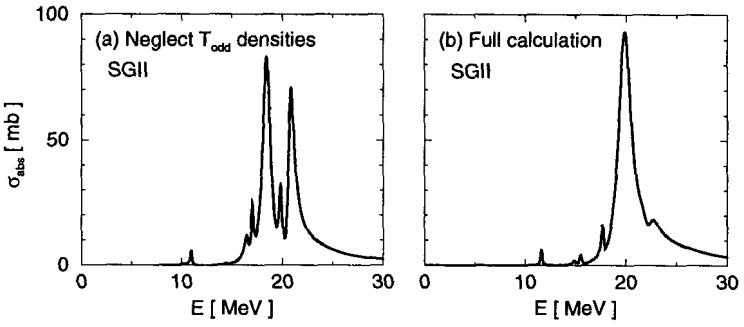

Figure 1. Photoabsorption cross section for ^{16}O calculated with different Skyrme energy functionals. (a) Functional with SGII parameter set but neglecting all the time-odd densities. (b) Full Skyrme functional with the SGII parameter set.

2.2. *Giant dipole resonance in ^{8,14}Be*

Utilizing the same parameters and model space as ^{16}O, we discuss $E1$ resonances in light deformed nuclei, ^{8}Be and ^{14}Be. The quadrupole deformation of the HF ground states of these nuclei are as large as $\beta \sim 1$ (prolate). Calculated $E1$ oscillator strengths are shown in Fig. 2. We can see a large deformation splitting of the GDR for ^{8}Be. The low-energy peak is sharper and located around 7 MeV of excitation energy. This peak is associated with the isovector dipole oscillation along the symmetry axis (z-axis). The higher peak is rather broad and located around 22 MeV. The difference in the broadening leads to a greater peak height for the low-energy resonance, although the integrated oscillator strength is twice larger for the high-energy resonance.

For ^{14}Be at the neutron drip line, the average peak positions for low- and high-energy resonances are similar to those in ^{8}Be. However, the excess neutrons significantly increase the peak width of both resonances. The large deformation splitting almost vanishes in the total strength (thick solid line). It is worth noting that the present calculation takes account of the escape and the Landau damping width but does not include the spreading width. Some additional broadening might make the total strength look like a single peak with a large damping.

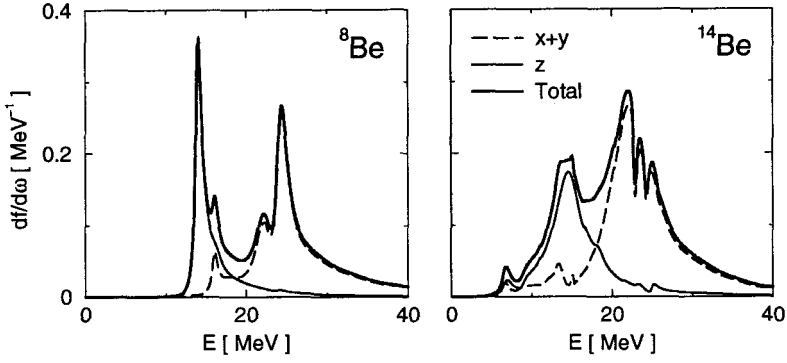

Figure 2. $E1$ Oscillator strength distribution for ^{8}Be and ^{14}Be calculated with the full Skyrme energy functional with the SGII parameters. The thin solid (dashed) line indicates the $E1$ oscillator strength associated with the oscillation parallel (perpendicular) to the symmetry axis.

3. Conclusion

We have carried out the Skyrme TDHF calculation with the ABC in real time for $E1$ resonances in the continuum. The time-odd density components in the Skyrme energy functional may influence considerably the isovector GDR strength distribution. The GDR in Be isotopes have been studied and the large deformation splitting and large broadening are predicted for a drip-line nucleus, ^{14}Be.

References

1. T. Nakatsukasa and K. Yabana, *J. Chem. Phys.* **114**, 2550, (2001).
2. T. Nakatsukasa and K. Yabana, Proceedings of the 7th International Spring Seminar on Nuclear Physics: *Challenges of Nuclear Structure*, p. 91, World Scientific, Singapore (2002).
3. T. Nakatsukasa and K. Yabana. *Prog. Theor. Phys. Suppl.* **146**, 447 (2002).
4. K. Yabana, M. Ueda, and T. Nakatsukasa, *Prog. Theor. Phys. Suppl.* **146**, 329 (2002).
5. M. Ueda, K. Yabana, and T. Nakatsukasa, *Phys. Rev. C* **67**, 014606 (2002).
6. M. Ueda, K. Yabana, and T. Nakatsukasa, Proceedings of 4th Italy-Japan Symposium on *Perspective in Heavy Ion Physics*, p. 69, World Scientific, Singapore (2002).
7. M.N. Harakeh and A. van der Woude, Oxford Studies in Nuclear Physics 24, *Giant resonances*, Oxford University Press, Oxford, (2001).
8. S. Shlomo and G. Bertsch, *Nucl. Phys.* **A243**, 507 (1975).
9. K.F. Liu and N. van Giai, *Phys. Lett.* **B65**, 23 (1976).
10. P.H. Heenen P. Bonche, H. Flocard, *Nucl. Phys.* **A467**, 115 (1987).

QUADRUPOLE STATES OF ^{20,22}O IN EXTENDED RPA WITH GROUND-STATE CORRELATIONS

M. TOHYAMA AND S. TAKAHARA
Kyorin University School of Medicine, Mitaka, Tokyo 181-8611, Japan
E-mail: tohyama@kyorin-u.ac.jp

P. SCHUCK
Institut de Physique Nucléaire, IN2P3-CNRS, Université Paris-Sud, F-91406 Orsay Cedex, France
E-mail: schuck@ipno.in2p3.fr

We present the first application of an extended RPA (ERPA) with ground-state correlations. The ERPA is formulated as the small amplitude limit of the time-dependent density-matrix theory, which is an extended version of the time-dependent Hartree-Fock theory. We obtain the correlated ground states of ^{20,22}O using an iterative gradient method and calculate the first 2^+ states and their two-phonon states using the ERPA.

1. Introduction

The Hartree-Fock Bogoliubov theory (HFB) and the quasi-particle random-phase approximation (QRPA) have recently been applied to unstable nuclei [1,2]. Introducing a pairing field, HFB and QRPA deal with pairing correlations in the framework of a mean field theory. In contrast to HFB and QRPA, the time-dependent density-matrix theory (TDDM) [3], which is one of extended time-dependent Hartree-Fock theories, deals with pairing correlations as genuine two-body correlations. TDDM has also been applied to low-lying collective states in unstable nuclei [4]. The correlated ground states used in these TDDM calculations, however, were approximate ones obtained using a time-dependent method [5]. In this paper we propose a *time-independent* approach based on Newton's gradient method and demonstrate its feasibility by calculating the ground states of ^{20,22}O. The first 2^+ states and their two phonon states in ^{20,22}O are also studied using an extended RPA (ERPA) which is formulated as the small amplitude limit of TDDM [6].

2. Formulation

2.1. *Method for finding a correlated ground state*

The ground state $|\Phi_0\rangle$ in TDDM is constructed so that

$$F_1(\alpha\alpha') = \langle\Phi_0|[a_\alpha^+ a_{\alpha'}, H]|\Phi_0\rangle = 0, \tag{1}$$

$$F_2(\alpha_1\alpha_2\alpha_2'\alpha_1') = \langle\Phi_0|[a_{\alpha_1}^+ a_{\alpha_2}^+ a_{\alpha_2'} a_{\alpha_1'}, H]|\Phi_0\rangle = 0, \tag{2}$$

are satisfied, where H is the total hamiltonian, [ ] stands for the commutation relation, and the single-particle wavefunction ψ_α is chosen to be an eigenstate of a mean field hamiltonian. In other words, the occupation matrix $n^0_{\alpha\alpha'} = \langle\Phi_0|a_{\alpha'}^+ a_\alpha|\Phi_0\rangle$ and the two-body correlation matrix $C^0_{\alpha_1\alpha_2\alpha_1'\alpha_2'} = \langle\Phi_0|a_{\alpha_1}^+ a_{\alpha_2'}^+ a_{\alpha_2} a_{\alpha_1}|\Phi_0\rangle - \mathcal{A}(n^0_{\alpha_1\alpha_1'} n^0_{\alpha_2\alpha_2'})$, where $\mathcal{A}$ is the antisymmetrization operator, are determined so that Eqs.(1) and (2) are satisfied. The expressions for Eqs.(1) and (2) are given in Ref.[6]. We propose an iterative gradient method to find a solution of Eqs.(1) and (2) [7]: We start from the HF ground state where $n^0_{\alpha\alpha'} = \delta_{\alpha\alpha'}$ (0) for occupied (unoccupied) single-particle states and $C^0_{\alpha_1\alpha_2\alpha_1'\alpha_2'} = 0$ and iterate

$$\begin{aligned}\begin{pmatrix} n^0(N+1) \\ C^0(N+1) \end{pmatrix} &= \begin{pmatrix} n^0(N) \\ C^0(N) \end{pmatrix} - \alpha \begin{pmatrix} \delta F_1/\delta n^0 & \delta F_1/\delta C^0 \\ \delta F_2/\delta n^0 & \delta F_2/\delta C^0 \end{pmatrix}^{-1} \begin{pmatrix} F_1(N) \\ F_2(N) \end{pmatrix} \\ &= \begin{pmatrix} n^0(N) \\ C^0(N) \end{pmatrix} - \alpha \begin{pmatrix} a & c \\ b & d \end{pmatrix}^{-1} \begin{pmatrix} F_1(N) \\ F_2(N) \end{pmatrix} \end{aligned} \tag{3}$$

until convergence is achieved, where the matrices a, b, c, and d are equivalent to those appearing in the hamiltonian matrix of ERPA [8]. We have to introduce a small parameter α to control the convergence process.

2.2. *Extended RPA*

TDDM gives the time-evolution of the one-body density-matrix ρ and the correlated part C_2 of a two-body density-matrix [3,9], and ERPA has been formulated by linearizing the equations of motion for ρ and C_2 [6]. The equations of ERPA for the one-body amplitude $x_{\alpha\alpha'}(\mu)$ and the two-body amplitude $X_{\alpha_1\alpha_2\alpha_1'\alpha_2'}(\mu)$ can be written in matrix form [8]

$$\begin{pmatrix} a & c \\ b & d \end{pmatrix} \begin{pmatrix} x \\ X \end{pmatrix} = \omega_\mu \begin{pmatrix} x \\ X \end{pmatrix}. \tag{4}$$

When the ground-state $|\Phi_0\rangle$ is assumed to be the HF one and only the particle (p) - hole (h) and 2p - 2h amplitudes (and their complex conjugates) are taken in Eq.(4), ERPA reduces to the second RPA [10].

3. Results

The calculations of ground states are performed using the neutron $1d_{5/2}$ and $2s_{1/2}$ states obtained from the Skyrme III force. The residual interaction used is a pairing-type force of the δ-function form: $v = v_0(1-\rho(r)/\rho_0)\delta^3(\boldsymbol{r}-\boldsymbol{r}')$ with $v_0 = -900\mathrm{MeVfm}^3$ and $\rho_0 = 0.16\mathrm{fm}^{-3}$. To demonstrate how the

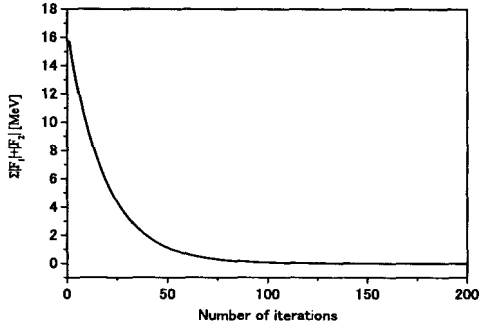

Figure 1. Sum of the absolute values of the matrix elements of F_1 and F_2 as a function of the number of iterations for ^{22}O.

gradient method works, we present a convergence process for ^{22}O in Fig. 1, where the HF ground state consisting of fully occupied $1d_{5/2}$ is taken as the starting ground state. In the case of ^{20}O, the starting ground state is assumed to be the two-hole state of $1d_{5/2}$.

We calculate the first 2^+ states and their two-phonon states using the same single-particle states and residual interaction as those used in the ground-state calculations. The strength functions for the first 2^+ state in ^{20}O are shown in Fig. 2. The 2^+ state in ERPA becomes more collective than that in RPA. This is due to the mixing of configurations consisting of two-hole states in the $d_{5/2}$ orbit. These configurations are degenerate with the ground state when the residual interaction is absent. The first 2^+ state in ^{22}O is shown in Fig. 3. Since ^{22}O is a nearly closed-shell nucleus, the first 2^+ state is slightly shifted upward due to weak ground-state correlations. The excitation energy of ^{22}O is larger than that of ^{20}O, which is consistent with experimental data. However, the excitation energies are larger than experimental values: An adjustment of the parameters of the Skyrme force may be necessary. The $B(E2 : 0^+ \rightarrow 2^+)$ values for ^{20}O and ^{22}O calculated assuming the neutron effective charge of $0.5e$ are 17 $e^2\mathrm{fm}^4$

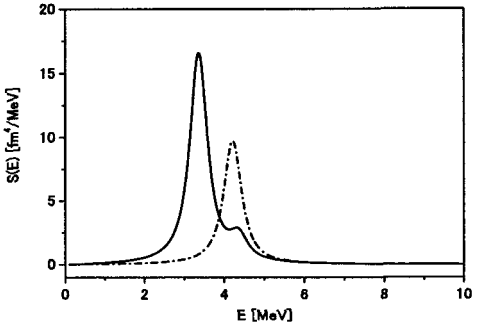

Figure 2. Strength distributions of the neutron quadrupole modes in ^{20}O calculated in ERPA (solid line) and RPA (dot-dashed line). The strength functions are smoothed with $\Gamma = 0.5$ MeV.

and 18 $e^2\text{fm}^4$, respectively. Although the $B(E2)$ value for ^{22}O is comparable with the experimental value of 21 ± 8 $e^2\text{fm}^4$, that for ^{20}O is about two thirds of experimental data: Apparently we have to include more configurations. The advantage of ERPA over QRPA is that the two phonon states

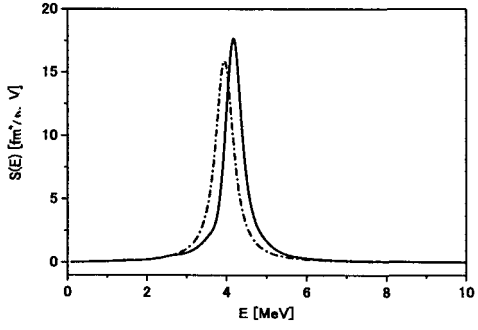

Figure 3. Strength distributions of the neutron quadrupole modes in ^{22}O calculated in ERPA (solid line) and RPA (dot-dashed line).

can be calculated simultaneously. The strength functions for the two-body operator $\hat{Q}_2 = [r^2Y_2 \otimes r^2Y_2]^J_0$ with J =0, 2, and 4 are shown in Fig.4 for ^{22}O. Although the excitation energies of the 2^+ and 4^+ states are about twice the energy of the first 2^+ state, the 0^+ state appears at very low

energy. This is similar to a shell model calculation [11].

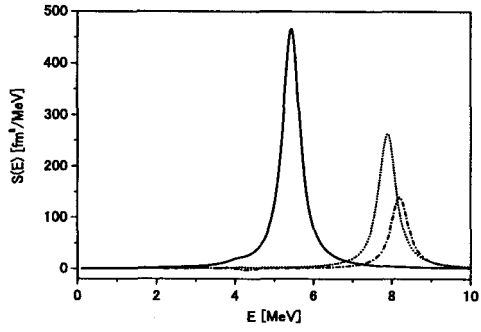

Figure 4. Strength distributions of the two-phonon states of the neutron quadrupole mode in ^{22}O calculated in ERPA. The solid, dotted, and dot-dashed lines depict the results for the 0^+, 2^+, and 4^+ states, respectively. The strength functions are smoothed with $\Gamma = 0.5$ MeV.

4. Summary

We presented the first application of ERPA formulated using a correlated ground-state. We used an iterative gradient method to obtain the correlated ground states of ^{20,22}O. The first 2^+ states and their two-phonon states were studied in ERPA. It was demonstrated that our ERPA with ground-state correlations is applicable to the study of low-lying collective states.

References

1. M. Matsuo, Nucl. Phys. **A696**, 371 (2001) and talk at this symposium.
2. E. Khan et al., Phys. Rev. **C66**, 024309 (2002).
3. M. Gong and M. Tohyama, Z. Phys. **A335**, 153 (1990).
4. M. Tohyama and A. S. Umar, Phys. Lett. **B516**, 415 (2001): Phys. Lett. **B549**, 72 (2002).
5. M. Tohyama, Prog. Theor. Phys. **92**, 905 (1994).
6. M. Tohyama and M. Gong, Z. Phys. **A332**, 269 (1989).
7. M. Tohyama, S. Takahara, and P. Schuck, nucl-th/0311016.
8. M. Tohyama and P. Schuck, nucl-th/0305088.
9. S. J. Wang and W. Cassing, Ann. Phys. **159**, 328 (1985).
10. S. Drożdż, S. Nishizaki, J. Speth, and J. Wambach, Phys. Rep. **197**, 1 (1990).
11. B. A. Brown, http://www.nscl.msu.edu/~brown/database.htm.

Density and gamma-transitions of unstable nuclei

This page intentionally left blank

NEUTRON DENSITIES OF TIN ISOTOPES EXTRACTED FROM THE PROTON ELASTIC SCATTERING AND THE RPS PROJECT AT RIKEN

H. SAKAGUCHI

Departmernt of Physics Kyoto University, sakaguchi@nh.scphys.kyoto-u.ac.jp

Cross sections and analyzing powers of proton elastic scattering off ^{58}Ni and ^{116,118,120,122,124}Sn at 295 MeV have been measured up to the angle of about 4 fm^{-1} in momentum transfer to deduce a systematic change of neutron density distribution. Since the shapes of neutron and proton distributions are supposed to be the same in ^{58}Ni, we have used the ^{58}Ni elastic scattering as a reference to tune the relativistic Love-Franey interaction used in the relativistic impulse approximation by introducing a medium effect. Then, we have applied the elastic proton scattering to deduce the neutron density distribution of tin isotopes. The result of our analysis shows a clear systematic behavior which shows a gradual filling in the $3s_{1/2}$ neutron single particle orbit. A recoil particle spectrometer(RPS) project at RIKEN to deduce the density distribution for unstable nuclei is reported.

1. Introduction

Density distributions of nuclei have been one of the fundamentals for nuclear physics. In β-stable nuclei it has been believed that proton and neutron distributions are almost the same and the electron scattering data offer a good basis for the density distribution. However, in unstable nuclei far from the β-stable line, we expect different proton and neutron density distributions. In addition, we cannot use the electron scattering to deduce charge distributions of unstable nuclei until the realization of the high luminocity collider between the electron beam and the unstable nuclear beam in the future.

In this report we propose to use intermediate energy proton elastic scattering to deduce density distributions of unstable nuclei, since by using solid hydrogen target and inverse kinematics we can measure proton elastic scattering of unstable nuclei at intermediate energies, where the mean free path of nucleons in the nucleus is large and the nuclear reaction process is simple. Before applying this proton elastic scattering to unstable nuclei we need to confirm how well we can deduce density distributions in stable nuclei. Thus

we have performed a series of proton elastic scattering measurements off ^{58}Ni and ^{116,118,120,122,124}Sn at RCNP, Osaka, Ring Cyclotron in the energy region between 200 MeV and 400 MeV.

For stable nuclei there have been many works until now, trying to deduce neutron density ditributions by strong interactions, such as intermediate energy proton elastic scattering. But most of them are hindered by the insufficient microscopic description of the scattering below 200 MeV/A and also the imaginary part of the optical potential above 500 MeV/A. Today we present a new approach to extract the neutron density distribution by using 300 MeV protons and the modified version of the relativistic impulse approximation. At the incident energy of 300 MeV the total cross section of p-p scattering shows a minimum compared to the energy regions below 200 MeV or above 500 MeV. In order to deduce nuclear densities by protons, the incident energy has to be high enough to describe the scattering by the impulse approximation, but must be well below the energy of the meson factory in order to obtain good information of nuclear interior which is easily masked by the meson production.

2. s-orbit effect

In tin isotopes it is suggested that the $3s_{1/2}$ orbit is filled gradually as the neutron number increases. First let me remind you s-orbit effects observed in the density distribution of protons. In Fig. 1 and 2 we show point proton density distributions unfolded from the charge distribution. In ^{16}O , ^{24}Mg, and ^{28}Si, which are nuclei before the filling of the proton 2 $s_{1/2}$ orbit, we can see decreases of densities at the nuclear center , whereas a bump structure appears in the nuclear center in the case of ^{32}S after the s-orbit filling. In the case of $3s_{1/2}$ we also see a decrease and an increase of density deitribution at the nuclear center in ^{205}Tl and ^{206}Pb, respectively, reflecting the effect of the s-orbit. We notice that before the filling of s-orbit the density distribution decreases in the nuclear center, preparing a room for the filling of the s shell. Our purpose of the elastic scattering of tin isotopes is to identify a similar s-orbit effect in the neutron density distribution.

3. Tuning the effective interaction in nuclei

Adding to the selection of the beam energy, we need to caliblate[ref. 1] the effective nucleon-nucleon interaction especially in the nuclear interior by the scattering from the nucleus, whose density distribution is well known.

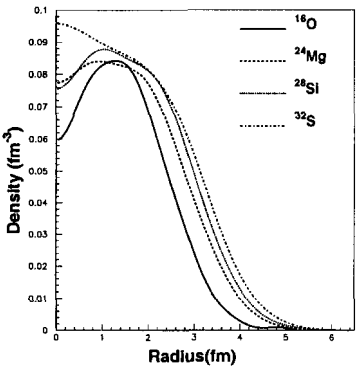

Fig. 1 Point proton density distributions for s-d shell nuclei

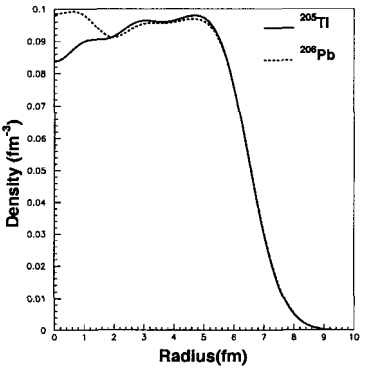

Fig.2 Point proton desity distributions for ^{205}Tl and ^{206}Pb

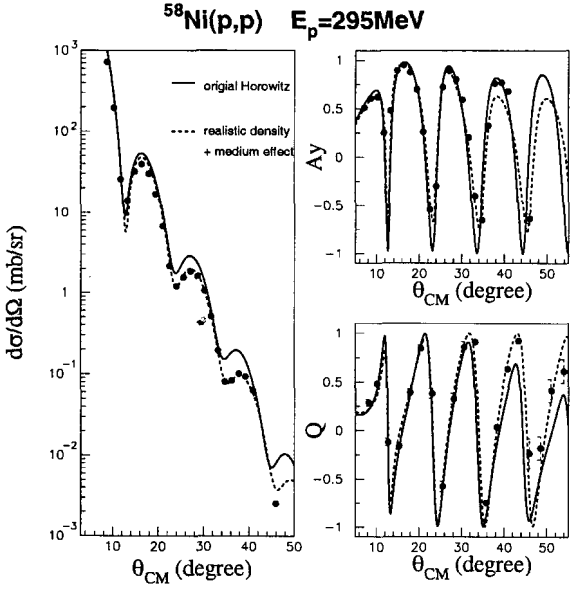

Fig.3 ^{58}Ni(p,p) at E_p=300 MeV and the RIA calculations. Broken curves are RIA with the medium effect and the solid curves are original calculation by the code of Horowitz[ref.2]

We used elastic scattering from ^{58}Ni to tune the interaction, since ^{58}Ni is the heaviest stable nucleus with N $\approx$ Z and the density distribution of neutrons in ^{58}Ni is well assumed to be the same as the one for protons. The relativistic Hartree (RH) calculation predicts the same shape for proton and neutron density distributions. In the density matrix expansion for the nonrelativistic Hartre Fock calculation the difference of the root

mean square radii of neutron and proton distributions is calculated to be 0.00[ref.3]. Thus our assumption is thought to be reasonable. In the RIA calculation we need scalar densities both for protons and neutrons, which are assumed to be 0.96 times of usual densties (vector densities). In the RH calculation for the medium and heavy nuclei the ratio of scalar to vector densities is well approximated to be 0.96.

The result of the RIA calculation is compared with our experimental data [ref.1] in Fig.3. Solid curves are the original Horowitz type calculations, which deviate from the experimental cross section data. In order to explain the experiment we have found that we have to modify the scattering amplitudes of 'Relativistic Love-Franey Interaction'[ref. 2] inside the nucleus as follows;

$$g_j^2, \quad \bar{g}_j^2 \longrightarrow \frac{g_j^2}{1+a_j\left(\frac{\rho(r)}{\rho_0}\right)}, \qquad \frac{\bar{g}_j^2}{1+\bar{a}_j\left(\frac{\rho(r)}{\rho_0}\right)}$$

$$m_j, \quad \bar{m}_j \longrightarrow m_j\left(1+b_j\left(\frac{\rho(r)}{\rho_0}\right)\right), \ \bar{m}_j\left(1+\bar{b}_j\left(\frac{\rho(r)}{\rho_0}\right)\right), \quad j=\sigma, \quad \omega.$$

Thus we have changed phenomenologically the masses of exchanged mesons and the coupling constants, depending on the nuclear densities, which is called medium effects. Then we can explain the scattering precisely as shown in the broken curves in Fig.3.

The form of density dependence is explained as follows by Kohmura[ref.4]. The medium effect of exchanged mesons is considered to be the change of the mass operator of meson propagator.

$$\frac{g_j^2}{q^2+m_j^2} \longrightarrow \frac{g_j^2}{q^2+m_j^2+\Pi_j}, \quad \Pi_j = a_j\left(\frac{\rho}{\rho_0}\right)+b_j\left(\frac{\rho}{\rho_0}\right)q^2+..$$

Here the additional term Π_j in the above meson propagator is introduced as a medium effect. If we expand Π_j in terms of the density ρ and the square of the transfered momentum q^2 , we have

$$\frac{g_j^2}{q^2+m_j^2+\Pi_j} \approx \left(\frac{g_j^2}{1+b_j(\frac{\rho}{\rho_0})}\right)\left(\frac{1}{q^2+m_j^2+(a_j-b_j)(\frac{\rho}{\rho_0})}\right).$$

The medium effect is thought to be one of the presentations for the partial restoration of chiral symmetry, Pauli- blocking, and multi-step processes.

4. Application of medium effects

In the previous section we have tuned the interaction in the RIA with the experimental data by introducing the medium effect. If this medium effect is a global one, we can predict the proton elastic scattering by using known density distributions and the same medium effect parameters as for ^{58}Ni. As an example we compare the proton elastic scattering data for ^{208}Pb measured at TRIUMF[ref. 5] with the RIA modified by the medium effect in Fig 4. The solid curves are the results of the original Horowits type calculation. If we adopt the point proton distribution unfolded from the charge distribution, the neutron density distribution measured at LAMPF and use the same medium effect parameters as in ^{58}Ni, the result of RIA calculation explains the scattering as shown by the broken curves remarkably. In this calculation there is no free parameter to tune the calculation. Thus we have confirmed the applicabilty of our medium effect. Since we now know the interaction, we can determine the density distribution from the scattering. In the case of stable nuclei we know already the density distribution of protons. Then we can deduce the neutron density distributions from the proton elastic scattering.

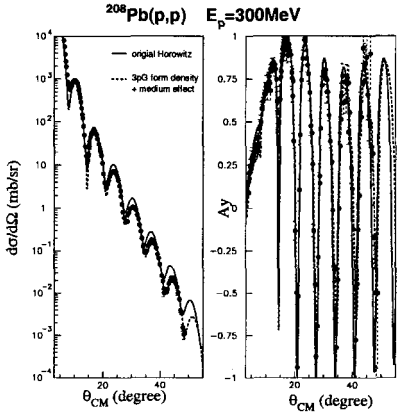

Fig.4 ^{208}Pb(p,p) data of TRIUMF and the predicton by using the medium effect(the broken curve)

5. Measurements of proton elastic scattering for Tin isotopes

We have performed a new experiment to measure the neutron density distributions of tin isotopes. In a naive shell model the $3s_{\frac{1}{2}}$ neutron orbit in ^{120}Sn is closed. We have measured differential cross sections and analyzing powers of proton elastic scattering off ^{116,118,120,122,124}Sn at $E_p = 300$ MeV. The experiment was performed at the Research Center for Nuclear Physics, using the Grand Raiden spectrometer and the focal plane detector system. In order to achieve an accurate measurement of relative cross sections we have installed a newly developed rapid target changer, which can change

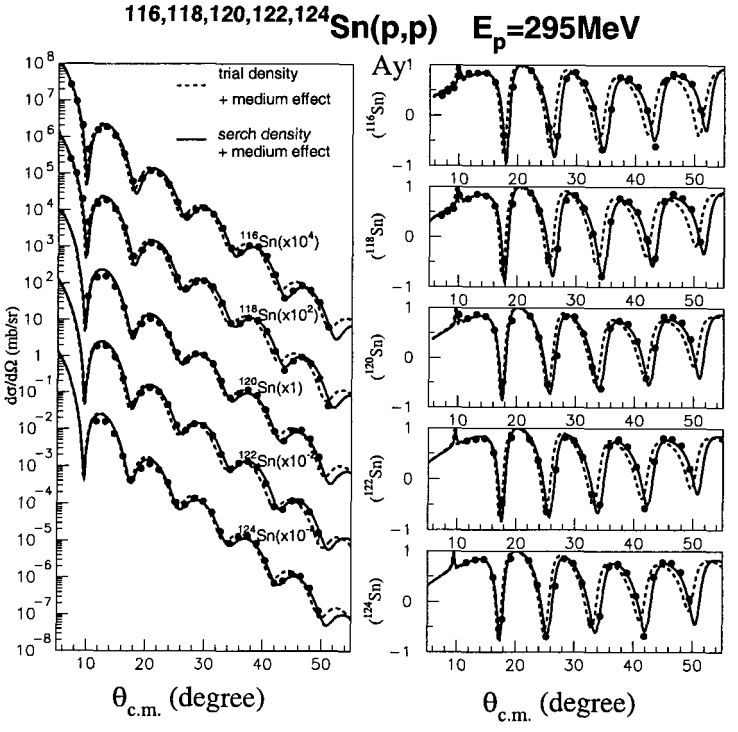

Fig.5 ^{116,118,120,122,124}Sn(p,p) data and RIA analysis

the target within 0.5 seconds and measured 3 isotopes in a single run. During the movement of the target changer the beam is stopped at the exit of the ion source. The precision of the target position reproducibility is better than 0.1 mm. Energy resolution of the beam was 200 keV in FWHM, which is due to the energy width of the beam itself, but is enough to separate elastic scattering from the inelastic peaks. Differential cross sections and the analyzing powers were measured up to the 50 degree(momentum transfer of 4.5 fm^{-1}) as shown in Fig.5. In order to deduce neutron density distributions from the scattering, we have used point proton density distribution unfolded from the charge distribution by electron scattering[ref.7]. For unfolding we used the sum of monopole type proton charge form factor obtained from the e-p scattering[ref.8]. The point proton density distribution are shown in Fig. 6 in the broken curves.

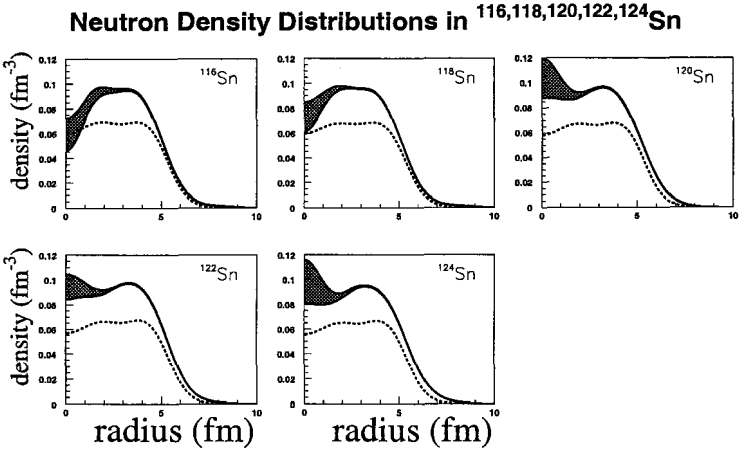

Fig. 6 Deduced neutron density distributions. The broken curves are point proton densities.

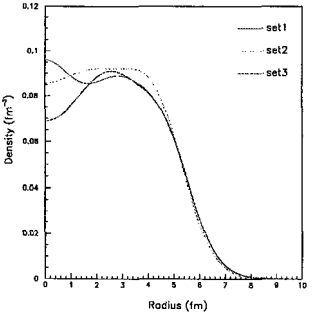

Fig. 7 3 initial neutron density distributions

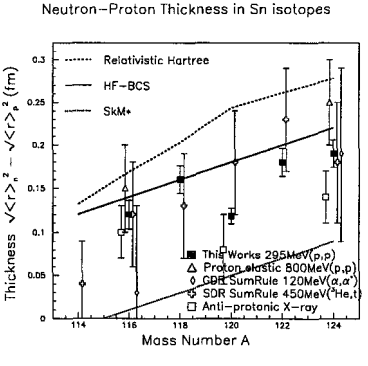

Fig. 8 Differences between proton and neutron RMS radii

6. Neutron density distributions

As for the form of neutron distribution we have used sum of Gaussian type form shown as follows; For neutron density search we have used 12 parameters of N_i . Other parameters such as γ, R_i , were taken from the SOG type charge distribution by Sick[ref.6].

$$\rho_n(\mathbf{r}) = \frac{N}{2\pi^{3/2}\gamma^3} \sum_{i=1}^{12} \frac{N_i}{1+2R_i^2/\gamma^2} \left(e^{-(r-R_i)^2/\gamma^2} + e^{-(r+R_i)^2/\gamma^2} \right),$$

$$\sum_{i=1}^{12} N_i = 1, \quad \int \rho_n(\mathbf{r}) d\mathbf{r} = N.$$

As initial densities for the search we have used 3 different forms as shown in Fig. 7. The set1 has a dip in the nuclear center, whereas set3 has a small bump due to the $3s_{1/2}$ orbit in the nuclear center. The set2 has the same shape as the proton distribution. In Fig.5 we show experimental data together with the results of the search(shown by solid curves) and the calculations using initial set1 neutron density distributions(broken curves). As for the medium effects we have used the same parameter defined by the scattering from the ^{58}Ni target.

In Fig.6 we show the obtained neutron density distributions for tin isotopes. The error bands shown by the hatched area in the figures are defined by the contour curves of the density distributions generated by the Monte Carlo calculation with the increase of the reduced χ^2 less than 1 as shown in the following formula, which take into account even the ambiguities of our RIA model.

$$\chi^2_\nu \leq \chi^2_{\nu min} + 1, \quad \chi^2_\nu = \frac{1}{\nu} \sum_i \frac{(x^i_{calcu} - x^i_{exp})^2}{\delta x^i_{exp}}$$

The point proton densities are also shown by the broken curves in the same figure. In this figure we notice phenomena of density decrease in the center of the nucleus for ^{116,118}Sn. But in ^{120,122,124}Sn we can see an increase of the central density of the nucleus and the nuclear radius gradually increases as the mass number. These behaviors clearly indicate the effects of s-obrbit filling. In this search and calculation we have neglected the medium effect for the ρ-meson, bacause a contribution of ρ-meson to the scattering is $\frac{(N-Z)}{A}$ of the normal vector mesons such as ω-meson. Fig. 8 displays the differences of root mean square radii between point protons and point neutron distributions. We can observe a small drop of the difference at ^{120}Sn, which also shows the effect of the $3s_{1/2}$ orbit filling.

7. Recoil particle spectrometer project at RIKEN

For the new Radio Isotope Beam Facility being constructed at RIKEN we are now constructing a recoil particle spectrometer(RPS) to measure elastic

scattering of unstable nuclear beam from the solid hydrogen target placed in the center of the system shown in the right figure. By measuring the recoil protons between the scattering angles 70 deg and 85 deg. we plan to deduce density distribution of unstable nuclei.

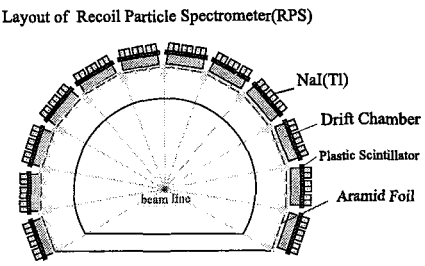

8. Acknowledgements

This report is mainly based on the master thesis by S. Terashima and the PhD thesis of H.Takeda at Kyoto Univ. I owe them very much. Experiments at RCNP are the collaboration of the following people of Kyoto Univ. and RCNP Osaka Univ.; S. Terashima, H. Takeda, H. Sakaguchi, Y. Yosoi, T. Taki, M. Itoh, M.Kawabata, M. Uchida and Y. Yasuda. And the RPS project at RIKEN is a joint project of the following people at Kyoto Univ. and RIKEN; S. Terashima, H. Sakaguchi, H. Takeda, I.Tanihata, R. Kanungo, T. Ohnishi, and T. Suda.

References

1. H. Sakaguchi, H. Takeda, S. Toyama, M. Itoh, A. Yamagoshi, A. Tamii, H. P. Yosoi, H. Akimune, I. Daito, T. Inomata, T. Noro, and K. Hosono , Phys. Rev. **C57**,(1998) 1749; H. Takeda,PhD Thesis(2002). Kyoto Univ.
2. C.J. Horowitz, Phys. Rev. **C31**,(1985) 1340; D.P. Murdock and C.J.Horowitz, Phys. Rev. **C35**,(1987) 1442; C.J. Horowitz, D.P. Murdock and B.D. Serot, *Computional Nuclear Physcs 1*, (Springer-Verlag, Berlin, 1991),Chapter 7.
3. L. Ray et al., Phys.Rev. C18(1978)2641, Phys.Rev. C19(1979)1855.
4. S.Kinpara, T. Kohmura, Prog. Theor. Phys. 93(1995)659.
5. D.A.Hutcheon et al., Nucl.Phys.A483(1988)429.
6. I.Sick, Nucl. Phys. A218(1974)509 .
7. H. de Vries *et al.*, Atomic Data and Nuclear Data Tables **36** (1987) 495, and references therein.
8. G.G.Simon et al., Nucl.Phys.A333(1980)381.

DETERMINATION OF MATTER SURFACE DISTRIBUTION OF NEUTRON-RICH NUCLEI

AKIHISA KOHAMA

RI Beam Science Laboratory, RIKEN
2-1 Hirosawa, Wako-shi, Saitama 351-0198, JAPAN
kohama@rarfaxp.riken.jp

I report the recent progress of our study on the determination of the nuclear density distributions from the proton-nucleus elastic scattering cross sections.

1. Introduction

Experimental facilities for unstable nuclei have been receiving much attention in the recent years. Adding to the present facilities, such as GSI in Germany and National Superconduction Cyclotoron Labratory, Michigan State University in the U.S., RI-Beam Factory (RIBF) is under construction at RIKEN in Japan [1], and the Rare Isotope Accelerator (RIA) facility is being proposed in the U.S. Such facilities will provide much data for the physics of unstable nuclei. Among various aspects of unstable nuclei, one of interest is the one-body matter density distribution, $\rho(\mathbf{r})$. The distribution is a fundamental quantity of nuclei, and will serve as an important measure to test how well we understand nuclear structure. It is perhaps an appropriate time to make a close investigation as to how well one could determine the one-body matter density distributions from the various kinds of data that are expected to emerge from the facilities.

In this article, I am going to report the recent progress of our study on the determination of the nuclear density distributions from the proton-nucleus elastic scattering cross sections. In the former half I present our simulation results of how to determine the matter density distribution of neutron-rich nuclei, taking ^{78}Ni as the example. In the latter half I show our trial to see the effect of nuclear outer surface of the density distribution to be appeared in the forward cross section.

2. Model-independent Determination of the Matter Density Distribution of Neutron-rich Nuclei

The unstable nuclei on the neutron-rich side (neutron-rich nuclei) are often characterized as those with a large surface region generated by loosely bound valence nucleons [2]. We focus on the determination of the matter density distributions in the surface and outer regions to clarify the feature. The surface is the region where $\rho(r)$ /$\rho(0)$ varies from 0.9 to 0.1 if we have a density distribution of monotonically decreasing function in r, such as the 2-parameter Fermi distribution, in mind.

In this section, we discuss how much we could determine the nuclear *matter* density distributions of neutron-rich nuclei from the proton-nucleus elastic scatterings [3]. To this end, we make simulations. The density distribution is determined in a model-independent way by generating pseudo data and by carefully applying a statistical and systematic error analysis. It is model-independent, because the density distribution is determined as a linear combination of basis functions. We do this by avoiding the use of specific analytic forms of the density distribution, which is the common practice in this field [4]. The elastic scattering cross section data that we will examine in our model calculation are generated artificially, and will be referred to as "pseudo data" [5]. At first, they are generated from a specific density distribution (of the three-parameter Fermi form) by the use of the above described procedure with the eikonal approximation [6] and are then shuffled statistically at each data point with an assigned experimental uncertainty (corresponds to a Gaussian width), simulating the situations expected in future experiments at the RIBF. We follow the traditional approach of the least-square method.

In Fig. 1 we demonstrate that the matter density distribution in the surface region is determined well by the use of the relatively low-intensity beams, such as 10 [$\sec^{-1}$] [3]. Those beams of the neutron-rich nuclei become available at the upcoming radioactive beam facilities. The determination deteriorates in the central region of the density, as the quality of data decreases [3].

The obtained density will give the information of the bulk structure of nuclei, which contributes to constrain parameter-sets of the equation of state of the nuclear matter [7], for example. Even with the low intensity beam, changes of the radius or the diffuseness due to the increase of the neutron number could be determined by these studies.

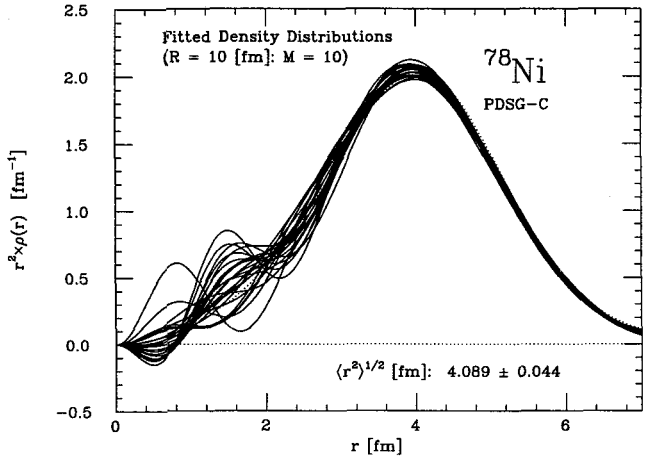

Figure 1. Results of the least-square fitting for the pseudo-data set group C of ^{78}Ni, which corresponds to a nuclear beam intensity of 10 [s^{-1}] at RIBF. R (= 10 [fm]) is the maximum distance to probe nuclei by the experiment, and M (= 10) is the number of basis functions. 25 fitted density distributions (solid curve), and the original distribution (dotted curve). The density distributions are drawn in the form of r^2 $\rho(r)$. We use here the Gaussian basis function.

3. Effect of Nuclear Outer Surface

For an extension of the discussion in the previous section, we discuss how the nuclear density distributions in the outer surface region affect the differential cross section of the proton-nucleus elastic scattering in this section [8]. This consideration would be useful for the analysis of nuclei whose surface structure does not change considerably when we approach the neutron drip line. This may occur for medium-heavy nuclei, such as Ni or Sn.

We apply the Glauber approximation with the Coulomb interaction of the finite extension of the point-proton density distribution [9], and concentrate on the observation of the behavior of the cross section. Since the proton of small momentum transfer probes the nucleus as a whole including the nuclear periphery, the effect of the outer surface is expected to appear in the forward direction. We mimic the halo structure of the neutron-rich nuclei, by artificially varying the one-neutron separation energy, S_n, from the original one, but kept the surface shape unchanged. The normalization

is also kept fixed.

In Fig. 2 one can see that in the forward direction where the nuclear and the Coulomb interactions compete with each other, the cross section of the halolike neutron density (the solid curve) oscillates around the one determined by the original S_n of ^{58}Ni (the dashed curve), which is due to Coulomb-nuclear interference. The smaller S_n becomes, the larger the effect becomes, though the net effect is rather small.

The precise measurements in the forward direction, which could be possible due to the large cross sections, will assist the minute (model-independent) determination of the nuclear density distributions of the neutron-rich nuclei.

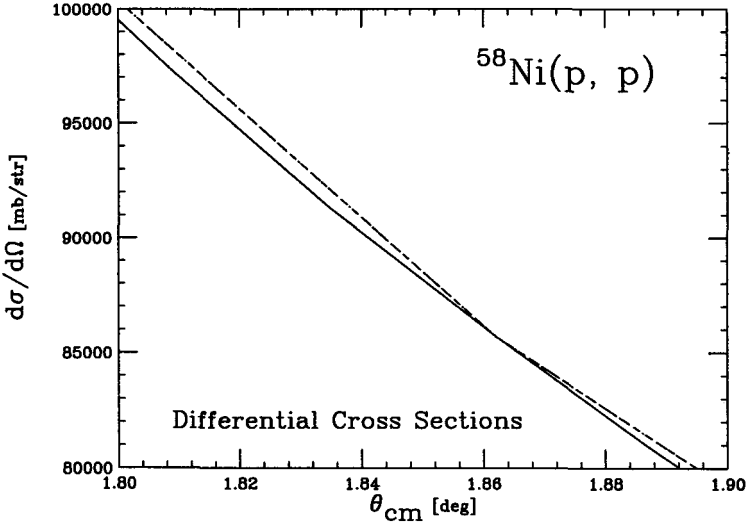

Figure 2. Effect of the outer surface of the neutron density distribution on the proton-"mock" ^{58}Ni elastic scattering cross section in the linear scale, not in the logarithmic scale. The dashed curve is calculated from the neutron density distribution of a linear combination of the two two-parameter Fermi distributions (2pFs) with the asymptotic behavior determined by S_n of the actual ^{58}Ni. The dot-dashed curve is from the neutron density distribution determined by 50 [%] of the original S_n, and the solid curve is by 10 [%] of the same S_n. The dot-dashed and the dashed curves are very close to each other, and cannot be identified separately by eye.

4. Summary and Conclusion

The matter density distribution in the surface region is shown to be determined well by a relatively low intensity beam in the order of 10 [sec^{-1}], which is an expected intensity of the ^{78}Ni beam at the RIBF of RIKEN [3]. The effect from the nuclear outer surface appears in the forward cross section through Coulomb-nuclear interference, but the net effect is rather small. Therefore, for the present, we should focus on the determination of the matter surface density of neutron-rich nuclei.

Acknowledgments

We acknowledge I.Tanihata for his invaluable suggestions and comments, and M.Kamimura, K.Yazaki, K.Iida, and K.Oyamatsu for stimulating discussions. We thank T.Ohnishi, T.Suda, and K.Katori for their assistance on our generation of the pseudo data to be realistic to the RIBF facilities. A part of this work is supported under the Special Postdoctoral Research Program at RIKEN.

At last but not least, I thank all the organizers of NENS03 for their hospitality.

References

1. H. Sakaguchi, in this volume.
2. I. Tanihata *et al.*, *Phys. Lett.*, **B160**, 380 (1985); *Phys. Rev. Lett.* **55**, 2676 (1985).
3. A. Kohama, R. Seki, A. Arima, and S. Yamaji, *J. Phys. Soc. Jpn.* **72**, 2766 (2003).
4. C.J.Batty, E.Friedman, H.J.Gils, and H.Rebel, *Adv. Nucl. Phys.*, **Vol.19**, 1 (1989).
5. J.L.Friar and J.W.Negele, *Adv. Nucl. Phys.*, **Vol.8**, 219 (1975).
6. R. J. Glauber, *Lectures in Theoretical Physics*, ed. W.E.Brittin and D.G.Dunham, Interscience, New York, **Vol.1**, 315 (1959).
7. K. Oyamatsu and K. Iida, *Prog. Theo. Phys.* **109**, 631 (2003).
8. A. Kohama, in preparation.
9. R. J. Glauber, *High-Energy Physics and Nuclear Structure*, ed. S.Devons, (Plenum Press, 1970), p.207.

NUCLEAR STRUCTURE STUDIES OF EXOTIC NUCLEI VIA THE STRENGTH OF E2 TRANSITIONS; ADVANCED TIME-DELAYED $\gamma\gamma$ SPECTROSCOPY AT THE EXTREME

H. MACH[a,1], I. MATEA[b], M. STANOIU[b], YU.E. PENIONZHKEVICH[c], F. DE OLIVEIRA SANTOS[b], D. VERNEY[b], S. LUKYANOV[c], B. CEDERWALL[d], A. COVELLO[e], Z. DLOUHY[f], B. FOGELBERG[a], L.M. FRAILE[g,h], G. DE FRANCE[b], G. GEORGIEV[b], M. GORSKA[i], H. GRAWE[i], R. GRZYWACZ[j], A. KORGUL[k], J. MRAZEK[f], W. PLOCIENNIK[l], Z. PODOLYAK[m], S. RAY[b], E. RUCHOWSKA[l], M-G. SAINT-LAURENT[b], M. SAWICKA[k], CH. STODEL[b], O. TARASOV[c]

[a] *ISV, Uppsala University, Nyköping, Sweden,* [b] *GANIL, Caen, France,* [c] *FLNR, JINR Dubna, Russia,* [d] *Physics Dept., KTH, Stockholm, Sweden,* [e] *DSF, Univ. di Napoli Federico II and Inst.Naz. di Fisica Nucl., Napoli, Italy,* [f] *NPI ASCR Rez, Czech Republic,* [g] *Univ. Complutense, Madrid, Spain,* [h] *ISOLDE, CERN, Geneva, Switzerland,* [i] *GSI Darmstadt, Germany,* [j] *Univ. of Tennessee, Knoxville, USA,* [k] *IFD, Warsaw Univ., Warsaw, Poland,* [l] *SINS, Swierk, Poland,* [m] *Dep. of Physics, Univ. of Surrey, UK.*

[1] *E-mail: Henryk.Mach@studsvik.uu.se, Website: www.studsvik.uu.se/fasttiming*

We report preliminary results from ultra-fast time-delayed $\gamma\gamma$(t) measurements on exotic nuclei just below ^{100}Sn. The measurements were performed at the LISE spectrometer in GANIL. Nuclei of ^{94}Ru and ^{96}Pd were populated in the isomeric states via the fragmentation of energetic ^{112}Cd beam. Preliminary lifetime or lifetime limits are reported for the 6^+, 4^+, and 2^+ states in ^{96}Pd and the 4^+ and 2^+ states in ^{94}Ru. These results indicate an unexpected and strong quenching of the B(E2) strength for the 4^+ to 2^+ E2 transition in ^{96}Pd in comparison with model predictions and the equivalent B(E2) strength in ^{94}Ru. The sequence of quenched B(E2) rates for the $8^+ \rightarrow 6^+$ E2 transition in ^{94}Ru, $4^+ \rightarrow 2^+$ E2 transition in ^{96}Pd and for the $8^+ \rightarrow 6^+$ E2 transition in ^{98}Cd, seems to represent a systematic pattern along the N=50 neutron number just below Z=50 and could imply a weak N=50 shell closure when approaching the doubly magic ^{100}Sn.

1. Introduction

We have recently extended the Advanced Time-Delayed $\beta\gamma\gamma$(t) Method[1,2] into the domain of $\gamma\gamma$(t) measurements[3] in order to determine with high precision the lifetimes of excited states in very exotic nuclei produced in

the fragmentation reactions. Using the Studsvik array of specially designed medium-large BaF_2 detectors one can obtain meaningful results even for very weak sources when the nuclei of interest are produced at the rate of 1 per minute, although precision measurements require the rates about 50 times higher. The newly measured E2 transition rates mostly concentrate on the neutron-rich side and particularly near the doubly magic ^{78}Ni and ^{132}Sn.[3] The most intriguing results, however, appear to come from the recent studies of the N=50 nuclei just below ^{100}Sn, performed at the LISE spectrometer at GANIL, where a number of new isomeric states have been identified. As an important finding this measurement has revealed a strongly quenched 4^+ to 2^+ E2 transition in ^{96}Pd and an enhanced equivalent transition in ^{94}Ru.

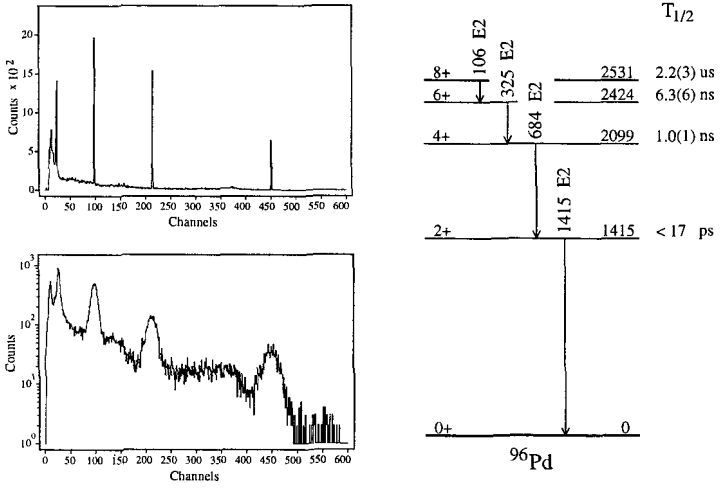

Figure 1. **Top Left:** Ge spectrum observed in the isomeric decay of ^{96}Pd showing four γ-rays at 106, 325, 684 and 1415 keV. **Bottom Left:** Same as above, but observed in the BaF_2 detector. **Right:** Decay scheme of the 8^+ isomer in ^{96}Pd; data from Ref.[4], except for the lifetimes (preliminary) of the 6^+, 4^+ and 2^+ levels, which are from this work.

2. Details of the measurements

The E389 experiment was performed at the LISE spectrometer in GANIL following fragmentation of the ^{112}Sn beam with the energy of 64 MeV/u on a ^{9}Be target. The A and Z determination of the fragments was obtained from the energy loss, total kinetic energy, and the time of flight of the

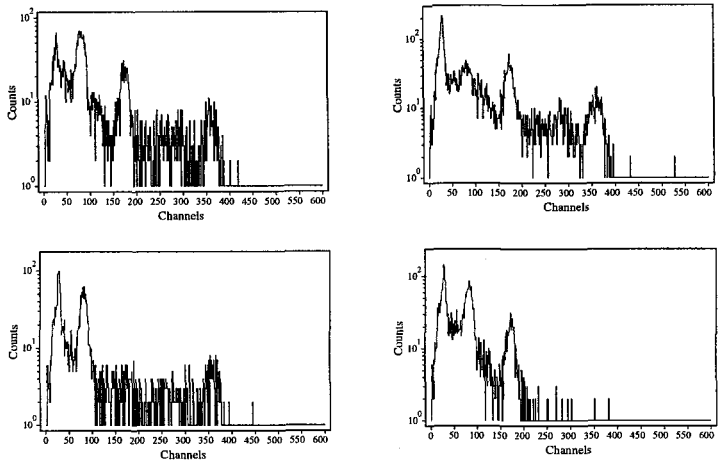

Figure 2. **Top Left:** Gamma-ray coincident spectrum observed in the BaF_2 detector, when gate is set on the full-energy-peak at 106 keV in the other detector. The other $\gamma\gamma$ coincidence spectra illustrated in this figure are gated by selecting the 325 (**Top Right**), 684 (**Bottom Left**) and 1415 keV peaks (**Bottom Right**) in the other BaF_2.

fragments, which were implanted into a Si detector at the point of measurement. The detection system included a small array of four fast timing BaF_2 detectors and a Ge spectrometer. They were positioned in a close geometry around the beam deposition point. The BaF_2 detectors were prepared and their time-response was calibrated at the OSIRIS separator at Studsvik. This system allowed for determination of level lifetimes in the range from about ~20 ns down to about 10 ps.

^{96}Pd: The results for ^{96}Pd are illustrated in figures 1-4 and table 1. Figure 1 presents the Ge and BaF_2 γ-ray spectra gated by the incoming ion, with the background subtracted. The spectra are very pure and include only peaks due to the decay of the 2.2 μs isomer in ^{96}Pd. Figure 2 shows the $\gamma\gamma$ energy spectra recorded in one BaF_2 detector when a gate on specific full energy peak was selected in the other BaF_2 detector. For example, the Bottom Left spectrum in Fig. 2 shows how cleanly one can sellect coincidences due to the 325 and 684 keV transitions, which we need to define the lifetime of the 4^+ state in ^{96}Pd. The time-delayed spectra are illustrated in Fig. 3. One can clearly distinguish the slopes due to the 6 and 1 ns half lives presented in the top and middle panels. The resultant E2 transition rates are listed in table 1. We note an unexpected quenching of the B(E2) value for the $4^+ \rightarrow 2+$ transition. In order to compare the

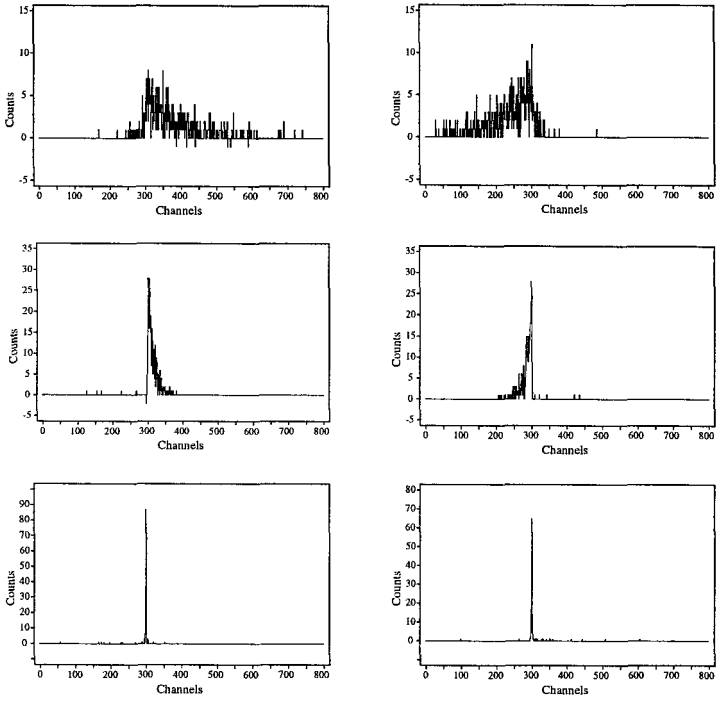

Figure 3. **Top Left:** Time-delayed $\gamma\gamma$(t) spectrum gated by the 106 keV (START) and 325 keV (STOP) transitions. The slope is due to the 6.3 ns half-live of the 2424-keV state in ^{96}Pd. **Top Right:** The time spectrum due to the inverted sequence of gating transitions, 325 keV (START) and 106 keV (STOP). Using these slopes one can determine very firmly the sequence of γ-rays in a cascade. **Middle Left and Right:** Equivalent time-delayed spectra due to the 325 keV (START) and 684 keV (STOP) transitions and their inverted gating sequence, respectively. A visible slope is due to the 1.0 ns half-life of the 2099 keV state in ^{96}Pd. **Bottom Left and Right** Semi-prompt time-delayed spectra due to the 684 keV (START) and 1415 keV (STOP) transitions and their inverted gating sequence, respectively. The centroids of these time aspectra are identical within the measurement uncertainty. Un upper limit of $T_{1/2} \leq 17$ ps (preliminary) can be deduced for the 1415 keV state in ^{96}Pd. Note, that the time response of BaF_2 detectors is not fully included into the analysis yet.

rate with the next N=50 even-even nucleus, we have turned our attention to the ^{94}Ru case, discussed next.

^{94}Ru: The experimental data for ^{94}Ru is illustrated in figures 5 and 6, and summarized in table 1. The γ-ray spectra shown in Fig. 5 are very pure, although a small background impurity line at 511 keV is also present. This is due to the long lifetime of the isomer (71 μs), which does not allow

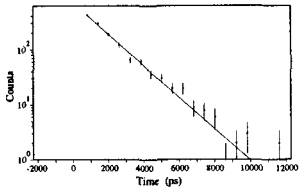

Figure 4. Fitting of the sum of the time spectra shown in the middle panel in Fig. 3, gives a half-life of 1.0(1) ns (preliminary) for the 4^+ 2099 keV state in ^{96}Pd.

for a proper subtraction of background events. Nevertheless, this impurity contribution is eliminated by energy selection in $\gamma\gamma$ coincidences. The time-delayed spectra due to the lifetimes of the 4^+ and 2^+ levels are shown in Fig. 6. One observes a small centroid shift due to the lifetime of the 4^+ state and no shift is observed due to the lifetime of the 2+ level.

3. Discussion

The results of the shell model calculations on the transition rates in ^{94}Ru, ^{96}Pd and ^{98}Cd are summarized in table 1. The calculations by Ball *et al.*[8], Gloeckner and Serduke[9] ("seniority" and "rates"), Ji and Wildenthal[10] and Sinatkas *et al.*[11] are marked as "B", "GS(s)", "GS(r)", "JW", and "S", re-

Table 1. Experimental and calculated B(E2) values in e^2fm^4 between the yrast states in ^{94}Ru, ^{96}Pd and ^{98}Cd. The experimental data are from Refs.[4,5,6,7], while results from this work are marked by superscript *a*. See text for explanation of the theoretical calculations marked by "B", "GS", "JW", "S", "C" and "IE" .

$J_i \rightarrow J_f$	Exp	B	GS(s)	GS(r)	JW	S	C	IE
^{94}Ru								
$2 \rightarrow 0$	≥ 9.5 [a]	266	216	213	282			
$4 \rightarrow 2$	≥ 46 [a]		8.0	8.0	2			
$6 \rightarrow 4$	2.89(10)	6.6	5.5	2.6	6	5		
$8 \rightarrow 6$	0.090(5)	3.1	2.2	0.10	0.9	2		0.064
^{96}Pd								
$2 \rightarrow 0$	≥ 6 [a]				254		164	
$4 \rightarrow 2$	3.8(4) [a]				43		20	
$6 \rightarrow 4$	24(2) [a]				22		13	
$8 \rightarrow 6$	8.9(13)				9		5.2	1.34
^{98}Cd								
$8 \rightarrow 6$	$31(4), 14.5^{+7.5}_{-3.5}$						32	6.9

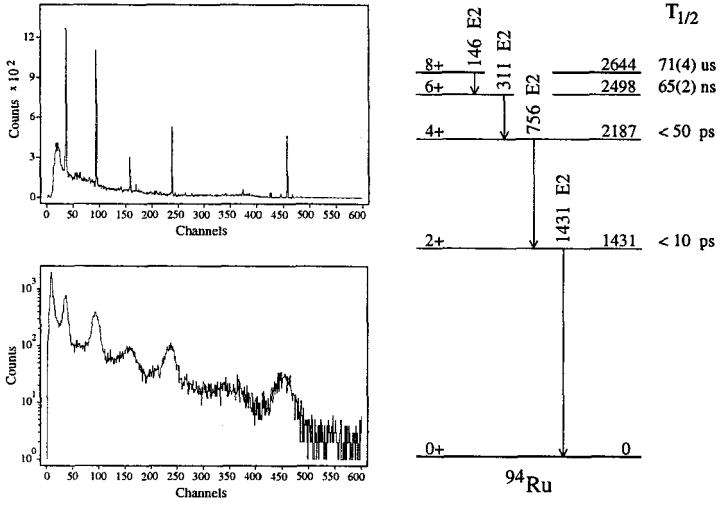

Figure 5. **Top Left:** Ge spectrum observed in the isomeric decay of ^{94}Ru showing four γ-rays at 146, 311, 756 and 1431 keV. A background line at 511 keV is also present in channel ~160. **Bottom Left:** Same as above, but observed in the BaF_2 detector. **Right:** A decay scheme of the 71 μs isomer in ^{94}Ru; data from Ref.[5], except for the (preliminary) lifetime limits for the 4^+ and 2^+ levels, which are from this work.

spectively. Recent calculations by Coraggio and co-workers using the realistic effective interaction derived from the Bonn-A nucleon-nucleon potential are marked by "C", while the calculations by Isakov and Erokhina are labelled by "IE". In the case of ^{94}Ru the calculations have difficulty reproducing the very small experimental B(E2) value for the $8 \rightarrow 6$ transition, and surprizingly also the much faster $4 \rightarrow 2$ value. The latter represents a new experimental result from this work. In the case of ^{96}Pd the calculations of Ji and Wildenthal[10] as well as those by Corraggio *et al.*[12] reproduce very well the experimental values for the $8 \rightarrow 6$ and $6 \rightarrow 4$ transitions, but strongly overestimate the rate for the $4 \rightarrow 2$ case.

To summarize, the new experimental B(E2;$4^+ \rightarrow 2^+$) values obtained in this work for ^{94}Ru and ^{96}Pd are both in disagreement with shell model predictions. The pattern of discrepancies in ^{94}Ru, ^{96}Pd and ^{98}Cd, could imply a weak N=50 shell closure when approaching the doubly magic ^{100}Sn.

Acknowledgments

This work was supported by the Swedish Research Council and the European Community-Access to Research Infrastructure action of the Improving

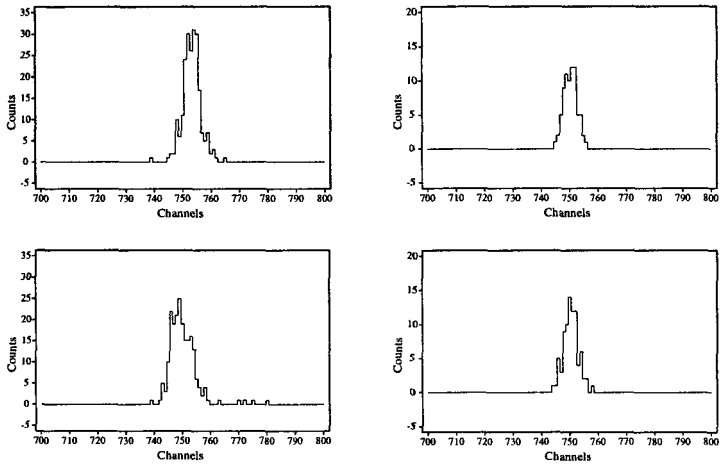

Figure 6. **Top Left and Bottom Left:** Time-delayed $\gamma\gamma(t)$ spectrum gated by the 311 keV (START) and 756 keV (STOP) transitions, and the one obtained by inverting the gating transitions. A visible shift in the centroids of time spectra from the prompt position in channel 750, is due to the mean life of the 4^+ 2187 keV state in ^{94}Pd, estimated (preliminary) as $T_{1/2} \leq 50$ ps. **Top Right and Bottom Right:** Semi-prompt time-delayed spectra due to the 756 keV (START) and 1431 keV (STOP) transitions and their inverted gating sequence, respectively. The centroids of these time aspectra are identical within the measurement uncertainty. Un upper limit of $T_{1/2} \leq 10$ ps (preliminary) can be deduced for the 1431 keV state in ^{94}Ru.

Human Potential Programme contracts N° HPRI-CT 1999-00019.

References

1. H. Mach, R.L. Gill and M. Moszyński, *Nucl. Instr. and Meth.* **A280**, 49 (1989), and references therein.
2. H. Mach *et al.*, *Nucl. Phys.* **A523**, 197 (1991).
3. H. Mach et al., *Nucl. Phys.* **A719**, 213 (2003).
4. L.K. Peker, *Nucl. Data Sheets* **68**, 165 (1993).
5. J.K. Tuli, *Nucl. Data Sheets* **66**, 1 (1992).
6. M. Górska *et al.*, *Phys. Rev. Lett.* **79**, 2415 (1997).
7. R. Grzywacz et al., *ENAM98, AIP Conf. Proc.* **455** (New York, 1998) p. 430.
8. J.B. Ball *et al.*, *Phys. Lett.* **29B**, 182 (1969)
9. D.H. Gloeckner and F.J.D. Serduke, *Nucl. Phys.* **A220**, 477 (1974).
10. Xiangdong Ji and B.H. Wildenthal, *Phys. Rev. C* **38**, 2849 (1988).
11. J. Sinatkas *et al.*, *J. Phys. G: Nucl. Part. Phys.* **18**, 1377 (1992).
12. L. Coraggio *et al.*, *J. Phys. G: Nucl. Part. Phys.* **26**, 1697 (2000).
13. V.I. Isakov and K.I. Erokhina, *Phys. At. Nucl.* **65**, 1431 (2002).

SYSTEMATICS OF LOW-LYING 2^+ STATES OF EVEN-EVEN NUCLEI IN NEUTRON-RICH SN AND NI REGION

J. TERASAKI AND J. ENGEL

Department of Physics and Astronomy,
University of North Carolina at Chapel Hill,
Phillips Hall, Chapel Hill, NC 27599-3255, USA

K. LANGANKE

Institute of Physics and Astronomy, University of Aarhus,
DK-8000 Aarhus C, Denmark

W. NAZAREWICZ[1,2,3] AND M. STOITSOV[1,2,4,5]

[1] *Department of Physics, University of Tennessee,*
Knoxville, Tennessee 37996, USA
[2] *Physics Division, Oak Ridge National Laboratory,*
P.O.Box 2008, Oak Ridge, Tennessee 37831, USA
[3] *Institute of Theoretical Physics, University of Warsaw,*
ul. Hoża 69, PL 00-681 Warsaw, Poland
[4] *Joint Institute for Heavy Ion Research,*
P.O.Box 2008, Bldg.6008, MS 6374 Oak Ridge, Tennessee 37831, USA
[5] *Institute of Nuclear Research and Nuclear Energy,*
Bulgarian Academy of Science, Sofia 1784, Bulgaria

We calculate energies E_{2+} and transition strengths $B(E2)\uparrow$ of the lowest 2^+ states of even neutron-rich Te and Sn isotopes, using the quasiparticle random phase approximation with simple separable interactions. With those calculations reproducing the experimental systematics very well, we discuss, first, an unusual relation between E_{2+} and $B(E2)\uparrow$ in the nuclei ^{132,136}Te; the relation does not follow the empirical formula $B(E2)\uparrow \propto 1/E_{2+}$. Second, we discuss the $B(E2)\uparrow$ of ^{132}Sn, which is larger than those of the neighboring even Sn isotopes. We also calculate g-factors for some of those 2^+ states. Finally, we argue that ^{68}Ni is not a doubly-magic nucleus.

1. Introduction

Recent developments in experimental technique have stimulated investigations of nuclei far from the stability line both experimentally and theoretically. The new region allows tests of theoretical methods that have been used to understand nuclear properties in or near the stable region. Our interest in this paper is in systematics of the lowest $J^\pi = 2^+$ excited states of even-even nuclei near ^{132}Sn and in neutron-rich Ni isotopes. Recently, an unusually small transition strength $B(E2)\uparrow$ in ^{136}Te was measured[1], one that does not follow the empirical formula rule $B(E2)\uparrow$ is inversely proportional to E_{2+} [2]. Reproducting and explaining this abnormal behavior is one of our purposes[3]. We shall also point out that $B(E2)\uparrow$ of ^{132}Sn is larger than those of ^{130,134}Sn, and display some g factors for the lowest 2^+ states of even-even nuclei around ^{132}Sn.

Another interesting problem is whether ^{68}Ni is doubly magic. There is an argument[4] that a large E_{2+} and a small $B(E2)\uparrow$ of ^{68}Ni indicate an $N = 40$ shell gap, but the binding energies do not show an irregularity expected from the shell gap. The authors of Ref. 4 stress the importance of the proton core excitations and neutron pairing correlations in the erosion of the $N = 40$ shell gap. We perform quasiparticle random phase approximation (QRPA) calculations with separable type phenomenological interactions and explain this phenomenon[5].

2. Around ^{132}Sn

We show results of our QRPA calculations of ^{132,134,136}Te in Fig. 1 along with experimental data[1]. Our Hamiltonian consists of single-particle poten-

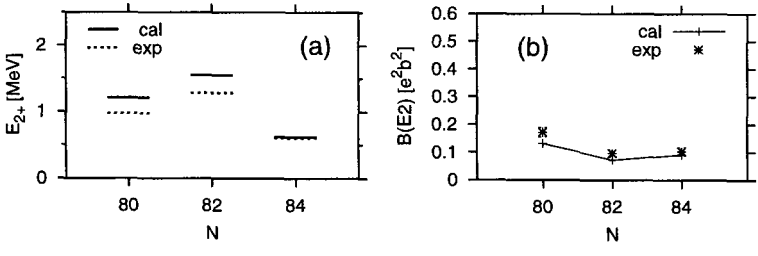

Figure 1. (a) E_{2+} of ^{132,134,136}Te isotopes. (b) $B(E2)\uparrow$ corresponding to (a).

tials, pairing potentials, and three separable interactions. The interactions used are isoscalar and isovector QQ forces and a quadrupole pairing force,

and the spherical symmetry is assumed. The detail of the calculation is given in Ref. 3. We see that the E_{2+} of ^{136}Te is lower than that of ^{132}Te, and the $B(E2)\uparrow$ of ^{136}Te is smaller than that of ^{132}Te. Thus, the two does are proportional here. The cause of this unusual behavior is the asymmetry of the neutron pairing gaps with respect to $N = 82$. We took the neutron pairing gaps from the experimental masses using the 3-point formula[6,7] and multiplied them by 0.6 to simulate the reduction of pairing correlations by the excitations. Those values used are 0.957×0.6 MeV and 0.626×0.6 MeV for ^{132}Te and ^{136}Te, respectively. It turned out that if the same neutron pairing gap is used in the two nuclei, the E_{2+} and $B(E2)\uparrow$ are both nearly identical.

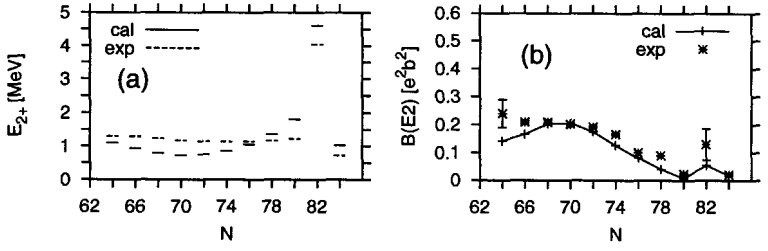

Figure 2. (a) E_{2+} of even Sn isotopes. (b) $B(E2)\uparrow$ corresponding to (a).

Another interesting phenomenon is the behavior of $B(E2)\uparrow$ in ^{130,132,134}Sn. Our theoretical values are shown in Fig. 2 along with experimental data including those three nuclei, which were measured very recently[8]. The $B(E2)\uparrow$ of ^{132}Sn is larger than those of ^{130,134}Sn. Among doubly magic nuclei, this behavior is seen only around ^{132}Sn and ^{208}Pb [2].

In the QRPA, the behavior can be explained in terms of the normalization relation of the amplitudes $\psi_{\mu\nu}$ and $\varphi_{\mu\nu}$

$$\sum_{\mu<\nu} ({\psi^{\lambda}_{\mu\nu}}^2 - {\varphi^{\lambda}_{\mu\nu}}^2) = 1, \tag{1}$$

where μ and ν denote the quasiparticle indices, and $\mu < \nu$ means ordered pairs. λ indicates a nuclear excited state. The summation includes both protons and neutrons. The excited state λ of the QRPA is created by an operator ${O_\lambda}^\dagger = \sum_{\mu<\nu}(\psi^{\lambda}_{\mu\nu} a^\dagger_\mu a^\dagger_\nu - \varphi^{\lambda}_{\mu\nu} a_\nu a_\mu)$, where $a^\dagger_\mu$ and a_μ are quasiparticle creation and annihilation operators. If the neutron number is not magic, then the neutron excitation is enhanced compared to the proton. If the neutron number is changed to a magic number, then Eq. (1) tells us

that the proton excitation is enhanced compared to the former case. In our calculation, $\sum_{\text{proton}} \psi^2_{\mu\nu}$ of ^{130}Sn (^{132}Sn) is 0.004 (0.071). ($\sum \varphi^2_{\mu\nu}$ is one order of magnitude smaller than $\sum \psi^2_{\mu\nu}$.)

G factors are also important observables. We show g factors for $^{134-138}$Xe and Sn isotopes in Fig. 3. Measurement of g factors for nuclei with $Z > 50$, $N = 84$, as well as Sn around $N = 82$, would be interesting.

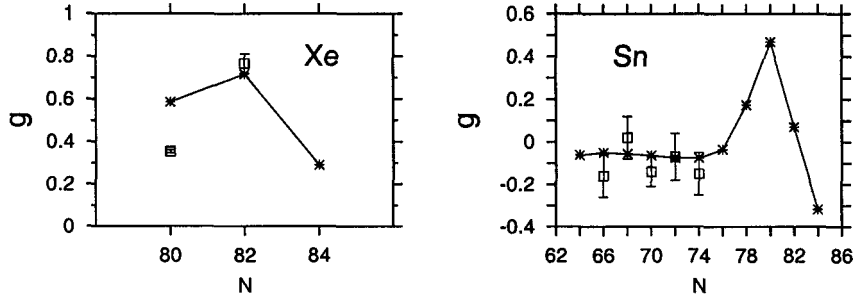

Figure 3. Calculated (connected by line) and experimental g factors for Xe (left) and Sn (right).

3. Neutron-Rich Ni Isotopes

The experimental E_{2+} of ^{68}Ni is 2.033 MeV, higher than those of the other neutron-rich Ni except for ^{56}Ni, where the value is 2.701 MeV (e.g. E_{2+} of ^{62}Ni is 1.173 MeV, cf. Ref. 2). The high E_{2+} of ^{68}Ni is understood in terms of the neutron single-particle spectrum[9], according to which the lowest neutron particle-hole excitation of ^{68}Ni is from $1f_{5/2}$ or $2p_{1/2}$ to $1g_{9/2}$; these excitations are inhibited in the 2^+ channel. Recently $B(E2)\uparrow$ of ^{68}Ni was measured[4], and a value 0.0255(60) e^2b^2 was obtained. This number is much smaller than, e.g., 0.0890(25) e^2b^2, measured in ^{62}Ni [2].

We performed QRPA calculations to investigate $B(E2)\uparrow$ as a function of E_{2+} (see Fig. 4). We see that as far as the low-energy region is concerned, all the transition strength of ^{56}Ni is concentrated in the first excited state, while ^{68}Ni shows fragmentation of the strength. We checked that other even Ni with $N = 58 - 70$ also have fragmentation of $B(E2)\uparrow$ in the low-energy region. Thus, the small $B(E2)\uparrow$ of ^{68}Ni is not evidence for an $N = 40$ closed shell.

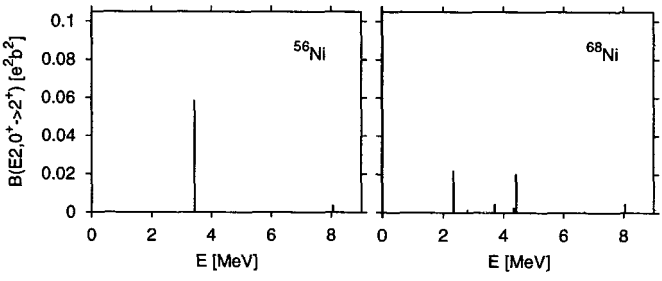

Figure 4. Calculated $B(E2)\uparrow$ of ^{56,68}Ni as a function of E_{2+}.

4. Summary

We have performed QRPA calculations — with a Hamiltonian consisting of mean field, a pair field and separable phenomenological interactions — for the 2^+ modes in even Te isotopes near ^{132}Sn, Sn and Ni. We have discussed the systematics of E_{2+} and $B(E2)\uparrow$ for the first 2^+ states in Te and Sn. We were able to reproduce the unusual behavior of Te, which does not follow the empirical formula; it turned out that the neutron pairing gap was important. We predicted unusual behavior of $B(E2)\uparrow$ around ^{132}Sn, and that prediction has been confirmed recently. We pointed out that $B(E2)\uparrow$ of ^{68}Ni is fragmented, and that the fragmentation is responsible for the small $B(E2)\uparrow$ of the first 2^+ state.

References

1. D.C. Radford et al., *Phys. Rev. Lett.* **88**, 222501 (2002).
2. S. Raman, C.W. Nestor, Jr. and P. Tikkanen, *At. Data Nucl. Data Tables* **78**, 1 (2001).
3. J. Terasaki, J. Engel, W. Nazarewicz and M. Stoitsov, *Phys. Rev.* **C66**, 054313 (2002).
4. O. Sorlin et al., *Phys. Rev. Lett.* **88**, 092501 (2002).
5. K. Langanke et al., *Phys. Rev.* **C67**, 044314 (2003).
6. A. Bohr and B.R. Mottelson, Nuclear Structure, vol.I, W.A. Benjamin, New York, 1969.
7. J. Dobaczewski, P. Magierski, W. Nazarewicz, W. Satuła and Z. Szymański, *Phys. Rev.* **C63**, 024308 (2001).
8. J.R. Beene, private communication.
9. H. Graw and M. Lewitowicz, *Nucl. Phys.* **A693**, 116 (2001).

Spectroscopy of unstable nuclei

This page intentionally left blank

METHODS FOR G-FACTOR MEASUREMENTS ON SHORT-LIVED EXCITED STATES USING RADIOACTIVE BEAMS

N.J.STONE

Department of Physics, Oxford University and University of Tennessee, Knoxville

Abstract. Complications which arise when the Transient Field method for determination of nuclear excited state g-factors is used with radioactive isotope beams, are surveyed. Ways to overcome the problems include allowing the Coulomb excited nuclei to recoil into vacuum. This has the disadvantage that the angular distribution of their gamma de-excitation, which forms the basis for the TF method, becomes attenuated. However it is argued that these attenuations may, in themselves, form the basis of a simple way to study g-factors. A simple theoretical introduction is given and recent preparatory experiments are outlined.

1. Introduction

The value of measurements of nuclear magnetic moments as a means to identify the single particle make-up of a nuclear state, and also to give evidence for collective contributions to the total wavefunction, is well established. In studies of excited nuclear states with lifetimes of order picoseconds the 'standard' technique is that of the Transient Field (TF)[1]. In this method the g-factor is extracted from observations of the small rotation of the angular distribution of gamma radiation emitted following Coulomb excitation which occurs when the excited nuclei pass through a magnetised ferromagnetic metal foil. The distribution is anisotropic since the Coulomb excitation process exerts a torque on the nuclei which is in the plane of the target and normal to the beam axis, and imparts angular momentum preferentially in this plane. It is desirable to extend the range of magnetic moment studies to levels in isotopes far from stability, which means those produced using radioactive beams which are becoming increasingly available. This paper points out problems which arise when extending this method to experiments using radioactive as opposed to stable isotope beams, and discusses ways in which they may be overcome.

2. The Transient Field Method with Radioactive Beams

The rotation of the gamma ray angular distribution produced by passing through the ferromagnetic layer is typically a few degrees. Even with detectors positioned at the points of greatest slope in the distribution, the change in counting rate is a few percent and this small difference needs to be measured accurately to yield g-factors to useful precision.

Radioactive beams are much less intense than stable beams, and moreover often contain isobaric contaminants which may also be radioactive. The usual practice in TF experiments has been to pass the Coulomb excited nuclei through a ferromagnetic layer in which rotation of the angular distribution takes place, and then to stop them in a layer of non-magnetic cubic metal, usually copper. The purpose of stopping the nuclei is to avoid them passing out of the back of the target into vacuum, where additional, uncontrolled, rotations of the angular distribution will occur in the hyperfine magnetic fields produced by the electrons of the recoiling ion. These fields may fluctuate with time, both in magnitude and direction, and, being randomly oriented they impart no net rotation to the average nuclear spin of the recoiling ensemble. However they will produce attenuation of the angular distribution which renders the small rotation in the ferromagnetic layer more difficult to detect. For this reason allowing the nuclei to recoil into vacuum in TF studies has been carefully avoided.

However, when a radioactive beam (RIB) is used, stopping all or part of the beam in the composite target is highly undesirable, producing a strong unwanted gamma source. That part of the beam which undergoes no interaction may be allowed to pass through the target. However there remains the Rutherford scattered portion, which has almost the same energy as the Coulomb excited fraction, but is several hundred times as strong, which will certainly be stopped in the target. Furthermore, the isobaric contaminant may well include nuclei which decay through the state which the experiment is designed to study, but which are not preferentially ordered in the Coulomb excitation process; such decays further dilute the observable rotation.

Thus with RIBs, the TF method, as usually followed, faces not only difficulty in obtaining the necessary statistical quality of data, but has to deal with serious additional background, not all of which can be eliminated by using coincidence requirements.

3. Possible solutions

One attractive possibility to avoid the background problems is to allow all the recoiling nuclei to pass out of the target into vacuum. Longer-lived beam nuclei will pass away from the target area without decaying, avoiding both non-excited beam and contaminant activity problems. The short-lived excited states will decay within a millimetre of the target with no loss of gamma detection efficiency. One is then left with the question of how seriously recoil into vacuum attenuates the angular distribution? It is possible that one has simply moved from one problem to another?

The phenomenon or attenuation of angular distributions following recoil of ions into vacuum (RIV) was studied quite extensively in the 1970's [2,3]. Several theories were advanced to explain the observed attenuation effects [4,5]. It became clear that detailed calculation of the precession of the angular distribution in hyperfine magnetic fields acting at nuclei in recoiling energetic ions is a complex and rather intractible problem. Thus, despite the fact that there are large anisotropies in the angular distribution, so that attenuations can be readily measured, their quantitative interpretation with a view to extraction of nuclear g-factors was problematic. Studies of this effect died away as the TF method was successfully developed

However, as outlined above, the advent of RIB physics suggests that RIV be re-examined. Higher beam energies and the use of inverse kinematics give access to larger recoil velocities in heavier nuclei than were available in the 70's. This leads to stronger perturbation, which is relevant for measurements on shorter lived states, as well as offering wider range in emerging velocity, an important variable relevant to understanding the perturbation mechanism.

Re-examination of the potential of RIV studies forms the basis of the present paper. An outline is given of the simplest theoretical approach, which indicates the nature of the effect, but does not cover all possibilities. This is followed by a brief description of some experimental data which give encouragement to further exploration of the possible use of RIV to give useful estimates of g-factors when using RIBs.

4. Outline Theory

The model of Abragam and Pound[4] considers the recoiling nucleus to experience a hyperfine magnetic field which fluctuates rapidly with time, in both direction and magnitude, as the electronic state of the ion changes. If the fluctuation time, τ_c, is short compared to the observation time, the

result is the introduction of attenuation factors G_K so that the observed angular distribution becomes

$$W(\theta,t) = \sum A_K G_K(t) P_K(cos\theta), \tag{1}$$

where

$$G_K(t) = e^{-t/\tau_K} \tag{2}$$

and

$$(\tau_K)^{-1} = \frac{[K(K+1) < \omega^2 > \tau_c]}{3}. \tag{3}$$

Here ω is the Larmor precession frequency of the nucleus in the hyperfine field. This depends directly upon the nuclear g-factor so that the characteristic attenuation time varies with g^{-2}. If the time dependence of the distribution is not observed, integration of $G_K(t)$, weighted with the decay probability, yields the result

$$G_K(\infty) = \frac{\tau_K}{\tau + \tau_K} \tag{4}$$

where τ is the nuclear state mean lifetime.

Within this theory full destruction of the anisotropy in the distribution can result for the case $\tau \gg \tau_K$. At an alternative extreme, if the nucleus is taken to experience a single magnetic hyperfine field over its lifetime, the result is partial attenuation, with a final 'hard core' anisotropy[5]. Billowes[5] has introduced a modified form of $G_K(t)$ incorporating such an experimental 'hard core' anisotropy a_K, leading to

$$G_K(\infty) = \frac{a_K \tau + \tau_K}{\tau + \tau_K} \tag{5}$$

For the single hyperfine field case, dependence of the attenuation upon the nuclear g-factor is as g^{-1}. For neither case is there sensitivity to the sign of the nuclear g-factor.

In view of the a-priori uncertainly of the relative magnitudes of the nuclear state lifetime τ and the hyperfine field fluctuation time τ_c it is clear that any application of G_K measurement to give g-factor information depends upon empirical calibration using known g-factors and state lifetimes. However, for example, the angular distribution from a Coulomb excited 2^+ state decaying to its 0^+ ground state shows a count rate difference close to a factor of 5 between detectors at 0° and at $\sim$ 45° to the alignment axis [depending on beam energy and geometry][6]. Thus determination of the G_K to useful precision will not require great statistical accuracy.

5. Preparatory experiments

We report briefly on two experiments which give encouragement to the idea that g-factor information may be obtained from measurement of g-factors using RIBs. Both involve beams of coulomb excited ^{130}Te ions which were allowed to recoil into vacuum. The first experiment was conducted by N.Koller et al.[7], working at the Wright Nuclear Structure Laboratory, Yale. Following Coulomb excitation in passing though a thin carbon layer on the front face of the target, 285 MeV ^{130}Te nuclei were

a) stopped in a thick Cu backing and
b) allowed to emerge from the rear surface of a thinner Cu backing at a velocity of about $0.02c$.

The angular distributions of gamma decay from recoiling Te nuclei, measured in coincidence with C recoils at small angles to the incident beam, were compared for the two targets. They showed that the RIV situation gave attenuation factors

$$G_2 = 0.93(1) and G_4 = 0.63(4). \tag{6}$$

The mean life of the Coulomb excited first 2^+ state in ^{130}Te is $3.3ps$. These results showed that, for this element and nuclear lifetime, RIV did not erode the angular distribution to the degree that TF measurement would become impossible, provided other problems associated with the RIB can be overcome. Also they showed that determination of the G_K was very straightforward.

The second experiment was done at the HRIBF facility at Oak Ridge National Laboratory by D.Radford et al.[8], again by observing the gamma emission from Coulomb excited ^{130}Te nuclei. This experiment was carried out in the CLARION detector array, with recoiling C from the target detected in the Hyball system[9]. No measurement of the unattenuated distribution has yet been made for this set-up, but the data showed a very strong angular distribution with a ratio of count rates at 90° and 49° to the alignment axis of 2.8(3).

Similar data have been taken using the RIB ^{132}Te [10]. These experiments at HRIBF have shown that angular distributions data can be taken without dedicated beam time in such arrays and the observation of large, but attenuated, anisotropy in the distribution following RIV clearly contains information concerning the g-factors of the Coulomb excited states.

6. Interest in the g-factors of Te isotopes

The g-factors of the first 2^+ states in even-even Te isotopes close to ^{132}Sn have become of great interest since the report of anomalous behaviour of their $B(E2)$'s[10]. Theoretical studies by Terasaki et al.[11], following that report, predict that the g-factors should show a strong increase from the value of 0.30 below the shell closure to 0.49 at ^{132}Te and 0.70 at ^{134}Te. Above the shell, the anomalously low $B(E2)$ is interpreted as due to predominantly neutron composition of the 2^+ state with predicted g-factor -0.17.

It is clearly desirable to develop methods to measure these g-factors of states accessible using RIBs. TF studies may be possible, and have the advantage of yielding the sign of the g-factor, but will require long dedicated beam time to yield g-factors to good precision. A TF study to measure the sign of the g-factor can be relatively short. The exploratory work referred to above suggests that the angular distribution attenuation coefficients G_K, measured when Te isotopes recoil into vacuum following Coulomb excitation , will be valuable in revealing changes in magnitude of the g-factors.

The challenge now is to calibrate the attenuation adequately so that quantitaive g-factors can be extracted.

7. Acknowledgements

The author acknowledges major contributions to the ideas presented here by A.Stuchbery, J.Billowes, J.Beene, N.Koller, G.Kumbartski, D.Radford and C.Bingham. This work is supported by the US Department of Energy under contract number DE-FG02-96ER40983.

References

1. G.Jakob et al., *Phys. Rev.* **C65**, 024316, (2002).
2. D.Ward et al., *Nucl. Phys.* **A193**, 479, (1972).
3. C.W.Townsley et al., *Nucl. Phys.* **A 250**, 381,(1975).
4. A.Abragam and R.V.Pound, *Phys. Rev.* **92**, 943, (1953).
5. J.Billowes, *Hyp. Int.* **30**, 265, (1986).
6. K.Alder and A.Winther Electromagnetic Excitation, [North Holland 1975] p III.4.
7. N.Koller priv comm.
8. D.Radford priv. comm.
9. for details see www.phy.ornl.gov/hribf.
10. D.Radford et al., *Phys. Rev. Lett.* **88**, 222501, (2002).
11. J. Terasaki et al., *Phys. Rev.* **C66**, 054313, (2002).

MAGNETIC HYPERFINE ANOMALY MEASUREMENTS USING NUCLEAR MAGNETIC RESONANCE ON ORIENTED NUCLEI

T. OHTSUBO, S. OHYA, M. SASAKI
Department of Physics, Niigata University, Niigata, 950-2181, Japan
E-mail: tohtsubo@np.gs.niigata-u.ac.jp

T. IZUMIKAWA
RI Center, Niigata University, Niigata 951-8510, Japan

K. NISHIMURA
Fuculty of Technology, Toyama University, Toyama, 930-8555, Japan

J. GOTO, M. TANIGAKI, A. TANIGUCHI, Y. OHKUBO, Y. KAWASE
Research Institute of Reactor, Kyoto University, Osaka, 590-0494, Japan

S. MUTO
Neutron Science Laboratory, KEK, Tsukuba, 305-0801, Japan

Nuclear magnetic resonance on oriented nuclei for ^{91}YFe experiments have been performed. Comparing the external field dependence of resonance frequencies with ^{91}YFe and ^{91m}YFe, the hyperfine anomaly in Fe was determined as $^{91m}\Delta^{91} = +4.2(8)\%$. The measured hyperfine anomaly was interpreted in terms of a microscopic theory including core polarization and meson exchange currents.

1. Introduction

The technique of nuclear magnetic resonance on oriented nuclei (NMR-ON) is a power method to study the nuclear structure. Many nuclear magnetic moments were measured by this method. In most cases, the radioactive nuclei were embedded in ferromagnetic host metals as very dilute impurities. The information of hyperfine fields in the hosts metals is required to deduced the magnetic moments. In general, hyperfine fields are deduced from the hyperfine interactions of another isotopes of which magnetic moment is

known. However, the hyperfine anomaly arises from the hyperfine interaction of the finite nuclear volume of nuclear magnetization and the hyperfine field due to the Fermi contact interaction[1]. Therefore the information of hyperfine anomaly is very important to measure the magnetic moment with the NMR-ON method. We have studied the hyperfine anomaly in Fe with Brute-force NMR-ON method[2]. Present study is to measure the hyperfine anomaly with a conventional NMR-ON method. The magnetic hyperfine interaction frequency ν in ferromagnetic metals with an external magnetic field of $B_{\rm ext}$ is given by

$$\nu = -\frac{g\mu_N}{h}B_{\rm hf} + (1+K)B_{\rm ext} = \nu_0 + \frac{d\nu}{dB}B_{\rm ext} \tag{1}$$

where g is the g-factor of the nucleus, $\mu_{\rm N}$ is the nuclear magneton, h is the Plank constant, $B_{\rm hf}$ is the hyperfine field in ferromagnetic metals and K is a parameter including the effects of Knight shift and diamagnetic shielding. The useful definition of the single-isotope hyperfine anomaly ϵ_i for the nuclear state i is as follows:

$$B_{\rm hf} = B_0(1+\epsilon_i) \tag{2}$$

where $B_{\rm hf}$ is the hyperfine field averaged over the radial distribution of nuclear magnetization of the nuclear state i and B_0 is the hyperfine field at $r = 0$. The ratio of the frequencies of the isotope $i = 1$ and 2 is

$$\frac{\nu_0^{(1)}}{\nu_0^{(1)}} = \frac{g_1}{g_2}\frac{1+\epsilon_1}{1+\epsilon_2} \approx \frac{g_1}{g_2}(1+{}^1\Delta^2), {}^1\Delta^2 = \epsilon_1 - \epsilon_2 \tag{3}$$

where ${}^1\Delta^2$ is the difference of the hyperfine anomalies of two nuclear states in the same host metals. If the difference of the Knight shift parameter between isotopes is negligible, the ratio of the g-factors can be derived from the ratio of the filed shift as following,

$$\frac{d\nu}{dB}^{(1)} \Big/ \frac{d\nu}{dB}^{(2)} = \frac{g_1}{g_2}\frac{(1+K_1)}{(1+K_2)} \approx \frac{g_1}{g_2}. \tag{4}$$

Therefore the hyperfine anomaly can be given by the ratios of the zero-field resonance frequencies and the field shift:

$${}^1\Delta^2 = \frac{\nu_0^{(1)}}{\nu_0^{(2)}}\left(\frac{d\nu}{dB}^{(1)} \Big/ \frac{d\nu}{dB}^{(2)}\right)^{-1} - 1. \tag{5}$$

We measured the external magnetic field dependence of NMR-ON for ^{91}Y and ^{91m}Y in Fe.

2. Principle of measurement

The angular distribution of β rays from polarized nuclei is written as

$$W_\beta(\theta) = 1 + \eta A P cos\theta, \tag{6}$$

where η is the geometrical parameter including solid-angle correction, A is the asymmetry parameter decided by the decay property, P is the nuclear polarization and θ is the angle between the polarization axis and the direction of β ray emission. The angular distribution of β rays from polarized nuclei is asymmetric. The angular distribution of γ rays from oriented nuclei is written as

$$W_\gamma(\theta) = 1 + \sum_{\lambda=even} A_k B_k Q_k P_k(cos\theta), \tag{7}$$

where A_k is the angular correlation coefficients, B_k is the orientation parameter, Q_k is the solid-angle correction and P_k is the Legendre polynomials. The angular distribution of γ rays from oriented nuclei is anisotropic. In the NMR-ON method, a change of the sublevel population by a radio-frequency (rf) magnetic field applied the sample is detected via the corresponding change of the β -rays or γ -rays angular distribution. The NMR-ON spectra were observed by the β-ray asymmetry for ^{91}YFe and the 555 keV γ-ray anisotropy for ^{91m}YFe, respectively.

3. Experiment and result

Samples of ^{91}YFe and ^{91m}YFe were prepared by ion-implantation method at the Research Reactor Institute, Kyoto University (KUR). ^{91}Rb nuclei were produced as fission products from a ^{235}U. After mass separation, the ^{91}Rb nuclei were implanted into an Fe foil with an accelerating voltage of 100 kV at room temperature. The sample was soft soldered to the copper cold finger of ^{3}He/^{4}He dilution refrigerator at Niigata University without any thermal treatment and cooled down to about 10 mK. The temperature of the sample was monitored by a $^{54}MnNi$ nuclear thermometer. An external magnetic field up to 2.5 T was applied in the foil plane to polarize the Fe foil. A Si detector was set at 0° with respect to the external field inside the cryostat to detect β rays. An Ge detector was set at 0° outside the cryostat to detect γ rays. A radio-frequency oscillating magnetic field with frequency modulation (FM) at 100 Hz was applied perpendicular to the external field. NMR-ON spectra were observed by detecting the asymmetry change of β rays. Observed NMR-ON spectra of ^{91}YFe and ^{91m}YFe are shown in Fig. 1, respectively. The solid lines are Gaussian fits of the data

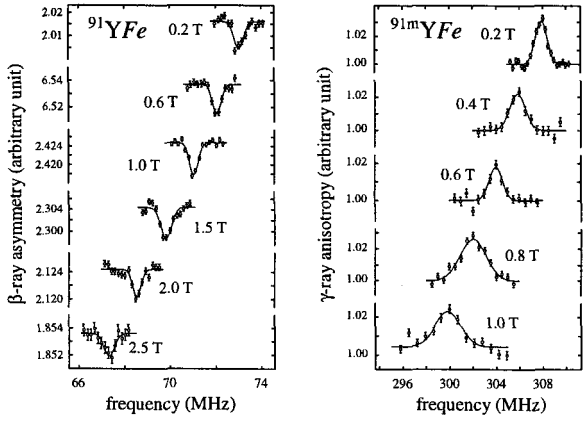

Figure 1. NMR-ON spectra of ^{91m}YFe and ^{91}YFe

points. Fig. 2 show the external field dependence of resonance frequency. In fig.5 the previous result of ^{91m}YFe[3] are also shown. Our present result is consistent the previous one. The solid lines are linear fits of the data points including previous results. A zero-field frequency and the field shifts of

$$\nu_0(^{91}YFe) = 73.566(22)\text{MHz}, \tag{8}$$

$$\frac{d\nu}{dB_{\text{ext}}}(^{91}YFe) = -2.501(17)\text{MHz/T} and \tag{9}$$

$$\nu_0(^{91m}YFe) = 310.005(23)\text{MHz}, \tag{10}$$

$$\frac{d\nu}{dB_{\text{ext}}}(^{91m}YFe) = -10.111(38)\text{MHz/T} \tag{11}$$

were derived from linear fits to the resonance frequency.

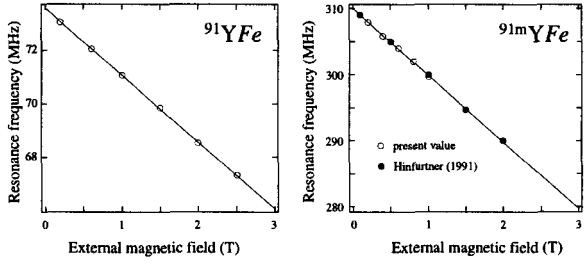

Figure 2. External field dependence of resonance frequencies of ^{91m}YFe and ^{91}YFe

4. Discussion

The hyperfine field of ^{91}YFe was derived to $B_{\rm hf}(^{91}YFe) = -29.41(14)T$ using the known magnetic moment of $\mu(^{91}{\rm Y}) = 0.1641(8)\mu_N$. This value is smaller than the value for ^{91m}YFe by Hinfurtner $B_{\rm hf}(^{91m}YFe) = -30.67(36)T$ [3]. They assumed that the uncertainty of K is less than 1 %. The present value of K was 0.0(8) % and it is consistent with their assumption. Therefore the deviation in the hyperfine field is due to the hyperfine anomaly between ^{91}Y and ^{91m}Y. Using present results, the hyperfine anomaly between ^{91}Y and ^{91m}Y was $^{91}\Delta^{91m} = +4.2(8)\%$. Storke et al. calculated the hyperfine anomaly with single particle model [4]. Using their numerical value, the hyperfine anomaly for single-particle model is $^{91m}\Delta^{91}_{sp} = +1.3\%$. It is rather smaller than the present value.

Fujita and Arima [5] introduced the theoretical formulas for the hyperfine anomaly including core polarization and meson exchange current. Taking into account the core polarization the hyperfine anomaly was calculated to be $^{91m}\Delta^{91}_{cp} = +2.2\%$. If the effect of meson exchange current with $\delta g_l(p) = 0.1$ is also considered, $^{91m}\Delta^{91}_{cp+mec} = +3.3\%$ was derived. This value is almost consistent with present value. The NMR-ON method is applied for ^{91}YFe and ^{91m}YFe, and the hyperfine anomaly between ^{91}Y and ^{91m}Y in Fe was derived. It is almost consistent with the theoretical calculation of nuclear shell model with core polarization and meson exchange current.

References

1. S. Buettgenbach, *Hyperfine Interactions* **20**, 1 (1984), N.J. Stone, *J. de Phys. Coll. C4* **34**, 69 (1973), E. Bodenstedt et al., *Z. Phys.* **A322**, 75 (1985).
2. S. Ohya et al. *Phys. Rev.* **C63**, 044314(2001).
3. B. Hinfurtner et al. *Phys. Rev. Lett.* **66**, 96(1991).
4. H.H. Stroke et al. *Phys. Rev.* **123**, 1326(1961).
5. T. Fujita and A. Arima *Nucl. Phys.* **A254**, 513(1975).

β STRENGTH DISTRIBUTIONS IN N$\sim$Z KR AND SR ISOTOPES USING TOTAL ABSORPTION SPECTROMETRY

F. MARÉCHAL,[1] E. NÁCHER,[2] E. POIRIER,[1] A. ALGORA,[2]
M.J.G. BORGE,[3] S. COURTIN,[1] P. DESSAGNE,[1] L.M. FRAILE,[4]
W. GELLETLY,[5] A. JUNGCLAUS,[3] G. LE SCORNET,[4] C. MIEHÉ,[1]
B. RUBIO,[2] J.L. TAÍN,[2] O. TENGBLAD[3]

[1] *IReS, IN$_2$P$_3$-CNRS, F-67037 Strasbourg Cedex 2, France*
[2] *IFIC, CSIC-Univ. Valencia, E-46071 Valencia, Spain*
[3] *IEM, CSIC, E-28006 Madrid, Spain*
[4] *ISOLDE, Division EP, CERN, CH-1211 Geneva, Switzerland*
[5] *Dept. of Physics, University of Surrey, Guildford, GU2 5XH, United Kingdom*

A total absorption spectrometer, dedicated to the study of very short lived atomic species, has been built and installed at the CERN/ISOLDE mass separator. The β decays of the neutron-deficient ^{74}Kr and ^{76}Sr nuclei have been studied using this new device. The experimental Gamow-Teller strength distributions obtained over the full Q_{EC} windows are presented and compared with self-consistent, deformed, HF-BCS-QRPA calculations.

1. Introduction

The N$\simeq$Z, A$\simeq$70 region of the nuclear chart is of particular interest in terms of nuclear structure because of the wide variety of nuclear shapes displayed in the region. Competing prolate and oblate deformations are predicted due to several different energy gaps in the shell model potential at Z, N = 34 - 40, the signature of such effects being rapid changes in nuclear shape when adding or removing only a few nucleons.

For nuclei close to the proton drip-line, theoretical calculations predict that the Gamow-Teller strength will be concentrated at high excitation energy in the daughter nucleus but will still be accessible through β-decay studies [1,2]. Furthermore, the Gamow-Teller strength distribution calculated as a function of the excitation energy in the daughter nucleus depends sensitively on the ground state deformation of the parent nucleus [2,3].

Although the Gamow-Teller strength distribution B(GT) carries fundamental information about nuclear structure, its experimental determination

is not straightforward. When germanium detectors are used, their limited high energy detection efficiency, combined with the β-strength fragmentation at high excitation energy, leads to large systematic errors in both the total B(GT) and the B(GT) distribution. An alternative method is to use the total absorption technique to extract the strength distribution. This method is based on measuring the total energy released in the γ-decay of each level populated in the β-decay, and therefore is sensitive to the β population of the nuclear levels rather than to the individual γ-rays.

We have revisited the β decay of neutron-deficient Kr and Sr isotopes using the total absorption spectrometry technique with the aim of determining the GT distribution over the whole Q_{EC} energy window. Here we present the results obtained for the ^{74}Kr and ^{76}Sr isotopes.

2. Experimental Procedure

A new total absorption gamma spectrometer (TAgS) [4] has been designed by a Madrid-Strasbourg-Surrey-Valencia collaboration to study very short-lived nuclei at the CERN/ISOLDE mass separator. The spectrometer consists of a large, cylindrical NaI(Tl) crystal (38 cm diameter, 38 cm length) with a 7.5 cm hole drilled perpendicular to the symmetry axis. Radioactive nuclei are collected in the centre of the crystal and are implanted on an aluminised mylar tape that can be moved in order to limit the build-up of daughter activity.

Ancillary detectors located close to the collection point are used to separate the β^+ and EC-components of the decay process. X-rays and γ-rays are detected using a Ge telescope and β particles are detected using a plastic scintillator located in front of the telescope. Finally, to reduce the contribution of the background due to the activity (neutrons and gammas) in the experimental hall, the spectrometer and its ancillary detectors are placed inside a 19 cm thick shielding made of a polyethylene-lead-copper-aluminium sandwich.

The experiments were carried out at the ISOLDE online isotope separator at CERN. The ^{74}Kr and ^{76}Sr ion beams were produced by spallation of a thick Nb target induced by an intense 1.4 GeV proton beam delivered by the CERN-PSB accelerator. After transfer from the target to the ion source, the ions were extracted in their 1^+ charge state, electrostatically accelerated to 60 keV, and analyzed using the HRS mass separator. The average production yields for ^{74}Kr and ^{76}Sr were 1.5×10^6 atoms/μC and 1.0×10^3 atoms/μC, respectively. The mass-separated isotopes were finally collected in the centre of the TAgS spectrometer.

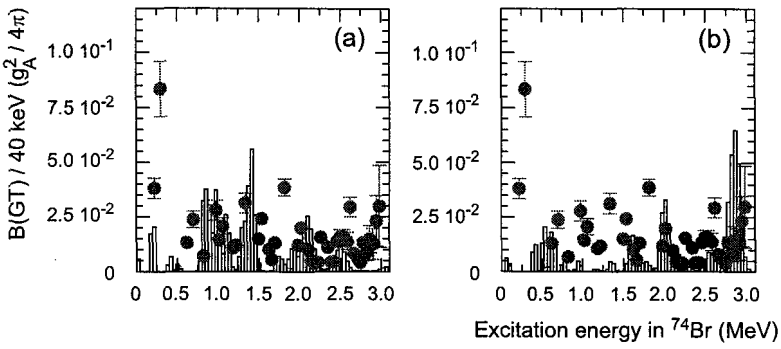

Figure 1. Gamow-Teller strength distribution measured for ^{74}Kr compared to HF-BCS-QRPA calculations assuming an oblate (a) or a prolate (b) ground state for ^{74}Kr.

3. Analysis Method

To extract an accurate value of the β-strength over the full energy range, experimental raw spectra must be corrected for different effects of distortion (background and daughter activity contributions as well as electronic pulse pileup). The corrected energy spectra, **d** (counts/ch), can then be related to the level feeding distribution **f** using the relation $\mathbf{d} = \mathbf{R}(\mathrm{b}).\mathbf{f}$ [5], where **R** (b) is the response function matrix of the spectrometer which depends on the emitted radiation and γ-branching ratios (b) in the daughter nucleus as well as on the characteristics of the spectrometer. The Monte-Carlo simulation package GEANT4 is used to calculate this response function. Finally, in order to obtain the feeding distribution **f**, the relation $\mathbf{d} = \mathbf{R}(\mathrm{b}).\mathbf{f}$ is inverted using the expectation-maximisation method based on the Bayes theorem.

4. Results

Figure 1 presents the experimental B(GT) strength distribution obtained for the decay of ^{74}Kr (solid circles) [4]. The total Gamow-Teller strength to states below 3 MeV is measured to be 0.69(3) $g_A^2/4\pi$. The experimental results are compared to calculated strength distributions that have been obtained for the two nuclear shapes, oblate ($\beta_0 = -0.15$) and prolate ($\beta_0 = 0.39$), that minimize the HF energy [6].

Figure 1 shows that neither of the two calculated GT strength distributions, for pure oblate and prolate shapes, can reproduce the experimental B(GT) values over the full range of excitation energy. While the oblate calculation (Fig. 1a) reproduces the strength distribution below 2.0 MeV of excitation energy, the prolate calculation (Fig. 1b) agrees better with

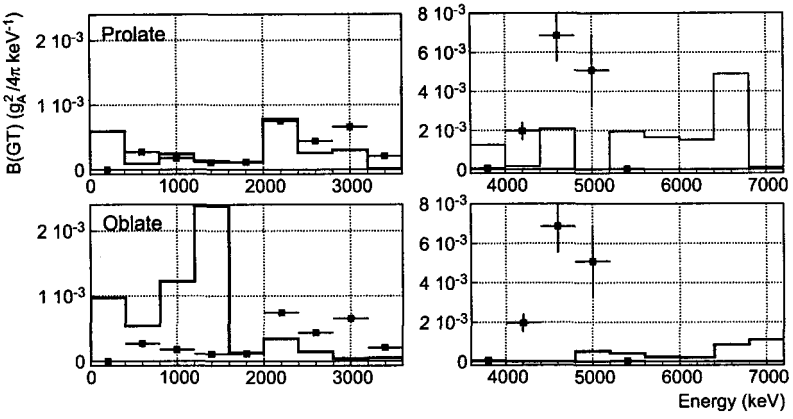

Figure 2. Average Gamow-Teller strength distribution measured for ^{76}Sr as a function of 400 keV excitation energy bins in ^{76}Rb. Experimental data are compared to HF-BCS-QRPA calculations assuming a prolate (top) or an oblate (bottom) ground state for ^{76}Sr.

the concentration found at higher energies. In that sense the two pictures complement each other. The same conclusion is obtained if one looks at the accumulated GT strength. Again, the data lie systematically in between the two calculations indicating a possible shape mixing in the ground state of ^{74}Kr. This result corroborates recent theoretical and experimental works [7,8].

In the case of the ^{76}Sr decay, β^+ and EC components were analyzed as a single set of data. Figure 2 shows the experimental B(GT) strength obtained for the decay of ^{76}Sr (solid squares) as a function of the excitation energy in ^{76}Rb [9]. For excitation energies below 6.0 MeV, the total Gamow-Teller strength is found to be 6.7(9) $g_A^2/4\pi$. Besides a fragmentation of the strength below 4 MeV, one observes a resonance, located at 4.5 MeV, that accounts for 70 % of the total strength measured in the Q_{EC} energy window. The experimental strength is compared to the results of Hartree-Fock calculations performed for the two deformations (oblate β_0=-0.11, and prolate β_0=0.42) that minimize the HF energy in ^{76}Sr [6].

The agreement of the experimental results with the prolate shape calculation is very good up to 3.6 MeV, while the oblate calculation strongly overestimates the strength measured below this energy. Similar conclusions can be drawn if one looks at the accumulated strength. However, above this energy, the prolate calculation diverges from the experiment mainly because of the resonance experimentally seen at 4.5 MeV. Still, the prolate calculation is the only one to predict a resonance above 4.0 MeV, and al-

though it is calculated to be mostly outside the Q_{EC} window, its intensity matches the experimental strength integrated between 4.0 and 5.0 MeV. Therefore, this analysis strongly supports a prolate ground state for ^{76}Sr in agreement with the results of previous experimental works [10,11].

5. Conclusions

A new TAgS spectrometer has recently been successfully used to study the neutron-deficient Kr and Sr isotopes at ISOLDE/CERN. The experimental Gamow-Teller B(GT) strengths of ^{74}Kr and ^{76}Sr have been measured for the first time over most of the Q_{EC}-window. Comparisons of the data with HF-BCS-QRPA calculations indicate a possible shape mixing in the ground state of ^{74}Kr and confirm the strong prolate deformation of ^{76}Sr.

For the first time, information on the nuclear shape of unstable nuclei in the A = 75 mass region has been inferred from β-decay studies. Although this method is model-dependent, it opens new possibilities for probing the nuclear structure of other nuclei. It offers an interesting alternative method to measure the deformation, including the sign, of nuclei produced in their ground state.

Acknowledgements

The authors would like to thank their colleagues, engineers and technicians, from the IReS-Strasbourg and CLRC-Daresbury, whose collaboration has been so valuable during the development of the TAgS project. The collaboration is grateful to M. de Saint Simon for providing us with the beam transport calculations, and D. Cano-Ott for providing us with the data analysis codes.

References

1. I. Hamamoto *et al.*, Phys. Rev. **C48**, 2960 (1993).
2. I. Hamamoto *et al.*, Z. Phys. **A353**, 145 (1995).
3. F. Frisk *et al.*, Phys. Rev. C **52**, 2468 (1995).
4. E. Poirier *et al.*, to be published in Phys. Rev. C.
5. D. Cano-Ott *et al.*, Nucl. Instrum. Methods Phys. Res. **A430**, 333 (1999).
6. P. Sarriguren *et al.*, Nucl. Phys. **A658**, 13 (1999).
7. A. Petrovici *et al.*, Nucl. Phys. **A665**, 333 (2000).
8. F. Becker *et al.*, Eur. Phys. J. **A4**, 103 (1999).
9. E. Nácher *et al.*, Proc. of the Int. Conf. on "The Labyrinth in Nuclear Structure", Crete, Greece 13-19 July 2003, to appear in AIP-Proceedings.
10. C.J. Lister *et al.*, Phys. Rev. C **42**, R1191 (1995).
11. P. Dessagne *et al.*, to be published in Eur. Phys. J. A.

Closing remarks

This page intentionally left blank

CLOSING REMARKS
A VERY PERSONAL VIEW OF AN EXPERIMENTALIST

G. MÜNZENBERG

Gesellschaft für Schwerionenforschung (GSI) mbH, Planckstr. 1, 64291 Darmstadt, Germany
and Johannes Gutenberg - Universität Mainz, D-55128 Mainz, Germany E-mail: g.muenzenberg@gsi.de

The atomic nucleus is the first major step of nature towards complexity. It links the fundamental physics and our real world. Various approaches are needed in experiment and theory to explore and understand its nature. The progress in creating a consistent picture, a common challenge for experiment and theory, was the topic of the symposium.

1. NEW DEVELOPMENTS

Big progress has been made in experimental techniques, heavy-ion accelerators, sensitivity, resolution, and the introduction of new probes to unstable nuclei by the reversed kinematics method. This allows us to look into far exotic regions of nuclei, to investigate nuclei along cosmic nucleo-synthesis paths and the early stages of creation of the chemical elements surrounding us, to investigate hadronic interaction for unstable nuclei, and to have new insights into the nuclear system revealing matter distributions, correlations, and the behavior of nuclear matter at the transition from bound to unbound.

2. CHALLENGES

The main goal of modern structure research is the exploration of nuclear structure in regions far off stability approaching the limits of nuclear binding. A basic property of nuclear matter which has also implications on our natural environment are closed shells. Their nature, location, and evolution with variation of isospin are central topics of structure research. First exciting results, predominantly in the region of light nuclei, were discussed. Another hot topic for experiment and theory as well is the behavior of

nuclear matter in the transition from bound to unbound, the theoretical treatment of the continuum interaction, and its implication on the structure and dynamics of nuclear matter. Correlations and clusterization in nuclei become accessible with modern experimental and theoretical methods, more realistic forces including the properties of nuclei far-off, stability are needed and under development. Data still lack from statistics and resolution. Stringent tests of theoretical models demand improvement.

3. PERSPECTIVES

The new high current driver accelerators of next generation rare isotope facilities including new instrumentation will certainly shed more light on the structure of the nucleus. Driver accelerators will cover the full Z-range up to uranium. To explore the full scale of nuclear reactions which probe different structure aspects the full energy range from astrophysics regime, near Coulomb barrier energies, the Fermi domain, up to the limiting fragmentation will cover more than five orders of magnitude.

Research at the limits requires highly specialized instruments in terms of sensitivity and precision and will allow the application of new probes, including more precise electromagnetic and hadronic probes, and strangeness. These instruments include the new gamma spectrometers with tracking capability, high resolving spectrometers with appropriate detection systems, and storage rings and low energy colliders for electron and even antiproton scattering. The challenge for theory is the development of a consistent picture of the atomic nuclei from the light few-body systems to the most complex superheavy nuclei with about 300 constituents.

4. THE SYMPOSIUM

The wonderful location of the symposium and the interesting and well balanced program generated a creative atmosphere with excellent contributions from the speakers and the audience, thanks to the advisory and organizing committees. Special thanks deserve the conference secretaries Dr. Masayuki Matsuo, Dr. Takeshi Othsubo, and the Conference chairman Professor Yasuyuki Suzuki. The excellent conference dinner, the cultural contribution and the contact with the local authorities gave us a small but memorable glance on the rich Japanese culture.

Poster session

This page intentionally left blank

This page intentionally left blank

BREAKUP EFFECTS IN ^{6}HE+^{12}C ELASTIC SCATTERING

B. ABU-IBRAHIM AND Y. SUZUKI

Department of Physics., Niigata University,
Niigata 950-2181, Japan

A Monte Carlo integration is used to evaluate the eikonal ^{6}He+^{12}C phase-shift function completely, which makes it possible to use a realistic 6-nucleon wave function for a halo nucleus ^{6}He. We show that the new ^{6}He+^{12}C experimental data can be reproduced in the eikonal approximation without introducing any *ad hoc* assumptions.

The optical phase-shift function $\chi(\mathbf{b})$ plays a basic role in the Glauber theory [1] and it is related to the NN scattering operator by

$$e^{i\chi(\mathbf{b})} = \langle \psi_0^{(\mathrm{P})} \psi_0^{(\mathrm{T})} | \prod_{i\in \mathrm{P}} \prod_{j\in \mathrm{T}} \left[1 - \Gamma_{\mathrm{NN}}(\mathbf{b} + \mathbf{s}_i^{(\mathrm{P})} - \mathbf{s}_j^{(\mathrm{T})}) \right] | \psi_0^{(\mathrm{P})} \psi_0^{(\mathrm{T})} \rangle. \quad (1)$$

The above matrix element contains a multi-dimensional integration, which is obviously not easy to perform in general. Recently it has been demonstrated [2] that the phase-shift function can be evaluated in good accuracy by Monte Carlo method without approximation.

The wave function used for ^{6}He is the variational Monte Carlo wave function [3]. The ^{12}C nucleus is not yet accessible in a realistic calculation and for the ^{12}C a three-α microscopic cluster-model wave function is used.

Results of calculation are shown in Fig. 1: Dotted line is obtained by using different profile functions for np and pp (also nn) pairs, i.e., $\sigma_{\mathrm{np}} = 21.8$ fm^2, $\alpha_{\mathrm{np}} = 0.493$, $\sigma_{\mathrm{pp}} = 7$ fm^2, $\alpha_{\mathrm{pp}} = 1.328$ [4]. Dashed line is calculated fully quantum-mechanically with the single-folding potential $U_{\mathrm{f}}(R) = \int d\boldsymbol{r}\, \rho^{(\mathrm{P})}(\mathbf{r}) V_{\mathrm{NT}}(\mathbf{R} + \mathbf{r})$ where $\mathbf{R}$ is the distance vector between the projectile and the target and V_{NT} is an NT optical potential [5] . The folding model is found to overestimate the measured cross sections [6,7] beyond 6°, which is in contrast to the full Glauber-model calculation. The overestimation of the single-folding model is due to neglecting the breakup effect of ^{6}He. In the above discussion we have observed that the Glauber model with the NN profile function does not necessarily reproduce the data.

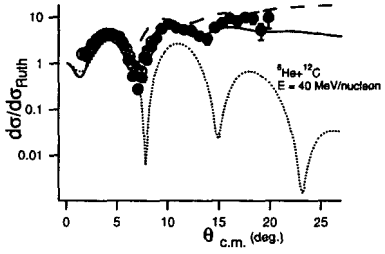

Figure 1. See text for detail.

Since the NN profile function is chosen to be consistent with the data of the elementary NN scattering in free space, this suggests that an appropriate effective interaction has to be employed in the calculation. Instead of using such an effective interaction like G-matrix, we proposed a simple, practical approach [8] to composite-particle scatterings by considering the target just a scatterer and taking an NT scattering as an elementary vehicle. The effective optical phase-shift function is thus calculated by

$$e^{i\tilde{\chi}(\mathbf{b})} = \langle \psi_0^{(\mathrm{P})} | e^{i \sum_{i \in \mathrm{P}} \chi_{\mathrm{NT}}(\mathbf{b}+\mathbf{s}_i^{(\mathrm{P})})} | \psi_0^{(\mathrm{P})} \rangle \qquad (2)$$

where $\Gamma_{\mathrm{NT}} = 1 - e^{i\chi_{\mathrm{NT}}}$ is related to V_{NT} through $\chi_{\mathrm{NT}}(\mathbf{b}) = -\frac{1}{v}\int_{-\infty}^{\infty} dz\, V_{\mathrm{NT}}(\mathbf{b} + z\hat{\mathbf{z}})$. The solid line in fig. 1 is the calculation using Eq. (2), and reproduces the data reasonably well. The energy dependence of the breakup effect has been discussed in Ref. 9.

References

1. R. J. Glauber, in *Lectures on Theoretical Physics*, edited by W. E. Brittin and L. C. Dunham (Interscience, New York, 1959), Vol.1, p.315.
2. K. Varga, S. C. Pieper, Y. Suzuki and R. B. Wiringa, Phys. Rev. C **66** (2002) 034611.
3. B. S. Pudliner, V. R. Pandharipande, J. Carlson, S. C. Pieper and R. B. Wiringa, Phys. Rev. C **56** (1997) 1720.
4. J. Y. Hostachy, Thèse d'Etat, I.S.N. 87-65, Université de Grenoble, unpublished.
5. J. Rapaport, Phys. Rep. **87** (1982) 25.
6. V. Lapoux *et al.*, Phys. Rev. C **66** (2002) 034608.
7. J. S. Al-Khalili *et al.*, Phys. Lett. B **378** (1996) 45.
8. B. Abu-Ibrahim and Y. Suzuki, Nucl. Phys. A **706** (2002) 111.
9. B. Abu-Ibrahim and Y. Suzuki, Nucl. Phys. A **728** (2003) 118.

STABILITY OF STRANGE MATTER WITH A MOLECULAR DYNAMICS APPROACH

Y. AKIMURA AND N. YOSHINAGA
Department of Physics, Saitama University,
Saitama City, 338-8570, Japan
E-mail: akimura@phy.saitama-u.ac.jp

According to the Witten's hypothesis, the true and absolute ground state of strong interaction is the deconfined state of quark matter consisting of an equal proportion of up, down, and strange quarks. Matter in such a state is called strange matter. Stabilization of matter due to inclusion of s quarks attracts attention by a recent experimental discovery such as a penta-quark. For this hypothesis, many theoretical studies[1,2,3] have given negative results, but a molecular dynamics approach has not been tried yet. In this study, we investigate the stability of strange matter in terms of molecular dynamics.

The quark wave function is defined as a direct product of coordinate and flavor space wavefunctions,

$$\Psi = \prod_{i=1}^{3A} \phi_i(\mathbf{r})\chi, \ \phi_i(\mathbf{r}) = \left(\frac{1}{\pi L^2}\right)^{3/4} \exp\left[-\frac{(\mathbf{r}-\mathbf{R}_i)^2}{2L^2} + \frac{i}{\hbar}\mathbf{P}_i\mathbf{r}\right],$$

where variables and parameters are the same as used in Ref. 4 and anti-symmetrization is neglected at present.

As for the flavor dependent interaction, we employ the chiral boson exchange interaction which reproduces some hadron masses at low energy. To take into account the Pauli effect, we employ the Pauli potential defined in Ref. 5 with $c_p = 20$ MeV, $q_0 = 0.7$ fm and $p_0 = 150$ MeV.

The total Hamiltonian is thus written as

$$\hat{H} = \sum_i \sqrt{m_i^2 + \hat{p}_i^2} + \frac{1}{2}\sum_{i\neq j} V^{cb}(\hat{r}_{ij}) + V^{Pauli}(\hat{r}_{ij}, \hat{p}_{ij}),$$

$$V^{cb}(\hat{r}_{ij}) = \frac{\sigma_i\sigma_j}{4}\left\{\sum_{a=1}^{3}\lambda_i^a\lambda_j^a V_\pi(\hat{r}_{ij}) + \sum_{a=4}^{7}\lambda_i^a\lambda_j^a V_K(\hat{r}_{ij}) + \lambda_i^8\lambda_j^8 V_\eta(\hat{r}_{ij})\right\},$$

$$V^{ps}(r) = \frac{g_{\sigma q}^2}{4\pi}\frac{m_{ps}^2}{4m_i m_j}\frac{\exp[-m_{ps}r]}{r},$$

where $g_{\sigma q} = 3.53$, $m_{u,d} = 320$, $m_s = 540$, $m_\pi = 139$, $m_K = 494$, $m_\eta = 547$ (in MeV). Because of lack of antisymmetrization, $\langle\sigma_i\ \sigma_j\ \lambda_i\lambda_j\rangle$ takes trivial values. To correct this, we use the averaged value in both the symmetric case and antisymmetric case.

We get the approximate ground state of a system by solving the molecular dynamics equations with the cooling method,

$$\dot{\mathbf{R}}_i = \frac{\partial H}{\partial \mathbf{P}_i} + \mu_r\frac{\partial H}{\partial \mathbf{R}_i},\ \dot{\mathbf{P}}_i = -\frac{\partial H}{\partial \mathbf{R}_i} + \mu_p\frac{\partial H}{\partial \mathbf{P}_i}.$$

At 1 ρ_0 for udd matter total energy per quark is 461 MeV (potential energy 92 MeV, kinetic energy 369 MeV), for uds matter 493 MeV (potential energy 66 MeV, kinetic energy 426 MeV), while at 1.5 ρ_0 for udd matter total energy per quark is 521 MeV (potential energy 135 MeV, kinetic energy 386 MeV), for uds matter it is 549 MeV (potential energy 95 MeV, kinetic energy 454 MeV).

In this calculation, udd matter is stable than uds matter. But at 1.5 ρ_0 energy difference per quark between udd matter and uds matter becomes smaller than 1 ρ_0's. Here we used the chiral boson exchange interaction, but at QGP phase meson condensate may occur and then gluon exchange becomes relevant.

For a high density calculation, color and spin degrees of freedom, and antisymmetrization should be considered. We assumed the QGP phase and neglected cluster configurations. However, these assumptions may provide a good approximation only at high density or high pressure. This is an open question.

References

1. P. Wang et al., *Phys. Rev.* **C67**, 015210 (2003).
2. W.Albelico et al., *Nucl. Phys.* **A706**, 143 (2002).
3. I.Wetzorke, *Nucl. Phys.* **B119**, 278 (2003).
4. T.Maruyama and T.Hatsuda, *Phys. Rev.* **C61**, 062201 (2000).
5. T.Maruyama et al., *Phys. Rev.* **C57**, 655 (1998).

RESONANCE STRUCTURE OF ^{9}BE AND ^{10}BE IN A MICROSCOPIC CLUSTER MODEL

KOJI ARAI

Department of Physics, University of Surrey, Guildford, Surrey, GU2 7XH, United Kingdom

Cluster or molecular structures among the excited states in ^{9}Be and ^{10}Be have been discussed through the microscopic cluster model.

Structures of the excited states in ^{9}Be and ^{10}Be have been theoretically explored by means of the α+α+n and α+α+n+n microscopic cluster models of the type of the resonating group method(RGM) respectively[1,2]. Resonance excited states are localized by solving the two-body scattering problems of $\{^8\mathrm{Be}(0^+,\ 2^+,\ 4^+)+n,\ ^5\mathrm{He}(3/2^-,\ 1/2^-)+\alpha\}$ in ^{9}Be and $\{^9\mathrm{Be}(3/2^-,\ 1/2^+,\ 5/2^-)+n,\ ^6\mathrm{He}(0^+,\ 2^+)+\alpha\}$ in ^{10}Be using the microscopic R-matrix method(MRM). In ^{9}Be these results are compared with those by the α+α+n three-body complex scaling method(CSM).

Our calculations have been performed up to $J^\pi=9/2^\pm$ in ^{9}Be and our model gives at least one state in each spin-parity state. Resonance energies by the MRM give good agreements with those by the three-body CSM whereas the resonance widths are generally underestimated. The $1/2^+$ first excited state of ^{9}Be, which is not localized by the three-body CSM, is obtained as a $^8\mathrm{Be}(0^+)+n$ virtual state in our model and our calculated $1/2^+$ state of ^{9}B supports the normal Thomas-Ehrman shift where the position of this resonance state is based on the S-matrix pole at the complex momentum plane.

In ^{10}Be the calculations have been performed up to $J^\pi=4^\pm$ and our model gives various resonance excited states above the ^{9}Be+n threshold. Our model can reproduce the ground and second 0^+ states simultaneously where the latter is well known as a intruder state in the shell model. Our model shows that the second 0^+ state is dominated by the $^6\mathrm{He}(0^+)+\alpha$ and $^9\mathrm{Be}(1/2^+)\otimes\nu_{s_{1/2}}$ configurations with the spatially extended relative wave functions. The former configuration suggests that this 0_2^+ state has a de-

veloped α+α(^{6}He+α) clustering which could constitute a K^π=0_2^+ (J^π=0_2^+, 2_4^+, 4_2^+) rotational band in our model. The latter configuration suggests that two neutrons excite into the $s_{1/2}$ orbit ($2\hbar\omega$ excitation) in the second 0^+ state while four neutrons fill the $p_{3/2}$ orbit in the ground 0^+ state. This shows an inversion between the $p_{1/2}$ and $1s_{1/2}$ orbits in ^{10}Be as have ^{9}Be and ^{11}Be. On the whole, the α+α clustering is enhanced at K^π=$1/2^+$ band in ^{9}Be and K^π=0_2^+ band in ^{10}Be, especially the latter has a remarkably developed α+α clustering.

Our present model elucidates that the two and three competing configurations are quite essential in order to reproduce the anomalous $1/2^+$ state in ^{9}Be and second 0^+ state in ^{10}Be respectively. Those are the α-n-α and α-α-n configurations in the $1/2^+$ state of ^{9}Be and the α-(nn)-α, α-α-(nn), and α-n-α-n configurations in the second 0^+ state of ^{10}Be. Among these configurations, the valence neutron(s) in the α-n-α and α-(nn)-α configurations stays near or inside the α+α core and induces the strong core distortion or deformation that is responsible for lowering the $s_{1/2}$ orbit and the parity inversion in these nuclei. On the other hand, in the α-α-n and α-α-(nn) configurations, the valence neutron(s) is far away from the α+α core and this produces the spatially extended neutron distribution, such as the neutron halo. The valence neutron motions in these two states seem to be consistent with the σ-orbit motion in the molecular orbital method[3,4,5], where the valence neutron moves preferentially along the α+α axis.

Acknowledgments

This work was funded by the CHARISSA collaboration grant GR/R38927/01 awarded by the EPSRC.

References

1. K. Arai, Y. Ogawa, Y. Suzuki, and K. Varga, Phys. Rev. C **54**, 132 (1996); K. Arai, P. Descouvemont, D. Baye and W. N. Catford, Phys. Rev. C **68** 014310(2003)
2. Y. Ogawa, K. Arai, Y. Suzuki, and K. Varga, Nucl. Phys. **A673**, 122 (2000); K. Arai, *submitted in* Phys. Rev. C.
3. W. von Oertzen, Z. Phys. A **354**, 37 (1996); *ibid.* **357**, 355 (1997).
4. Y. Kanada-En'yo, H. Horiuchi, and A. Doté, Phys. Rev. C **60**, 064304 (1999); A. Doté, H. Horiuchi, and Y. Kanda-En'yo, *ibid.* **56**, 1844 (1997).
5. N. Itagaki and S. Okabe, Phys. Rev. C **61**, 044306 (2000); N. Itagaki, S. Okabe, and K. Ikeda, *ibid.* **62**, 034301 (2000); N. Itagaki, S. Hirose, T. Otsuka, S. Okabe, and K. Ikeda, *ibid.* **65**, 044302 (2002).

INVARIANT-MASS SPECTROSCOPY OF ^{14}O VIA THE (α, α') REACTION

H. BABA[A], S. SHIMOURA[B], T. MINEMURA[C], Y. U. MATSUYAMA[A], A. SAITO[A], H. AKIYOSHI[C], N. AOI[C], T. GOMI[A], Y. HIGURASHI[C], K. IEKI[A], N. IMAI[C], N. IWASA[D], H. IWASAKI[E], S. KANNO[A], S. KUBONO[B], M. KUNIBU[A], S. MICHIMASA[B], T. MOTOBAYASHI[C], T. NAKAMURA[F], H. SAKURAI[E], M. SERATA[A], E. TAKESHITA[A], S. TAKEUCHI[C], T. TERANISHI[B], K. UE[E], K. YAMADA[A] AND Y. YANAGISAWA[C]

[A] *Department of Physics, Rikkyo University, Nishi-Ikebukuro 3-34-1, Toshima, Tokyo 171-8501, Japan*

[B] *Center for Nuclear Study, University of Tokyo, RIKEN campus, Hirosawa 2-1, Wako, Saitama 351-0198, Japan*

[C] *The Institute of Physical and Chemical Research (RIKEN), Hirosawa 2-1, Wako, Saitama 351-0198, Japan*

[D] *Department of Physics, Tohoku University, Aza-Aoba, Aramaki, Aoba, Sendai, Miyagi 980-8578, Japan*

[E] *Department of Physics, University of Tokyo, Hongo 7-9-1, Bunkyo, Tokyo 113-0033, Japan*

[F] *Department of Applied Physics, Tokyo Institute of Technology, Ookayama 2-12-1, Meguro, Tokyo 152-8551, Japan*

Email: baba@ne.rikkyo.ac.jp

We measured inelastic scattering of alpha particle on the unstable nuclei ^{14}O with the inverse kinematics. The present experiment aimed at measuring the cross sections to the known excited states and obtaining high excitation energy spectra by using the invariant-mass method for various particle decay channels. We obtained the excitation energy spectra of the ^{14}O* (0.0 – 22.0 MeV) from the invariant masses for the decay channel. For several observed states at 4.6 – 8.6 MeV, the differential cross sections are obtained and compared with a Distorted-Wave Born Approximation calculation.

Inelastic scattering of alpha particle by stable nuclei have been successfully used for investigation of natural parity excited states including isoscalar monopole states[1]. For unstable nuclei, excited states above particle threshold can be investigated by measuring all the decaying particles using inverse kinematics.

We have measured alpha inelastic scattering by the unstable nuclei ^{14}O. The excitation energy spectra of the $^{14}O^*$ (0.0 – 22.0 MeV) are shown in Fig.1. These spectra were reconstructed from the momentum vectors of decay particles for various channels of $^{14}O^* \rightarrow {}^{13}N + p$, $^{12}C + p + p\ (+ \gamma_1)$, $^{10}C + \alpha\ (+ \gamma_1)$, and $^{11}C + {}^3He$ with invariant-mass method. The angular distribution of the differential cross sections for several states (Ex = 4.6 – 8.6 MeV) is shown in Fig.2. The solid curves represent a Distorted-Wave Born Approximation (DWBA) calculation carried out with the code ECIS97[2] using the folded-potential model[3]. With an good agreement between the experimental data and the DWBA calculation, spectroscopic information can be obtained for the state excited by the (α, α') reactions on unstable nuclei. In order to extract spin and strength of several states (Ex = 8.6 – 22.0 MeV), an analysis using the DWBA calculations with a multipole-decomposition is in progress.

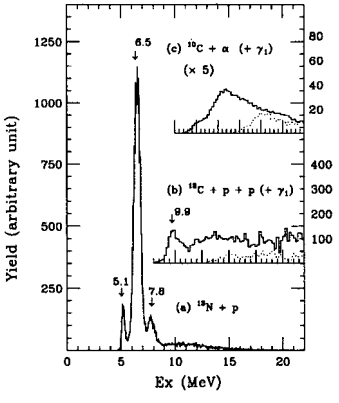

Figure 1. The excitation energy spectra of the $^{14}O^*$ (Ex = 0.0 – 22.0 MeV).

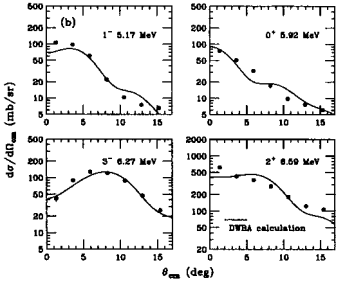

Figure 2. The angular distributions of the differential cross section (Ex = 4.6 – 8.6).

References

1. D. H. Youngblood *et al.*, *Phys. Rev.* **C57**, 2748 (1998).
2. J. Raynal, ECIS97, unpublished.
3. G.R. Satchler, *Nucl. Phys.* **A472**, 215 (1987).

THREE-BODY SYSTEMS WITH THE LAGRANGE-MESH TECHNIQUE

E.M. TURSUNOV, D. BAYE, AND P. DESCOUVEMONT

Physique Nucléaire Théorique et Physique Mathématique, C.P. 229, Université Libre de Bruxelles, B-1050 Brussels, Belgium

We investigate three-body systems in the hyperspherical formalism. The wave functions are expanded over a Lagrange basis. The method is applied to bound and scattering states of the $\alpha + n + n$ system.

Three-body systems play an important role in the physics of exotic light nuclei [1]. For example, ^{6}He and ^{11}Li are well described by $\alpha + n + n$ and $^9\mathrm{Li} + n + n$ structures, respectively. As exotic nuclei present a low separation energy, the study of continuum states is essential [2]. Here we aim at extending a previous work dealing with three-body bound states [3] to continuum states. The three-body hamiltonian reads

$$H = \sum_{i=1}^{3} T_i \; + \; \sum_{i<j} V_{ij}(\boldsymbol{r}_j - \boldsymbol{r}_i), \tag{1}$$

where $\boldsymbol{r}_i$ is the coordinate of nucleus i, T_i its kinetic energy, and V_{ij} a two-body interaction. Two-body forbidden states are accounted for by adding a projection operator to V_{ij}, or by using its supersymmetric transform.

To solve the Schrödinger equation associated with (1), we use the hyperspherical coordinate formalism [4]. The Jacobi coordinates are replaced by the hyperradius ρ, and by 5 angles denoted as Ω_5. The wave function in partial wave $J\pi$ is written as

$$\Psi^{JM\pi}(\rho, \Omega_5) = \rho^{-5/2} \sum_{\gamma K} \chi^{J\pi}_{\gamma K}(\rho) \mathcal{Y}^{JM}_{\gamma K}(\Omega_5), \tag{2}$$

where K is the hypermomentum, γ a set of additional quantum numbers, and $\mathcal{Y}^{JM}_{\gamma K}(\Omega_5)$ the hyperspherical harmonics. In this work, we expand the radial wave functions $\chi^{J\pi}_{\gamma K}(\rho)$ in a Lagrange basis [5]. This method has been applied to various fields in physics. Associated with the Gauss approximation to evaluate integrals, the matrix elements of the potential are very

simple. More detail about the application to the hyperspherical formalism can be found in Ref.[3]. The method is first applied to the ground state of ^{6}He (see Ref.[3] for the conditions of the calculation). We find a binding energy $E = -0.87$ MeV and $E = -0.38$ MeV, using the projection technique or supersymmetric transform, respectively.

More recently, the Lagrange-mesh technique has been extended to three-body continuum states. To correct the asymptotic behaviour of the basis functions, we use the R-matrix method [6]. A specificity of three-body systems in hyperspherical coordinates comes from the coupling potentials which extend to very large ρ values (typically up to $\rho \approx 1000$ fm). To avoid the use of huge bases, we use a propagation technique [7]. This provides very accurate phase shifts, with reasonable basis sizes (typically 20-30 Lagrange functions). In Fig. 1, we present the eigenphases of the $\alpha + n + n$ system for $J = 0^+, 1^-, 2^+$. The $\alpha + n$ ($\ell = 0$) forbidden state is removed by using the supersymmetric transform. As expected we find a narrow 2^+ resonance near $E = 0.5$ MeV, and broad structures in the 0^+ and 1^- partial waves.

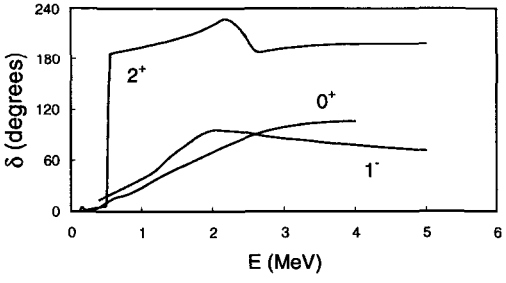

Figure 1. Eigenphases of the $\alpha + n + n$ system.

References

1. M.V. Zhukov *et al.*, Phys. Rep. **231**, 151 (1993).
2. I.J. Thompson *et al.*, Phys. Rev. **C61**, 024318 (2000).
3. P. Descouvemont, C. Daniel and D. Baye, Phys. Rev. **C67**, 044309 (2003).
4. R. Krivec, Few-Body Systems **25**, 199 (1998).
5. D. Baye and P.-H. Heenen, J. Phys. **A19**, 2041 (1986).
6. A.M. Lane and R.G. Thomas, Rev. Mod. Phys. **30**, 257 (1958).
7. V.M. Burke and C.J. Noble, Comput. Phys. Commun. **85**, 471 (1995).

ROLE OF PROTON AND NEUTRON EXCITATIONS TO THE 2_1^+ STATE IN ^{16}C

Z. ELEKES[1] *, ZS. DOMBRÁDI[2], A. KRASZNAHORKAY[2], H. BABA[3], M. CSATLÓS[2], L. CSIGE[2], N. FUKUDA[1], ZS. FÜLÖP[2], Z. GÁCSI[2], J. GULYÁS[2], N. IWASA[4], H. KINUGAWA[3], S. KUBONO[5], M. KUROKAWA[5], X. LIU[5], S. MICHIMASA[5], T. MINEMURA[5], T. MOTOBAYASHI[1], A. OZAWA[1], A. SAITO[3], S. SHIMOURA[5], S. TAKEUCHI[1], I. TANIHATA[1], P. THIROLF[6], Y. YANAGISAWA[1], K. YOSHIDA[1],

[1] *The Institute of Physical and Chemical Research, 2-1 Hirosawa, Wako, Saitama 351-0198, Japan*

[2] *Institute of Nuclear Research of the Hungarian Academy of Sciences (ATOMKI), P.O. Box 51, Debrecen, H-4001, Hungary*

[3] *Rikkyo University, 3 Nishi-Ikebukuro, Toshima, Tokyo 171, Japan*

[4] *Tohoku University, Sendai, Miyagi 9808578, Japan*

[5] *University of Tokyo, Tokyo 1130033, Japan*

[6] *Ludwig-Maximilians-Universität München, D-85748 Garching, Germany*

Email: elekes@rarfaxp.riken.go.jp

Angular distribution of the ^{16}C+^{208}Pb inelastic scattering populating the 2_1^+ state has been measured. The extracted neutron and proton transition matrix elements, M_n and M_p, were quite different: M_n/M_p=7.6 ± 1.7. The small M_p value, corresponding to 0.28 ± 0.06 Weisskopf units of $B(E2; 2_1^+ \rightarrow 0^+)$, is consistent with a recent lifetime measurement.

Recent calculations [1] suggest different deformations for proton and neutron distributions in carbon isotopes. We applied the Coulomb–nuclear interference method to study proton and neutron contribution to excitation of the first 2^+ state.

The experiment was carried out in RIKEN. The beam of ^{16}C at 52.7 A·MeV of $4{\cdot}10^5$ particles/s was transmitted to a ^{208}Pb target of 50 mg/cm^2 thickness. The scattered particles were identified by a plas-

*On leave from ATOMKI

tic scintillator hodoscope. For tracking the beam, four parallel plate avalanche counters (PPAC's) were used. The angular resolution was 0.28° at 1σ value. The deexciting γ–rays in coincidence with the ^{16}C particles were detected by an array of 68 NaI(Tl) scintillator detectors. The resulting angular distribution is shown in Fig. 1. The minimum from the Coulomb–nuclear interference can be seen at about 2.6°. For the analysis of the angular distribution, we used the coupled channel code ECIS95 [2]. The optical model parameters were taken from [3]. The standard collective form factors were applied. Two parameters for the coupling potential, the "Coulomb deformation" length δ_C and the "matter deformation" length δ_M, characterizing respectively the Coulomb and nuclear interactions between the target and projectile, have been determined by a χ^2-minimization analysis. Two χ^2-minima can be found at δ_M/δ_C=0.67 and δ_M/δ_C=3.1 with reduced χ^2=1.6. In Fig. 1, the solid and dashed curves correspond to the results of the two minima. The errors include the systematic ones from background fitting, selection of optical potential set and uncertainty in the efficiency of the γ ray setup. The resultant δ_M and δ_C are connected to the neutron and proton transition matrix elements M_n and M_p via the Bernstein formula [4]. The deduced ratio is M_n/M_p=7.6 ± 1.7. The proton matrix element corresponds to an electromagnetic transition probability of B(E2)=0.28 ± 0.06 Weisskopf units, while the neutron one represents a value slightly higher than the single particle one. Our B(E2) value being significantly less than 1 W.u. is consistent with the result of a recent direct lifetime measurement, which gives B(E2)=0.26±0.05 [5], and is the smallest transition probability ever observed, while the deduced M_n/M_p ratio is the highest so far. Our experimental results clearly show that a very small proton deformation, or more strictly a very small amount of proton excitation, contributes to the 2_1^+ state in ^{16}C. The excitation is dominated by neutron transitions.

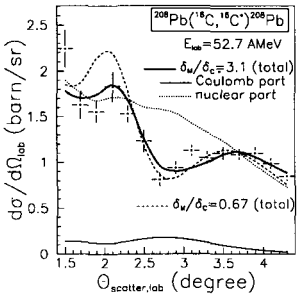

Figure 1. Differential cross sections for the inelastic scattering exciting the 2_1^+ state in ^{16}C. The solid line represent the best fit with ECIS calculation (dotted line: Coulomb part, dash–dotted line: nuclear part). Dashed line is plotted with δ_M/δ_C = 0.67 local minimum value.

Acknowledgments

The authors would like to express their thanks to Kanada-En'yo, T. Otsuka and J. Raynal. This work was partly supported by OTKA T38404 and T42733.

References

1. Y. Kanada-En'yo, et al., Phys. Rev. C 55 (1997) 2860.
2. J. Raynal, Phys. Rev. C 23 (1981) 2571.
3. J. Barrette, et al., Phys. Rev. C 62 (2000) 0340306.
4. A.M. Bernstein, et al., Phys. Rev. Lett. 42 (1979) 425.
5. N. Imai, et al., Phys. Rev. Lett. (submitted) (2003).

EFFECT OF ISO-SPIN AVERAGING AND FINITE RANGE OF THE NN FORCE ON REACTION CROSS SECTION FOR NEUTRON RICH NUCLEI

M. ISMAIL, A. Y. ELLITHI, AND H. ABOU-SHADY
Department of Physics, Cairo University, Giza 12613, Egypt

The optical limit to Glauber theory is used to calculate the reaction cross section, σ_R, for neutron rich nuclei. In-medium and iso-spin dependence of the effective nucleon-nucleon (NN) reaction cross-section, σ_{NN}, are treated correctly assuming both finite and zero range NN interaction. We find that the combined effect of iso-spin dependence and finite range of NN force can increase up to 20% for neutron rich nuclei compared to σ_R calculated using zero range approximation and constant matter density value 0.16 fm^{-3} in σ_{NN}. The maximum percentage increase is reduced to 13% compared with σ_R based on free NN cross section.

In the optical limit approximation to Gauber theory[1] the nucleus-nucleus reaction cross section is

$$\sigma_R(\frac{E_L}{A_P}) = 2\pi \int_0^\infty db\, b\,[1-T], \tag{1}$$

where E_L/A_P stands for the incident energy per projectile nucleon, in the Laboratory system, the transmission function T is given by [2]

$$T(\mathbf{b}) = \exp[-\int_{-\infty}^{\infty} dz \int \sum_{i,j=n,p} \sigma_{ij}(\rho_T^i + \rho_P^j, \frac{E_L}{A_P}) f(\mathbf{s}) \rho_T^i(\mathbf{r}_1) \rho_P^j(\mathbf{r}_2)\, d\mathbf{r}_1\, d\mathbf{r}_2], \tag{2}$$

where, σ_{ij} is the in-medium nucleon-nucleon reaction cross section at incident energy per projectile nucleon E_L/A_P, $\rho_{T(P)}^{n,p}$ stands for the target(projectile) neutron(n) or proton(p) density distribution. The reaction cross section σ_R is drawn against the incident energy per projectile nucleon E_L/A_P for the three interacting pairs ^{238}U+^{9}Li, ^{12}C+^{9}Li and ^{12}C+^{11}Li in Figs.(1,2,3) respectively. σ_{NN} is taken in different ways,(free σ_{NN}^f,iso-spin average σ_{NN}[3], constant density dependence,ρ=0.16 fm^{-3}) with zero range approximation, and (iso-spin average σ_{NN}, local density, p,n are the same, or p,n are different 'exact')with finite range approximation. As shown from figures that comparing σ_R for finite range with exact iso-spin dependence

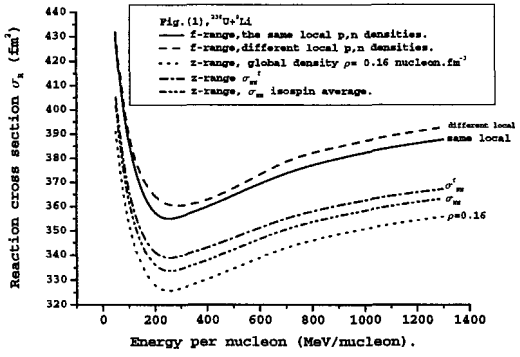

a 10% increase compared to that averaged iso-spin σ_{NN} with zero range approximation for heavy target ^{238}U, and increased to 16% for light targets ^{9}Li, ^{11}Li, with an overall increase for σ_R for ^{11}Li halo. The effect of accurate iso-spin dependence to that of the average for finite range calculations as such is less than 3.7% for light target, and less than 1.3% for heavy target. Similar ratios are found for zero range calculations which means that such accurate isospin(local density) has small effect compared to that of the usual average.

References

1. R. J. Glauber, in *Lectures on Theoretical Physics*, edited by W. E. Brittin and L. C. Dunham (Interscience, New York, 1959), Vol.1, p.315.
2. R. E. Warner, *et al.*, Phys. Rev. C **62** (2000) 0241608, w. Q. Shen, Y. G. MA, and Z. Y. Zhu, Phys. Lett. B. **305** (1993)9.
3. Cai. Xiangzhou *et al.*, Phys. Rev. C **58** (1998) 572.

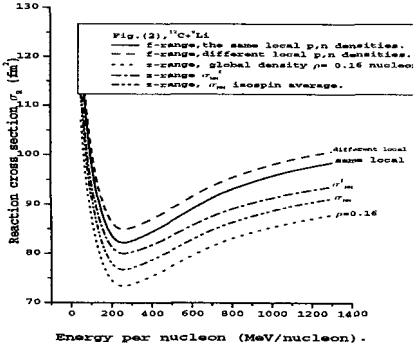

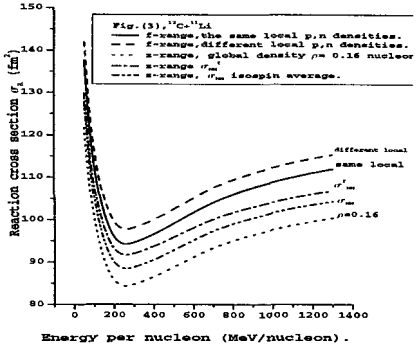

HIGH-SPIN ISOMER IN ^{93}Mo

T. FUKUCHI, Y. GONO[a], A. ODAHARA[b], H. WATANABE[c], S. TANAKA[a], M. INOUE[a], Y. WAKABAYASHI[a], T. SASAKI[a], M. KIBE[a], N. HOKOIWA[a], T. SHINOZUKA[d], M. FUJITA[d], A. YAMAZAKI[d], T. SONODA[d], C.S. LEE[e], Y.K. KWON[e] *and*, J.H. LEE[e]

Center for Nuclear Study (CNS), University of Tokyo, JAPAN
2-1 Hirosawa, Wako, Saitama 351-0198
fukuchi@cns.s.u-tokyo.ac.jp
[a] *Department of Physics, Kyushu University, JAPAN*
[b] *Nishinippon Institute of Technology, JAPAN*
[c] *RIKEN, JAPAN*
[d] *Cyclotron and Radioisotope Center (CYRIC),Tohoku University, JAPAN*
[e] *Department of Physics, Chung-Ang University, KOREA*

The high-spin states of ^{93}Mo have been studied in ^{82}Se(^{16}O,5n)^{93}Mo reaction at a beam energy of 100 MeV using techniques of in-beam γ spectroscopy. Measurements of γ-t, γ-γ-t coincidences, γ-ray angular distributions, and γ-ray linear polarizations were performed. The high-spin isomer was discovered at 9.7 MeV excited state. The near yrast states in ^{93}Mo were well described using the weak coupling picture of a $d_{5/2}$ neutron to a neutron magic core nucleus ^{92}Mo.

As results of recent studies, high-spin isomers which have lifetime between $\sim$10 *ns* and few μs were reported in N=83 isotones systematically, ^{144}Pm,^{145}Sm,^{146}Eu,^{147}Gd,^{148}Tb,^{149}Dy,^{150}Ho and ^{151}Er[1]. The excitation energy of these high-spin isomers are close each other in a range of 8.5 – 9.0 MeV. Their spins and parities are $49/2^+$ and 27^+ for odd and odd-odd nuclei, respectively except for ^{150}Ho and ^{151}Er. The configuration of these isomers are extracted experimentally and theoretically to be stretch coupled $[\nu(f_{7/2}h_{9/2}i_{13/2})\otimes\pi(h^2{}_{11/2})]_{49/2+}$ for odd nuclei and $[\nu(f_{7/2}h_{9/2}i_{13/2})\otimes\pi(h^2{}_{11/2}d^{-1}{}_{5/2})]_{27+}$ for odd-odd nuclei. These isotones have near sperical shapes in the ground states and oblate shapes in the isomeric states. This shape change causes the high-spin isomers. By analogy with mechanism of high-spin isomers in N=83 isotones, existence of the isomers of the same origin were expected in N=51 isotones. In this paper, results of search for high-spin isomer in ^{93}Mo which is a member of N=51

isotnes are presented. In the past, a level scheme of ^{93}Mo was established up to the spin 35/2 state at 7.3 MeV and the high-spin isomer have never been reported[2] .

Experiment to search for the high-spin isomer in ^{93}Mo was performed at Cyclotron and Radioisotope Center (CYRIC) in Tohoku University. The high-spin states in ^{93}Mo were populated using the reaction ^{82}Se(^{16}O,5n)^{93}Mo at beam energy of 100 MeV. For the γ-ray detection anti-Compton shielded 4 Clover type Ge detectors were used. Measurements of γ-t, γ-γ-t coincidences, γ-ray angular distributions, and γ-ray linear polarizations were carried out. A linear-polarization measurements were performed using the 2 Clover type Ge detectors located at angle of θ = 90°.

A decay scheme of ^{93}Mo was constructed based on the γ-γ coincidence data. Eleven γ-rays and 11 levels were newly found and spins and parities of states were assigned for 5 levels based on angular distribution and linear polarization measurements. To search for isomer, a γ-γ delyed coincidence analysis was performed. In the 1 μs delayed spectrum, several γ-rays in ^{93}Mo were observed. The observation of delayed γ-rays of ^{93}Mo indicate the existence of an isomer. Based on the delayed γ-rays, a high-spin isomer was located at 9.7 MeV excited state. Using the time distribution of γ-rays deexciting the high-spin isomer, the half life of the high-spin isomer was determined to be $T_{1/2}$ = 1.1(4)μs. By the life time information, a population of this high-spin isomer is extracted to be 1.8(4)%.

A configuration of this high-spin isomer of $(39/2^-)$ was deduced to be $[\nu(d_{5/2}g_{7/2}h_{11/2})\otimes\pi(g^2{}_{9/2})]_{39/2^-}$ based on the analogy of configuration of the high-spin isomers in N=83 isotones. The high-spin isomer in ^{93}Mo is excited 1-2 MeV from the yrast line. This non-yrast character of the isomer may explain the small population of the high-spin isomer. To interpret level structure of ^{93}Mo, a comparison between yrast line of ^{93}Mo and ^{92}Mo. Two yrast lines of ^{92}Mo[3] and ^{93}Mo have similar shapes. This similarity was made implies validity of weak coupling of one neutron with ^{92}Mo in case of ^{93}Mo.

References

1. Y. Gono et al., *Eur. Phys. J.* **A13**, 5 (2002).
2. A. Zobov et al., *Nucl. Data. Sheets.* **80**, 1 (1997).
3. P. Singh et al., . *Phys. Rev. C.* **45**, 45 (1992).

PRECISE QUADRUPOLE MOMENT OF PROTON HALO NUCLEUS ^{8}B

T. SUMIKAMA, T. NAGATOMO, M. OGURA, T. IWAKOSHI,
Y. NAKASHIMA, H. FUJIWARA, K. MATSUTA, T. MINAMISONO,
M. FUKUDA AND M. MIHARA

Department of Physics, Osaka University, Toyonaka, Osaka 560-0043, Japan
E-mail: sumikama@vg.phys.sci.osaka-u.ac.jp

K. MINAMISONO

TRIUMF, 4004 Wesbrook Mall, Vancouver, B.C., V6T 2A3, Canada

The quadrupole moment of ^{8}B ($I^\pi = 2^+$, $T_{1/2} = 838$ ms) has been remeasured in high precision. The obtained value, $Q = +64.5 \pm 1.3$ mb, is compared with several theoretical calculations.

1. Introduction

^{8}B nucleus has a very small proton-separation energy 137 keV, thus the last proton of ^{8}B is expected to form halo structure inspite of Coulomb and centrifugal potentials. Existence of this proton halo structure has been discussed since the large quadrupole moment of ^{8}B was measured[1]. In the present study, we measured the quadrupole coupling constant of ^{8}B in the TiO_2 (rutile) to determine the quadrupole moment of ^{8}B in high precision.

2. Measurement of the quadrupole moment of ^{8}B

The experimental setup and procedure are essentially the same as previous works[2]. It is known that the TiO_2 crystal fully maintains the polarization of ^{12}B($I = 1$) and the ^{12}B nuclei occupies two different implantation sites[2]. To determine the precise quadrupole moment Q of ^{8}B, we observed the β-NQR spectrum of ^{8}B($I = 2$) in the major site as a function of ν_Q ($= 3eqQ/2I(2I-1)h$) in the external magnetic field $H_0 = 3$ kOe as shown in Fig. 1. By fitting the symmetrical spectrum using Gaussian, we obtained the resonance frequency as $\nu_Q(^8\mathrm{B}) = 144.5(5)$ kHz, where the much smaller systematic error was ignored. Combined with $\nu_Q(^{12}\mathrm{B}) = 177.7(7)$ kHz for the same site[2],

the ratio of Q-moment was precisely determined to be $|Q(^8\mathrm{B})/Q(^{12}\mathrm{B})| = 4.879(26)$. The present value is more reliable than the previous value of $|Q(^8\mathrm{B})/Q(^{12}\mathrm{B})| = 5.18(13)$ with Mg catcher[1], because the sharp resonance was observed by use of TiO_2 crystal and the narrow FM width ± 5 kHz. Combined with the precise $|Q(^{12}\mathrm{B})| = 13.21(26)$ mb[1] and the sign[3] $Q(^8\mathrm{B}) > 0$, the electric quadrupole moment of ^{8}B was determined precisely to be $Q(^8\mathrm{B}) = +64.5(13)$ mb which is slightly smaller than the previous one, $|Q(^8\mathrm{B})| = 68.3(21)$ mb[1].

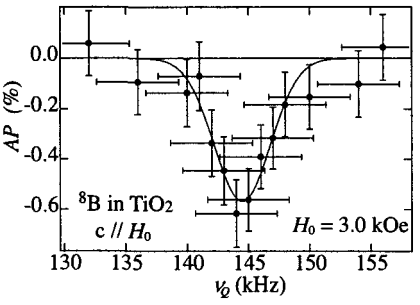

Figure 1. Typical β-NQR spectrum.

Both the present quadrupole moment of ^{8}B and that of the mirror nuclei ^{8}Li, $Q(^8\mathrm{Li}) = +32.7(6)$[1,4], are well reproduced not only by the $(0+2)\hbar\omega$ shell-model calculation with small effective charge by Nakada and Otsuka[5], but also by the *ab initio* calculation using the Green's function Monte Carlo method (GFMC)[6] with AV18/IL2 (two-/three-nucleon interactions) as shown in Table 1. However both calculations do not show the density distribution of ^{8}B. Microscopic cluster model by Csótó[7] reproduces only $Q(^8\mathrm{B})$. The density distribution calculated by the cluster model suggests the proton skin structure.

Table 1. Quadrupole moments of mirror nuclei ^{8}B and ^{8}Li.

Method	^{8}B	^{8}Li	Reference
Experiment	+64.5(13)*	+32.7(6)[1,4]	*Present
Shell Model (0+2$\hbar\omega$)	62.7	32.1	5
GFMC with AV18/IL2	64(1)	32(1)	6
Microscopic Cluster Model	65.8	22.5	7
Shell Model (Hartree-Fock)	56.2	30.8	8

References

1. T. Minamisono, T. Ohtsubo, I. Minami et al, *Phys. Rev. Lett.* **69**, 2058 (1992).
2. M. Ogura, K. Minamisono et al., *Hyperfine Interactions* **136/137**, 195 (2001).
3. T. Yamaguchi, K. Sato et al., *Hyperfine Interactions* **120/121**, 689 (2001).
4. H.J. Jänsch, M. Detje, H.D. Ebinger et al., *Nucl.Phys.* **A568**, 544 (1994).
5. H. Nakada and T. Otsuka, *Phys. Rev.* **C 49**, 886 (1994).
6. S.C. Pieper, V.R. Pandharipande et al., *Phys. Rev.* **C 64**, 014001 (2001).
7. A. Csótó, *Phys. Lett.* **B315**, 24 (1993).
8. H. Kitagawa, *Prog. Theor. Phys.* **102**, 1015 (1999).

GAMOW-TELLER DECAY OF THE T=1 NUCLEUS ^{46}Cr

T. K. ONISHI[1], A. GELBERG[2], H. SAKURAI[1], K. YONEDA[3], N. AOI[1], N. IMAI[1], H. BABA[4], P. VON BRENTANO[2], N. FUKUDA[3], Y. ICHIKAWA[1], M. ISHIHARA[3], H. IWASAKI[1], D. KAMEDA[5], T. KISHIDA[3], A. LISETSKIY[6] H. J. ONG[1], M. OSADA[1], T. OTSUKA[1], M. K. SUZUKI[1], K. UE[1], Y. UTSUNO[7], AND H. WATANABE[3]

1. Department of Physics, University of Tokyo, 2. Institut für Kernphysik der Universität zu Köln, 3. RIKEN,
4. Rikkyo University, 5. Tokyo Institute of Technology
6. Michigan State University, 7. Japan Atomic Energy Research Institute

1. Introduction

Even-even nuclei with $|N-Z| = 2$ ($T = 1$) and $A = 4n+2$ (n-integer) decay by favoured allowed Gamow-Teller (GT) transitions to $I^\pi = 1^+, T = 0$ states in odd-odd, N=Z nuclei. We define $B(GT; I_f, T_f, T_{zf} \rightarrow I_i, T_i, T_{zi}) = (2I_i + 1)^{-1} \langle I_f, T_f, T_{zf} || \sigma t_\pm || I_i, T_i, T_{zi} \rangle^2$

Such favoured allowed GT transitions have been observed in light nuclei and also in light-medium mass nuclei, e.g. in the pf shell. The beta decay of ^{46}Cr to the N=Z nucleus ^{46}V has been studied[1], but the authors observed only the Fermi transition to the ground state of ^{46}V. The absence of the GT decay would represent a striking anomaly. **The aim of the present work was the search for the GT beta decay of ^{46}Cr to the 1^+_1 state of ^{46}V[2].**

2. Experiment

The experiment was carried out at the RIPS[3] separator of the RIKEN accelerator research facility. A ^{46}Cr beam was produced by the fragmentation of ^{50}Cr on a Be target. The intensity of the ^{46}Cr beam was 20 s^{-1}. The ^{46}Cr ions were implanted into a 5 mm thick plastic scintillator. The pulsed beam was on for 500 ms, and off for 790 ms. The identification of the ^{46}Cr beam was described in ref.[4]. The ^{46}Cr β-rays were detected by two sets of $\Delta E - \Delta E - E$ plastic scintillators. Gamma-rays, both in singles spectra and in coincidence with β-rays, were detected by 4 Clover type Ge detectors.

The number of ^{46}Cr implanted in the plastic scintillator was determined from the purity of ^{46}Cr and the total beam intensity. The ^{46}Cr purity was 0.1%. A gamma-peak at 993±1.0 keV was observed in singles and at 992.3±0.9 keV in the coincidence gamma spectra. These peaks correspond to the $1_1^+ \rightarrow 0_1^+$ transition in ^{46}V at 993±0.4 keV[2]. The numbers of counts in these peaks, after background subtraction and dead time correction, were 1998±210 and 361±79 in the singles and coincidence spectra, respectively.

3. Results and discussion

The GT decay of ^{46}Cr has been observed for the first time. The branching ratio of the decay to the 1^+ state in ^{46}V is $b_\beta = 0.258 \pm 0.033$. The half-life of ^{46}Cr was deduced from the time structure of the 993 keV peak. We obtained $T_{1/2} = 223 \pm 54$ ms, which is consistent with the previous value $T_{1/2} = 260 \pm 54$ms[1]. The partial half-life of the GT transition is $t = 930 \pm 190$ ms. This leads to $ft = 4631 \pm 953$ s (log ft=3.66), and $B(GT; I = 0, T = 1 \rightarrow I = 1, T = 0) = 0.83 \pm 0.17$. This value of B(GT) is larger than B(GT)=0.59±0.15 and B(GT)=0.68±0.15 measured in the decays of ^{50}Fe and ^{54}Ni, respectively[6]. Shell-model calculations with the two-body interactions FPD6[2] and KB3[2] have been done. The GXPF2 effective interaction[5] has also been used. The Quasi-deuteron (QD) calculation is a phenomenological one, in which two nucleons in the same subshell are coupled to a T=0, N=Z core[7]. The experimental and unquenched theoretical results can be seen in the table.

Exp.	FPD6	KB3	GXPF2	QD
0.83±0.17	0.934	0.560	0.641	0.748

References

1. J. Zioni et al., *Nucl. Phys.* **A181**, 465 (1972)
2. C. Friessner et al., *Phys. Rev.* **C60**, 011304 (1999) and references within
3. T. Kubo et al., *Nucl. Instr. Methods* **B70**, 309 (1992)
4. T. K. Onishi et al., *RIKEN Accel. Prog. Rep.* **36**, 84 (2003)
5. M. Honma et al., *Phys. Rev.* **C65**, 061301 (2002)
6. V. Koslowsky et al., *Nucl. Phys.* **A624**; I. Reusen et al., *Phys. Rev.* C59, 2416 (1999)
7. A. Lisetskiy et al., *Phys. Rev.* **C60**, 06431 (2001); *Phys.Lett.* **B512**, 290 (2001)

MICROSCOPIC DESCRIPTION OF DOUBLET BANDS IN LANTHANUM-134

K. HIGASHIYAMA AND N. YOSHINAGA

Department of Physics, Saitama University,
Saitama City, 338-8570, Japan
E-mail: higashi@phy.saitama-u.ac.jp

Recently, systematic doublet bands based on $\nu h_{11/2} \otimes \pi h_{11/2}$ configurations have been observed in many odd-odd nuclei in A$\sim$130 region[1,2]. The structure of these bands may be understood as a manifestation of chiral symmetry in the sense of angular momentum coupling, which was predicted by Frauendorf and Meng[3]. In the past these bands had been investigated theoretically in terms of mean field approaches. However, there was no microscopic study which preserves both rotational symmetry and particle number of interactions.

In this study, we apply the SD version of the pair-truncated shell model (PTSM)[4] to the odd-odd nucleus ^{134}La. We take full 50$\sim$82 configuration spaces for both neutrons and protons, and employ the monopole and quadrupole pairing plus quadrupole-quadrupole interaction as an effective interaction. The force strengths of the interaction are determined so as to reproduce energy levels of the even-even nuclei around this region. The model (PTSM) and details of interactions are presented in the paper by N. Yoshinaga in the same volume of this proceedings.

The experimental energy spectrum of the odd-odd nucleus ^{134}La corresponding to $\nu h_{11/2} \otimes \pi h_{11/2}$ configurations[2] is compared with that obtained by the PTSM in Fig. 1. A good agreement between the theoretical spectrum of the PTSM and the experimental data is achieved. The PTSM result predicts the existence of the 9_2^+ and 10_2^+ levels in low-lying states.

Detailed accounts of the theoretical frameworks for $E2$ and $M1$ transition rates are given in Refs. 4. The adopted effective charges are e_ν=$-1.20e$ and e_π=$+2.20e$, and the adopted gyromagnetic ratios are $g_{\ell\nu} = 0.10$, $g_{\ell\pi} = 1.10$, $g_{s\nu} = -2.68$ and $g_{s\pi} = 3.91$. In the upper panel of Fig. 2, calculated $B(M1)/B(E2)$ values in yrast band are compared with experimental data. The $B(M1)/B(E2)$ values are well reproduced except for the

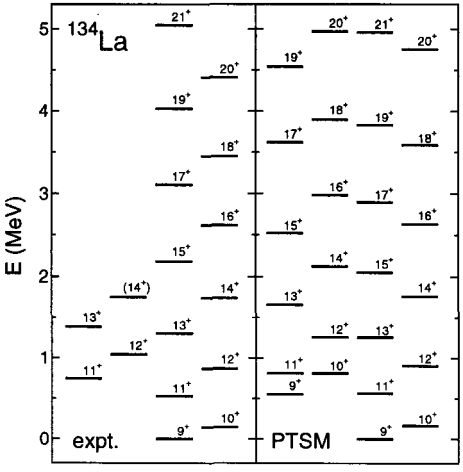

Figure 1. Comparison of energy spectra in experiment (expt.) with the PTSM (PTSM) result for the odd-odd nucleus ^{134}La. The experimental data are taken from Ref. 2.

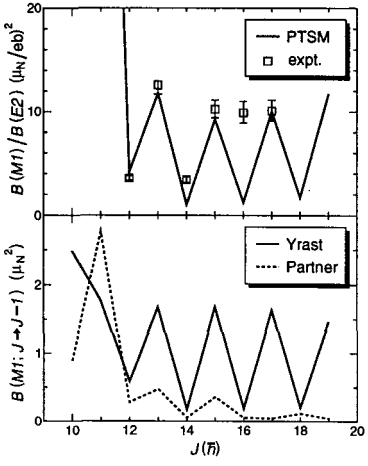

Figure 2. Upper panel: Comparison of $B(M1)/B(E2)$ ratios in experiment with the PTSM result. The experimental data are taken from Ref. 2. Lower panel: The $B(M1)$ values calculated in the PTSM.

value at spin $J = 16$.

Theoretical prediction of $B(M1)$ values of the yrast and partner states are shown as a function of spin J in the lower panel of Fig. 2. The $B(M1)$ values between yrast states show a large amplitude staggering. On the other hand, for the partner band $B(M1)$ values become very small, and the staggering pattern almost disappears after $J = 12$. These results suggest that the yrast and partner bands have very different structures, and the doublet bands of the nucleus ^{134}La cannot be interpreted as a manifestation of chirality. Further experimental and theoretical investigations are necessary to understand the internal structures of doublet bands for A$\sim$130 nuclei.

References

1. G. Rainovski et al., *Phys. Rev.* **C68**, 024318 (2003), and references therein.
2. R. A. Bark, A. M. Baxter, A. P. Byrne, G. D. Dracoulis, T. Kibedi, T. R. McGoram and S. M. Mullins, *Nucl. Phys.* **A691**, 577 (2001).
3. S. Frauendorf and J. Meng, *Nucl. Phys.* **A617**, 131 (1997).
4. K. Higashiyama, N. Yoshinaga and K. Tanabe, *Phys. Rev.* **C67**, 044305 (2003).

ON THE ORDER-CHAOS TRANSITION AS AN EXPLANATION OF THE DECAY-OUT OF SUPERDEFORMED BANDS

M. S. HUSSEIN, A. J. SARGEANT, M. P. PATO
Instituto de Física, Universidade de São Paulo, 05315-970, São Paulo, Brazil

N. TAKIGAWA
Department of Physics, Tohoku University, Sendai, 980-8578, Japan

M. UEDA
Akita National College of Technology, Akita, 011-8511, Japan

We calculate the maximum effect which an order-chaos transition in the normally deformed states can have on the total relative intra-band decay intensity of a superdeformed band. Our results show that the sharp attenuation of the decay intensity cannot be explained solely by an order-chaos transition.

Recently, a new explantion of the sharp decay-out observed in superdeformed (SD) bands was proposed by Åberg[1]: an order-chaos transition in the normally deformed (ND) states enhances the tunneling probability and consequently the decay-out is an example of "chaos assisted tunneling". Sargeant *et al.*[2] used Åberg's model to calculate the decay intensity of a SD band as given by

$$I_{\rm av} = \frac{\Gamma_S}{2\pi} \int_{-\infty}^{\infty} dE \frac{1}{[E - E_0]^2 + \Gamma_S^2 [1 + \Gamma^{\downarrow}/\Gamma_S S_d(E)]^2/4}, \qquad (1)$$

and concluded that the decay-out was mostly due to the spin-dependence of the barrier separate the SD and ND wells. (See also Åberg's comment[4].) The energy of the SD state under consideration is E_0 and it's electromagnetic width is Γ_S. $S_d(E)$ describes the manner in which $|0\rangle$ is distributed in energy over the ND states[3]. We assume that $|0\rangle$ only mixes with one ND doorway state $|d\rangle$ whose energy is E_d. The state $|d\rangle$ is subsequently mixed by the residual interaction with the remaining ND states. The spreading width is $\Gamma^{\downarrow} = 2\pi |V_{0d}|^2/D$ where V_{0d} is the interaction energy of $|0\rangle$ and $|d\rangle$.

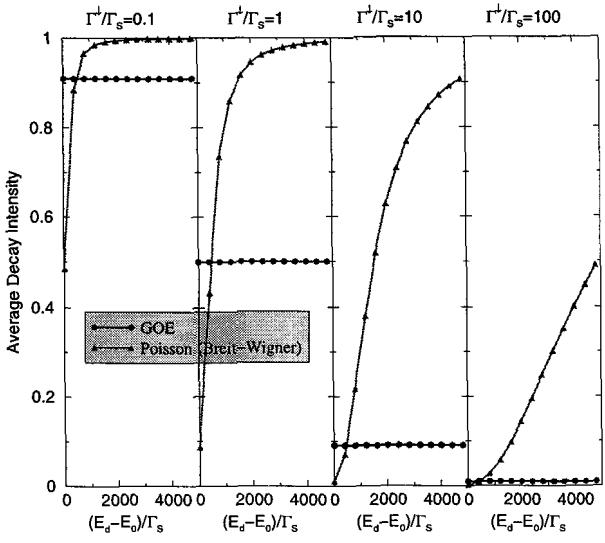

Figure 1. Average decay intensity vs. $(E_d - E_0)/\Gamma_S$ for $\Gamma_N/\Gamma_S = 300$.

When the ND states obey GOE statistics Eq. (1) yields[2] $I_{\rm av}^{\rm GOE} = (1 + \Gamma^{\downarrow}/\Gamma_S)^{-1}$. When the ND states obey Poisson statistics $S_d(E) \approx \delta(E - E_d)$ and we represent it by the Breit-Wigner function, $S_d^{\rm BW}(E) = \frac{1}{2\pi}\frac{\Gamma_N}{(E-E_d)^2+\Gamma_N^2/4}$. Figure 1 shows $I_{\rm av}$ versus $(E_d - E_0)/\Gamma_S$. The triangles represent $I_{\rm av}$ calculated using the Breit-Wigner strength function whilst the circles represent the GOE case. The decay-out is enhanced by increasing the degree of chaos if the triangles are above the circles and it is hindered if the triangles are below the circles. It is seen that the transition from Poisson to GOE statistics cannot exhaust all of the intra-band decay intensity unless $\Gamma^{\downarrow}/\Gamma_S \to \infty$. These observations reinforce our belief[2] that the attenuation of the intra-band intensity is mostly due to the spin dependence of the barrier. Finally, we note that a fluctuation contribution should be added to $I_{\rm av}$[5,6].

References

1. S. Åberg, Phys. Rev. Lett. **82**, 299, (1999).
2. A. J. Sargeant, M. S. Hussein *et al.*, Phys. Rev. C **65**, 024302, (2002).
3. A. J. Sargeant, M. S. Hussein *et al.*, Phys. Rev. C **61**, 011302, (2000).
4. S. Åberg, Phys. Rev. C **68**, 069801, (2003).
5. J.-z. Gu and H. A. Weidenmuller, Nucl. Phys. **A660**, 197, (1999).
6. A. J. Sargeant, M. S. Hussein *et al.*, Phys. Rev. C **66**, 064301, (2002).

DEDUCING THE DENSITY DEPENDENCE OF THE SYMMETRY ENERGY FROM UNSTABLE NUCLEI

KEI IIDA

The Institute of Physical and Chemical Research (RIKEN), Hirosawa, Wako, Saitama 351-0198, Japan

KAZUHIRO OYAMATSU

Department of Media Theories and Production, Aichi Shukutoku University, Nagakute, Nagakute-cho, Aichi-gun, Aichi 480-1197, Japan

BADAWY ABU-IBRAHIM

Department of Physics, Cairo University, Giza 12613, Egypt

We explore a possible method to deduce from unstable nuclei the parameter L characterizing the density dependence of the symmetry energy near normal nuclear density.

We calculate[1] differential cross sections for proton-nucleus elastic scattering by using a Glauber theory in the optical limit approximation and nucleon distributions that can be obtained in the framework of macroscopic nuclear models[2] in a way dependent on the equation of state of uniform nuclear matter near the saturation density. These nuclear models reasonably reproduce empirical data for masses and radii of stable nuclei and allow for uncertainties in the values of the symmetry energy density-derivative coefficient, L, and the incompressibility of symmetric nuclear matter, K_0. The matter radii of heavy unstable nuclei predicted from such models depend appreciably on L, while being almost independent of K_0.

Comparison of the angular distributions calculated for proton elastic scattering off heavy stable nuclei with the empirical values shows[1] that the Glauber model is satisfactory for sufficiently high proton incident energy, T_p, and small scattering angle, $\theta_{\rm c.m.}$. We thus focus on the angle and height of the first scattering peak; the values calculated for various sets of the parameters L and K_0 in the case of Ni isotopes including a very neutron-

rich nucleus ^{80}Ni are plotted in Fig. 1. We find that the peak angle decreases with L more remarkably for larger neutron excess, while the peak height increases with K_0 almost independently of neutron excess. We suggest the possibility that comparison of the calculations with experimental data for the peak angle may be useful for determination of L.

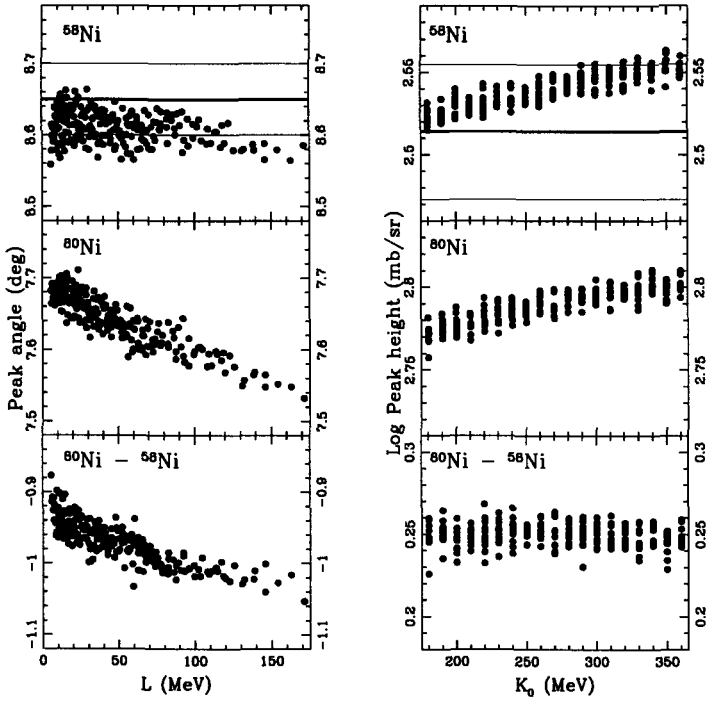

Figure 1. The angles and heights of the scattering peak in the small angle regime, calculated as functions of L and K_0 for p-^{58}Ni and p-^{80}Ni elastic scattering at $T_p = 800$ MeV. The experimental angle and height including errors (from Ref.[3]) are denoted by the horizontal lines (thick lines: central values, thin lines: upper and lower bounds).

References

1. K. Iida, K. Oyamatsu, and B. Abu-Ibrahim, *Phys. Lett.* **B**, **576**, 273 (2003).
2. K. Oyamatsu and K. Iida, *Prog. Theor. Phys.* **109**, 631 (2003).
3. L. Ray, W. Rory Coker, and G.W. Hoffmann, *Phys. Rev.* **C18**, 2641 (1978).

STATIC AND DYNAMIC NON-AXIAL OCTUPOLE DEFORMATIONS SUGGESTED BY SKYRME-HF AND SELFCONSISTENT RPA CALCULATIONS

T. INAKURA, M. YAMAGAMI, AND K. MATSUYANAGI
Department of Physics, Graduate School of Science, Kyoto University, Kitashirakawa, Kyoto 606-8502, Japan

S. MIZUTORI
Department of Human Science, Kansai Women's College, Kashiwara City, Osaka 582-0026, Japan

H. IMAGAWA AND Y. HASHIMOTO
Institute of Physics, University of Tsukuba, Tsukuba 305-8571, Japan

Quite recently, Imagawa and Hashimoto[1,2] constructed a new computer code that carries out a selfconsistent RPA in the mixed representation (the coordinate and configuration representations are used for particles and holes, respectively)[3] on the basis of the Skyrme-Hartree-Fock (SHF) mean field, taking into account all terms of the residual interaction (including the time-odd terms and the residual Coulomb interaction as well). Solving these RPA eigenvalue equations on the 3D Cartesian mesh in a box, Imagawa[1] obtained a strongly collective octupole vibrational mode with $K^\pi = 1^-$ at about 1.1 (0.6) MeV excitation from the superdeformed (SD) band head of ^{40}Ca, for the SIII (SkM*) interaction.

With the use of this RPA code, we have investigated properties of negative-parity collective excitations that are built on SD states in neutron-rich Sulfur isotopes. In a recent paper,[4] Inakura *et al.* suggested that the SD states are expected to exist in the neutron-rich ^{36}S and the drip-line nuclei, ^{48}S and ^{50}S, in addition to the well-known candidate ^{32}S. The result of the RPA calculation is presented in Fig.1. It is seen that the collective excitations in neutron-rich Sulfur isotopes are created mainly by neutron excitations. These excitation modes built on the SD states (in particular, in drip-line nuclei possesing the superdeformed neutron skin) exhibit

interesting new features, on which we shall discuss in detail elsewhere.

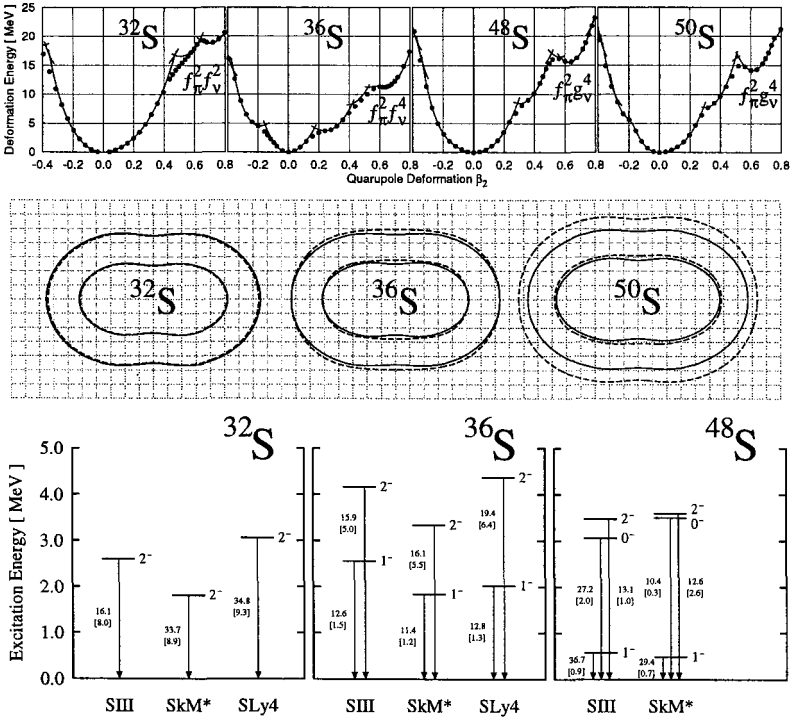

Figure 1. Top panel: Deformation energy curves for Sulfur isotopes calculated at I=0 as functions of β_2 by means of the constrained SHF procedure with the SkM* interaction.[4] Middle panel: Density distributions in the (z,x)- plane of the SD band at I=0 in ^{32}S, ^{36}S, and ^{50}S, calculated with the use of the SLy4 interaction. Neutron (proton) equi-density lines with 50% and 1% of the central density are shown by dashed (solid) lines (the inner and outer lines correspond to the 50% and 1% lines, respectively).
Bottom panel: Lowest few intrinsic excitations with negative parity on the SD states in Sulfur isotopes, obtained by the selfconsistent RPA calculation with the use of the SIII, SkM* and SLy4 interactions. The SD state in ^{48}S calculated with SLy4 is unstable,[4] so that the RPA spectrum is not shown for this case. Numbers beside the arrows indicate the squared transition matrix elements for the mass octupole operators (sums of proton and neutron contributions) in the Weisskopf unit. Compare them with the numbers in parentheses that indicate the proton contributions only. The RPA matrix in the mixed representation is constructed using 30 mesh points in each direction with mesh size h=0.6 fm. See Refs. [1,2] for details of numerical calculation and convergence check with respect to the mesh size.

References

1. H. Imagawa, Docter Thesis, University Tsukuba, April 2003, and to be published.
2. H. Imagawa and Y. Hashimoto, Phys. Rev. 67 (2003), 037302.
3. A. Muta, J-I. Iwata, Y. Hashimoto, and K. Yabana, Prog. Theor. Phys. 108 (2002), 1065.
4. T. Inakura, S. Mizutori, M. Yamagami and K. Matsuyanagi, Nucl. Phys. A 728 (2003) 52.

THE ^{9}LI+D REACTION AT REX-ISOLDE

HENRIK JEPPESEN*

Department of Physics and Astronomy, University of Aarhus, DK-8000 Aarhus, Denmark, E-mail: henjep@phys.au.dk

Introduction: With the completion of the post-accelerator REX-ISOLDE [1,2] at ISOLDE (CERN) in the autumn of 2001 it has become possible to perform low energy (up to 2.3 MeV/u) reactions with a large fraction of the 700 radioactive isotopes presently available at ISOLDE. We here report on the ^{9}Li+d reaction at 2.36 MeV/u. This reaction was used to search for information on the excited states in ^{10}Li. We will here shortly review the experiment and show a few results from our first experiment with this new instrument.

Experimental setup: The ^{9}Li beam was produced by bombarding a Ta-foil target with a 1.4 GeV proton pulse every 2.4 sec. The produced ^{9}Li then diffused out of the target and into a surface ion source. From the ion source the 1+ ions were extracted by a 30 kV potential and guided to REX-ISOLDE. The ISOLDE beam first entered a trap which collected and cooled the ions before they were injected into a Electron-Beam Ion Source (EBIS) for charge breeding. The ^{9}Li^{2+} beam was then accelerated through a linac to a final energy of 2.36 MeV/u.

The accelerated ^{9}Li beam entered the detector setup through a 4 mm collimator and was incident on a 6 μg deuterated polypropylene target (CD_2). On the right hand side of the beam direction a Double Sided Si Strip Detector (DSSSD) of thickness 64 μm and total area of 5×5 cm^2 was situated covering from 18° to 80° in the laboratory system. The DSSSD was backed by a thick Si pad detector (1000 μm) to form a telescope which could identify protons with energy higher than $\sim$ 2.5 MeV. On the other side of the beam a small telescope was situated at 45°.

Data analysis: From the time-structure of the ISOLDE beam (^{9}Li produced every 2.4 sec) it is possible to gate on periods with primarily ^{9}Li (0-

*for the is367 and rex-isolde collaborations

600 ms after proton impact), and periods with only long-lived background (1200-2400 ms after proton impact) which is mainly ^{18}O from rest-gas in the EBIS. In the DSSSD telescope protons, deuterons, tritons, alphas and ^{6}He could be identified.

As an example we here present the triton data from the reaction ^{9}Li+d $\rightarrow$ ^{8}Li+t. The time distribution of the tritons show that they are only produced by the ^{9}Li beam. In Figure 1 a scatter-plot of the total triton

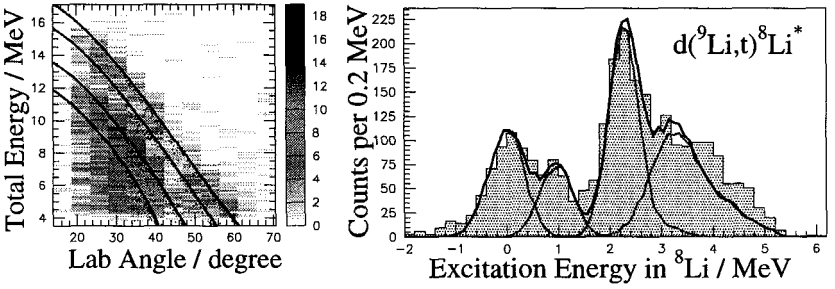

Figure 1. Left: Scatter-plot of total energy vs. lab. angle for identified tritons. Lines indicates position of gs, 1st, 2nd and 3rd excited state in ^{8}Li. Right: The extracted excitation energy spectrum in ^{8}Li from triton events.

energy vs. lab. angle is shown superimposed with the ground state and first three excited states in ^{8}Li (left) and the extracted excitation energy spectrum (right). The excitation energy spectrum is very nicely explained by the four states mentioned above - showing the efficiency of the method.

Conclusion: We have shown that the new post-accelerator REX-ISOLDE is very suitable for extracting spectroscopic information on exotic nuclei. The first four states in ^{8}Li have been seen and agree very well with literature.

We have seen a low-lying state in ^{10}Li at 300 keV above the ^{9}Li+n threshold but are limited by the beam energy to see states at higher excitation energy. An experiment at higher energy (3.1 MeV/u) will most likely take place in the spring/summer of 2004 allowing us to see states at higher excitation energy in ^{10}Li.

References

1. D. Habs, *Hyp. Int.* **129**, 43-66 (2000).
2. http://www.ha.physic.uni-muenchen.de/okester/rex/rex.html

APPLICATION OF THE ADIABATIC SELF-CONSISTENT COLLECTIVE COORDINATE METHOD TO THE PROLATE-OBLATE SHAPE COEXISTENCE PHENOMENA

M. KOBAYASHI, AND K. MATSUYANAGI
Department of Physics, Graduate School of Science, Kyoto University, Kitashirakawa, Kyoto 606-8502, Japan

T. NAKATSUKASA
Physics Department, Tohoku University, Sendai 980-8578, Japan

M. MATSUO
Graduate School of Science and Technology, Niigata University, Niigata 950-2181, Japan

Shape coexistence phenomena are typical examples of large amplitude collective motion in nuclei. These phenomena imply that different solutions of the Hartree-Fock-Bogoliubov (HFB) equations (local minima in the deformation energy surface) appear in the same energy region and that the nucleus exhibits large amplitude collective motion connecting these different equilibrium points. The identities and mixings of these different shapes are determined by the dynamics of such collective motion.

Recently, we have proposed a new method of describing such large-amplitude collective motion, which is called Adiabatic Self-consistent Collective Coordinate (ASCC) method.[1] It yields a new method of solving the basic equations of the SCC method[2] using an expansion in terms of the collective momentum. It does not assume a single local minimum, so that it is expected to be suitable for the description of the shape coexistence phenomena. The ASCC method also enables us to include the pairing correlations self-consistently, removing the spurious number fluctuation modes.

To examine the feasibility of the ASCC method, we have first applied it to an exactly solvable model called the multi-$O(4)$ model, which is a simplified version of the pairing-plus-quadrupole (P+Q) interaction model.[3] It is shown that the method yields a faithful description of tunneling motion through a barrier between the prolate and oblate local minima in the col-

lective potential.[4] The emergence of the doublet pattern characteristic to this model is clearly described.

Quite recently, with use of the P+Q interaction model, we have applied the ASCC method to the shape coexistence phenomena in ^{68}Se discovered by Fisher *et al.*,[5] where the oblate ground band and the prolate excited bands compete in energy, and investigated the collective path connecting the oblate and prolate local minima in the collective potential energy landscape. A preliminary result of this microscopic calculation is shown in Fig. 1, which indicates that the collective path goes through the change of the axially asymmetric quadrupole moment Q_{22}; in the terminology of the Bohr-Mottelson collective Hamiltonian, it roughly corresponds to the path along which the triaxial deformation parameter γ changes between 0° and 60° keeping the axially symmetric deformation parameter β approximately constant. Details of this work will be published elsewhere.[6] This result is consistent with the Skyrme-HFB calculation by Yamagami *et al.*,[7] which shows that the potential barrier between the oblate and prolate local minima is much lower in the γ direction compared with that in the β direction. Currently, the generater coordinate method has often been used to describe variety of shape coexistence phenomena taking the β as the generater coordinate. The result of the ASCC calculation, however, strongly indicate the necessity of taking into account the γ degree of freedom at least for describing the oblate-prolate shape coexistence in ^{68}Se.

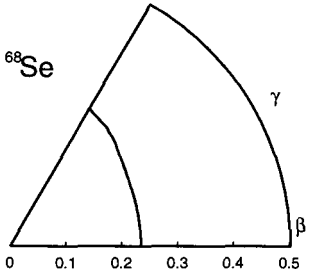

Figure 1.

References

1. M. Matsuo, T. Nakatsukasa and K. Matsuyanagi, Prog. Theor. Phys. 103 (2000), 959.
2. T. Marumori, T. Maskawa, F. Sakata and A. Kuriyama, Prog. Theor. Phys. 64 (1980), 1294.
3. M. Baranger and K. Kumar, Nucl. Phys. A 110 (1968), 490.
4. M. Kobayasi, T. Nakatsukasa, M. Matsuo and K. Matsuyanagi, Prog. Theor. Phys. 110 (2003), 61.
5. S. M. Fischer *et al.*, Phys. Rev. Lett. 84 (2000), 4064.
6. M. Kobayasi, T. Nakatsukasa, M. Matsuo and K. Matsuyanagi, in preparation.
7. M. Yamagami, K. Matsuyanagi and M. Matsuo, Nucl. Phys. A 693 (2001), 579.

LIGHT NUCLEI AT HIGH EXCITATION: ALPHA-CLUSTER STATES AT "LOW" LEVEL DENSITIES

TOM LÖNNROTH

Department of Physics, Åbo Akademi, FIN-20500 Turku, Finland
E-mail: tlonnrot@abo.fi

We have studied α-cluster states in light nuclei using reverse-geometry elastic α-particle scattering, $HI+\alpha$, in helium gas. Further, we have determined level densities experimentally in ^{27,28}Si, ^{50,51}V and $^{94-98}$Mo, using (^{3}He,α) and (^{3}He,^{3}He') reactions. From these results we argue that α-cluster states are embedded in a relatively "low-density continuum".

Alpha-cluster states in reverse geometry have been studied in many A=20-44 nuclei, *viz.* ^{16,18}O+α, ^{18}Ne+α (r/b experiment) Ref.[1], and ^{20,22}Ne+α. Results from low-spin resonances in ^{32}S+α are given in Ref.[2]. Large-scale results[3] from ^{32}S are shown in Figure 1. Note the drop-off in intensity of nearly two decades at $E_{exc} = 31$ MeV. Recently performed experiments are ^{28,30}Si+α, ^{36}Ar+α and ^{40}Ar+α. Preliminary analyses show that ^{40}Ar+α has *much less* structure. Indeed, the excitation structure of ^{22}Mg is also very different from ^{22}Ne, the underlying structures being ^{16}O+α+2p and ^{16}O+α+2n, respectively. The ^{22}Ne structure can also be interpreted as ^{16}O+^{6}He, giving rise to doublet bands.

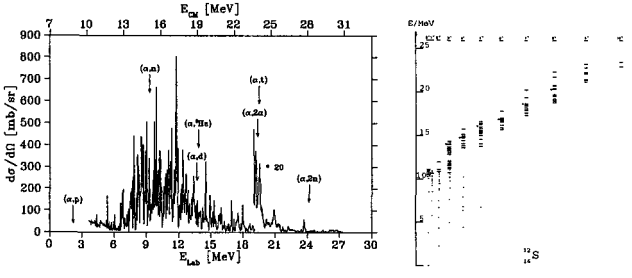

Figure 1. Left: Excitation function of $\alpha + {}^{28}\mathrm{Si} \rightarrow {}^{32}\mathrm{S}$ from the Coulomb barrier up to $E_{exc} = 31$ MeV. Right: Yrast plot of the α-cluster states, which follow an $\ell(\ell+1)$ dependence, indicative of a rotational structure.

A method has been developed[4] that allows almost model-independent extraction of level densities up to fairly high excitation energy. It works well in the rare-earth region[4,5], and the new results[6] for ^{27,28}Si support the applicability of the method also in light nuclei, see Figure 2. The analysis uses the Brink-Axel hypothesis, namely the γ-ray matrix is factorized as

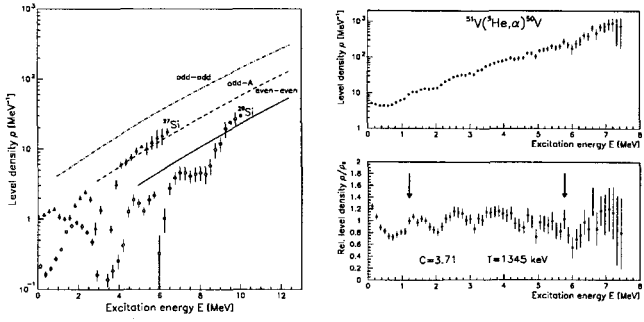

Figure 2. Level densities in ^{27,28}Si (left) and preliminary ^{50}V (right).

$P(E, E_\gamma) \propto \rho(E - E_\gamma) \cdot \mathcal{T}(E_\gamma)$, where ρ is the level density and $\mathcal{T}$ is the radiative transmission coefficient. The experimental level density data reach up to $E \sim B_n - 1$ MeV, and we extrapolate with the back-shifted Fermi gas model $\rho_{\rm BS}(E) = \eta \cdot \exp(2\sqrt{aU})/12\sqrt{2}a^{1/4}U^{5/4}\sigma_I$, where a constant η is introduced to fix $\rho_{\rm BS}$ to the experimental level density at B_n.

We conclude that our work shows that the α-cluster states indeed lie at excitations where the level density is still fairly low, albeit at several tens of MeV. This conclusion is also supported by shell-modell calculations[7].

Acknowledgments. This work is a collaboration with the Kurchatov Institute (contact person V.Z. Goldberg), Jyväskylä (W.H. Trzaska), Oslo (M. Guttormsen), Dubna (M.S. Golovkov) and Catania (M. Lattuada), which I gratefully acknowledge.

References

1. V.Z. Goldberg *et el.*, Phys. Rev. C, in press
2. V.Z. Goldberg *et al.*, Phys. At. Nucl. **63**, 1518 (2000)
3. K.-M. Källman *et al.*, Eur. Phys. J. A **16**, 159 (2003)
4. A. Schiller *et al.*, Nucl. Instr. Meth. **A447**, 498 (2000)
5. M. Guttormsen *et al.*, Phys. Rev. C **61**, 067302 (2000)
6. M. Guttormsen *et al.*, J. Phys. G **29**, 263 (2003)
7. W.E. Ormand, Phys. Rev. C **56**, R1678 (1997); T. Lönnroth, T. Siiskonen, K.-M. Källman and M. Grigorescu, in preparation.

FOUR-BODY CDCC ANALYSIS OF ^{6}He + ^{12}C SCATTERING

T. MATSUMOTO, K. OGATA AND M. KAMIMURA

Department of Physics, Kyushu University, Fukuoka 812-8581, Japan

E. HIYAMA

Institute of Particle and Nuclear Studies, High Energy Accelerator Research Organization (KEK), Tsukuba, 305-0801, Japan

M. YAHIRO

Department of Physics and Earth Sciences, University of the Ryukyus, Nishihara-cho, Okinawa 903-0213, Japan

Y. ISERI

Department of Physics, Chiba-Keizai College, Todoroki-cho 4-3-30, Inage, Chiba 263-0021, Japan

To study how halo structure affects on ^{6}He + ^{12}C elastic scattering at 38.3 MeV/nucleon, we propose the four-body CDCC (continuum-discretized coupled-channels) method. In this method, three-body wave functions of ^{6}He nucleus are obtained by Gaussian expansion method. ^{6}He halo effects are investigated by comparing ^{6}He + ^{12}C scattering with ^{6}Li + ^{12}C scattering.

For scattering of a two-neutron-halo nucleus, four-body breakup processes are very important. In order to analyze four-body reactions precisely, we propose the four-body CDCC (continuum-discretized coupled-channels [1]) method. As an example, the elastic scattering of ^{6}He on ^{12}C at 38.3 MeV/nucleon, which has been measured at GANIL [2] recently, is analyzed.

In a four-body reaction system, the CDCC method needs a set of an approximate complete set including three-body bound and discretized-continuum states of the projectile. As a method to calculate such states, in

our previous work, we proposed the pseudo-state method [3] using Gaussian expansion method (GEM) [4].

In the present analysis, coupled-channel (CC) potentials are calculated by doubly-folding model with the M3Y nucleon-nucleon interaction; the nucleon density of ^{12}C target and the transition densities of ^{6}He are used. Then each CC potential is multiplied by a complex factor, $N_R + iN_I$. We fix N_R to unity and optimize N_I to fit the experimental data [2].

As the result of the present calculation, taking $N_I = 0.2$, the experimental data can be well reproduced. In the previous CDCC analysis [5] of ^{6}Li-induced scattering in a wide range of incident energy, calculation with $N_I \sim 0.5$ explained experimental data. This difference of N_I between ^{6}He- and ^{6}Li-induced scattering may be evidence of halo effects of ^{6}He. To draw a definite conclusion, however, more detailed study is necessary and more systematic experimental data are highly desirable.

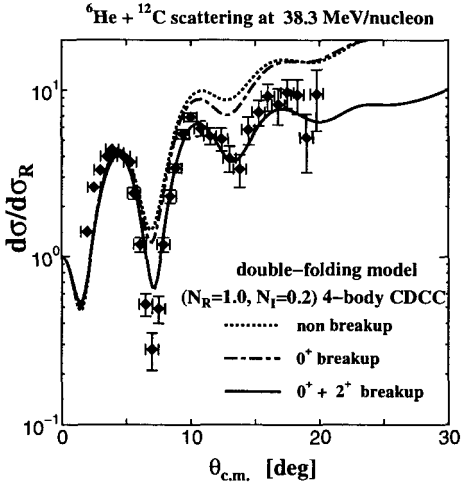

Figure 1. Angular distribution of the elastic differential cross section as a ratio to the Rutherford one for ^{6}He + ^{12}C scattering at 38.3 MeV/nucleon. The dotted line represents the result with no breakup effects and the dash-dotted (solid) line shows the result including 0^+ (both 0^+ and 2^+) breakup states.

References

1. M. Kamimura *et al.*,*Prog. Theor. Phys. Suppl.* **89**, 1 (1986).
2. V. Lapoux *et al.*, *Phys. Rev.* **C66**, 034608 (2002).
3. T. Matsumoto *et al.*, *Phys. Rev.* **C68**, 064607 (2003).
4. E. Hiyama *et al.*, *Progress in Particle and Nuclear Physics*, **51**, 223 (2003).
5. Y. Sakuragi *et al.*, *Prog. Theor. Phys. Suppl.* **89** 136 (1986).

3α BOSON STRUCTURE OF 0^+ STATES OF ^{12}C

H. MATSUMURA AND Y. SUZUKI†

Graduate School of Science and Technology, Niigata University, Niigata 950-2181, Japan

†*Department of Physics, Niigata University, Niigata 950-2181, Japan*

The structure of ^{12}C has been studied in a microscopic 3α model by several authors. In particular, the second excited state with $J^\pi = 0^+$ attracted much attention as it plays a key role for the synthesis of ^{12}C in stars. Recently this state has been reinvestigated from the point of view of α-condensation[1]. The purpose of this contribution is to extend our previous study[2] based on a macroscopic α-boson model and to quantify the amount of α-condensation on a microscopic level. Through this analysis we will be able to "extract" the geometrical structure of ^{12}C more reliably.

The wave function for ^{12}C is represented as

$$\Psi_{\rm F} = \mathcal{A}\left\{\phi(\alpha_1)\phi(\alpha_2)\phi(\alpha_3)\chi(\boldsymbol{R}_1, \boldsymbol{R}_2, \boldsymbol{R}_3)\right\},$$

where $\boldsymbol{R}_i$ is the position vector of the α-particle and the relative motion function χ is expressed in terms of a superposition of explicitly correlated Gaussians

$$\chi(\boldsymbol{R}_1, \boldsymbol{R}_2, \boldsymbol{R}_3) = \sum_i C_i \exp\left\{-\sum_{k<l} b_{kl}^{(i)} (\boldsymbol{R}_k - \boldsymbol{R}_l)^2\right\}.$$

We used Minnesota and Volkov potentials. The parameters of $b_{kl}^{(i)}$ are determined by the stochastic variational method[3,4]. The boson wave function $\Psi_{\rm B}$ corresponding to $\Psi_{\rm F}$ is defined by

$$\Psi_{\rm B} = \mathcal{N}^{\frac{1}{2}}\chi$$

with the norm kernel $\mathcal{N}$. This mapping has the property that the orthonormality of the fermionic wave functions is preserved in the boson space as well. As it is difficult to construct $\mathcal{N}^{1/2}$, we approximate the above boson wave function by

$$\Psi_{\rm B} \approx \frac{1}{\sqrt{\langle g|g\rangle}}\mathcal{N}\chi, \quad g = \mathcal{N}\chi.$$

With this $\Psi_{\rm B}$, we can study the 3α boson structure emerging from the microscopic wave function $\Psi_{\rm F}$. A pair correlation function is often used to get a geometrical arrangement of the particles. It is defined by

$$P(\boldsymbol{r},\boldsymbol{r}') = \langle\Psi_{\rm B}|\delta(\boldsymbol{R}_1 - \boldsymbol{x}_N - \boldsymbol{r})\delta(\boldsymbol{R}_2 - \boldsymbol{x}_N - \boldsymbol{r}')|\Psi_{\rm B}\rangle\,,$$

where $\boldsymbol{x}_N$ is the center of mass coordinate of the system. Figure shows the contour map of P obtained with Volkov 1 potential for the 0_2^+ state as a function of $r = |\boldsymbol{r}| = |\boldsymbol{r}'|$ and θ.

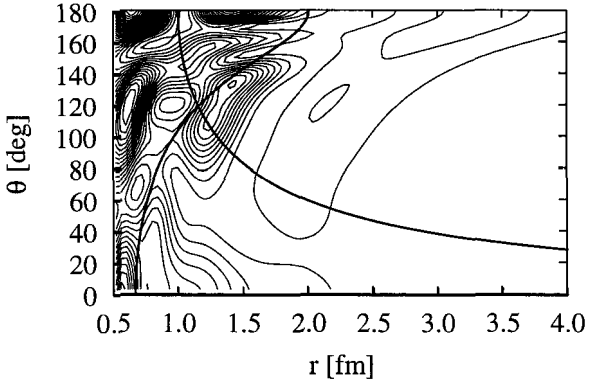

In the upperright part enclosed by two lines, 3α clusters are separated by 2-fm from each other. Here the α clusters form broad structure including regular triangle and chain configuration. To investigate the amount of α-condensation in the 0_2^+ state, we construct the density matrix of the 3α particles,

$$\rho(\boldsymbol{R},\boldsymbol{R}') = 3\langle\psi|\delta(\boldsymbol{R}_1 - \boldsymbol{x}_N - \boldsymbol{R})\rangle\langle\delta(\boldsymbol{R}_1 - \boldsymbol{x}_N - \boldsymbol{R}')|\psi\rangle,$$

and solve its eigenvalue problem. The amount of the condensation can be quantified by the distribution of the eigenvalues. We obtained the result that the amount of α-condensation was about 70% for the 0_2^+ state.

1. A. Tohsaki, H. Horiuchi, P. Schuck and G. Röpke, Phys. Rev. Lett. 87 (2001) 192501.
2. Y. Suzuki and M. Takahashi, Phys. Rev. C65 (2002) 064318.
3. K. Varga and Y. Suzuki, Phys. Rev. C52 (1995) 2885.
4. Y. Suzuki and K. Varga, *Stochastic Variational Approach to Quantum-Mechanical Few Body Problems* (Springer, Berlin, 2003).

LOW-ENERGY OF POLARIZED RI ATOMIC BEAM

H. MIYOSHI, K. SHIMADA, K. ASAHI, D. KAMEDA, K. SAKAI, S. EMORI AND G. KATO

Department of Physics, Tokyo Institute of Technology, Oh-okayama 2-12-1, Meguroku, Tokyo 152-8551, Japan

H. UENO, A. YOSHIMI, H. WATANABE AND Y. KOBAYASHI

Applied Nuclear Physics Lab, RIKEN, Hirosawa 2-1, Wako-shi, Saitama 351-0198, Japan

J. MURATA

Nuclear and Radiation Physics Laboratory, Department of Physics, Rikkyo University 3-34-1 Nishi-Ikebukuro, Toshima, Tokyo 171-8501, Japan

W. SATO

Department of Chemistry, Graduate School of Science, Osaka University, 1-1 Machikaneyama, Toyonaka, Osaka 560-0043, Japan

H. OGAWA

Photonics Research Institute, National Institute of Advanced Industrial Science and Technology (AIST), 1-1-1 Umezono, Tsukuba, Ibaraki 305-8568, Japan

W. -D. SCHMIDT-OTT

Zweotes Physikalisches Institut, Der Universitär Göttingen, Bunsenstrasse 7-9, D-37073 Göttingen, Germany

Spin polarized low-energy (eV $\sim$ meV) radioactive isotope (RI) beam is useful not only for nuclear physics but also in condensed matter physics and surface physics. We have so far determined a number of nuclear moments by using a spin polarization produced in the fragmentation reaction, with the β-NMR method at the RIKEN Ring Cyclotron facility. To overcome the difficulties forecast of β-NMR method when the measurement is

extended to the heavier mass region, we are developing a new method which has advantages quite complementary to the present method. This method based on *atomic beam resonance technique.* We call it the *RI atomic-beam resonance method* (RIABR).

An intermediate-energy (several tens of MeV/nucleon) RI beam from the projectile fragment separator is moderately decelerated by a degrader, and finally stopped in a gas volume filled with a rare gas. In the stopping gas volume a number of electrodes are arranged so that the field lines are parallel to each other in the most part of the volume. Towards the outlet orifice opened at the downstream end of the gas chamber, the electric field strength becomes so high that the field lines from the stopping volume are bunched into a small bundle which pass through the outlet orifice. The gas flow through the orifice also assists the extraction of RI ions. The RI ions are guided by the electric field acting in the next chamber while the carrier gas is highly evacuated out. The RI ions are then neutralized and transported by a sextupole magnetic field arrangement to an RF cavity. we select desired nuclear spin states and thus produce a polarized atomic beam by using an RF cavity and a quadrupole magnet. The total setup is illustrated in Fig. 1. With this system, we can get rid of the difficulties pertinent to the β-

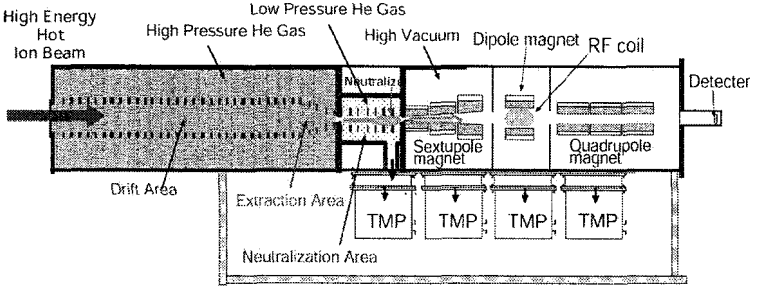

Figure 1. Total design of *RI atomic-beam resonance method*(RIABR).

NMR method, and expect to be able to measure electromagnetic moments of nuclei over the wide region of nuclei.

A prototype, including a fragment stopping and collecting chamber, jet separator, atomic-beam forming nozzle and spin-selecting sextupole magnet is almost completed. We are now developing and testing the prototype chamber by using a RI beam and simulating the flight orbits of RI in some conditions.

PROPERTIES OF SOFT-DIPOLE EXCITATION IN CALCIUM AND NICKEL ISOTOPES NEAR NEUTRON DRIP-LINE: MICROSCOPIC DESCRIPTION BY MEANS OF THE CONTINUUM QRPA METHOD*

KAZUHITO MIZUYAMA, YASUYOSHI SERIZAWA, MASAYUKI MATSUO
Graduate School of Science and Technology, Niigata University

In our study of the soft dipole excitation in oxygen isotopes by means of the continuum QRPA theory[1], we found that the di-neutron correlation plays important role. In the present work we investigate calcium and nickel isotopes in order to establish generality of the di-neutron correlation in the medium mass nuclei near near drip-line.

Focus is put on $^{50-58}$Ca and $^{80-86}$Ni, which are neighboring to the drip-line. In the calcium isotopes, a large amount of the dipole strength exists in an interval of a few MeV just above the one-neutron threshold energy. Similarly, the low-lying dipole strength just above the one-neutron threshold energy is seen in the nickel isotopes (Fig.1).

We examined the pair correlation effect by comparing with a calculation which does not take into account the pairing correlation ('no pairing' in Fig.1). The effect on the dipole strength is visible for the low-lying region near the threshold, but it is not as large as in the case of oxygen isotopes[2]. In a few cases, eg. in ^{54}Ca and ^{86}Ni, the E1 strength of the soft dipole excitation is slightly reduced by the pair correlation, which is an opposite tendency against the case of oxygen. The static pair correlation may enhance or reduce the E1 strength of the soft dipole excitation depending on the Fermi surface, while the dynamical pairing effect causes increase.

A significant pair correlation effect is evident when we look into the transition density $P^{add}(r)$ for the transfer of a spin singlet neutron pair (pair-add) to the soft dipole excitation. Its amplitude is as large as (or even larger than) that of the normal particle-hole transition density $\rho^{tr}(r)$ in several isotopes, indicating that a particle-particle character of the soft

*Work supported by the JSPS Grant-in-Aid for Scientific Research No. 14540250.

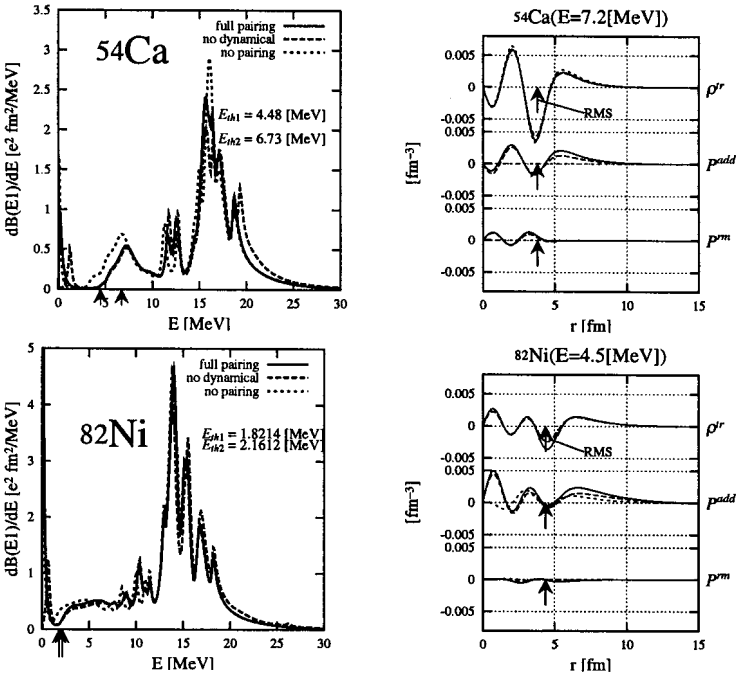

Figure 1. Left top: The calculated B(E1) strength function in ^{54}Ca (solid line). The dotted curve represents the results where the pairing correlation is neglected. The results neglecting only the dynamical pairing in the excited state is also shown by the dashed curve. Right top: The transition densities of the soft dipole excitation in ^{54}Ca. The upper, middle and lower plots show the normal, pair-add and pair-remove transition densities, respectively. Bottom: The same, but for ^{82}Ni.

dipole excitation. The dynamical pair correlation dramatically enhances the pair-add transition density.

Consequently, we find that the pair correlation plays an important role for the soft dipole excitation in Ca and Ni isotopes near neutron drip-line especially for the neutron pair transition density, in qualitative agreement with the case of oxygen. This suggests that the di-neutron correlation has generic importance for the soft dipole excitation in medium mass nuclei.

References

1. M. Matsuo, Nucl. Phys. **A696**, 371 (2001); Prog. Theor. Phys. Suppl. **146**, 110 (2002).
2. M. Matsuo, K. Mizuyama, Y. Serizawa, in this proceedings, and in preparation.

PROTON HALOS IN LIGHT PROTON-RICH NUCLEI

ZHONGZHOU REN

Department of Physics, Nanjing University, Nanjing 210008, China
zren@nju.edu.cn

X. Z. CAI, H. Y. ZHANG, W. Q. SHEN

Shanghai Institute of Nuclear Research, Shanghai 201800, China

The current study on proton halos in exotic light nuclei is simply reviewed and discussed. This includes the recently-observed proton halos in ^{17}F, ^{23}Al, $^{26-28}$P. We place emphasis on the newly discovered proton halo in ^{23}Al. The possible cause for a proton halo in ^{23}Al is analyzed and it is found deformation can be important for it.

1. Introduction

There are systematic studies on neutron halos in exotic neutron-rich nuclei [1,2,3,4,5]. However, studies on proton-rich nuclei are relatively few [6,7,8,9,10]. Recently there are some evidences of proton halos in the first excited state of ^{17}F and in the ground state of ^{26,27,28}P [8,9]. These agree well with the mean-field calculations [6,7,10]. The existence of proton halo in ^{27}P is also confirmed by Shen's group in China [11,12]. The existence of proton halo in ^{23}Al is proposed based on the measurement of the reaction cross section [11,12]. In this article we will discuss the experimental results on proton-rich nuclei near ^{23}Al and point out that deformation should be important for a proton halo nucleus ^{23}Al.

2. Proton halo in ^{23}Al

As the systematic analysis of reaction cross sections for proton-rich nuclei around ^{23}Al shows there is a proton halo in ^{23}Al [11,12], it is interesting to analyze why there is a proton halo in ^{23}Al.

If we review the experimental proton separation energy of ^{23}Al, we notice its proton separation energy is very small $S_p = 0.125$ MeV [13]. This demonstrates the last proton is very weakly bound in this nucleus. The

proton separation energy in its neighboring nucleus ^{22}Mg is as high as $S_p = 5.497$ MeV [13]. So ^{22}Mg is possibly a good inert core in ^{23}Al. This supports that there can be a proton halo in ^{23}Al.

The experimental ground state spin and parity of ^{23}Al is not available now. For its neighboring nucleus ^{22}Mg, there is a strong quadrupole deformation $\beta_2 = 0.56$ [14]. Because the last proton in ^{23}Al is very weakly bound, the deformation of ^{23}Al can be close to that of ^{22}Mg. According to the level sequence of deformed light nuclei by Bohr and Mottelson [15], the last proton in ^{23}Al should occupy the deformed state $(1/2)^+$ which is from the $2s_{1/2}$ state in a spherical case.

3. Conclusions

The proton halos in ^{17}F, ^{23}Al and ^{26,27,28}P are reviewed and discussed. For ^{23}Al, the deformation could play an important role for the appearance of the proton halo.

Acknowledgments

This work is supported by the National Natural Science Foundation of China under contract No. 10125521, by the fund of Education Ministry of China under contract No. 20010284036, by the Major State Basic Research Development Program in China under contract No. G2000077400.

References

1. I. Tanihata et al., *Phys. Lett.* **B206**, 592 (1988).
2. W. Mittig et al., *Phys. Rev. Lett.* **59**, 1889 (1987).
3. Zhongzhou Ren and Gongou Xu, *Phys. Lett.* **B252**, 311 (1990).
4. M. V. Zhukov et al, *Phys. Rep.* **231**, 151 (1993).
5. T. Otsuka et al, *Phys. Rev. Lett.* **70**, 1385 (1993).
6. Zhongzhou et al, *Phys. Rev.* **C53**, R572 (1996).
7. B. A. Brown and P. G. Hansen, *Phys. Lett.* **B381**, 391 (1996).
8. R. Morlock et al., *Phys. Rev. Lett.* **79**, 3827 (1997).
9. A. Navin et al., *Phys. Rev. Lett.* **81**, 5089 (1998).
10. Zhongzhou Ren, A. Faessler, A. Bobyk, *Phys. Rev.* **C57**, 2752 (1998).
11. X. Z. Cai et al., *Phys. Rev.* **C65**, 024610 (2002).
12. H. Y. Zhang, W. Q. Shen et al., *Nucl. Phys.* **A707**, 303 (2002).
13. G. Audi and A. H. Wapstra, *Nucl. Phys.* **A565**, 1 (1993).
14. S. Raman et al., *Ato. Dat. Nucl. Dat. Tab.* **36**, 1 (1987).
15. A. Bohr and B. Mottelson, *Nuclear Structure* , Vol. II.

DEVELOPMENT OF AN EXTRACTION CHAMBER FOR THE RI ATOMIC BEAM RESONANCE METHOD

K. SHIMADA, K. ASAHI, H. MIYOSHI, D. KAMEDA, K. SAKAI, S. EMORI, G. KATO, G. KIJIMA, AND M. TSUKUI
Department of Physics, Tokyo Institute of Technology

A. YOSHIMI, H. UENO, Y. KOBAYASHI, H. WATANABE, AND T. HASEYAMA
Applied Nuclear Physics Laboratory, RIKEN

J. MURATA
Department of Physics, Rikkyo University

A method to produce slow neutral radioactive isotopes (RI) beam and to measure their electromagnetic moments is under development, which is expected to be applied quite generally to an almost whole region of the nuclear chart. The method is essentially based on the atomic beam resonance technique (ABR)[1], and has a few advantages over the fragmentation-based polarization method, which has so far been employed in the nuclear moment measurements in light unstable nuclei. A key issue to the successful application of the present method to RI produced in the projectile-fragmentation (PF) reaction is the formation of a slow, neutral RI ions[2] from the PF reaction which inevitably have high kinetic energies.

To produce slow RI beam, the RI ions produced by the PF reaction is introduced into a high pressure helium volume where most of them are eventually stopped (Fig.1). In this volume, we apply a parallel and rather strong electric field, so that the stopped RI ions are swiftly separated from plasma region around the track of the RI ions and are drifted downstream. Close to the end of this volume, the increase in the field strength compresses the field lines into a small-diameter bundle at the outlet orifice. The RI ions drift following the field lines and thus they are compressed into the orifice. In the region close to the orifice, there exists a flow of the helium gas going out through the orifice. The velocity of the flow rapidly increases forward

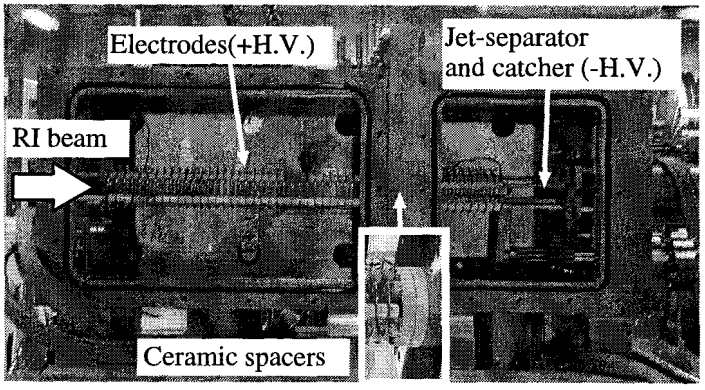

Figure 1. Schematic picture of the gas stopping chamber which consists of the RI-stopping and RI-drifting volume and JS volume.

a converging corn placed upstream of the orifice, and helps the RI ions to be transported through the orifice. As soon as the RI ions and the carrier helium gas enter the downstream chamber (jet-separator (JS) chamber), the helium gas is evacuated out by a high-power vacuum pumping system, while the RI ions are forced to proceed downstream by a strong parallel electric field. In the section located after this, the neutralization is achieved by passage of the ion beam through the charge exchange gas[3], but the detailed design of the neutralization section is under investigation.

In the present work, we have designed and fabricated an RI extraction chamber (Fig.1). In addition, test experiments with this chamber are undertaken. After testing an efficiency of the RI extraction by these experiments, we would start designing and fabrication of the neutralization section and spin selection section with the ABR methods.

References

1. H. Miyoshi et al., *RIKEN Accel. Prog. Rep.* **34**, 181 (2001).
2. H. Miyoshi et al., *RIKEN Accel. Prog. Rep.* **35**, 143 (2002).
3. T.M. DeTurck et al., *Nucl. Instr. and Meth.* B **172**, 293 (2000).

ON THE PRACTICAL INTEREST OF ONE-BODY OVERLAP FUNCTIONS

JEAN-MARC SPARENBERG

TRIUMF Theory Group, 4004 Wesbrook Mall, Vancouver, BC, Canada V6T 2A3, E-mail: jmspar@triumf.ca

BYRON JENNINGS

TRIUMF Theory Group, 4004 Wesbrook Mall, Vancouver, BC, Canada V6T 2A3, E-mail: jennings@triumf.ca

One-body (or few-body) functions extracted from full many-body microscopic wave functions provide a simplified and intuitive insight into the physics of complex nuclear structure. They also provide a detailed comparison tool between nuclear models, which can otherwise only be compared through the quality of their fit of a few experimental results (spectra, decay widths, etc.). Since particular one-body functions are also known[1] to be solutions of Schrödinger equations with simple potentials, they can be used to deduce such potential models from microscopic calculations by inversion of the Schrödinger equation. In the present work, we deduce the nuclear mean field in ^{8}B from microscopic models; in the future, we plan to generalize this formalism to one-cluster functions, which would allow us to deduce nucleus-nucleus potentials from nuclear cluster models and baryon-baryon potentials from quark cluster models.

There is however a basic problem for the use of one-body functions: two alternative functions appear in different theoretical frameworks of nuclear physics[1] and it is not clear which one of them (if any) has the most physical content. On the one hand, the particle-hole Green-function many-body formalism suggests to use the one-body overlap function $\phi(\mathbf{r})$, whereas the cluster model suggests to use the auxiliary function $\bar{\phi}(\mathbf{r}) = N_{\mathrm{p}}^{-1/2}\phi(\mathbf{r})$, where N_{p} is the particle-state norm operator. In the following, we present first attempts to distinguish between these two functions.

We have studied the possible difference between $\phi(\mathbf{r})$ and $\bar{\phi}(\mathbf{r})$ with respect to the properties of one-particle decay[2]. A reduction of the many-

body formalism to a one-body formalism for that case shows that both functions, because of their identical behavior outside the nuclear range, lead to identical decay widths and hence cannot be distinguished from one another. However, we have shown that these two functions lead to different definitions and possibly to different values for the spectroscopic factor.

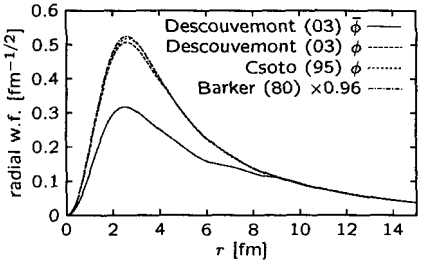

Figure 1. Radial part of the one-nucleon overlap functions $\phi(\mathbf{r})$ and of the auxiliary functions $\bar{\phi}(\mathbf{r})$ deduced from microscopic cluster models, compared with a phenomenological wave function, for the dominant component of the ^{8}B ground state.

More recently, we have compared two microscopic cluster models[3,4] with one another and with a phenomenological potential model[5], for the ^{7}Be$(3/2^-)$ + p component of the ^{8}B ground state with spin 2 and angular momentum 1. The corresponding functions are shown in Figure 1: the microscopic $\phi(\mathbf{r})$'s are close to one another and to the phenomenological wave function, which tends to prove that they have a strong physical meaning. Moreover, $\bar{\phi}(\mathbf{r})$ is significantly different from $\phi(\mathbf{r})$ for the model of Ref. 4 ($\bar{\phi}(\mathbf{r})$ is not available for the model of Ref. 3), which suggests that $\bar{\phi}(\mathbf{r})$ does not have such a strong physical content. This conclusion is however preliminary since the microscopic functions from Ref. 4 display a small oscillation between 5 and 9 fm, which shows that the numerical convergence of this calculation is not perfect.

References

1. J. Escher and B. K. Jennings, *Phys. Rev. C* **66**, 034313 (2002).
2. J. Al-Khalili, C. Barbieri, J. Escher, B. K. Jennings, and J.-M. Sparenberg, *Phys. Rev. C* **68**, 024314 (2003).
3. A. Csótó, K. Langanke, S. E. Koonin, and T. D. Shoppa, *Phys. Rev. C* **52**, 1130 (1995).
4. P. Descouvemont and D. Baye, *Nucl. Phys.* **A567**, 341 (1994), updated (private communication, 2003).
5. F. C. Barker, *Aust. J. Phys.* **33**, 177 (1980).

REACTION CROSS SECTIONS OF ^{12}C ON ^{12}C, ^{27}Al AND DENSITY DISTRIBUTION OF UNSTABLE NUCLEI*

M. TAKECHI, M. FUKUDA, M. MIHARA, K. TANAKA, T. CHINDA, T. MATSUMASA, Y. NAKASHIMA, K. MATSUTA, AND T. MINAMISONO

Department of Physics, Osaka University, Toyonaka, Osaka, 560-0043, Japan
E-mail: takechi@vg.phys.sci.osaka-u.ac.jp

R. KOYAMA, W. SHINOSAKI, M. TAKAHASHI, T. OHTSUBO, AND T. SUZUKI†

Department of Physics, Niigata University, Niigata 950-2102, Japan

T. IZUMIKAWA

RI Center, Niigata University, Niigata 951-8510, Japan

S. MOMOTA

Kochi University of Technology, Kami, Kochi 782-8502, Japan

T. SUDA

RIKEN, Wako, Saitama 351-0106, Japan

M. SASAKI‡ S. SATO, AND A. KITAGAWA

National Institute of Radiological Sciences, Chiba 263-8555, Japan

Reaction cross sections (σ_R) of $^{12}C + ^{12}C$ and $^{12}C + ^{27}Al$ systems were precisely measured in the energy range of $30A - 200A$ MeV, in order to make firm the basis of σ_R studies of unstable nuclei for density distribution of them. A $\sim$10% enhancement of σ_R over the optical-limit calculation, which gradually decreases as the energy increases, was observed in this energy range.

*This work was performed under the Research Project with Heavy Ions at NIRS-HIMAC.
†Present address: Department of Physics, Saitama University, Saitama 338-3570, Japan
‡Present address: Faculty of Science and Engineering, Ritsumeikan University, Kusatsu, Shiga 525-0055, Japan

Reaction cross sections (σ_R) of unstable nuclei provide a valuable chance to pursue the nucleon density distribution of exotic nuclei at the nuclear surface[1]. σ_R at lower energies of several tens MeV/nucleon are considered to be more sensitive to thinner nucleon densities, like a halo, because of much larger σ_{NN} at those energies compared with at higher energies. However, at these lower energies, optical limit of the Glauber theory that is successfully used at high energies to connect the density with σ_R gives somewhat smaller values of σ_R by 10-20 %[2].

In order to clarify the origin of this difference and also the reaction mechanism, we have precisely measured the σ_R of ^{12}C on ^{12}C and ^{27}Al at 30A - 200A MeV, where there was a lack of precise and systematic σ_R data of stable nuclei the densities of which are well known. The ^{12}C beams of a wide energy range were provided by the HIMAC synchrotron and the secondary beam facility.

Fig. 1(a) shows the present results of σ_R plotted as a function of beam energy. Based on this result, we discussed, i) more precise enhancement of experimental σ_R compared to the optical-limit calculations, ii) analysis with finite-range nucleon-nucleon interactions[3], iii) re-analysis for the density of ^8B[1] using the enhancement obtained in i) as a phenomenological correction factor to the optical-limit calculation and also using the result of ii), in the ^8B case. The density distribution of ^8B shown in Fig. 1(b) is a preliminary result of such an analysis in iii), which shows a good agreement with the Hartree-Fock calculation by Kitagawa and Sagawa[4].

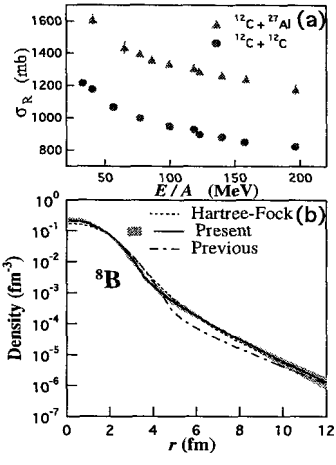

Figure 1. (a) σ_R results, (b) preliminary result of re-analysis for ^8B.

References

1. M. Fukuda et al., *Nucl. Phys.* **A656**, 209 (1999).
2. A. Ozawa et al., *Nucl. Phys.* **A608**, 63 (1996).
3. T. Zheng et al., *Nucl. Phys.* **A709**, 103 (2002).
4. H. Kitagawa, private communication; H. Kitagawa, N. Tajima, and H. Sagawa, *Z. Phys.* **A358**, 381 (1997).

MAGNETIC MOMENT OF ^{33}Cl

K. MATSUTA, K. ARIMURA, T. NAGATOMO, K. AKUTSU, T. IWAKOSHI, S. KUDO, M. OGURA, M. TAKECHI, K. TANAKA, T. SUMIKAMA, K. MINAMISONO, T. MIYAKE, T. MINAMISONO, M. FUKUDA, AND M. MIHARA

School of Science, Osaka Univ., Toyonaka, Osaka 560-0043, Japan
E-mail: matsuta@vg. phys.sci.osaka-u.ac.jp

A. KITAGAWA, M. SASAKI, M. KANAZAWA, M. TORIKOSHI, M. SUDA, M. HIRAI

National Institute of Radiological Sciences, Chiba 263-0024, Japan

S. MOMOTA, Y. NOJIRI, A. SAKAMOTO, M. SAIHARA

Kochi Univ. of Technology, Tosayamada, Kochi 782-8502, Japan

T. OHTSUBO

Faculty of Science, Niigata Univ., Niigata 950-2102, Japan

J.R. ALONSO, G.F. KREBS, AND T.J.M. SYMONS

Lawrence Berkeley Laboratory, Berkeley, CA 94720, USA

The magnetic moment of ^{33}Cl ($I^\pi = 3/2^+, T_{1/2} = 2.51$ s) has been re-measured precisely by β-NMR method. The obtained magnetic moment $|\mu| = 0.7549(3)\ \mu_N$ is consistent with the old value $0.7523(16)\ \mu_N$, but is 5 times more accurate. The value is well reproduced by the shell model calculation, $\mu_{SM} = 0.70\ \mu_N$. Combined with the magnetic moment of the mirror partner ^{33}S, the nuclear matrix elements $\langle l_p \rangle$, $\langle l_n \rangle$, $\langle S_p \rangle$, and $\langle S_n \rangle$ were derived.

The magnetic moment of short-lived β-emitter ^{33}Cl ($I^\pi = 3/2^+, T_{1/2} = 2.51$ s) was first measured in 1986 by W.F. Rogers et al. by means of β-NMR combined with the tilted foil technique [1]. However, the data was not so confident and had large error. In the present experiment, this magnetic moment has been re-measured by β-NMR technique for the more reliable and precise value.

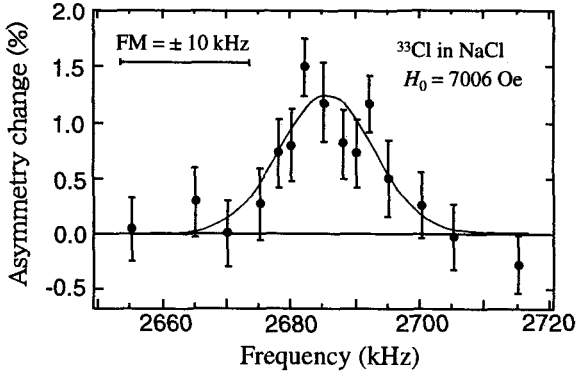

Figure 1. Typical NMR Spectrum.

The ^{33}Cl nuclei were produced in the $^{32}S(d,n)^{33}Cl$ reaction using d beam extracted from the Van de Graaff accelerator at the energy of 4.0 MeV. Reaction angle of 20° was selected to polarize the product nuclei. Thus polarized ^{33}Cl nuclei were implanted in a single crystal NaCl catcher, placed in a strong magnetic field H_0 of about 7 kOe. NMR was observed by means of asymmetric β-ray emission.

Typical NMR spectrum is shown in Fig. 1. The obtained NMR spectrum was analyzed by the least squares fit with a shape function based on a Gaussian, to extract the center frequency. The uncorrected magnetic moment was determined to be $|\mu_{uncorr.}| = 0.7540(3)\mu_N$. Correcting diamagnetism of 1180 (11) ppm, the magnetic moment was determined to be $|\mu(^{33}Cl)| = 0.7549(3)\mu_N$.

This value is larger by 0.35 % and 5 times more precise than the previously known value 0.7523(16). The present experimental magnetic moment is reproduced well by the shell model value 0.70 calculated by the OXBASH code [2]. Combined with the μ of the mirror partner ^{33}S (= 0.6438212(14)) and the β-decay transition rate, all the 4 angular momenta $\langle l_p \rangle = 1.3, \langle l_n \rangle = 0.3, \langle S_p \rangle = -0.12$, and $\langle S_n \rangle = -0.02$ were determined, assuming free nucleon g-factors.

References

1. W.F. Rogers, D.L. Clark, S.B. Dutta and A.G. Martin, *Phys. Rev. B* **177**, 293 (1986).
2. B.A. Brown, A. Etchegoye and W.D.M. Rae, *MSUCL Report* No. 524 (1988).

NUCLEON DENSITY DISTRIBUTION OF PROTON DRIP-LINE NUCLEUS ^{17}Ne

K. TANAKA, M. FUKUDA, M. MIHARA, M. TAKECHI, T. CHINDA, T. SUMIKAMA, S. KUDO, K. MATSUTA, AND T. MINAMISONO

Department of Physics, Osaka University, Toyonaka, Osaka, 560-0043, Japan
E-mail: ktanaka@vg.phys.sci.osaka-u.ac.jp

T. SUZUKI*AND T. OHTSUBO

Department of Physics, Niigata University, Niigata 950-2102, Japan

T. IZUMIKAWA

RI Center, Niigata University, Niigata 951-8510, Japan

Kochi University of Technology, Kami, Kochi 782-8502, Japan

S. MOMOTA, T. YAMAGUCHI, T. ONISHI, A. OZAWA, I. TANIHATA, AND ZHENG TAO

RIKEN, Wako, Saitama 351-0106, Japan

Reaction cross sections (σ_R) for ^{17}Ne were measured at intermediate energies. Nucleon density distribution of ^{17}Ne was deduced with the present σ_R data combined with those at high energies, using the Glauber-type calculation. The deduced density distribution was discussed by comparing with theoretical calculations.

The ground-state ^{17}Ne(I^π=1/2$^-$) is a candidate of a proton halo nucleus[1,2]. In order to clarify the halo structure, we studied the nucleon density distribution of ^{17}Ne through the precise measurements of reaction cross sections (σ_R) at beam energies of several tens MeV/nucleon. At these energies, the σ_R become sensitive to thin density region at the nuclear surface. Therefore comparing the σ_R at these energies with those at

*Present address: Department of Physics, Saitama University, Saitama 338-3570, Japan

high energies, the shape of the density distribution at the surface can be deduced[3].

For this purpose, we measured the reaction cross sections for ^{17}Ne at 40A MeV and 60A MeV on Be, C, and Al targets with a transmission method, using the secondary beam facility at RIKEN. To deduce the density distribution from σ_R data, the optical limit of Glauber calculation (OL) that connects both of them was used with a correction for the few-body effect[4]. A problem with this method is that a difference of σ_R between the experimental data and the Glauber calculation is seen at intermediate energies, even for a stable nucleus[5]. In order to deal with this problem, we corrected the difference phenomenologically using σ_R data of stable nuclei the density of which are well known from the electron scattering data. By fitting the calculated σ_R to the data including the present results and the high energy data [2], the optimized shape parameters of density distribution were determined.

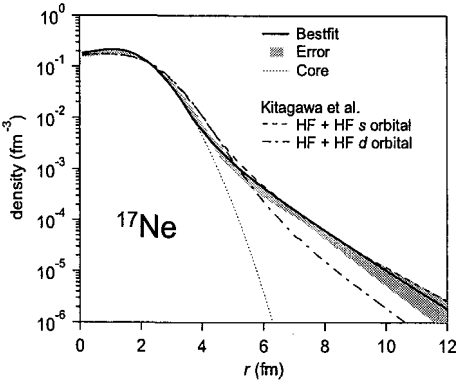

Figure 1. Density distribution of ^{17}Ne deduced in the present study (preliminary) compared with Hartree-Fock calculations.

Fig. 1 shows the preliminary result of the deduced density distribution compared with Hartree-Fock calculations [6] in which the valence two protons occupy the $2s_{1/2}$ orbital, or $1d_{5/2}$ orbital. This result shows the tail in the density is consistent with that the valence protons mainly stay in $2s_{1/2}$.

References

1. M.J.G. Borge et al., *Phys. Lett.* **B317**, 25 (1993).
2. A. Ozawa et al., *Phys. Lett.* **B334**, 18 (1994).
3. M. Fukuda et al., *Nucl. Phys.* **A656**, 209 (1999).
4. J. S. Al-Khalili, J. A. Tostevin, and J. J. Thompson, *Phys. Rev.* **C54**, 1843 (1996); Y. Ogawa, K. Yabana, and Y. Suzuki, *Nucl. Phys.* **A543**, 722 (1992).
5. A. Ozawa et al., *Nucl. Phys.* **A608**, 63 (1996).
6. H. Kitagawa, N. Tajima, and H. Sagawa, *Z. Phys.* **A358**, 381 (1997).

International Symposium
"A New Era of Nuclear Structure Physics" (NENS03)
Program

Tuesday, 18th November 2003
17:00-19:00 REGISTRATION
GET-TOGETHER DRINK

Wednesday, 19th November 2003
8:00-9:00 REGISTRATION
9:00-9:15 **Opening address**
A. Hasegawa (President of Niigata University)
Y. Suzuki (Chairman of the organizing committee)

.....

Session 1: **Nuclear force and few-body systems**
Chairperson: Y. Koike (Hosei Univ.)
9:15-9:45 W. Glöckle (Ruhr Universität Bochum)
Nuclear forces and few-nucleon studies based on chiral perturbation theory
9:45-10:05 K. Sekiguchi (RIKEN)
Measurement of nucleon-deuteron scattering as a good probe to study three nucleon forces
10:05-10:25 E. Uzu (Tokyo Univ. of Science)
Four-body Faddeev-Yakubovsky calculation using complex energy method
10:25-10:45 Y. Fujiwara (Kyoto Univ.)
A realistic baryon-baryon interaction in the SU_6 quark model and its applications to few-body systems

.....

10:45-11:10 COFFEE BREAK

.....

Session 2: **Hypernuclei and computational methods**
Chairperson: T. Kishimoto (Osaka Univ.)
11:10-11:40 O. Hashimoto (Tohoku Univ.)

Structure of Λ hypernuclei

11:40-12:00 M. Kohno (Kyushu Dental College)
Brueckner rearrangement energies in s-shell hypernuclei

12:00-12:20 M. Kamimura (Kyushu Univ.)
The 2003 update of antiproton mass by precision three-body calculation of antiprotonic helium atom

12:20-12:40 J. Usukura (Tokyo Univ. of Science)
Spectroscopy of the positronium molecule with the stochastic variational method

12:40-14:00 LUNCH

Session 3: **Nuclear structure from realistic forces and shell model**
Chairperson: Y. Suzuki (Niigata Univ.)

14:00-14:30 H. Feldmeier (GSI)
Nuclear structure – ab initio

14:30-14:50 S. Fujii (Univ. of Tokyo)
Shell structures in nuclei around ^{24}O described with modern nucleon-nucleon interactions

14:50-15:10 A. Poves (Universidad Autonoma)
Shell model spectroscopy and the bare NN and NNN forces

15:10-15:40 COFFEE BREAK

Session 4: **Nuclear shapes and rotation**
Chairperson: Y. Gono (Kyushu Univ.)

15:40-16:00 N. Yoshinaga (Saitama Univ.)
Triaxial deformation and chiral bands in nuclei around mass 130

16:00-16:20 A. Odahara (Nishinippon Inst. of Technology)
Development of unstable nuclear beam ^{17}N to search for high-spin isomers in $N = 51$ isotones

16:20-16:40 M. Koizumi (JAERI)
Coulomb excitation of stable even-even Zn isotopes

16:40-17:00 H. Watanabe (RIKEN)
Application of the high-spin isomers to the secondary fusion reaction and the g-factor measurement

18:30-20:30 WELCOME PARTY

Thursday, 20th November 2003

Session 1: **Light exotic nuclei**

Chairperson: A. Ellithi (Cairo Univ.)

8:45-9:15 I.J. Thompson (Univ. of Surrey)
Threshold and continuum structures in exotic nuclei

9:15-9:35 Y. Yamaguchi (Niigata Univ.)
Halo structure of ^{17}B studied via its reaction cross section

9:35-9:55 D. Baye (Universite Libre de Bruxelles)
Higher-order resolution of the time-dependent Schrödinger equation

9:55-10:15 M.S. Hussein (Universidade de Sao Paulo)
Three-body model for the complete fusion of a two cluster composite projectile with a heavy target

10:15-10:40 COFFEE BREAK

Session 2: **Light exotic nuclei and clustering**

Chairperson: Y. Fujiwara (Kyoto Univ.)

10:40-11:10 W. Mittig (GANIL)
Direct and resonant reactions at low energy with secondary beams

11:10-11:40 R.G. Lovas (Institute of Nuclear Research, Debrecen)
Resonating cluster

11:40-12:00 M. Ito (Univ. of Tsukuba)
Study on Be isotopes based on the generalized two-center cluster model

12:00 Conference Picture (B1F Royal Tainai Park Hotel)

12:00-13:30 LUNCH

Session 3: **Heavy exotic nuclei**

Chairperson: P. Descouvemont (Université Libre de Bruxelles)

13:30-14:00 G. Münzenberg (GSI)
Nuclear structure at GSI – some new developments

14:00-14:30 W. Nazarewicz (Univ. of Tennessee)
Structure of exotic nuclei

14:30-14:50 L.S. Ferreira (Instituto Superior Tecnico, Lisbon)
Proton radioactivity

14:50-15:20 COFFEE BREAK

Session 4: **Mean-field methods and effective interactions**
Chairperson: K. Matsuyanagi (Kyoto Univ.)
15:20-15:40 V.E. Oberacker (Vanderbilt Univ.)
Solution of the HFB continuum problem on a 2-D lattice: Neutron-rich and dripline nuclei
15:40-16:00 H. Nakada (Chiba Univ.)
Mean-field approach with M3Y-type interactions
16:00-16:20 M. Serra (Univ. of Tokyo)
Density and isospin dependencies in relativistic mean field models
16:20-16:40 J.R. Stone (Oxford Univ.)
Hartree-Fock mean field model with a separable nucleon-nucleon interaction

16:40-18:30 **POSTER SESSION**

Friday, 21st November 2003
Session 1: **Shell structure in exotic nuclei**
Chairperson: N. Zeldes (The Hebrew Univ. of Jerusalem)
9:00-9:30 T. Glasmacher (Michigan State Univ.)
Studying the structure of exotic nuclei at the coupled cyclotron facility at Michigan State University
9:30-10:00 T. Otsuka (Univ. of Tokyo)
Perspectives in the shell model
10:00-10:20 S. Ota (Kyoto Univ.)
Spectroscopy of ^{13}B via ^{4}He(^{12}Be, ^{13}B γ) reaction

10:20-10:40 COFFEE BREAK

Session 2: **Deformation and shell structure**
Chairperson: K. Asahi (RIKEN/Tokyo Inst. of Technology)
10:40-11:00 N. Imai (RIKEN)

Anomalously long lifetime of 2_1^+ state of ^{16}C

11:00-11:20 H. Sagawa (Univ. of Aizu)

New structure problems in carbon isotopes

11:20-11:40 M. Yamagami (Kyoto Univ.)

A self-consistent QRPA study of quadrupole collectivity around ^{32}Mg

11:40-12:00 D. Kameda (Tokyo Inst. of Technology)

g-factor measurement of ^{19}N

12:00-13:15 LUNCH

Session 3: **Excitation of exotic nuclei**

Chairperson: K. Kato (Hokkaido Univ.)

13:15-13:45 T. Aumann (GSI)

The structure of exotic nuclei investigated via scattering experiments with fast fragmentation beams at GSI

13:45-14:05 M. Matsuo (Niigata Univ.)

Di-neutron correlation and soft dipole excitation in medium mass nuclei near neutron drip-line

14:05-14:25 T. Nakatsukasa (Tohoku Univ.)

Response in the continuum for light deformed neutron-rich nuclei

14:25-14:45 M. Tohyama (Kyorin Univ.)

Quadrupole states of ^{22}O in extended RPA with ground-state correlations

14:45– FREE TIME

17:30-18:30 OPEN SESSION FOR LOCAL RESIDENTS

19:00-21:00 SYMPOSIUM DINNER

Saturday, 22nd November 2003

Session 1: **Density and gamma-transitions of unstable nuclei**

Chairperson: W. Nazarewicz (Univ. of Tennessee)

8:45-9:15 H. Sakaguchi (Kyoto Univ.)

Neutron densities of tin isotopes extracted from the proton elastic scattering and the RPS project at RIKEN

9:15-9:35 A. Kohama (RIKEN)

Determination of matter surface distribution of neutron-rich nuclei

9:35-10:05 H. Mach (Uppsala Univ.)

Nuclear structure studies of exotic nuclei via the strength of E2 transitions;

Advanced time-delayed $\gamma\gamma(t)$ spectroscopy at the extreme

10:05-10:25 J. Terasaki (Univ. of North Carolina)
Systematics of low-lying 2^+ states of even-even nuclei in neutron-rich Sn and Ni region

10:25-10:45 W.C. Ma (Mississippi State Univ.)
Triaxial superdeformation and wobbling mode in Lu-Hf isotopes

10:45-11:10 COFFEE BREAK

Session 2: **Spectroscopy of unstable nuclei**
Chairperson: G. Münzenberg (GSI)

11:10-11:40 N. Stone (Oxford Univ.)
g-factor measurement of short-lived excited states with radioactive ion beams

11:40-12:00 T. Ohtsubo (Niigata Univ.)
Magnetic hyperfine anomaly measurements using nuclear magnetic resonance on oriented nuclei

12:00-12:20 F. Maréchal (Institut de Recherches Subatomiques)
Beta strength distributions in $N \sim Z$ Kr and Sr isotopes using total absorption spectrometry

12:20– **Closing Remarks**
G. Münzenberg (GSI)

LUNCH

List of Participants

Badawy Abu-Ibrahim Sarhan
Dept. of Physics Niigata Univ.
Niigata 950-2181
JAPAN
badawy@nt.sc.niigata-u.ac.jp

Yuka Akimura
Dept. of Physics, Saitama Univ.
Shimo-Okubo 255, Saitama City, Saitama
338-8570
JAPAN
akimura@phy.saitama-u.ac.jp

Koji Arai
Dept. of Physics, Univ. of Surrey
Guildford, Surrey GU2 7XH
UNITED KINGDOM
k.arai@surrey.ac.uk

Koichiro Asahi
Dept. of Physics, Tokyo Inst. of Tech.
Oh-okayama 2-12-1, Meguro-ku, Tokyo
152-8551
JAPAN
asahi@phys.titech.ac.jp

Thomas Aumann
GSI
Planckstr. 1, D-64291 Darmstadt
GERMANY
t.aumann@gsi.de

Hidetada Baba
Rikkyo Univ.
Tokyo Toshima-ku, nishiikebukuro 3-34-1
JAPAN
baba@daq.rikkyo.ac.jp

Daniel Baye
Université Libre de Bruxelles
PNTPM, CP229,B1050 BRUSSELS
BELGIUM
dbaye@ulb.ac.be

Pierre Descouvemont
Université Libre de Bruxelles
Physique Nucléaire Théorique, CP229,
ULB, 1050 Bruxelles,
BELGIUM
pdesc@ulb.ac.be

Zoltan Elekes
RIKEN
2-1 Hirosawa, Wako, Saitama 351-0198
JAPAN
elekes@rarf.riken.jp

Ali Yehia Ellithi
Dept. of Physics, Facul. of Science, Cairo Univ.
Giza, 12613
EGYPT
ali@mailer.eun.eg

Hans Feldmeier
GSI
Planckstr. 1, D-64291 Darmstadt
GERMANY
h.feldmeier@gsi.de

Lídia Ferreira
CFIF/IST
Av. Rovisco Pais P-1049-001 Lisboa Portugal
PORTUGAL
flidia@ist.utl.pt

Shinichiro Fujii
Univ. of Tokyo
7-3-1 Hongo, Bunkyo-ku, Tokyo 113-8654
JAPAN
sfujii@nt.phys.s.u-tokyo.ac.jp

Yoshikazu Fujiwara
Dept. of Physics, Kyoto Univ.
Kitashirakawa, Oiwake-cho, Sakyo-ku, Kyoto
602-8431
JAPAN
fujiwara@ruby.scphys.kyoto-u.ac.jp

Tomonori Fukuchi
Center for Nuclear Study, Univ. of Tokyo
2-1 Hirosawa, Wako, Saitama 351-0198
JAPAN
fukuchi@cns.s.u-tokyo.ac.jp

Mitsunori Fukuda
Dept. of Phys., Osaka Univ.
1-1 Machikaneyama, Toyonaka, Osaka 560-0043
JAPAN
mfukuda@vg.phys.sci.osaka-u.ac.jp

Hans O. Fynbo
Dept. of Physics, Univ. of Aarhus
Ny Murkagade, OK-8000 Aarhus C
DENMARK
fynbo@phys.au.dk

Adrian Gelberg
Inst. für Kernphysik Univ. zu Köln
Zulpicherstr, 77, 50937 Köln
GERMANY
gelberg@ikp.uni-koeln.de

Thomas Glasmacher
MSU, NSCL
164 South Shaw Lane, East Lansing,
Michigan 48824
USA
glasmacher@nscl.msu.edu

Walter Glöckle
Theoretische Physik II, Ruhr Universität
Bochum
44780 Bochum
GERMANY
Walter.Gloeckle@tp2.ruhr-uni-bochum.de

Yasuyuki Gono
Dept. of Physics, Kyusyu Univ.
Hakozaki 6-10-1, Higashi-ku, Fukuoka
812-8581
JAPAN
gono@kutl.kyushu-u.ac.jp

Akira Hasegawa
President, Niigata Univ.
2-8050, Ikarashi, Niigata 950-2181
JAPAN

Osamu Hashimoto
Dept. of Physics, Tohoku Univ.
Sendai 980-8578
JAPAN
hashimot@lambda.phys.tohoku.ac.jp

Yukio Hashimoto
Univ. of Tsukuba
Ten-nou dai 1-1-1, Tsukuba, Ibaraki 305-8671
JAPAN
hashi@nucl.ph.tsukuba.ac.jp

Koji Higashiyama
Dept. of Physics, Saitama Univ.
Shimo-Okubo 255, Saitama City,
Saitama 338-8570
JAPAN
higashi@phy.saitama-u.ac.jp

Takatoshi Horibata
Aomori Univ.
2-3-1 Kobata Aomori-city, Aomori 030-0943
JAPAN
horibata@aomori-u.ac.jp

Mahir S. Hussein
Instituto de Física-USP
C.P.66318, 65315-970, São Paulo
BRAZIL
hussein@if.usp.br

Kei Iida
RIKEN
2-1 Hirosawa, Wako, Saitama 351-0198
JAPAN
keiiida@riken.go.jp

Nobuaki Imai
RIKEN
2-1 Hirosawa, Wako, Saitama 351-0198
JAPAN
imai@rarf.riken.jp

Tsunenori Inakura
Dept. of Physics, Kyoto Univ.
Kitashirakawa Oiwake-cho, Sakyo-ku, kyoto
606-8502
JAPAN
inakura@ruby.scphys.kyoto-u.ac.jp

Makoto Ito
Univ. of Tsukuba
1-1-1 Tennodai, Tsukuba, Ibaraki
JAPAN
itom@nucl.ph.tsukuba.ac.jp

Henrik Jeppesen
Dept. of Physics and Astronomy, Univ. of
Aarhus
8000 Aarhus
DENMARK
henjep@phys.au.dk

Daisuke Kameda
Tokyo Inst. of Tech.
2-1, Hirosawa, Wako, Saitama 351-0198
JAPAN
kameda@yap.nucl.ap.titech.ac.jp

Masayasu Kamimura
Kyushu Univ., Science Faculty
6-10-1 Hakozaki, Higashi-ku, Fukuoka
812-8581
JAPAN
kami2scp@mbox.nc.kyushu-u.ac.jp

Kiyoshi Kato
Division of Physics, Hokkaido Univ.
Kita 10 Nishi 8, Sapporo 060-0810
JAPAN
kato@nucl.sci.hokudai.ac.jp

Tadafumi Kishimoto
Dept. of Physics, Osaka Univ.
Toyonaka, Osaka 560-0043
JAPAN
kisimoto@phys.sci.osaka-u.ac.jp

Masato Kobayashi
Dept. of Physics, Kyoto Univ.
Kitashirakawa Oiwake-cho, Sakyo-ku,
Kyoto 606-8502
JAPAN
kobayasi@ruby.scphys.kyoto-u.ac.jp

Michio Kohno
Kyusyu Dental College
Manazuru 2-6-1, Kokurakita-ku,
Kitakyusyu 803-8580
JAPAN
kohno@kyu-dent.ac.jp

Mitsuo Koizumi
Japan Atomic Energy Research Inst.
(JAERI)
Shirane 2-4, Toukaimura, Naka, Ibaraki
319-1195
JAPAN
koizumi@jball4.tokai.jaeri.go.jp

Tom Lönnroth
Dept. Physics, Åbo Akademi Univ.
Porthansgatan 3, 20500 Turku
FINLAND
tlonnrot@abo.fi

Wenchao Ma
Dep. of Physics, Mississippi State Univ.
Mississippi State, MS39762
USA
mawc@ra.msstate.edu

Enrico Maglione
Dept. of Physics, Univ. of Padova and
INFN
Via Marzolo 8, I-35131 Padova
ITALY
maglione@pd.infn.it

Yohei Masamori
Niigata Univ.
2-8050, Ikarashi, Niigata 950-2181
JAPAN
yohei@np.gs.niigata-u.ac.jp

Hideki Matsumura
Niigata Univ.
2-8050, Ikarashi, Niigata 950-2181
JAPAN
hideki@nt.sc.niigata-u.ac.jp

Kenichi Matsuyanagi
Dept. of Phys, Graduate Schl. of Science,
Kyoto Univ.
Kitashirakawa, 606-8502 Kyoto
JAPAN
ken@ruby.scphys.kyoto-u.ac.jp

Akihisa Kohama
RI Beam Science Lab, RIKEN
2-1 Hirosawa, Wako-shi, Saitama 351-0198
JAPAN
kohama@rarfaxp.riken.go.jp

Yasuro Koike
Dept. of Physics, Hosei Univ.
2-17-1 Fujimi, Chiyoda-ku, 102-0071 Tokyo
JAPAN
koike@i.hosei.ac.jp

Ryo Koyama
Niigata Univ.
2-8050, Ikarashi, Niigata 950-2181
JAPAN
koyama@np.gs.niigata-u.ac.jp

Rezso Gyorgy Lovas
Inst. of Nuclear Research
Debrecen, PO BOX 51, H-4001
HUNGARY
rgl@atomki.hu

Henryk Mach
ISV, Uppsala Univ.
S 61182, Nyköping
SWEDEN
Henryk.Mach@Studsvik.uu.se

Francois Maréchal
Inst. de Recheches Subatomiques
23, Rue ow Loess BP28, F67037 Strasbourg
Cedex 2
FRANCE
francois.marechal@ires.in2p3.fr

Takuma Matsumoto
Dept. of Physics, Kyusyu Univ.
6-10-1 Hakozaki, Higashi-ku, Fukuoka 812-8581
JAPAN
taku2scp@mbox.nc.kyushu-u.ac.jp

Masayuki Matsuo
Niigata Univ.
2-8050, Ikarashi, Niigata 950-2181
JAPAN
matsuo@nt.sc.niigata-u.ac.jp

Wolfgang Mittig
GANIL
B9 5027 CAEN-Cedex 5
FRANCE
mittig@ganil.fr

Hisanori Miyoshi
Tokyo Inst. of Tech.
2-12-1, O-okayama, Meguroku, Tokyo
152-8551
JAPAN
miyoshi@yap.nucl.ap.titech.ac.jp

Kazuhito Mizuyama
Niigata Univ.
2-8050, Ikarashi, Niigata 950-2181
JAPAN
mizu@nt.sc.niigata-u.ac.jp

Hitoshi Nakada
Dept. of Physics, Chiba Unv.
Yayoi-cho 1-33, Inage, Chiba 263-8522
JAPAN
nakada@faculty.chiba-u.jp

Witold Nazarewicz
Univ. of Tennessee/ORNL
Knoxville, Tennessee 37996
USA
witek@utk.edu

Volker E. Oberacker
Dept. Physics, Vanderbilt Univ.
VU Station B351807, Nashville, TN37235
USA
volker.e.oberacker@vanderbilt.edu

Hiroshi Ohba
Niigata Univ.
2-8050, Ikarashi, Niigata 950-2181
JAPAN

Susumu Ohya
Niigata Univ.
2-8050, Ikarashi, Niigata 950-2181
JAPAN
ohya@np.gs.niigata-u.ac.jp

Masahiro Ota
Niigata Univ.
2-8050, Ikarashi, Niigata 950-2181
JAPAN
o-masa@np.gs.niigata-u.ac.jp

Alfredo Poves
Dept. o de Fisica Teorica
Universidat Autonoma, 28049-Madrid
SPAIN
alfredo.poves@uam.es

Hiroyuki Sagawa
Center for Mathematical Science,
Univ. of Aizu
Aizu-Wakamatsu, Fukushima 965-8580
JAPAN
sagawa@u-aizu.ac.jp

Shoujirou Mizutori
Kansai Women's College
Asahigaoka 3-11-1, Kashiwara, Osaka
JAPAN
mizutori@kwc.ac.jp

Gottfried Heinz Münzenberg
GSI
Planckstr. 1, D-64291 Darmstadt
GERMANY
G.Muenzenberg@gsi.de

Takashi Nakatsukasa
Physics Dept., Tohoku Univ.,
Sendai 980-8578
JAPAN
takashi@nucl.phys.tohoku.ac.jp

Thomas Neff
GSI
Planckstr. 1, D-64291 Darmstadt
GERMANY
t.neff@gsi.de

Atsuko Odahara
Nishinippon Inst. of Tech.
Aratsu 1-11, Kanda, Miyako, Fukuoka
800-0394
JAPAN
odahara@nishitech.ac.jp

Takashi Ohtsubo
Niigata Univ.
2-8050, Ikarashi, Niigata 950-2181
JAPAN
tohtsubo@np.gs.niigata-u.ac.jp

Shinsuke Ota
Kyoto Univ.
Kitashirakawa-oiwake-cho, Sakyo-ku, Kyoto
JAPAN
ota@nh.scphys.kyoto-u.ac.jp

Takaharu Otsuka
Dept. of Physics, Univ. of Tokyo
Hongo, Bunkyo-ku, Tokyo 113-0033
JAPAN
otsuka@phys.s.u-tokyo.ac.jp

Zhongzhou Ren
Dept. of Physics, Nanjing Univ.
Nanjing, Jiangsu 210093
P.R. CHINA
zren@nju.edu.cn

Harutaka Sakaguchi
Dept. of Physics. Kyoto Univ.
Kyoto 606-8502
JAPAN
sakaguchi@nh.scphys.kyoto-u.ac.jp

Kimiko Sekiguchi
Cyclotron Center, RIKEN
2-1 Hirosawa, Wako, Saitama 351-0198
JAPAN
kimiko@rarfaxp.riken.go.jp

Yasuyoshi Serizawa
Niigata Univ.
2-8050, Ikarashi, Niigata 950-2181
JAPAN
serizawa@nt.sc.niigata-u.ac.jp

Milena Serra
Department of Physics, Univ. of Tokyo
3-3-1 Hongo, Bunkyo-ku, Tokyo 113-0033
JAPAN
mserra@nt.phys.s.u-tokyo.ac.jp

Kenzi Shimada
Tokyo Inst. of Tech.
2-12-1, O-okayama, Meguroku, Tokyo 152-8551
JAPAN
shimada@yap.nucl.ap.titech.ac.jp

Wakako Shinozaki
Niigata Univ.
2-8050, Ikarashi, Niigata 950-2181
JAPAN
wakako@np.gs.niigata-u.ac.jp

Jean-Marc Sparenberg
TRIUMF
4004 Websbrook Mall, Vancouver, B.C.,
CANADA V6T 2A3
CANADA
jmspar@triumf.ca

Sergey Stepantsov
Flerov Lab. of Nucl. Reaction, Joint Inst. for Nucl. Research
Joliot Curie6, 141980 Dubna, Moscow region
RUSSIA
stepan@suntimpx.jinr.ru

Mario V. Stoitsov
Oak Ridge National Lab.
P.O. Box 2008, Oak Ridge, Tennessee 37831
USA
stoitsovmv@ornl.gov

Jirina R. Stone
Oxford Univ.
(home) 888 West Outer Drive, Oak Ridge, TN 37830
USA
j.stone@physics.ox.ac.uk

Nicholas J. Stone
Oxford Univ.
(home) 888 West Outer Drive, Oak Ridge, TN 37830
USA
n.stone@physics.ox.ac.uk

Takeshi Suzuki
Dept. of Physics, Saitama Univ.
Shimo-Okubo 255, Saitama City, Saitama 338-8570
JAPAN
suzuki@siva.ne.phy.saitama-u.ac.jp

Yasuyuki Suzuki
Niigata Univ.
2-8050, Ikarashi, Niigata 950-2181
JAPAN
suzuki@nt.sc.niigata-u.ac.jp

Masa Takahashi
Niigata Univ.
2-8050, Ikarashi, Niigata 950-2181
JAPAN
masa@np.gs.niigata-u.ac.jp

Maya Takechi
Dept. of Phys., Osaka Univ.
1-1 Machikaneyama, Toyonaka, Osaka 560-0043
JAPAN
takechi@vg.phys.sci.osaka-u.ac.jp

Aiko Takisawa
Niigata Univ.
2-8050, Ikarashi, Niigata 950-2181
JAPAN
aiko-t@np.gs.niigata-u.ac.jp

Kanenobu Tanaka
Dept. of Phys., Osaka Univ.
1-1 Machikaneyama, Toyonaka, Osaka 560-0043
JAPAN
ktanaka@vg.phys.sci.osaka-u.ac.jp

Iouri Tchouvilski
Skobeltsyn Inst. of Nucl. Phys. Moscow State Univ.
119992, Moscow, Russia
RUSSIA
tchuvl@nucl-th.sinp.msu.ru

Jun Terasaki
Dept. of Physics and Astronomy, Univ. of North Carolina
Chapel Hill, North Carolina 27599
USA
jterasak@physics.unc.edu

Ian J. Thompson
Dept of Physics, Univ. of Surrey
Guildford, Surrey GU2 7XH
UNITED KINGDOM
I.Thompson@surrey.ac.uk

Junko Usukura
Dept. of Physics, Tokyo Univ. of Science
1-3 Kagurazaka, Shinjyuku-ku, Tokyo
162-8601
JAPAN
usukura@neppliza.ph.kagu.tus.ac.jp

Hiroshi Watanabe
RIKEN
2-1 Hirosawa, Wako, Saitama 351-0198
JAPAN
hiroshi@rarfaxp.riken.go.jp

Yoshitaka Yamaguchi
RIKEN (Niigata Univ.)
2-1 Hirosawa, Wako, Saitama 351-0198
JAPAN
yamaguch@rarfaxp.riken.go.jp

Naotaka Yoshinaga
Saitama Univ.
Shimo-Okubo 255, Saitama City, Saitama
338-8570
JAPAN
yoshinaga@phy.saitama-u.ac.jp

Mitsuru Tohyama
Kyorin Univ. School of Medicine
6-20-2 Shinkawa, Mitaka, Tokyo 181-8611
JAPAN
tohyama@kyorin-u.ac.jp

Eizo Uzu
Dept. of Physics, Tokyo Univ. of Science
2641 Yamazaki, Noda, Chiba, 278-8510
JAPAN
j-uzu@ed.noda.tus.ac.jp

Masayuki Yamagami
Kyoto Univ., Dept. of Physics, Graduate
School of Science
Kitashirakawa, 606-8502, Kyoto
JAPAN
yamagami@ruby.scphys.kyoto-u.ac.jp

Kenichi Yoshida
Dept. of Physics, Kyoto Univ.
Kitashirakawa, Sakyo-ku, Kyoto 606-8502
JAPAN
kyoshida@ruby.scphys.kyoto-u.ac.jp

Nissan Zeldes
The Racah Inst. of Physics
The Hebrew University of Jerusalem,
Jerusalem 91904
ISRAEL
zeldes@vms.huji.ac.il

This page intentionally left blank

A New Era of

Nuclear Structure Physics

This book is a collection of invited talks, oral contributions and poster contributions devoted to advances in nuclear physics. It covers a broad range of topics on nuclear physics including nuclear force, hypernuclei, nuclear structure, exotic nuclei, clustering, mean-field method, shell structure, nuclear deformation, unstable nuclei, and related topics.

World Scientific
www.worldscientific.com
5666 hc

ISBN 981-256-054-8
9 879812 560542